Università degli Studi di Palermo

AREA RICERCA E TRASFERIMENTO TECNOLOGICO
SETTORE DOTTORATI E CONTRATTI PER LA RICERCA
U. O. DOTTORATI DI RICERCA

Dottorato di Ricerca in Scienze Fisiche e Chimiche
Dipartimento di Fisica e Chimica – Emilio Segrè
Settore Scientifico Disciplinare PHYS/05A

THIN-FILM FILTERS FOR SOLAR ASTROPHYSICS: SCIENCE AND TECHNOLOGY DEVELOPMENT FOR THE NASA MUSE MISSION

IL DOTTORE
EDOARDO ALAIMO

IL COORDINATORE
PROF. MARCO CANNAS

IL TUTOR
PROF. FABIO REALE

IL CO-TUTOR
PROF. MARCO BARBERA

CICLO XXXVIII
ANNO CONSEGUIMENTO TITOLO 2026

Pirates are evil? The Marines are righteous? These terms have always changed throughout the course of history! Kids who have never seen peace and kids who have never seen war have different values! Those who stand at the top determine what's wrong and what's right! This very place is neutral ground! Justice will prevail, you say? But of course it will! Whoever wins this war becomes justice!

Donquixote Doflamingo (Eichiiro Oda, One Piece)

Contents

List of Acronyms

2D Two-dimensional 11

3D Three-dimensional 27

AFM Atomic Force Microscopy 32

AIA Atmospheric Imaging Assembly (SDO) 4

APS Active Pixel System (PROBA-2/SWAP) 14

AR Active Region 4

ASI Agenzia Spaziale Italiana (Italian Space Agency) 13

AU Astronomical Unit 55

BF Blocking Factor 21

BGFA Bi-Gaussian Fitting Analysis 118

BKG Background 40

CBM Common Beam Mask 63

CCD Charge-coupled Device 8

CDR Critical Design Review 6

CfA Harvard-Smithsonian Center for Astrophysics 118

CI Context Imager (MUSE) 6

CMA Chinese Meteorological Administration 15

CME Coronal Mass Ejection 4

CNSA China National Space Administration 15

CNT Carbon Nanotube xv

CODATA Committee on Data for Science and Technology 55

DC Direct Current 94

DEM Differential Emission Measure 121

DKIST Daniel K. Inouye Solar Telescope 7

DM Demonstration Model (also Development Model) 14

DM Qualification Model 107

List of Figures

List of Tables

List of Prior Publications and Copyright Statement

The ensuing chapters of the manuscript are partly or mostly based on the following prior publications, either authored or co-authored by me, including proceedings, research papers, conference presentations, and the M.Sc. thesis.

Chapter 2 Filter Designs and Diffraction Studies

E. Alaimo, D. Spiga, A. Daw, F. Reale, B. De Pontieu, P. Boerner, P. Testa, U. Lo Cicero, M. Todaro, L.Sciortino, F. D'Anca, G. Cozzo, F. Fiorentino, C. Argiroffi, P. Pagano, P. T. Törmä, I. Varjos, M. Moisanen, B. Mikladal, J. Etula, D. Brienza, D. Perrone, M. Stangalini and M. Barbera. "Investigation on the role of optical filters on the point spread function of the NASA MIDEX solar mission MUSE" **2025**, *Proc. SPIE 13699, International Conference on Space Optics — ICSO 2024, 136995J.* DOI: 10.1117/12.3075223.

M. Barbera, F. D'Anca, M. Todaro, L. Sciortino, U. Lo Cicero, E. Alaimo, F. Fiorentino, S. Varisco, R. Candia, G. Di Cicca, N. Montinaro, F. Reale, C. Argiroffi, G. Cozzo, P. Pagano, D. Spiga, D. Brienza, Denise Perrone, M. Stangalini, P. T. Törmä, J. Kostamo, I. Varjos, M. Moisanen, B. Mikladal, P. Boerner, B. De Pontieu, V. Knagenhjelm, P. Cheimets, E. Hertz and P. Testa. "Metal-coated carbon nanotube ultrathin pellicles: a high-performance solution for the optical blocking filters of the NASA MIDEX solar mission MUSE" **2025**, *Proc. SPIE 13699, International Conference on Space Optics — ICSO 2024, 136991P.* DOI: 10.1117/12.3075219.

E. Alaimo. "Simulation of Point Spread Functions of EUV Entrance Filters for the NASA MUSE Mission" **2025**, Presentation at "The International Workshop on Physics of X-Ray and Neutron Multilayer Structures", *PXRNMS2025, 9-11 April 2025, Università degli Studi di Padova, Italy.* HANDLE: 10447/693053 CONFERENCE: pxrnms2025.dei.unipd.it.

Chapter 3 Visible Performance

E. Alaimo. "Optical performance of Aluminum-coated carbon nanotube pellicles for the NASA MUSE space mission" **2025**, Presentation at the "111° National Congress of the Italian Physical Society", *22-26 September 2025, Università degli Studi di Palermo, Italy.* CONFERENCE: en.sif.it/activities/congress/111 HANDLE: 10447/693051 URL: 2025.congresso.sif.it/talk/568.

E. Alaimo. "Characterisation and Modelling of the UV-Vis/IR Transmission of Multilayer Thin Film Filters for Applications in High Energy Astrophysics" **2022**, M.Sc. Thesis, *Zenodo*. DOI: 10.5281/zenodo.7213579.

Chapter 4 Extreme-Ultraviolet and X-ray Transmittance

E. Alaimo, M. Todaro, L. Sciortino, U. Lo Cicero, F. Fiorentino, F. D'Anca, S. Varisco, R. Candia, G. Di Cicca, F. Reale, P. Pagano, C. Argiroffi, A. Petralia, P. Testa, G. Cozzo, P. N. Cheimets, P. Boerner, B. De Pontieu, V. Knagenhjelm, P. T. Törmä, M. Moisanen, B. Mikladal, B. Haq, B. R. Zeiger, P. Mercère, P. Da Silva, D. Brienza, D. Perrone, M. Stangalini and M. Barbera. "Optical blocking filters for the Multi-slit Solar Explorer mission: in-band extreme ultraviolet and soft X-ray transmittance spectroscopy measurements and analysis", *J. Astron. Telesc. Instrum. Syst.* **2025**, *11* (4), 048001. DOI: 10.1117/1.JATIS.11.4.048001.

The **Introduction** contains elements from **all of the above**, and the following.

G. Cozzo, J. Reid, P. Pagano, F. Reale, P. Testa, A. W. Hood, C. Argiroffi, A. Petralia, E. Alaimo, F. D'Anca, L. Sciortino, M. Todaro, U. Lo Cicero, M. Barbera, B. De Pontieu and J. Martinez-Sykora, "Coronal energy release by MHD avalanches - II. EUV line emission from a multi-threaded coronal loop", *A&A*, 689 **(2024)** A184. DOI: 10.1051/0004-6361/202450644.

Abstract

Extreme ultraviolet (EUV) filters are key components for space missions to the solar environment, providing the necessary wavelength selection and attenuation of visible light. My thesis contributes to the optical and technological consolidation of the NASA MUSE (Multi-slit Solar Explorer) mission, an EUV solar observatory designed to probe coronal dynamics with unprecedented spatio-temporal resolution, with the primary objective to enable the first observations of the EUV solar corona able to aid the required physical modeling to hone the theories answering open questions in astrophysics, such as the Coronal Heating problem.

My dissertation aids the mission through the study, design, and characterization of thin-film input filters optimized for extreme ultraviolet (EUV) observations, while also proposing a few methodological contributions to the analysis of multi-slit spectral data. The work focuses on input filters for the spectrograph and context sensor, which must offer high EUV transmittance, high UV-VIS-IR rejection to prevent CCD signal degradation, limited diffraction-induced image degradation, and mechanical robustness to withstand launch vibro-acoustic loads.

In **Chapter 1** **(Introduction)** I introduce the state-of-the-art of thin optical blocking filters, their use in solar space missions, and discuss the role of diffraction, transmittance in various wavelength bands, and mechanical resistance. I also introduce the MUSE mission, its scientific objectives, and how this work contributes to the consolidation of the mission's payload and to advancing the scientific and technological maturity of the proposed thin films. Furthermore, alternative applications of EUV thin films are also detailed, along with the broader EUV space missions state of the art.

In **Chapter 2** **(Filter Designs and Diffraction Studies)** I present the filters' designs, both based on heritage missions and on novel carbon nanotube (CNT) substrates, and introduce the techniques employed numerically to assess their diffraction impact at the focal plane of the mission. I conclude that the proposed CNT-based thin film filters can offer augmented performance diffraction-wise when compared to heritage-based solutions. At the same time, in the channel of the Fe XV line at 284 Å , I show how a study of the trade-off between raw signal in the core encircled-energy and relative intensity of the diffracted secondary peaks is required, since the CNT-based solutions produce less relative diffraction. In contrast, the heritage-based solution proves to be more intense at the core.

In **Chapter 3** **(Visible Light Attenuation Performance)** I discuss the filters' visible performance, with a detailed description of the requirement definition and the experimental assessment over aluminized small witness samples. I present the transmittance requirement for the Context Imager telescope to have $T < 10^{-6}$ in the UV-VIS-IR range as a flat-band requirement and discuss experimentally how all Al-coated designs satisfy it, with the heritage-based filters satisfying it

with a greater margin.

In **Chapter 4** **(Extreme-Ultraviolet and X-ray Transmittance)** I detail the transmittance of small witness samples of all filter designs evaluated with experiments of X-ray Absorption Spectroscopy (XAS) carried out with synchrotron radiation, to provide MUSE in-band transmittance curves and to derive by analysis the inner-layer compositional data for the different filter designs. More native oxidation on the metal coatings deposited on CNT substrates is observed. Yet, even with worse oxidation, the CNT-based filters outperform heritage-based solutions with a PI substrate in all channels in terms of raw transmittance. On the other hand, heritage-based solutions with no substrate remain the most transmissive across all channels. The results confirm the expected performance of heritage solutions and expand knowledge of the new technology of CNT as a valid substrate for applications in space astrophysics.

In **Chapter 5** (**Work in Progress: Penning Discharge Source Set-Up**), a technical note paragraph, I showcase the ongoing progress towards the set-up and operation of an EUV Penning discharge source of interest for the ground calibration of the MUSE instrumentation.

Chapter 6, the **Conclusion**, rounds up the thesis.

Appendices follow, serving to complement the information provided throughout the main text. A special mention goes towards **Appendix E** **(Bi-Gaussian Fitting Software for MUSE)**, where I briefly introduce MUSE's data processing and information retrieval machinery, complementing almost entirely the experimental part, and I detail the development of a novel software strategy aiming to address some expected complexities. This approach demonstrated initial successes, possibly inspiring future approaches in which the complexity of the data analysis induced by the novelty of the multi-slit in MUSE can be diminished or even solved completely, even with a simple physics-based approach.

1 Introduction

1.1 Once upon a time ...

This begins on a solemn note, drawing inspiration from the Greek myth of *Daedalus and Icarus*. The uninterested reader can skip to the introduction's contents →p.2. Daedalus was a renowned craftsman, inventor, and architect who built the Labyrinth for King Minos of Crete to confine the Minotaur. Due to reasons related to vengeance and a series of unfortunate events, Minos forced the citizens of Athens to provide fourteen tributes to the Minotaur every nine years. Daedalus – seeking peace – wanted to end the tributary agony, and decided to aid Theseus, legendary king of Athens, in escaping the Minotaur's labyrinth after defeating the Minotaur in battle. This help did not go unnoticed by Minos, who decided to retaliate by locking Daedalus and his son, Icarus, in a tower in the middle of the ocean. The tower had guards and locks at the entrance, akin to a prison, and this was where the genius of Daedalus unfolded, gazing at the sky above and expressing his vision to his son.

> *"'He may thwart our escape by land or sea' he said 'but the sky is surely open to us: we will go that way: Minos rules everything but he does not rule the heavens'"*
>
> Ovid, VIII.183-235, Metamorphoses, c. 8 CE – *Translation by A. S. Kline (2000)*

They were limited by sea and land, but had no limit in the sky. Daedalus came up with a plan: constructing two pairs of wings with feathers that fell from the birds above, and wax likely gotten from the candles in the prison, and using them just like the birds to fly towards freedom: an almost spotless plan. Daedalus made sure to instruct his son on proper flying and warned him not to fly too close to the sun. Tragically, Icarus ignored his father's counsel, delightfully believing that he could reach the heavens by soaring as high as possible. This quickly led to sunshine's reality check, the melting of the wax, and his demise in the sea. Daedalus kept flying in a controlled manner, and, after catching sight of the feathers on the sea underneath, he quickly understood the situation and cursed his own inventions. There are a few aspects regarding this story that make it quite fitting for this work. First of all, the contributions share a bit of Icarus' arrogance: that of enabling unprecedented observations of the sun, giving way to finding the solution to some of its *faintest secrets*. Secondly, and most importantly, the work imparts lessons and wisdom from Daedalus on the relevance of proper testing and guidance in the context of materials and technologies for space applications. Particularly in the case of novel inventions, it is mandatory to respect and explore their limits by conducting proper research to increase their reliability for use in aerospace and to avoid unwanted outcomes. That is the main scope of this work and of my contributions: to improve the knowledge of largely unknown materials, and to prove knowledge of known materials again. Among many encompassing science,

simulations, and technological advancements, this work is part of a great journey towards a major problem. As novel and proven technologies are tested, risks are also minimised to ensure the mission's flawless conduct. The whole group involved in the mission is planning to fly close to the sun and is also planning all the measures to ensure its success. One big difference stands between Icarus and us: had he used filters to shield the wings from the solar visible light, *just like the ones studied and developed here*, nobody would be talking about his demise.

Remark 1 (introduction's contents)**.** The introduction ensues with a top-down approach, from the space mission scale to its optical filters and their *soap bubble* thicknesses, which compound the experimental, simulative, and modeling core of my work. I will describe:

- A discussion of the phenomenology of the solar corona, along with details of the open question of the *coronal heating problem*
- A description of the MUSE space mission, its payload, and objectives.
- A description of EUV thin film filters, their crucial role in solar space missions, and their requirements, along with details of their applications in other areas, and other complementary filtering and/or rejection approaches found in the solar space missions state of the art.
- A direct link between these requirements and the different parts of the thesis, with contributions to most aspects regarding the thin film optical blocking filters for the mission

Tables and figures will use an independent incremental numbering system throughout the work, which will always begin with the chapter number. Remarks, used more sparingly, will employ an incremental system with a single number. **Let's begin.** ⌟

1.2 Scientific context: the sun and the mission

A brief introduction to the solar corona

The solar corona is not plain in sight in visible light: it's hidden by the luminous solar main body. There is no way to appreciate it with the naked eye, as one needs dedicated equipment for observation, and since it is millions of times fainter than the sun itself, total eclipses are great opportunities to capture it. An example of a processed picture of the solar corona obtained during an eclipse with a system of cameras is shown in Fig. 1.1, where both the solar corona and the earthshine reflected on the moon are visible.

Figure 1.1 High-dynamic-range composite of the solar corona during totality of the 8 April 2024 total solar eclipse. The image is an HDR blend of multiple exposures captured with Nikon D850 systems at different focal lengths and processed to reveal the faint coronal structure and preserve local contrast. Credit: Jonathan Hill, all rights reserved. Used with permission. Original Source: ASTROBIN/jdh_astro (last accessed 2025-11-14).

The intricate structures of the solar corona are a clear fingerprint of the highly energetic phenomena arising from within the sun and propagating outward. For a long time, humans have been looking at our star relentlessly, either out of curiosity or for scientific reasons, in the visible light: accounts of the total number of sunspots

– also related to *solar activity* and to the *solar cycle* – date back to the 1700s [1]. Sun's warmth does not just tickle the imagination. There are correlations between what is seen on the solar's surface and what happens on Earth, and one great example of such happenings is the *Carrington's Event* of 1859, in which telegraph operators stated that they could use their systems disconnected from direct power supply by virtue of the currents induced by the aurora. Events of such strengths could have a huge impact on the global economy today [2]. There is so much that visible light can reveal: by *changing glasses*, one can see a plethora of phenomena hidden deep within the electromagnetic spectrum of this region and linked to different atomic physics at different temperatures. Observations of the solar corona by Vaiana et al. had shown a structured solar corona with magnetized plasma and bright spots on the sun in the X-rays, implying extremely hot temperatures of the corona even during lows of the solar cycle [3]. Recent missions, such as SDO (Solar Dynamics Observatory), with its instruments HMI (Helioseismic and Magnetic Imager) and AIA (Atmospheric Imaging Assembly), have collected images showing how diverse the sun appears when observed at various lines in the EUV or visible range. Indeed, the AIA wavelength channels probe different temperatures, altitudes in the corona, and main ions, as described in Lemen et al. [4]. In contrast, the HMI continuum image probes the visible photosphere. Decades of space and ground based observations – made with observatories such as Solar Orbiter's Extreme Ultraviolet Imager (EUI) [5], Hinode's Extreme-ultraviolet Imaging Spectrometer (EIS) [6] [7] and SDO/AIA [8] [4] – allowed solar physicists and scientists to establish the ground phenomenology that occurs on the solar corona in various wavelength bands, and the picture currently arising is that the solar corona is a laboratory for magnetized plasma far from equilibrium where impulsive energy releases, waves, turbulence and magnetic reconnection operate across various spatio-temporal scales. Higher temperatures and energies probe the solar atmosphere from the chromosphere up to the solar corona, and, to state a few of the solar corona regions and phenomena currently studied by the scientific community, there are observations and studies regarding, and not limited to: the quiet corona or quiet sun (QS), the transition region (TR), active regions (ARs), solar flares or flaring corona, coronal holes, coronal loops, coronal mass ejections (CMEs), and solar prominences. [9] [10] [11] [12] [13] [14]. The variety of appearances and structures in the solar corona is shown in Fig. 1.2.

An important aspect is that, while the photosphere of the Sun – i.e., the layer which emits most of the solar light – has temperatures of the order of 5800 K, the solar corona is composed of plasmas with temperatures of the order of 10^6 K. Temperatures can skyrocket to 10^7 K and above in highly energetic events. A few major questions are currently being tackled in the field of solar astrophysics: How does the corona heat up to such high temperatures, starting from a cooler layer? Which physical mechanisms allow for the conversion of the energy to heat and bulk coronal flows? How do these processes couple the transition region and corona during flares and CMEs? While the latter question concerns the understanding of the microphysics underlying the triggering and evolution of strong CME events, the first two questions form the core of the *coronal heating problem*, a currently

Table 1.1 Indicative primary ions and characteristic temperatures of a selection of SDO/AIA's channels, adapted from Lemen et al. [4]. Avg. $\log_{10}(T)$ indicates the characteristic (log-)temperatures of the emitting plasma probed by the given wavelengths of the channel, and Main ion(s)'s column indicates the main ionic population probed (i.e., responsible for the wavelength emission). TR is the transition region, AR is the active region.

Channel	Main ion(s)	Solar atmospheric regions	Avg. $\log_{10}(T)$
	SDO / AIA		
4500 Å	continuum	photosphere	3.7
304 Å	He II	chromosphere, TR	4.7
171 Å	Fe IX	quiet sun, upper TR	5.9
193 Å	Fe XII, XXIV	∼1-2 MK corona, hot flare plasma	6.2, 7.3
211 Å	Fe XIV	AR corona	6.3
335 Å	Fe XVI	AR corona	6.4
94 Å	Fe XVIII	flaring corona	6.8
131 Å	Fe VIII, XXI	TR, flaring corona	5.6, 7.0

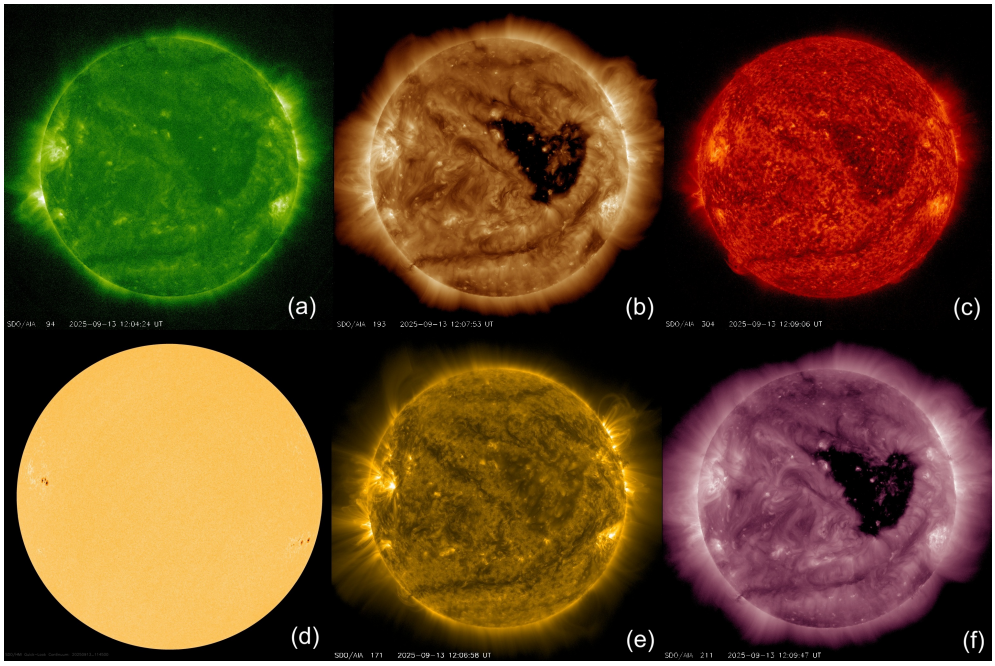

Figure 1.2 Composite multi-wavelength montage of the Sun observed by NASA's Solar Dynamics Observatory on 2025-09-13. Panels: (a) AIA 94 Å; (b) AIA 193 Å; (c) AIA 304 Å; (d) HMI continuum (photosphere); (e) AIA 171 Å; (f) AIA 211 Å. The sequence reveals coronal loops, prominences, and active regions, and highlights a large *heart*-shaped dark region – a coronal hole – visible as a in (b) and (f). Images have been contrast-enhanced and colour-mapped for display clarity. Credit: NASA / SDO (AIA, HMI). Images source: sdo.gsfc.nasa.gov/data (last accessed 2025-11-14).

open problem in astrophysics [15] [16]. It was shown that definite progress in answering both questions requires observations that capture variability, flows, and line broadening at high cadence (raster times < 20 s) over active-region scales, alongside modeling efforts that bridge energy conversion and solar coronal plasma thermodynamics and magnetohydrodynamics [17] [18] [19] [20]. Current solar space missions have required minutes to capture portions of the Sun during rastering, thereby losing evolution and detail; this highlights the NASA MUSE mission.

The NASA MUSE mission: objectives and payload

MUSE, the Multi-Slit Solar Explorer [17] [18] [19], is a Medium-Class Explorer (MIDEX) NASA future mission that will be operating in the EUV. It will orbit Earth in a Sun-synchronous (SSO) and low-earth orbit (LEO) altitudes of about $\sim 600 \div 650$ km. Its primary objective is to provide EUV spectroscopic and imaging observations of the solar corona and transition region with unprecedented spatiotemporal resolution to address the aforementioned fundamental and currently open questions, such as coronal heating and the energetics and dynamics of the unstable solar atmosphere, with a particular focus on the phases preceding, following, and during solar flares or coronal mass ejections [9]. On May 9, 2025, the MUSE mission passed the Critical Design Review (CDR), a key milestone on its path to launch, scheduled for 2027. The MUSE payload includes a state-of-the-art spectrograph (SG), an EUV telescope capable of achieving sub-arc-second (< 0.5”) spatial resolution over a field-of-view (FOV) of approximately $\approx 156'' \times 170''$. The SG operates simultaneously with 35 slits, enabling sampling times of < 20s and sampling spectra from three key narrow wavelength bands, [17] i.e., 171 Å, 284 Å , and 108 Å including respectively strong Fe IX, Fe XV and Fe XIX / Fe XXI lines, with an expected spectral resolving power of $\approx 2,500 - 4,200$, which is extremely pronounced with respect to the existing literature and space missions. A second telescope complements the SG, a context imager (CI), which will capture high-spatial-resolution imaging data over a larger FOV ($580'' \times 290''$) at high-cadence in complementary EUV channels, 195Å and 304Å , containing respectively Fe XII and He II lines, and which will operate simultaneously with the SG observations. The primary emitting ions collectively enable MUSE to explore layers of the solar atmosphere, from the transition region to the corona [19], enabling detailed studies of coronal heating and dynamics on appropriate timescales, as well as visualizing the context in the transition region and corona surrounding these solar phenomena. Moreover, the pronounced spectral power of the SG telescopes allows MUSE to gather detailed diagnostics of the plasma (or ionized gas) in the parts of the solar corona observed, including temperature, velocity, line broadening, and turbulent motions, pieces of information that will be inferred with the Doppler-shift information of the main-line emitted by the plasma captured. Table 1.2 →p.7 summarizes how different main ions probe different temperatures in the solar atmosphere in the case of MUSE. At the same time, an illustration of the MUSE satellite is provided in Fig. 1.3, where the filters, the main topic

of this thesis, are shown in the entrance pupil. MUSE builds on the legacy of

Table 1.2 Indicative main ions and characteristic temperatures of MUSE's main lines, i.e., wavelength channels. Avg. $\log_{10}(T)$ indicates the characteristic (log-)temperatures of the emitting plasma probed by the given wavelengths, and Main ion(s) indicates the main ionic population probed (i.e., responsible for the main lines emission), based on De Pontieu et al. [17] and Lemen et al. [4], with partial overlap with Table 1.1. AR is Active Region, TR is Transition Region.

Main Line	Main ion(s)	Solar atmospheric regions	Avg. $\log_{10}(T)$
MUSE [Context Imager (CI) / Spectrograph (SG)]			
304 Å (CI)	He II	chromosphere, TR	4.7
195 Å (CI)	Fe XII	∼1-2 MK corona / AR corona	6.2
171 Å (SG)	Fe IX	quiet/AR corona, upper TR	5.9
284 Å (SG)	Fe XV	AR corona	6.4
108 Å (SG)	Fe XIX, Fe XXI	flaring corona, hot flare plasma	7.0, 7.1

previous successful missions such as SDO/AIA [8] [4] and IRIS [21]. MUSE will provide unprecedented data revealing the key processes governing solar activity, and its extremely high spectral purity requirements require the utmost rigor in characterizing the thin films positioned at the entrance of the mission's telescopes. MUSE, along with other ground observatories and satellites either currently functioning or under development – such as the *Daniel K. Inouye Solar Telescope* (DKIST) [22] and the EUV High-throughput Spectroscopic Telescope (EUVST) [23] among others – does align with the Next Generation Solar Physics Mission (NGSPM) report call by NASA/ESA/JAXA which will enable the capture of processes heavily involved in solar coronal heating and solar flares or CMEs, and thus bringing forward solar astrophysical science. Regarding the optical schemes of the mission's telescopes, they differ. The CI telescope's scheme will be quite similar to a standard Cassegrain's geometry telescope with a primary and a secondary reflective mirror – quite identical to SDO/AIA's optical scheme [24], while the SG along with its 35 slits is the main innovative piece, and in place of a secondary mirror a reflective grating is employed, with the CCDs being placed in the second or first order of diffraction position. In both telescopes, entrance filters (EFs) and filter wheel filters (FWFs) are present, for the purpose described in the following Section 1.3: the filter wheel filters are crucial either to extend the capabilities of the mission, aiding the observation of highly energetic solar events with strongly absorbing filters, or as redundancy solution in case the entrance filters are damaged unexpectedly, avoiding failure of the scope of the mission. A simulation-based description of the capabilities of the MUSE mission regarding the diagnostics, detection, and context imaging potential during the evolution of coronal loops at various heights in the solar atmosphere is given in Fig. 1.4. Since the main objective of MUSE is to provide new data that will enable observations of the fundamental processes that drive solar activity, its requirements for extremely high spectral purity in the data require the utmost care in the characterization of

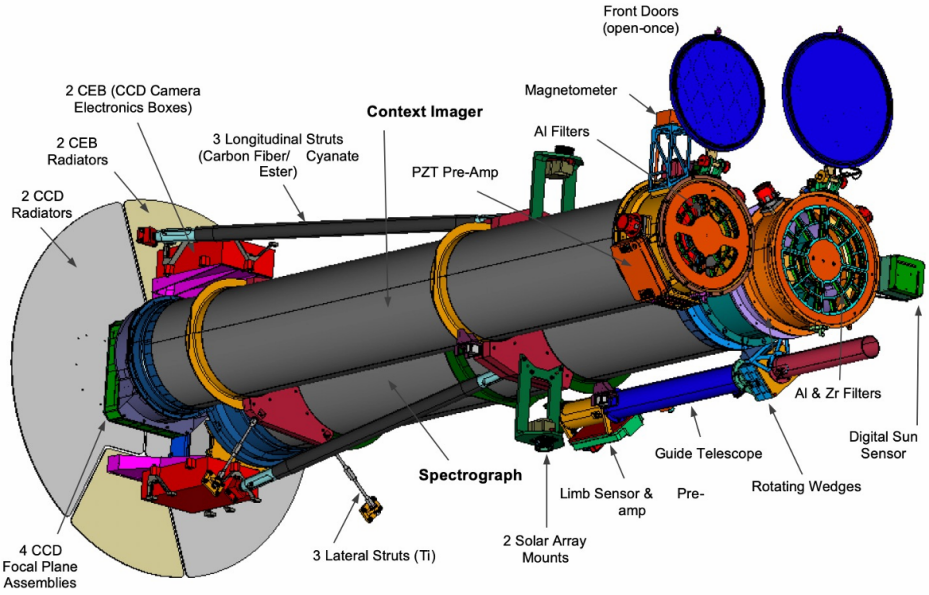

Figure 1.3 Illustration of MUSE's payload, showing the context imager, spectrograph, guide telescope, and housekeeping sensors (magnetometer, sun and limb sensors). The front end includes open-once doors and filter wheels with Al/Zr entrance optical-blocking filters; the aft end houses the CCD focal-plane assemblies, with camera electronics and radiators. Credit: NASA. Used with permission. Source: "Next Generation Solar Physics Mission—MUSE and EUVST information (April 2022)" ntrs.nasa.gov/citations/20220006091 (last accessed 2025-11-16).

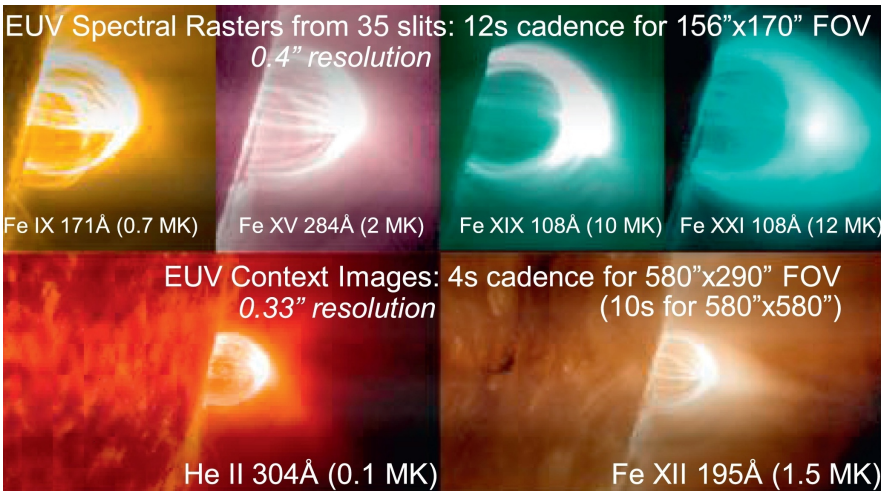

Figure 1.4 Illustration of MUSE's spectroscopy and context imaging capabilities. Top row: EUV spectral rasters (with SG telescope), showing also FOV and resolution specifications, of a simulated coronal loop with images from (main emitting ion, wavelength channel, temperature) Fe IX 171 Å (∼ 0.7 MK), Fe XV 284 Å (∼ 2 MK), Fe XIX 108 Å (∼ 10 MK), and Fe XXI 108 Å (∼ 12 MK). Bottom row: EUV context images (with CI telescope) around the loop, shown for He II 304 Å (∼ 0.1 MK) and Fe XII 195 Å (∼ 1.5 MK). Credit: Cheung et al. [19]. Corrected the slits number and FOV to recent values. License: CC BY 4.0.

the thin films placed on the entrance pupil of the mission's telescopes.

> **Note.** MUSE is led by the Lockheed Martin Solar and Astrophysics Laboratory of Palo Alto, California. MUSE is managed by the Explorer's Program Office of NASA's Goddard Space Flight Center in Greenbelt, Maryland, for the Heliophysics Division of NASA's Science Mission Directorate, and it is supported by NASA contract 80GSFC21C0011. Lockheed Martin Advanced Technology Center, along with partner institutions, builds the MUSE instrument and spacecraft, and the University of California, Berkeley, provides the mission operations center. MUSE benefits from international contributions supported by the Norwegian Space Agency (NOSA), the Italian Space Agency (ASI), the German Space Agency at DLR, and the Max Planck Institute for Solar System Research (MPS).

I will now go into great detail on the state of the art of the thin film filters in current solar astrophysics and their main requirements.

1.3 Thin films in solar missions

General requirements of EUV thin film filters

Thin-film filters are critical components in EUV space missions, as they are an EUV passband component that rejects most of the visible and infrared light with their metal coating parts: this is very important due to the CCD detectors being sensitive to those wavelengths. The design and performance of EUV filters have evolved over the last thirty years, drawing heavily on the heritage of the thin film filters used in the state-of-the-art past space missions and solar observational instruments like the aforementioned SDO/AIA, Hinode/EIS [6] [7], but also STEREO/SECCHI [25], and SOHO/EIT [26].

> **Note.** An implicit assumption throughout my work is that, unless otherwise specified, all of the ensuing thin films, pellicles, or membranes described are **free-standing**: they are not deposited on a substrate. This is because their purpose is to be used as entrance filters in a telescope. Thus, they are required to be completely free-standing, to avoid the substrate–say, a silicon wafer–from further absorbing light and impeding the scope of the filter.

Many are the properties required for filters to be used in EUV space missions, a brief description of which is presented in Chkhalo et al. [27]:

- **High EUV transmittance** to maximize the signal in the target wavelength bands while blocking transmitted radiation in the ultraviolet (UV), visible (VIS) and infrared (IR) range, i.e. **minimizing out-of-band UV-VIS-IR leakage**.
- **Protect the telescope optics during launch and operation** from particle cross-contamination, i.e. release of particles from external surfaces of the

telescope/payload/spacecraft, while withstanding the mechanical stresses of the vibration loads and shocks during the rocket's propulsion, without compromising their out-of-band rejection properties.

– **Resistance to extreme space conditions** such as cyclical temperature variations and damage by atomic oxygen exposure, while maintaining their optical and mechanical properties under such conditions.

– **Minimal impact from the native oxide layers** that can build on top of the thin metal layers that compound the film, since this can decrease the transmittance in the EUV range.

– Use of a structural supporting mesh or substrate allowing the filter system to resist vibration while **minimizing the impact of diffraction patterns** that could degrade the image quality or interfere with scientific observations.

An ideal filter would transmit 100% of EUV at the wavelengths of interest, it would be completely opaque to UV-VIS-IR light, it would resist all of the vibro-acoustic loads during launch without hindering its characteristics, and the mechanical structure employed would not cause any diffraction out of the core signal required by the angular diffraction: i.e. an ideal, fully transmissive, fully opaque in the visible and diffraction-less solution. This solution does not exist, and these stringent requirements highlight the inherent trade-offs in designing filters for EUV space missions. For instance, a very finely spaced mesh employed to resist vibration loads can lead to strong diffracted secondary lobes content in the focal plane, introducing complexity in the data analysis needed for scientific objectives [28]. Another possibility is to use a multilayer thin film reinforced with polyimide (PI), which relaxes the requirements on the mesh. However, the presence of such substrate lowers the transmittance signal, particularly at wavelengths such as 284 Å , which negatively affects the effective area in comparison to other less conservative options. Thus, these aspects underline the complexity of the most suitable choice of filter design in EUV space missions, particularly keeping in mind groundbreaking scientific objectives that will push thin films to their technological limit even further in the ensuing years.

Additionally, thin film filters satisfying these properties are not only best suited for space missions studying the sun in the EUV band, but can also be versatile in other fields unrelated to solar astrophysics, such as experimental science with laboratory sources and EUV lithography. In the context of EUV lithography, filters similar in concept to those developed in the space missions and to those studied, designed, and characterized in this work could be extremely useful, as some of the requirements are in overlap–such as the need for out-of-band rejection, high EUV transmittance, and high thermal resilience [29]. There are some other requirements needed in EUV lithography as well, such as the extreme resistance to powerful EUV irradiation (something to wish for in EUV solar observations), and, while approaches involving periodic multilayer thin films are being developed and employed in the industry [30], the exploration of novel thin film materials,

such as coated CNTs with Zr, could potentially be extremely beneficial to this industrial application as well. Another such example is the usage of filters in synchrotron radiation beamlines (an example of a synchrotron beamline will be provided in the experimental study of EUV performance of filters for MUSE in Chapter 4): in such scenarios, filters able to filter out visible or infrared light, while transmitting EUV or X-ray wavelengths, could function either as a great bandpass selectors (*upstream filters*)–since synchrotron radiation is broadband and thus emits also UV/Vis/IR alongside X-rays or EUV–or as a filter in front of the detector (*downstream*) responsible for removing any visible/infrared/UV stray light due to any other out-of-band emitting sources present in the experimental chambers, in experiments not limited to biology, materials science, physics or chemistry. One particular case scenario is that of peculiar experiments in which a laser photo-excites a sample while it is also subject to X-ray or EUV irradiation: if the scientist is interested only in collecting EUV or X-rays, a filter might be required to reject all of the leftover laser beam scattered around the sample chamber.

The cases of heritage filter designs that satisfied the EUV thin film filter requirements for solar astrophysics and EUV detection applications will be detailed in the following section.

EUV optical filters in heritage missions

Heritage filter designs have addressed the stated general requirements as optimally as possible and, traditionally, with filters made of aluminum (Al) and zirconium (Zr), either with a polyimide (PI) substrate supported by a coarse (a few mm pitch) nickel (Ni) mesh, or deposited directly on a fine (sub-millimetric pitch) mesh without a substrate. In STEREO-SECCHI [25], the instrument utilized Al-coated PI thin films, particularly 150 nm Al coated on 70 nm PI membranes supported by a coarse five lines-per-inch (LPI) Ni mesh – for channels 171 Å and 195 Å – while for the 284 Å and 304 Å channels, 150 nm Al foils were deposited directly on a fine 70 LPI Ni mesh. A picture of the optical blocking filters at the entrance pupil of the STEREO-SECCHI Extreme Ultraviolet Imager (EUVI) telescope is given in Fig. 1.5, where the coarser mesh has a pitch, i.e., distance between centers of adjacent mesh cells, of ~ 5.08 mm while the finer mesh has a pitch of ~ 363 µm. To convert LPI to pitch and vice versa, please follow the description in Remark 2.

Remark 2 (On LPI and pitch)**.** Throughout the entire thesis, terms like pitch and lines-per-inch, or LPI, will be recalled frequently and interchangeably; thus, it is relevant to display their meaning to avoid any misunderstanding. The pitch is a measurement of the period of the 2D structure representing the studied mesh. LPI, on the other hand, is just the *frequency* of such pitches as they occur over a 1-inch length. Thus, by calling pitch as variable p, the following transformation

ensues (and also shows the particular case pitch value in mm as unit, or p_{mm}):

$$\mathrm{LPI} = \frac{1\,\mathrm{in}}{p} = \frac{1\,\mathrm{in}}{1\,\mathrm{mm} \cdot p_{\mathrm{mm}}} = \frac{25.4}{p_{\mathrm{mm}}} \tag{1.1}$$

Thus, it is easy to go back and forth from one definition to the other of 2D periodicity expressed either as pitch or LPI.

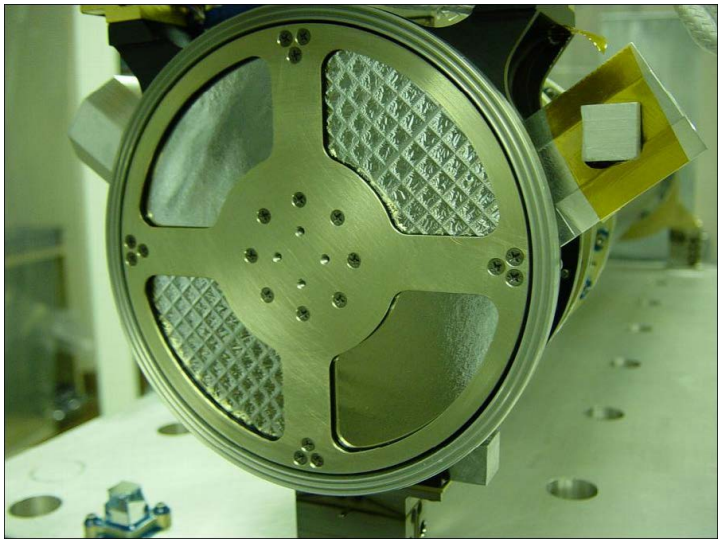

Figure 1.5 EUVI entrance filters on the structural test model of the STEREO-SECCHI telescope. Top-left and bottom-right apertures show 70 LPI Ni-mesh-supported Al filters (fine mesh), while the other quadrants use a multilayer thin film with 70 nm of PI coated with Al supported on 5 LPI Ni-mesh (coarse grid). All entrance filters use 150 nm thick Al layers. Credit: Fig. 4 from J.-P. Wülser et al. [25]. Used with permission. License: SPIE Copyright (2004), all rights reserved to SPIE.

In SDO/AIA, the telescope entrance filters (EFs) employed were made of thick or thin Al or Zr layers supported by finely spaced nickel meshes, or, in one case, the use of a PI-supported Zr film without any mesh. [31] In both space missions, the finely spaced meshes caused some severe diffraction, especially in the case of bright flares [25], and diffraction removal algorithms were developed to clean the collected data [28]. Since flight-like areas of the EFs were on the order of $10 - 20\,\mathrm{cm}$, this also emphasizes not only finding the correct materials and properties, but also the need for a very scalable production of these thin films, especially in a future where capturing greater solar surface portions with a high spatio-temporal resolution will require larger filters. Moreover, in-flight degradation and aging under environmental effects could have an impact on the film transmittance in X-ray and EUV space missions [27]. Common among the contamination of optics and filters is carbon, which was studied extensively with X-ray laboratory assessments in the case of Chandra/ACIS [32], and it was used to model the filter degradation seen in solar missions such as SOHO/EIT and SDO's Extreme Ultraviolet Variability Experiment (EVE) [33]. As recent developments, it has been proposed that UV-induced oxidation in the presence of water vapor out-gassed by the thermal blankets on SDO/EVE may have contributed to the

significant reduction of the transmittance of Al-based EFs during the initial 5 years of the space mission, while Zr filters employing an anti-oxidation carbon capping layer were not influenced as much [34] [35]. The suggestion is that this could also partially explain some of the degradation seen in SDO/AIA since launch, particularly for channel 304 Å, and for which various empirical and automated calibration strategies have been employed and developed. [36]

A brief note on CNT-based filters

It is only natural for the filters baseline proposed for MUSE to stem from the heritage solutions from previous missions such as STEREO/SECCHI and SDO/AIA, as these have a proven high Technology Readiness Level (TRL), a concept which has similar definitions by NASA [37] and in the European Cooperation for Space Standardization (ECSS) [38]. Other than filters based on high flight TRL, such as PI, Zr, and Al, a new technology is currently being explored to overcome some of the challenges found in recent EUV missions. Recent advancements in filter technology include the development of novel materials such as carbon nanotube (CNT) pellicles, either in their single- or multi-walled structures (SW/MWCNT), which have been proposed for applications in EUV nanolithography [39] and X-ray astrophysics [40]. As part of the Italian contribution to MUSE (managed by the Italian Space Agency, ASI), the innovative filter technology based on thin pellicles of carbon nanotube (CNT) bundles is proposed as support for the metal layers necessary to reflect the out-of-band solar light. The CNT-based filter technology for MUSE, which will be described in Section 2.1 – alongside the heritage-based one – is built upon initial research efforts carried out by the INAF-OAPA/UNIPA team within contracts funded by the European Space Agency in partnership with Ametek Finland OY (Prime Contractor) and Canatu Finland OY, see Barbera et al. (2022) [40], and Etula et al. (2023) [39] and references therein for a description of the material and technology. The main goal of this effort is to provide a set of EFs that significantly reduce diffraction effects, making it easier to analyze the data and to exploit the instrument performance for MUSE fully, and to increase the TRL of this novel technology for its implementation in EUV observatories, current and future alike.

There are a few reasons for the recent developments of CNT-based filters and for their proposal. Firstly, they are mechanically really sturdy [39]. The strength of the pellicles is quite relevant: although a comprehensive review of the optical, physical, and mechanical properties of CNT pellicles is not present in the current literature, an investigation is currently ongoing [41]. The CNT pellicles are found to be very light (their density is close to $\sim 0.3\,\mathrm{g\,cm^{-3}}$), about 4 to 5 times lighter than PI with $\rho_{\mathrm{PI}} = 1.4\,\mathrm{g\,cm^{-3}}$) and can be manufactured very thin. Another relevant detail is that the CNT technology allows for the implementation of a CNT-based mesh that is not glued to the substrate but is chemically bound to it, avoiding glue-based defects, which might become centers of stress during launch (which happens for PI-based films glued to metal meshes). Aspects regarding the

mechanical sturdiness of CNT-based MUSE filters are not tackled in this thesis. Still, relevant details regarding the demonstration models (DMs) qualification under vibro-acoustic load tests representative of launch can be found in D'Anca et al. [42] in which these thin film structures with CNT passed these tests and confirmed their outstanding mechanical performance, even in cases where no mesh was used with filters with 56 mm for the CI FWFs. A second important reason is the transparency: CNT EUV pellicles can be manufactured thin, and since they are lighter than PI ones, they can be more transparent than polyimide in the EUV range [40] [43]. Therefore, using CNT pellicles could be more efficient for the total EUV throughput in the solar mission: an experimental proof of the performance of the multilayer thin film with CNT as substrate outperforming the PI-based filter is provided in Chapter 4 →p.71. A further important reason is that regarding diffraction: given a situation where a PI pellicle is employed, it is usually used with a lower thickness and thus requiring the usage of finer and more blocking structural meshes as otherwise the structure would break under launch loads (such as in STEREO-SECCHI [25] or in SDO/AIA [31]). An important aspect is that by employing thicker structures of CNT thin films, not requiring as demanding structural meshes, one could avoid the use of an impactful structural mesh diffraction-wise. Design of the filters proposed for MUSE, both heritage and CNT-based, and also the impact of diffraction caused by the various designs will be detailed in Chapter 2. In some cases, particularly for FWFs, one could also forgo a structural mesh entirely. Clearly, if future studies could prove that a riskier mesh-less solution is feasible and satisfies requirements, it would be the perfect solution to avoid all of the potential diffraction issues. Having laid out the main properties of thin film filters in EUV, I now link the various chapters of the thesis to the various needs

Additional solar missions and filter concepts

In addition to the cases of the aforementioned solar missions–STEREO/SECCHI, SDO/AIA, and the future MUSE–several other recent or ongoing solar missions offer relevant examples of EUV/X-ray instrumentation, kinds of solar observations, and optical blocking strategies. A selection of these missions is briefly discussed below to contextualize the present work and illustrate a broader view of solar imaging and spectroscopy and diversity of filtering techniques and concepts currently employed in solar instrumentation.

The *PROBA-2* mission, launched by ESA in 2009, carries the *Sun Watcher using APS detector and image Processing* (SWAP) EUV imager employing an Active Pixel System (APS) detector operating in a wavelength bandpass centered on 174 Å [44]. The peculiar specifications of PROBA2/SWAP, such as the large FOV of ($54' \times 54'$), render it capable of showcasing and tracking CMEs and other events of relevance to space weather at distances up to $\simeq 1.7 - 2$ solar radii even today after 16 years of its launch. SWAP is built upon SOHO/EIT heritage and functions similarly to the MUSE/CI concept, employing a compact

off-axis Ritchey–Chrétien-Cassegrain telescope and using various stages of solar light rejection. A 38 mm diameter filter, composed of a multilayer of 150 nm thin aluminum deposited on 50 nm of PI reinforced by a 20 LPI Ni mesh, is employed for the entrance (or front) filter by SWAP, together with additional focal plane filtering to further suppress visible and infrared radiation by a 28 mm diameter-wide 70 LPI Ni mesh supported 150 nm Al thick thin film filter which cause negligible diffraction [45]. In both cases, the filters are quite in line with the filter choices and examples of SDO/AIA and STEREO/SECCHI: which is also expected, given that SDO and PROBA2 were developed almost simultaneously. The PROBA2/SWAP instrument is both an excellent example of a functional and sturdy mission, working well past its 2-year original nominal operation duration, while also being an extremely successful example of space mission development and environmental testing for the filters subsystems [46] and the whole integrated system [45].

The satellite Fengyun-3E (FY-3E) [47], developed collaboratively by the China National Space Administration (CNSA) and the Chinese Meteorological Administration (CMA), launched in 2021 and designed primarily for terrestrial weather, carries the X-ray and Extreme Ultraviolet Imaging Telescope (X-EUVI) [48] which aims at improving the forecasting of space weather providing full disk solar images either in the X-rays ($\lambda \geq 6$ Å, and wavelength upper limit depending on band) or in the EUV range around 195 Å utilizing an ingenious selective dual-band X-ray/EUV optics approach. In X-EUVI Wolter-I type X-ray grazing or Cassegrain perpendicular-incident EUV optics are selected by moving the CCD-assembly via a stepping motor, with switching speeds between modes of the order of a second. The two optical modes share the same CCD, the same filter wheel, and the same entrance pupil filter to reject visible light and ultraviolet with wavelengths ($\lambda > 30$ nm)–a multilayer film filter of Al/Ti/Polyimide was employed for the scope. The EUV mode employs Mo/Si multilayer coatings on the reflective mirrors to select the 195 Å bandpass–similarly in concept to that of the MUSE/CI–and an Al-based thin film pre-filter to further reject visible light in the more visible and infrared sensitive EUV mode. The detailed composition of the eight thin-film filters in the filter wheel is not publicly disclosed, but their functionality is similar to both the filters based on Al/Zr for MUSE/CI or SG and the line filters employed in X-ray synchrotron laboratories, such as those discussed in Section 4.2, in the section of X-ray and EUV transmittance measurements of filters for MUSE. Therefore, this instrument exemplifies a modern design philosophy in which spectral selectivity is distributed between reflective coatings and entrance or filter wheel thin-film filters, similarly to MUSE.

The mission Aditya-L1 [49], designed and developed by the Indian Space Research Organisation (ISRO) and launched in 2023, carries several solar payloads spanning observations of the sun from the visible and infrared wavelengths all the way up to hard X rays. While none of the payload's instruments are capable of EUV detection, the Solar Low Energy X-ray Spectrometer (SoLEXS) [50] observes from the soft X-rays to hard X-rays in the photon energy range 2-22 keV, while the Solar

Ultraviolet Imaging Telescope (SUIT) [51] observes the near-ultraviolet (NUV) wavelength range 200-360 nm: both of these instruments on board the mission can observe events such as flares, although they are optimized for different altitudes in the solar corona, and they employ interesting filtering strategies to observe the sun in the X-rays or NUV while rejecting most of the visible and infrared light. The SUIT instrument employs UV Band Pass filters in a filter wheel assembly close to the detector–characterized and described in terms of calibration curves and bandpasses in Tripathi et al. [52]–while also employing a front Thermal Filter, which has been extensively detailed in another publication by Sarkar et al. [53], being composed of a 10 mm thick fused silica substrate coated with Cr/Al/SiO2 multilayer thin films (∼30 nm for each layer). The Thermal Filter provided the initial rejection in the NUV range, while the subsequent bandpass filters allowed for further refinement of the bandpass selection at the preferred wavelength. In the case of SoLEXS, the two Silicon Drift Detectors (SDDs) of the mission are coupled to an 8 µm thick Be entrance window which selects energies higher than 2 keV. In both cases, in favour of using a thin film filter, which poses extreme challenges to the mechanical resilience during launch of the payload, a very thick film is employed for the filter as an entrance filter, which conservatively follows mission requirements while allowing for safety margins in launch and resisting vibration loads. Although Aditya-L1 does not operate in the EUV range, its filters provide a complementary example of visible light rejection and band-passing approaches at adjacent wavelengths (X-rays or NUV).

As a final example, the CORONAS-Photon satellite, developed by Roscosmos (formerly Russian Space Agency) and launched in 2009, was designed for observing the solar atmosphere and tackling many of the open problems in solar physics. Of interest due to similarities with MUSE is the Telescope-Spectrometer for Imaging Solar Spectroscopy in X-rays, or TESIS, experiment [54]. While in some wavelength channels the idea is pretty similar to those of the aforementioned missions, employing thin film filters and periodic multilayer coatings on the mirrors, the channels at 132Å/171Å and 171Å/304Å worked in a Herschel optics geometry. In those cases, a periodic multilayer filter was deposited directly on the CCD detector, with certain flown examples of Zr/Si and Al/Si as the basis for the multilayer filters. An extensive characterization of these types of filters is detailed by Chkhalo et al. [27], with other examples of materials tested for the periodic layers being Be/Si, Cr/Si: in all cases, usually with a few-nanometer-thick bilayers stacked up to 55 periods. Thus, the effective area and bandpasses around relevant EUV lines were obtained via the synergy between (periodic) multilayer coatings in reflection and multilayer filters in transmission. Albeit short-lived, being lost 10 months after launch, CORONAS-PHOTON was a successful proof of concept of multilayer filtering for EUV detection, and future missions–such as the upcoming Russian-led Interhelioprobe mission [55] developed for close flybys of the Sun and including X-ray and EUV imaging instruments–could include such peculiar filtering techniques.

Taken together, these missions demonstrate that, while Al or Zr-based thin films

on polymer substrates remain a standard and strong solution for EUV entrance and detector filtering in solar space missions, alternative strategies (thick-windows, periodic multilayer on-chip solutions) have been adopted either in the EUV or in adjacent wavelengths, and they can be actively pursued depending on mission constraints. The development of MUSE's filters builds upon these insights while simultaneously exploring alternative technologies, such as CNT-based support materials, to meet the specific requirements of high-throughput, high-resolution EUV spectroscopy.

1.4 A bridge to the thesis

The requirements defined in Section 1.3 →p.9 are directly connected to parts of my work.

- Chapter 2 →p.19 introduces the filter designs —- including the designs based on the older space mission and new CNT-based substrates —- along with the numerical and analytical framework used to assess the **diffraction content** at the MUSE focal plane for all of the designs. The diffraction contents are design-dependent and can impact the scientific capabilities of the mission, as will be discussed.
- Chapter 3 →p.53 defines the filters' **out-of-band blocking requirements** and presents the optical characterization of Al-based witness samples. The chapter also discusses the difference in the performance experimentally investigated with UV-VIS-IR transmittance spectroscopy over various substrates, comparing them with both the requirements and among themselves.
- Chapter 4 →p.71 reports the **EUV transmittance**, soft-X-ray transmittance measurements, and XAS-based inner-layer analyses for the various designs under study, delivering calibration-ready curves and inner-layer compositional diagnostics making use of the analysis of the photo-absorption edges in the materials. The EUV transmittance is compared between designs, and the efficiency of the novel CNT-based filters is assessed.

The other chapters are not directly connected to the thin film requirements but do support the development of the MUSE mission as a whole with respect to other aspects.

- Chapter 5 →p.92 describes the work-in-progress development of a Penning Discharge Source for potential use as a **EUV calibration support** for MUSE. A physical description of the source, which is intended to simulate the solar EUV emission lines and is itself an amazing modern physics laboratory, will be provided.
- Appendices will be **complementing the text** with niche experimental details and other aspects. An appendix in particular, Appendix E →p.117, stands out in providing complementary **software-based data analysis details** on

the proposed approach to solve complexities in the data analysis expected for MUSE, which arise from the novel and complex idea of employing the 35-multi-slit mechanism working at the same time while rastering the Sun.

I delve now into the filters' design, while also discussing at length the diffraction impact of the various solutions studied for MUSE.

2 Filter Designs and Diffraction Studies

2.1 Preamble to the chapter

What this chapter is about

In this chapter, I delve into the description of the designs studied for MUSE as Demonstration Models (DMs) and Structural Thermal Models (STMs), terms that indicate the various steps during the development of the space missions, borrowing terminology from the ECSS [56]. This chapter serves a few relevant purposes.

In a first, more introductory physical and mathematical section, I detail aspects that are of relevance to the following treatments. A formula for the optical blocking factor of meshes is proven. I detail how the optical blocking factor modulates the expected diffraction core, and I follow this up with a prediction of the secondary lobes center position – which remarkably uses concepts from solid state physics and X-Ray Diffraction (XRD). All of these aspects were developed during my work of analysis and simulations supporting the filters' design. This activity allowed me to find and corroborate numerical values of interest, figures of merit to describe the filters' designs' performance, and mathematical equations useful as *controls* for the results of the numerical simulations.

The second section is about detailing the filters' designs for MUSE delivered by the INAF-OAPA-UNIPA research team as part of the Italian contribution to the NASA mission, both in the case of the DMs and subsequently STMs. This means describing the filters' geometry, the selected materials, and further details related to manufacturing and assembly.

The third section of this chapter involves more of the simulative studies I carried out on the impact of diffraction for the various designs, allowing for the comparison between them. Particularly, I studied the performance of the Point Spread Functions (PSFs) – synonym for figure of diffraction, or diffraction pattern – in the case of ideal mirrors, mirrors with realistic roughness, and then the PSFs of the various designs, devising figures of merits for the transmittance at the core, the Half-Energy Width (HEW), and other quantities of interest.

Point Spread Functions, and Relevance in Space Missions

Accurate estimates of the PSFs at the focal plane due to the structural mesh of a given telescope entrance pupil thin-film optical blocking filter design are relevant, as shown in the case of SDO/AIA to improve the scientific quality of datasets

[28]. To evaluate the performance of filters for MUSE, and in collaboration with D. Spiga (INAF/Brera), I analyzed a series of simulations made using an IDL-based software developed for the design of optics for space missions, described in a previous publication by Spiga et al. [57] although opportunely modified for the scope in the case of MUSE. Diffraction patterns at the focal plane due to the filter supporting mesh were simulated for all the designs described in the following sections. The novel CNT structures use a partially-transmissive CNT-based mesh, which was also modeled, despite the higher complexity when compared to a fully opaque thick metal mesh. The simulations include the mirror roughness and the mirror profile errors, as modeled or measured by the Italian team responsible for the development and manufacturing of the MUSE optics [58]. This allowed me to study realistic scenarios for the simulation of PSF figures.

I found interesting results in assessing the quality of filters and meshes in terms of the produced PSFs, and I observed how a realistic mirror profile should affect these figures, further emphasizing the importance of simulations. A comprehensive discussion with the science teams regarding the potential effect of a figure of diffraction on science cases (such as solar behaviour as seen from MUSE in terms of QS, AR, or flare events) is ongoing. Different filter designs can likely enhance the appearance of various features, thus requiring a tradeoff study in the near future.

Deconvolutional aspects

A further important aspect of the construction and study of relevant PSFs for MUSE in Section 2.4 → p.35 is that, theoretically, if one knows exactly the point spread function that is responsible of the degradation of the image at the focal plane (usually in the form of a convolution between the true image and the PSF), it is possible to improve the quality of the data collected by MUSE by employing *deconvolutional* approaches. Deconvolution approaches have been relevant in the past to dramatically increase the reliability of the data retrieved by telescopes in the case of the mission TRACE [59], or the aforementioned SDO/AIA. The approaches include Wiener filtering [60] [28], and in the space context other relevant deconvolution algorithms such as the *Van-Cittert* and the *Richardson-Lucy*, both detailed in the appropriate review by Starck et al. [61]. The latter was famously employed to correct the Hubble telescope images during the period in which it suffered from spherical aberration problems in the years 1990-1993 [62]. Thus, the general context of my work is to develop PSF inputs depending on the filters' design choice, both to compare the designs using figures of merit built on the PSFs, and as part of future potential deconvolution approaches towards the correction of the true image data of MUSE *if need be*.

2.2 Mathematical and physically useful concepts for diffraction

In this section, I will describe the mathematical and physical context of filters' diffraction and design. This will be somewhat of a break with respect to the MUSE context, although it is relevant in general for Astrophysics space missions.

Optical Blocking Factor of a 2D Periodic Mesh

The general formula for the transmittance of a 2D mesh grid–that is, the blocking factor (BF) that a plane wave impinging on the surface of a 2D periodic structure would face–is described in this section. An image example of the structure to which the formula applies is given in Fig. 2.1, closely mimicking the mesh appearance of the thin film filters of STEREO-SECCHI in Fig. 1.5 ignoring the film. It is a

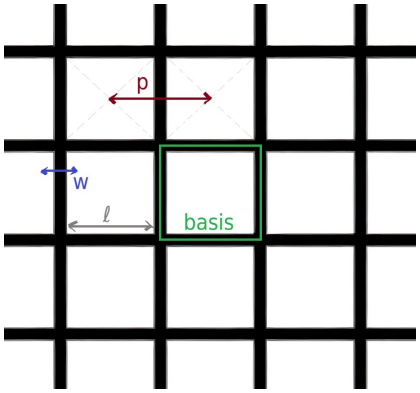

Figure 2.1 Excerpt of a square grid mesh. Open area squares are white, and the opaque mesh bars are black. The mesh width w, pitch p, inner side length ℓ, and the basis square are displayed.

square grid with pitch p, i.e. smallest distance between the centers of adjacent cells, and width w of the mesh bars (same in all of the bars' directions). The following formula applies for the theoretically expected optical blocking factor of the *infinitely extended* structure in the completely blocking or reflective scenario.

$$\mathrm{BF} = \frac{2w}{p}\left(1 - \frac{w}{2p}\right) \tag{2.1}$$

Such formula will also be denoted as the formula for the *geometric blocking factor* of the mesh, as it only depends on the mesh geometry (width, pitch), and not on its transmission properties, as it is assumed opaque. The proof of the formula is given in Appendix B. The same formula applies to honeycomb grids described by pitch p and width w. While the mesh transmittance M in the case of a 100% blocking mesh material is given by Equation (2.2).

$$M = 1 - \mathrm{BF} \tag{2.2}$$

The mesh transmittance M is, in general, given by Equation (2.3), where BF retains its geometrical blocking factor definition of Equation (2.1), and the materials compounding the mesh are assumed to transmit at wavelength λ a $t(\lambda)$ fraction of light.

$$M = 1 - \ \mathrm{BF} \cdot (1 - t(\lambda)) \tag{2.3}$$

For $t(\lambda) = 0$, i.e., the case of a fully opaque mesh, we obtain the earlier formula, while for $t(\lambda) = 1$, i.e., the case of a fully transmissive mesh, a completely open area is found. Another term that will find occasional use throughout the work is that of an *effective blocking factor*, which is just the product of the geometric blocking factor of the mesh and the fraction of light that is truly blocked by the mesh, with the notation above, and detailed in Equation (2.4)

$$\mathrm{BF}_{\mathrm{eff}} = \mathrm{BF} \cdot (1 - t(\lambda)) \tag{2.4}$$

Light Diffracted by 1D Multiple Slits / Diffraction Gratings

Here, I introduce another relevant figure that will become crucial for the ensuing analysis of the PSFs. I have treated the amount of light blocked by a fully opaque periodic mesh structure in the earlier paragraph. It is now of interest to build up an understanding of how the blocking due to an opaque 2D periodic mesh affects the proportion of diffracted light inside the diffraction core – that, in the context of an integrated telescope system, will also be described as a PSF core. This is an extension from 1D to 2D of the study of 1D transmissive diffraction gratings obtained via multiple-period adjacent 1D slit structures. A solution for the 1D case is provided by G. R. Fowles. [63] which predicts the intensity distribution of light deflected by an angle θ and as it appears on a screen after it is transmitted by an N-slit grating with each open slit having width a, separation between adjacent slits h, and wavelength of incident light λ. The formula describing this is given as follows.

$$I(\theta) = I_0 \cdot \left(\frac{\sin(\alpha)}{\alpha}\right)^2 \cdot \left(\frac{\sin(N\beta)}{N\sin(\beta)}\right)^2 \tag{2.5}$$

Where: $\alpha = \frac{1}{2} \cdot \frac{2\pi a}{\lambda} \sin(\theta)$, $\beta = \frac{1}{2} \cdot \frac{2\pi h}{\lambda} \sin(\theta)$, and I_0 is an arbitrary normalization constant that, if unitary, makes the value $I(\theta = 0) = 1$, proportional to the impinging light intensity. A particular case of this diffraction figure for 13 slits is given in Fig. 2.2 and a few general lessons will be useful in the proceeding of the thesis. It is noteworthy that the diffraction figure is modulated primarily by three geometrical quantities: the size of the single slit, a, that modulates the highest value of the intensity at each angle; the size of the pitch, b, that modulates the principal maxima; and finally, the size Nb, i.e. *the largest size of the structure* or the total size of the structure, that modulates the smaller angles and their secondary maxima in between principal maxima. In this case, the angular size of these minima goes as $\Delta\theta \simeq \lambda/d$ where d is the geometrical quantity of relevance (size of slit, or pitch, or total size of the structure). A relevant aspect is the diffraction core, in this case defined by the ratio between the integrated

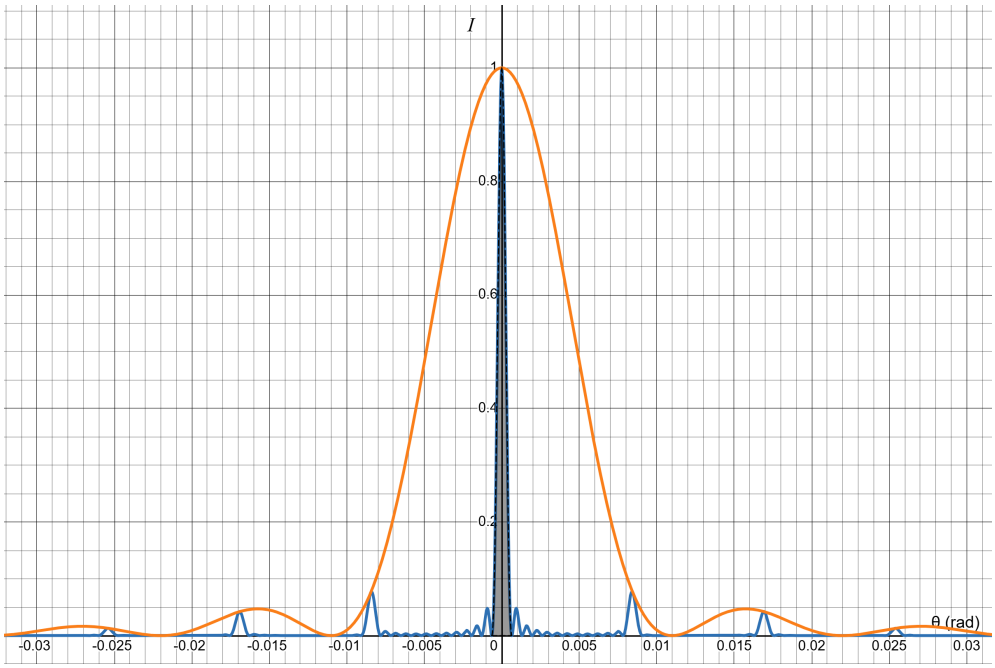

Figure 2.2 Example of N-slit Diffraction Figure by a 1D N-slit structure (blue plot). X-axis is angle θ (in radians) of deflection of the light, Y-axis is intensity (in arb. units) normalized to the first peak value to 1. Values used: number of slits $N = 13$, single-slit open side length $a = 50\,\mu\text{m}$, pitch $b = 65\,\mu\text{m}$, wavelength $\lambda = 550\,\text{nm}$. The yellow envelope is the figure of diffraction by a single slit of aperture a. Shaded in grey is the core of the diffraction figure in between the first two secondary minima, whose proportion of integrated intensity to the total in the given example is 70%. Source: Live-graph in Desmos (last accessed: 2025-11-20). License: CC BY-SA 4.0

intensity over the angles in between the first two secondary minima in the figure of diffraction and the total integrated signal, which contains 70% of the total signal in the example.

Furthermore, Equation (2.5) encodes more complex behaviour for the diffraction figure when the number of slits is higher, such as what happens in real transmission gratings. Another visual example is given in Fig. 2.2 for 43 slits.

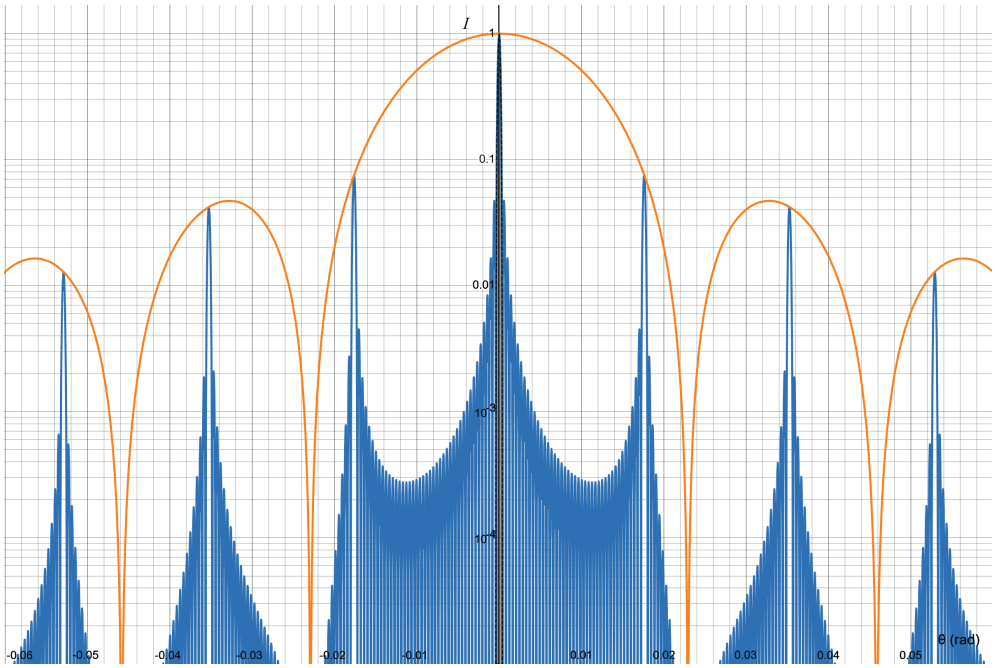

Figure 2.3 More complex example of N-slit Diffraction Figure by a 1D N-slit structure (blue plot). X-axis is angle θ (in radians) of deflection of the light, Y-axis is intensity (in arb. units) normalized to the first peak value to 1, and on a log-scale. Values used: number of slits $N = 43$, single-slit open side length $a = 24\,\mu\text{m}$, pitch $b = 31.2\,\mu\text{m}$, wavelength $\lambda = 550\,\text{nm}$. The yellow envelope is the figure of diffraction by a single slit of aperture a. Shaded in grey is the core of the diffraction figure in between the first two secondary minima, whose proportion of integrated intensity to the total in the given example is 70%. Source: Live-graph in Desmos (last accessed: 2025-11-20). License: CC BY-SA 4.0

On the Fraction of Light Diffracted by a 2D Periodic Mesh

I will now transition to discuss the 2D diffraction case. An incident plane wave of unit power interacts at normal incidence and is diffracted by a 2D periodic mesh (whose bars are perfectly blocking, and whose open areas are perfectly transmissive), then focused via a series of optics (such as mirrors in a Cassegrain geometry) towards a screen. The mesh transmits a fraction $M = 1 - \text{BF}$ of the incident power or intensity – where M will be used throughout the text as mesh transmittance or equivalently mesh open area– resulting in a central order at zero angle (the core of the diffraction figure) and an array of diffraction orders

at nonzero field angles (the so-called *lobes*). A visual description of the problem is given in Fig. 2.4. To assess what fraction of the transmitted light is in the

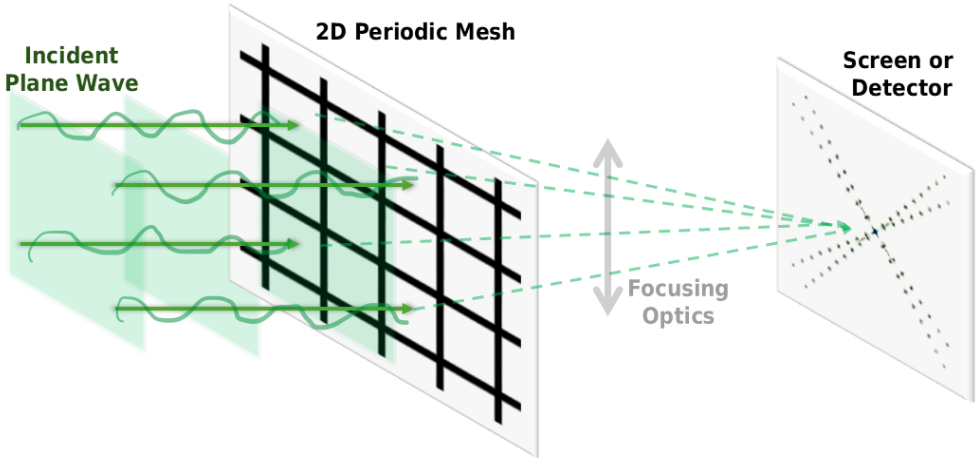

Figure 2.4 Example of Diffraction Figure of an incident plane wave by a 2D periodic mesh structure. The mesh on the left is the same as Fig. 2.1. The central diffraction figure core and secondary order lobes are easily distinguishable. The figure of diffraction on the right is taken and modified from P. Grigis et al. [64], courtesy of NASA/SDO and the AIA, EVE, and HMI science teams.

core, and what fraction is distributed inside the diffraction lobes, it is possible to obtain a derivation as a consequence of the Babinet's Principle [65] [63]. With this approach, valid for completely opaque meshes, *it is found that, given a 2D periodic mesh with mesh transmittance M, the transmitted power in the core is M^2 and that in the lobes is $M(1-M)$*. A proof is detailed in Appendix C, while a somewhat simpler approach could be given in terms of Fourier optics, and I refer the reader to the specialized literature [63] [66] [67].

The consequences found for the Babinet's Principle are both remarkable, but they are also limited by their assumptions. One important assumption is that the mesh is made of a completely opaque material in its non-open areas: thus, the predictions are not expected to be correct in the situation of a partially transmissive mesh material. Another relevant aspect is that the proof assumes that the core is a Dirac-delta-like disk. Still, this assumption depends on the characteristic of the mesh, the finiteness of the entrance pupil limiting the incident plane wave, and the overall requirements one is trying to adhere to: for example, considering MUSE's angular resolution requirement of $\Delta\theta < 0.5''$, this aspect might not be completely given for granted in practical scenarios. These caveats are presented for reference, and they will be discussed more in the subsequent chapters and sections; thus, what is presented here is deemed as an *approximation* that gives important physical insight into the true phenomena. Generally speaking, a blocking mesh pushes a fraction M^2 of the total signal in the core, and the more it blocks, the more it deflects towards secondary order lobes. Still, there are feasible scenarios in which this simple picture could only be qualitative.

Position of Secondary Order Lobes in Figure of Diffraction by a 2D Periodic Mesh

In this section, I derive a consistent approach to predict where the position of secondary order-lobes will appear in the angular screen. This aspect is quite important to assess the goodness of a given simulation. I will practically consider situations where diffraction at very small angles occurs, as the field of view for MUSE is at most a few mrads and thus small-angle approximation is excellent ($\sin(\theta) \simeq \theta$) in all cases.

The 2D meshes, both square or hexagonal as seen in Section 2.2 and as will be discussed in the following design filters sections of the same chapter, can be thought of as a lattice with a provided basis. Following X-ray Diffraction and Crystallography treatments [68] [69], I will drive a parallelism between the diffraction by a crystal and the diffraction by a mesh. The main difference is the geometry: a crystal has inter-planar distances d of the order of nm, or Å and thus the angle λ/d appearing in the Bragg conditions will deflect light to a few degrees in general if the wavelength is in the EUV/X-rays, whereas mesh geometries in 2D have pitches of the order of 300 µm to 5 mm, and thus λ/p will be of the order of arcsec (which can be relevant in the case of the MUSE mission).

I hereby state the Bragg principle. The pictorial idea is that two beams of equal wavelength λ are interacting with two co-planar surfaces and are reflected by these parallel surfaces in the crystal, and the allowed scattering angles are those that satisfy a given constructive interference relationship, which follows.

$$2d\sin(\theta) = n\lambda \tag{2.6}$$

Where d is the minimum inter-planar distance, n is a diffraction order integer, λ is the wavelength of the incident light, and θ is half of the angle of deflection of the incident light with respect to the reflected one. A visual representation is given in Fig. 2.5.

In the small-angle approximation, considering the scattering angle $\alpha = 2\theta$, I rewrite Bragg's statement in terms of the scattering angle when it is extremely small.

$$\alpha = \frac{n\lambda}{d} \tag{2.7}$$

The main idea is that this equation also applies to the geometry of interest to the work, i.e., to the diffraction problem described in Fig. 2.1 → p. 21. A famous identity in lattice theory – i.e., the equivalence between Bragg's law and Laue equations – states that the infinite set of parallel planes of symmetry in a periodic lattice possess a minimum inter-planar distance d obtainable by a vector $\mathbf{g}$ of the reciprocal lattice via the formula $d = 2\pi/|\mathbf{g}|$, and that the $\mathbf{g}$ vectors modulate the

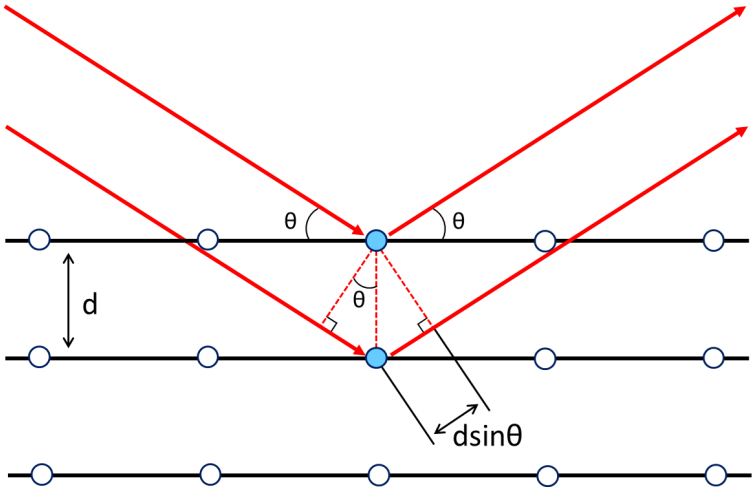

Figure 2.5 Bragg diffraction from a cubic crystal lattice. Plane waves incident on a crystal lattice at angle θ are partially reflected by successive parallel crystal planes with inter-planar minimum spacing d. The superposed reflected waves interfere constructively if the Bragg condition of Equation (2.6) is satisfied. The Bragg condition is equivalent to stating that the path difference, $2d\sin(\theta)$, is an integer multiple of the wavelength. Author: Σ64. License: CC BY 3.0

feasible scattered wave vectors $\mathbf{k}'$ from the incident wave vector $\mathbf{k}$ by $\mathbf{k}' - \mathbf{k} = \mathbf{g}$. Since this application is about diffraction by a 2D geometry, the infinite planes of symmetry of a 3D lattice would become infinite lines of symmetry, or so-called Bragg rods [70], but the idea stands. The protocol to retrieve the feasible secondary diffraction lobes positions in the (scattering) angular space would be:

1. Understand which 2D lattice is the structure under study, isolate its basis, and the primitive translational vectors.
2. Evaluate the reciprocal lattice, and the vectors $\mathbf{g}$ compounding it. These vectors in the reciprocal lattice encode the feasible scattering directions of the secondary lobes in the angular space.
3. Utilize this to find the possible inter-planar distances via $d = \frac{2\pi}{|\mathbf{g}|}$ which can be plugged in the Bragg's condition.
4. Via Bragg's condition Equation (2.7) with $n = 1$ (without loss of generality as the reciprocal lattice vectors also follow translational symmetry), find the feasible minimum scattering angles via $\alpha = \lambda \cdot \frac{|\mathbf{g}|}{2\pi}$, or, defining the vectorial nature of these angles as that of the reciprocal vectors, $\boldsymbol{\alpha} = \lambda \cdot \frac{\mathbf{g}}{2\pi}$.

I will deal with either hexagonal lattices or square lattices, and thus I will derive angular expressions for these.

In the case of **2D hexagonal lattices** with pitch p, the reciprocal vector space is also a 2D hexagonal lattice of points with pitch in the reciprocal lattice units of $g_{\text{hex}} = \frac{4\pi}{\sqrt{3}p}$. However, the orientation of the reciprocal lattice is changed

by 90° with respect to the initial lattice (a similar treatment is done by C. M. Krowne [71]). Thus, feasible scattering angles are found in a hexagonal lattice, as predicted by the reciprocal vectors, with an angular pitch as seen in the screen of:

$$\alpha_{\text{hex}} = \frac{2}{\sqrt{3}} \frac{\lambda}{p} \tag{2.8}$$

In the case of **2D square lattices** with pitch p, the reciprocal vector space is also a 2D square lattice with pitch in the reciprocal lattice units of $g_{\text{square}} = \frac{2\pi}{p}$. Thus, one quickly recovers the angular pitch expected in the screen as:

$$\alpha_{\text{square}} = \frac{\lambda}{p} \tag{2.9}$$

Notice that while these formulae predicts the periodicity and possible position of secondary order lobes in the diffraction figure, they do not predict their intensity, as – inferring from X-ray Crystallography and 3D previously known results – the *geometrical structure factor*, which describes the scattering from the basis in the form of a particular Fourier transform of the basis components, is proportional the intensity of the peaks predicted by the reciprocal lattice in direction $\mathbf{k}' = \mathbf{k} + \mathbf{g}$, meaning the basis can cause some peaks to become stronger and others weaker. Thus, this can be seen as general guidance.

It is in principle possible to find a *Structure Factor Modulation for 2D Mesh Diffraction*: there are known Fraunhofer treatments for diffraction gratings and periodic aperture arrays where a sinc-envelope modulation formula is found [63] [67] [72]; in XRD and in the 3D geometry, crystal lattices and bases are frequently studied [69], although the geometry and the algorithms employed are fundamentally different, as big angles are experimentally probed and small atomic structures are explored, while the situation of interest to my work is almost the opposite; and some treatments explore the diffraction of 2D metallic meshes but they are not treated organically and in an extendable way to EUV general meshes [73] [74].

Since a comprehensive treatment with applications to the specific scenario of interest to MUSE, and applicable to various types of meshes (square, hexagonal), various types of pitch (fine, coarse) and also various types of materials (completely blocking, partially transmissive mesh bars) is not present in the literature, this might be a genuine opportunity for a future technical contribution where: (i) the structure factor for hex/square 2D meshes with finite bar thickness w is derived; (ii) the intensity modulation envelope as a function of pitch p, w, and mesh bars' material transmittance T is derived, (iii) possibly with both Fresnel and Fraunhofer treatments; and (iv) where applications to MUSE's specific parameters with simulations akin to the one explored in my work or to realistic scenarios are assessed. This is outside the scope of this work.

2.3 MUSE Filters Designs

Note. The pieces of information provided in this and the following sections reflect the situation during the development up to demonstration and structural models of the filters for MUSE. Still, they are not final regarding the exact set of filters that will be flown in the mission (so-called flight models, or FMs). Furthermore, alternative solutions employing no mesh are under study at the moment, and could prove interesting as they do not produce diffraction, as studied in the following designs.

Hereinafter, the terms heritage or heritage-based will be used to index the filter designs based on very similar designs from STEREO/SECCHI and SDO/AIA, as discussed in Section 1.3.I will begin by detailing the heritage-based filter design(s). Afterwards, I will discuss the design of the DM and STM CNT-based filters, as their design changed throughout their development as a result of the findings of the relevant potential diffraction impact that I will cover in Section 2.4 → p. 35.

Heritage-based Filter Designs

The baseline design for the MUSE SG telescope (250 mm outer diameter) and the CI telescope (200 mm outer diameter) entrance filters described below are under investigation as high TRL filters for the MUSE SG, and are based on the heritage of the successful space missions STEREO/EUVI [25], and SDO/AIA [31], as mentioned in Section 1.3. Due to the difference in outer diameter of the telescope, the EF filters for the CI will thus be slightly smaller than those of SG. Inside the telescope(s) entrance pupils, there is a 90 mm diameter internal blind spot to accommodate the secondary mirror or the reflecting grating in a Cassegrain-like telescope geometry. The EF is divided into four quadrants as follows, very similarly to the STEREO-SECCHI EUVI filters presented in Fig. 1.5 → p. 12, and their design is as follows in terms of materials and geometries of the mesh.

Spectrograph Telescope Entrance Filters (Heritage-based solutions)

- two quadrants (108 Å channel) out of four are made of a filter with a multi-layer thin-film with 200 nm of Zr deposited on a PI film 75 nm thick supported by a Ni square coarse mesh (5 LPI, or 5.08 mm pitch) and ∼75 µm width of the mesh bars (mesh open area ∼ 97 %). An alternative solution under consideration is a thin-film with 200 nm of Zr supported solely by a Ni square fine mesh (70 LPI) with 363 µm pitch and ∼35 µm width of the mesh bars (mesh open area ∼ 82 %).
- one quadrant (171 Å channel) out of four with a filter composed of a multi-layer thin-film with 150 nm of Al deposited on a 75 nm PI film thick supported by a Ni square coarse mesh (5 LPI, or 5.08 mm pitch) with ∼75 µm width of the mesh bars (mesh transmittance ∼ 97 %).
- the last quadrant (284 Å channel) of the four with a filter with a thin-film made

of 150 nm of Al supported by a Ni square fine mesh (70 LPI) with 363 µm pitch and ∼35 µm width of the mesh bars (mesh open area ∼81 %). Alternatively, a filter with the same design as the 171 Å channel filter, described above, is considered.

Table 2.1 summarizes the heritage-based SG entrance filterchannels: the filter materials and their thicknesses, the mesh type, and transmittance of the sole mesh, of the sole film, and their combination. The filter transmittance value in the rightmost column can be considered the energy input into the MUSE mirrors, as this is the maximum amount of energy that will reach the whole FOV. For the thin film transmittance F, the ideal scenario with no native oxide is employed in this design introduction section, and the transmittance was evaluated via the scattering factors available from Henke et al. [75] [76]. Moreover, Ni meshes are assumed to be completely opaque. The mesh transmittance M is provided by Equation (2.1).

Remark 3. Native oxide is expected to grow on metals [77] in general, and thus on thin films of PI/CNT coated with metal. Even if oxide is neglected in this part, the results of the optical simulations and analyses work are general: it is always possible to scale any resulting PSF obtained with a given thin film transmittance F to the realistic filter transmittance F_R including the oxide simply by re-scaling the PSF via the constant factor F_R/F, where F is taken from the values used in this work, and given in the tables detailing all of the geometries. These hypotheses will be relaxed in the experimental investigation of the films carried out in Chapter 4 →p.71 where the amount of oxide is retrieved and compared between different substrates. ⌟

Table 2.1 List of the heritage-based entrance filter channelsfor the MUSE SG. The "Materials" column provides multi-layer thin films by specifying the sequence of materials and the thickness t in nm. Tran. is transmittance. The mesh is specified by its material (Ni in this case) with a square geometry with the given LPI. The transmittance of each mesh (M), that of the ideal multi-layer thin-film with no oxide (F), and the combined filter transmittance (MF) are given.

Channel (Å)	Materials Film (t); Mesh(LPI)	Mesh Tran. (M)	Film Tran. (F)	Filter Tran. ($M \cdot F$)
108	Zr 200 / PI 75; Ni(5)	0.971	0.387	0.376
171	Al 150 / PI 75; Ni(5)	0.971	0.392	0.381
284	Al 150; Ni(70)	0.816	0.717	0.585

Context Imager Telescope Entrance Filters (Heritage-based solutions)

– two quadrants (195 Å channel) are composed of filters with the same thin-film multi-layer and mesh solution proposed for SG's 171 Å wavelength channel's filter.

– two quadrants (304 Å channel) are composed of filters with the same thin-film multi-layer and mesh solution proposed for SG's 284 Å wavelength channel's filter (both main and alternative).

Besides the telescope pupil entrance filters, there will also be Filter Wheel filters (FWF) with the same design as above, for redundancy purposes (although smaller in dimensions, as they will be closer to the detector). In addition, other thicker FWF are considered to extend the versatility of the mission in observing strong events, such as the thick filters in SDO/AIA [31].

Demonstration Model CNT-based Designs

As stated in the introductory paragraphs, the baseline filters described so far are part of the general design. In my work, an important effort went into developing, characterizing, investigating, and improving the design of the novel CNT-based proposed solutions. The following designs were under investigation as demonstration model (DM) filters proposed with a novel technology: instead of a substrate with polyimide or a fine metal mesh, they use a CNT membrane, and instead of a structural supporting metal mesh, they use a conservative CNT-mesh that is chemically bound to the substrate, avoiding any glue and consequential glue-based defects that are common in thin-film productions. The embedded CNT structural meshes are obtained by laser cutting of a CNT pellicle consisting of high-density (HD) oriented multi-wall (MW) CNT bundles [39]. The designs presented in this section are detailed in Barbera et al. [43] along with the FW filters.

The density $\rho = 0.3$ g/cm^3 is employed for the density of the carbon structures, and this is an educated guess based on the thickness formulae provided by the manufacturer CANATU, but further studies for the exact determination of the density of these structures are ongoing [41]. All the filter/mesh transmittances in the EUV range are modeled with Henke scattering factors [75], and a tool is available for the calculation of transmittance of thin solid films in the related website [76]. Here, I detail the properties of the CNT membranes, coatings, and meshes used as models for the DM designs of the SG and CI EFs in MUSE.

Spectrograph and Context Imager Telescope Entrance Filters (DM CNT-based solutions)

– For the 108 Å wavelength channel of MUSE SG, 200 nm of Zr deposited on a CNT membrane with 40% T @ 550 nm ($t = 283.3$ nm, $\rho = 0.3$ g/cm^3, chem. formula C) supported by a CNT honeycomb pattern mesh with 15% T @ 550 nm ($t = 576.7$ nm, $\rho = 0.3$ g/cm^3 chem. formula C) with 5 mm pitch and 600 µm width of the mesh bars are employed. The CNT-membrane transmits 85.7% at 108 Å , while the CNT-film compounding the mesh transmits 73.0% at the same wavelength. With such a design, the total geometric blocking factor of the mesh is 22.56%; however, the effective blocking factor, which accounts for the transmittance of the mesh, is 6.1%,

obtained with $6.1\% \simeq 22.56\% \cdot (1 - 73\%)$ as per Equation (2.3).

– For the 171 Å and 284 Å MUSE SG channels, and all of the channels for the CI telescope, the design consists of 150 nm of Al deposited on the same kind of membrane and mesh. The CNT-membrane transmits 66.3% and 32.4% respectively at 171 Å and 284 Å , while the membrane the mesh is made of transmits 43.4% and 10.1% respectively at the same wavelengths. The mesh geometric blocking factor is 22.56%, whereas the effective blocking factor is 12.8% and 20.3% at 171 Å and 284 Å , respectively.

Table Table 2.2 shows the wavelength ranges, the materials and films used (along with the multi-layer material and thickness composition of the layers), as well as the properties of the transmittance of the sole mesh, the sole film, and the compound material.

Remark 4 (CNT thickness notation in terms of %T)**.** In the case of CNT films, instead of a direct thickness such as what was done in Table 2.1 for PI substrates, the figure of a percentage %T is given: that is the transmittance of the bare CNT pellicle used as substrate measured @550 nm, which is directly related to a measurement of the thickness of the pellicle as shown in the study by Ermolaev et al. [78] where the thickness measurement obtained with transmission spectroscopy is shown to be correlated to that obtained with atomic force microscopy (AFM) step-height measurements. ⌟

Table 2.2 List of filter Demonstration Model (DM) designs under investigation in this work with novel CNT pellicles and using conservative membrane and mesh. The "Materials" column provides multi-layer thin films by specifying the sequence of materials and thickness t in nanometers or, in the case of CNT pellicles, its optical transmittance at 550 nm (CNT pellicle being implicitly assumed in that case). The mesh is specified by its material (CNT in this case) with a hexagonal geometry (HEX) with the given LPI. The transmittance of each mesh (M), that of the ideal multi-layer thin-film with no oxide (F), and the combined filter transmittance (MF) are given.

Channel (Å)	**Materials Film (t); Mesh(LPI)**	**Mesh Tran. (M)**	**Film Tran. (F)**	**Filter Tran. (MF)**
108	Zr 200 / 40%T; HEX (5)	0.939	0.436	0.409
171	Al 150 / 40%T; HEX (5)	0.872	0.526	0.459
284	Al 150 / 40%T; HEX (5)	0.797	0.233	0.186

The mechanical design of the DM structural frames has been shown to prove that the proposed filter technology can satisfy the main MUSE instrument's requirements. Figure Fig. 2.6 shows an exploded view of the SG EF quadrant; more details on the mechanical design and preliminary Finite-Element Method (FEM) model-analysis of the DM filters are available in the paper by D'Anca et al. 2024 [42]. An Al-coated manufactured piece with the design described is given in Fig. 2.7.

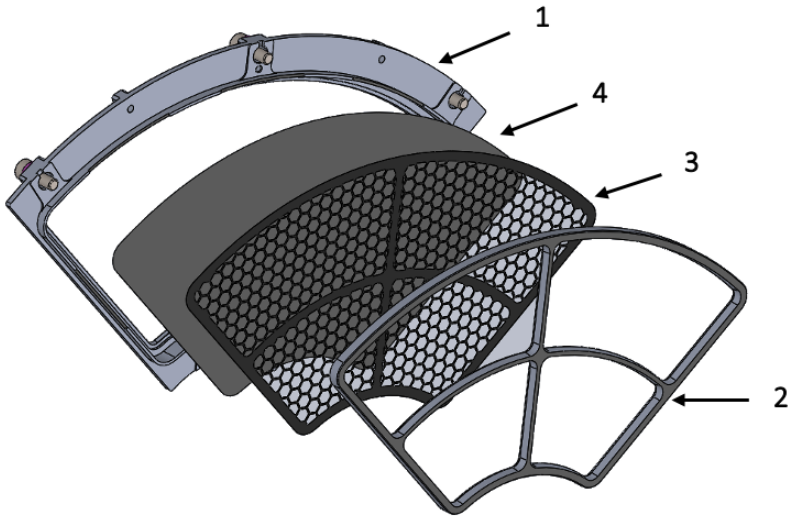

Figure 2.6 Exploded view of one quadrant of the DM EF for the SG instrument on MUSE, manufactured with CNT technology. 1. Outer frame, 2. Inner frame, 3. CNT Mesh, 4. CNT/metal pellicle (either Zr or Al). Credit: Barbera et al. [43]

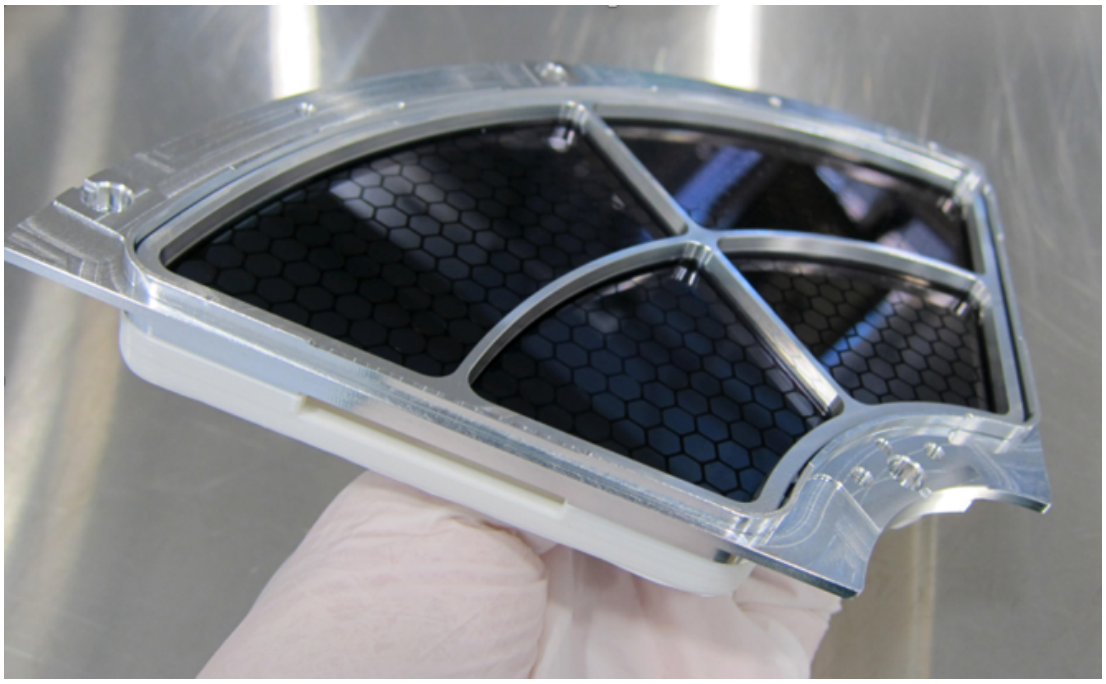

Figure 2.7 Manufactured piece of one quadrant of the DM EF for the SG instrument on MUSE with CNT technology, Al-coated. The point-of-view (POV) looks at the inner-frame where the CNT-mesh is attached to the CNT-membrane. Credit: INAF-OAPA/UNIPA/Canatu/Ametek.

The outer frame of the EF filter is the structural part that interfaces the filter with the telescope; the inner frame is a secondary structure that supports both the mesh and the membrane. The mesh supports the few hundred nm thick membrane consisting of a multi-layer comprising the CNT pellicle coated with either Al or Zr. The mesh follows a hexagonal pattern instead of a square one, like in heritage-based solutions, because of recent results which showed a reduction in overall stress level under vibrational loads in filters if a hexagonal mesh is used to replace a square one [79]. The metal coating is on the outer frame side, which is assumed to directly face the sun. The membrane and structural mesh adhere to each other and to the inner frame through van der Waals forces. A structural adhesive bond joins together the inner and outer frames. Some conductive adhesive points ensure the electrical and thermal conductivity between the membrane and the outer frame.

Filter wheel filters (FWFs) are almost identical to the entrance filters (EFs), with the only difference being meshless and in having a smaller internal diameter (ID): SG FWFs have an ID $\sim$27 mm, CI FWFs have an ID $\sim$56 mm.

Structural and Thermal Model Designs

The designs presented in this section are the same as those used for the Structural and Thermal Models (STMs) filters detailed in Barbera et al. [43]. These models were devised in part also as a consequence of the work to be discussed on diffraction in Section 2.4 → p. 35, which details how reducing the size of the width of the CNT-based mesh also reduced the diffraction content of a design. Also in this case, a CNT-based laser-cut mesh is used. Still, the thicknesses of both the mesh and the CNT-membrane employed overall are lower, as the CNT-membranes have a transmittance increasing from 40% in the DMs to 55%, while the mesh used here mimics the membranes employed in the DMs. Here are the properties for the CNT membranes, coatings, and meshes used as models for the STM designs of the CNT-based SG and CI EFs in MUSE.

Spectrograph and Context Imager Telescope Entrance Filters (STM CNT-based solutions)

- For the 108 Å channel of MUSE SG, a filter with a thin film multi-layer composed of 200 nm of Zr are deposited on a CNT membrane with 55% T @ 550 nm (t = 200 nm, ρ = 0.3 g/cm^3, chem. formula C) supported by a CNT honeycomb pattern mesh with 40% T @ 550 nm (t = 283.3 nm, ρ = 0.3 g/cm^3 chem. formula C) with 5 mm pitch and 250 µm bar width. The membrane transmits 89.7% at 108 Å , while the CNT-film the mesh is made of transmits 85.7% at the same wavelength (CNT-mesh has the same thickness as the CNT-membrane had in the DM designs). The geometric blocking factor of the mesh is 9.8%; however, the real blocking factor, which accounts for the partial transmittance of the mesh (as per Equation (2.3)), is just 1.4%.
- At 171 Å and 284 Å channels of MUSE SG, and all of the channels for the

CI telescope, the design consists of 150 nm of Al deposited on the same membrane and mesh as above. The CNT-membrane transmits 74.9% and 45.2% respectively at 171 Å and 284 Å . In contrast, the membrane the mesh is made of transmits 66.3% and 32.4% respectively at the same wavelengths, with a mesh also in this case having the same CNT-film thickness as the DMs. In this way, the geometric blocking factor is 9.8%, whereas the real blocking factor is 3.3% and 6.6% at 171 Å and 284 Å , respectively.

Table 2.3 shows the wavelength ranges, the materials and films used (along with the multi-layer material and thickness composition of the layers), as well as the properties of the transmittance values of the mesh, thin film, and the compound material. In the case of CNT films, the transmission at 550 nm is given.

Table 2.3 List of filters' Structural and Thermal Model (STM) designs under investigation in this work with novel CNT pellicles and using thinner membrane, mesh thickness, and mesh width. The Materials column provides multi-layer thin films by specifying the sequence of materials and thickness t in nm or, in the case of CNT pellicles, its optical transmittance at 550 nm (CNT pellicle being implicitly assumed in that case). HEX stands for hexagonal CNT-based mesh.

Channel (Å)	**Materials Film (t); Mesh(LPI)**	**Mesh Tran. (M)**	**Film Tran. (F)**	**Filter Tran. (MF)**
108	Zr 200 / 55%T; HEX (5)	0.986	0.456	0.451
171	Al 150 / 55%T; HEX (5)	0.967	0.593	0.574
284	Al 150 / 55%T; HEX (5)	0.934	0.324	0.303

The mechanical design of the EF and FWF frames was also slightly modified from the DM ones to satisfy development needs and ensure that the interfaces with the telescope entrance pupil and filter wheels are compatible with the needed requirements for mechanical testing, as discussed with the MUSE engineering team. Further details can be found in the paper by Barbera et al. [43] on the engineering details of these designs. I hereby present the changes to the designs. Fig. 2.8 provides an exploded view of the STM EF quadrant of the SG instrument, while Fig. 2.9 provides exploded views of the STM Filter Wheel Filters (FWFs) for the SG (left panel) and CI (right panel) instruments. Importantly, the shape of the FWFs for the CI remained circular, while those for the SG became more square-like.

2.4 Diffraction Simulation Setup and Metrics

Simulation Setup

I analyzed simulations of the PSFs via a purely diffractive approach for a selection of the designs described in Section 2.3 →p.29, and I compared them with the cases

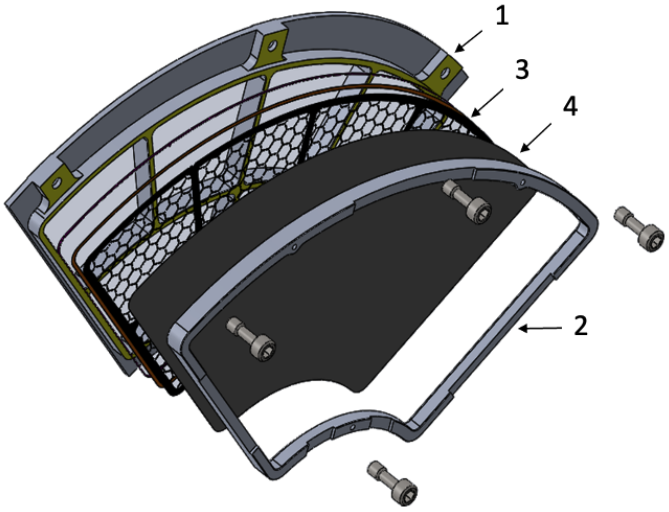

Figure 2.8 Exploded view of one quadrant of the STM EF for the SG instrument on MUSE based on CNT technology. 1. Outer frame, 2. Inner frame, 3. CNT Mesh, 4. CNT/metal pellicle (either Zr or Al). Credit: Barbera et al. [43]

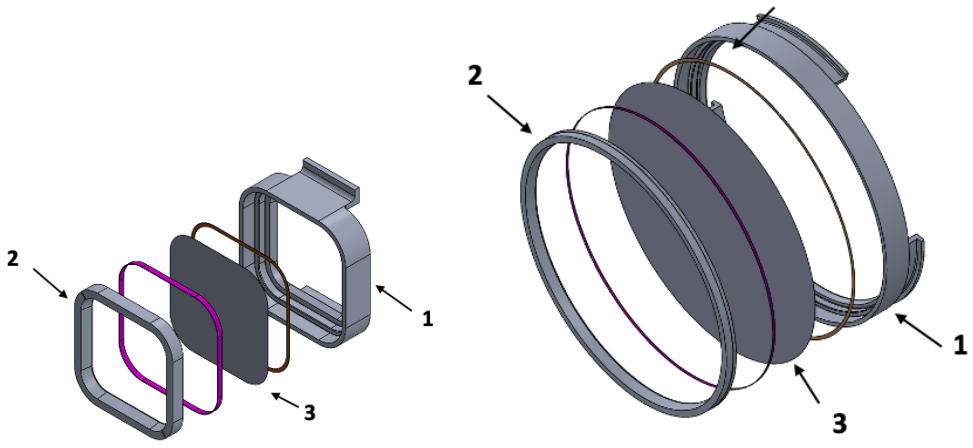

Figure 2.9 Exploded view of the STM FWF for the SG (left panel) and CI (right panel) instruments on MUSE based on CNT technology. 1. Outer frame, 2. Inner frame, 3. CNT/metal pellicle (either Zr or Al). Credit: Barbera et al. [43]

of an ideally-smooth focusing mirror, and with a mirror with realistic roughness, aiming at disentangling the influence of the various factors. The DM filters are not presented here, although presented in Alaimo et al. [80], because their impact is much stronger in terms of diffraction, as will be shown, while the most interesting aspect is to compare the most up-to-date designs between themselves.

The simulations provided by D. Spiga are based on a method employed in one of his papers [57], using an IDL-based code derived from the approach adopted to simulate the diffraction in silicon pore optics for Athena. Although originally applied to X-rays in a grazing-incidence configuration, the underlying well-known principles of modeling the diffraction and evaluating the PSF – i.e., developing the Fourier transform of the complex pupil function from the phase shift and attenuation – remain applicable to our filter mesh geometries and to the case of the MUSE mission. The approximation involved can be applied *a fortiori* in normal incidence transmission through a membrane with inhomogeneous optical properties. The formalism can be applied to EUV wavelengths without limitations, besides adjusting the entrance pupil sampling, based on the value of lambda and the need to adequately over-sample the mesh wire thickness.

To accurately model the PSFs, the *Fraunhofer approximation* of the *Fresnel diffraction*is employed [57], which is valid in the far-field regime [67]. Fresnel's diffraction assumes that the longitudinal dimensions of the diffracting element along the propagation direction of the electromagnetic wave are negligible as compared to the observation distance z, which is well-satisfied by the filters and supporting meshes. The Fraunhofer approximation is a simplified version of Fresnel's, which also assumes that the angular dimensions of the diffracting element ($\simeq d/z$, with d the real dimension of the element), as seen from the observational POV, are much smaller than the angular dimension of the diffraction figure ($\simeq \lambda/d$). In the Fraunhofer approximation, the Fresnel number is required to be much less than unity $N_F = d^2/(\lambda z) \ll 1$. For our typical experimental parameters (mesh size $d \approx 5$ mm, mirror size $d \approx 200$ mm, wavelength $\lambda \approx 10$ nm, and propagation distance $z \approx 3500$ mm assuming the traveled path to be the path inside the Cassegrain's geometry), the calculated Fresnel number found is usually $N_F > 1000$, a value that would place the system in the near-field regime with important geometric shadow effects. However, in the configuration employed, and also shown in Fig. 2.4, the detector observes the image at the *focal plane* of the focusing apparatus. Thus, as a definition, all of the diffracting objects are placed effectively at an infinite distance ($z \to +\infty$), causing the effective Fresnel number to approach zero ($N_F \to 0$), and rendering the Fraunhofer approximation and its associated Fourier transform methods valid.

The simulation setup involves a monochromatic plane wave passing through an entrance pupil comprising a thin film, which introduces a constant phase shift, and a mesh that modulates the transmittance in amplitude and phase: thus the simulated setup is just like Fig. 2.4 → p. 25 with the addition of realistic optics from MUSE and the addition of a thin-film on top of the mesh. In some cases, the

mesh can be completely opaque, and the diffraction stems from a pure amplitude modulation. In others, the mesh is – at least partly – transmitting and so as to introduce phase changes; therefore, the modeling of attenuation and phase at the mesh wires requires the knowledge of the optical constants as a function of lambda. In all cases, a FOV of $100'' \times 100''$ was employed for the description of the PSF. Realistic mirror sizes, apertures, shape errors, and the roughness values expected for MUSE mirrors [18] [58], were included in the models as simulation inputs. The mirror adopted in all the simulations is the 200 mm diameter primary mirror of the CI instrument onboard MUSE. The entrance pupil sampling was conducted with a step size that ensures enough lateral resolution, usually at least 10 times finer than the filter lateral thickness. The pixel size was initially selected to match the diffraction-limited resolution.

Aliasing, as seen in some test simulations for the 70 LPI nickel mesh in Table 2.1, was detected and mitigated for that particular filter design by increasing the entrance pupil sampling. The impact on results was negligible beyond the third significant digit of the core PSF transmittance. In the future, studies devoted to studying diffraction peaks in detail (beyond the scope of this work) will be required to eliminate aliasing effects fully.

Finally, the simulated PSFs were processed using Python scripts, which took the outputs from the IDL simulations and calculated key metrics such as normalization values (i.e., filter transmittance), Half Energy Width (HEW), core PSF transmittance (T_{core}) evaluated within an angular radius of $0.5''$. This angular radius aligns with the desired angular resolution for MUSE, thus providing a practical quantity for the mission. It is important to note that the core PSF values were found to be consistent within a few percent when the integration of the encircled energy was carried out beyond the first-order diffraction peaks. The Python scripts also computed the core-to-total transmittance ratio, providing insight into the efficiency of light collection at the core versus diffraction. Additionally, the Python scripts elaborated the images, degrading them to an angular resolution near the pixel sizes of MUSE (Section 2.4).

Most of the coding for the IDL-based PSF simulation software was carried out by Dr. Spiga. I aided the optimization process by assessing key aspects in the simulations, and most of my work was involved in the PSF Analysis via Python, and the results and performance evaluation across wavelengths and scenarios, and in assessing and implementing the positive feedback contributions from the discussions held with Lockheed Martin Solar and Astrophysical Laboratory (LMSAL) and NASA. I developed a code that performed the *fits* reading files generated by the IDL code, and then performed all of the numerical integrations, pixel degradation (where necessary), plot outputs, and benchmarking. All of the numerical, visualization, figure generation operations were performed using the `NumPy` [81], `SciPy` [82], `Matplotlib` [83]. FITS data handling was performed with `Astropy` [84] [85], and auxiliary datasets stored in NetCDF format were accessed using the `netCDF4` Python interface maintained in the respective Github

[86]. All of the Python routines I developed were validated against analytical limiting cases where applicable.

Useful Diffraction-related Metrics

This section defines all of the metrics of interest to the diffraction chapter. In all of the simulations, the incident electromagnetic wave intensity I_0 is assumed to be of unitary total energy, which would be encoded in the following integral, given the entrance pupil's surface region R and infinitesimal area $dS = dx\,dy$ in such region.

$$\iint_R I_0(x, y)dS = 1$$

After interacting with the filter system (blocking / partially transmissive mesh, absorbing thin film) and being focused on the detecting plane, the intensity is intended as an (arbitrary) energy per unit angle area in the angular space ($I(\theta_x, \theta_y)$), which will be displayed as color maps in the ensuing subsections. All of the integrals of the intensity described below are a form of *encircled energy* over a prescribed angular region. Describing the CCD's FOV as the angular simulation region of choice (i.e. $100'' \times 100''$), the normalization value (Norm.) of the electromagnetic wave would be the following, with infinitesimal angular area $d\Omega \simeq d\theta_x\,d\theta_y$ (valid in the small angle approximation).

$$\text{Norm.} = \iint_{\text{FOV}} I(\theta_x, \theta_y)d\Omega \tag{2.10}$$

This value is expected to be about equal to the filter's transmittance $T = MF$, i.e., the product between the transmittance of the film (F) and the transmittance of the mesh (M), since it is a measure of the energy-throughput from the filter system. Practically, some light could be diffracted out of the simulations' FOV, and thus usually Norm. $\lesssim MF$. This metric can be used to compare the simulation's output with the designs' expected values as described in Table 2.1, and Table 2.3.

θ_{HEW}, the angle at half-energy-width, is defined as the angle at which the encircled energy is half of the total energy, as follows.

$$\theta_{\text{HEW}} \to \frac{\text{Norm.}}{2} = \iint_{\theta \le \theta_{\text{HEW}}} I(\theta_x, \theta_y)d\Omega \tag{2.11}$$

An important aspect is guaranteeing that the half-energy-width is always smaller than the intended MUSE resolution ($0.5''$). This will be verified.

Another crucial aspect is the T_{core} value. This will be defined in the ensuing paragraphs and sections as the encircled energy up to the MUSE resolution's angle $0.5''$, as follows.

$$T_{\text{core}} = \iint_{\theta \le 0.5''} I(\theta_x, \theta_y)d\Omega \tag{2.12}$$

Usually, the core is defined as the encircled energy up to the first secondary minimum in the diffraction peaks. This is quite impractical in the 2D regime for two reasons: firstly, in some cases the angular spacing of the secondary-order diffraction lobes falls within the Airy disk of the mirror, and this is always expected to be part of the convolution defining $I(\theta_x, \theta_y)$, thus making it hard to decide whether or not the core should be defined before the first minima due to the Airy disk oscillations or due to the diffraction lobes; secondly, the secondary diffraction lobes spacing heavily depends on the design, and in some cases it is small, or in some cases it is extremely large, making it not useful to compare different designs. Using the definition for T_{core} proposed here serves the purposes of both allowing for comparison designs with an *apples to apples* stand, and to provide useful values for MUSE, as this will precisely describe the diffraction content to be expected in the MUSE resolution prescription.

While T_{core} will be used to describe the PSF-core-transmission of a filter system, the term T_{mir} will be used to describe the PSF-core-transmission of the mirror without any filter, encoding the effect of the mirror roughness on the core broadening.

Let's now describe simple models. I already described the model of the Norm. figure, here again written as the product of film and mesh transmittances, and it is repeated hereinafter. This is also a model of the energy throughput that accesses the FOV in the simulated system (and the CCD in the focal plane in the real scenario).

$$\text{Norm.}_{\text{model}} = MF \tag{2.13}$$

The core modeling should contain both the modeling information encoded in the mesh transmittance, which, as described in Section 2.2 → p. 24, should be M^2, as well as the throughput of the film F, and the encircled energy due to the mirror roughness properties, T_{mir}. Thus, the simplest model possible is the following, encoding the total energy signal to be transmitted in the core.

$$T_{\text{core model}} = M^2 F \cdot T_{\text{mir}} \tag{2.14}$$

The zero-order diffraction efficiency – i.e., the ratio of the intensity of the central peak with respect to the throughput intensity [87] – is thus expected to be about $T_{0^{\text{th}}\,\text{order eff}-\text{model}} = M \cdot T_{\text{mir}}$.

The following two metrics are stated for completeness, and, while they are not used in this work, they will be useful in the future to assess the efficiency of a filter in terms of how much of the signal is diffracted in secondary order lobes, which is an analysis outside of the scope of this work. Following a similar logic, by multiplying the total energy throughput MF by the diffused energy outside of the core fraction $1 - T_{\text{core}}$, one obtains the content of the background (or BKG) noise (i.e., large wings of the central zero-diffraction lobe in the rough case), which is the following.

$$T_{\text{BKG noise model}} = MF \cdot (1 - T_{\text{mir}}) \tag{2.15}$$

And the secondary lobes following this description and the consequences of Babinet's theorem would be $MF - T_{\text{BKG noise model}} - T_{\text{core model}}$, i.e., the following.

$$T_{2^{\text{nd}}-\text{lobes model}} = MF(1-M) \cdot T_{\text{mir}} \tag{2.16}$$

Another metric model to better describe and justify what is seen in the simulation is the angular pitch seen in the secondary diffraction peaks: these should follow the scattering angle laws proven in Section 2.2 → p. 26, with spacing for square meshes expected to be $\Delta\theta_{\text{square}} = \lambda/d$ with d mesh pitch size, and spacing for the hexagonal meshes expected to be $\Delta\theta_{\text{hex}} \simeq 1.1547\,\lambda/d$.

Finally, *mid-vertical*, *mid-horizontal*, and *radial density* profiles will be used. These are, respectively: the restriction of $I(\theta_x, \theta_y)$ to $I(\theta_x = 50'', \theta_y)$; the restriction of $I(\theta_x, \theta_y)$ to $I(\theta_x, \theta_y = 50'')$; and the spectrum of encircled energies evaluated in an annular angular region $\theta_0 < \theta < \theta_0 + \Delta\theta$ around an angle θ_0 with angular size $\Delta\theta$.

This summarizes all of the metrics of interest. Let's proceed to describe the results.

Results of PSF Studies on Realistic Mirrors

Mirrors' PSFs are studied to isolate the contribution of the mirror roughness, without including a masking mesh at the entrance pupil. In the mirror-only case, EUV rays propagate unperturbed from the mirror to the focal plane, without any absorption or phase shifts besides those introduced by the mirror roughness imperfections (if present). As a result, 100% of the incoming light reaches the $100'' \times 100''$ focal plane in the simulation. While the ideal mirror would appear in the focal plane as an Airy-disk shape whose size would be comparable to $\sim \lambda/D$ where D is the mirror size, roughness would add diffuse intensity *noise* to the PSF, also diffusing light out of the $0.5''$ core. An example for the ideal and rough mirror at 108 Å is given in Fig. 2.10.

Retrieving the mid-vertical profiles from these PSFs of the mirrors yields the resulting plots in Fig. 2.11

Table 2.4 shows the results for ideal and rough mirrors, and the effects of roughness on the PSF; the pixel size is always the simulation diffraction limit size (determined by λ and the mirror diameter); the HEW is dominated by the Airy disk in the ideal mirror and at low energies. Whereas in the rough mirror, scattering due to roughness takes over for increasing energies. However, the HEW values never exceed $0.11''$ in any case, thus remaining within MUSE requirements. Finally, the integrated PSF-core-transmittance intensity T_{core} always remains just below 100% in the ideal mirror, whilst it decreases for increasing energy in the real mirror. At 108 Å, about 30% of the input light is scattered outside the $0.5''$ radius, even before simulating any interaction with the filter mesh, which is a relevant input when assessing the efficiency of a given filter design (as this aspect is *independent* from the filter choice).

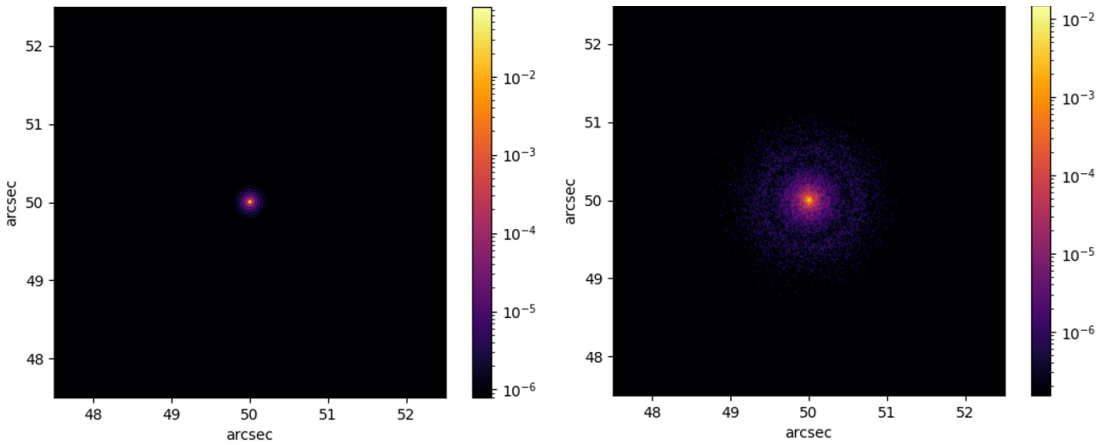

(a) PSF of the ideal mirror at 108 Å .

(b) PSF of the mirror with realistic roughness at 108 Å .

Figure 2.10 Simulated PSF color-maps with log-scale intensity at 108 Å with mirror and no filter. **Panel (a)** on the left shows the case of an ideal mirror with no roughness, where the core appears as an Airy disk due to a circular aperture. **Panel (b)** on the right presents the effect of realistic mirror roughness, which leads to a broader PSF core and enhanced diffuse intensity in the wings. Both simulations use a FOV restricted to 5″ around the center.

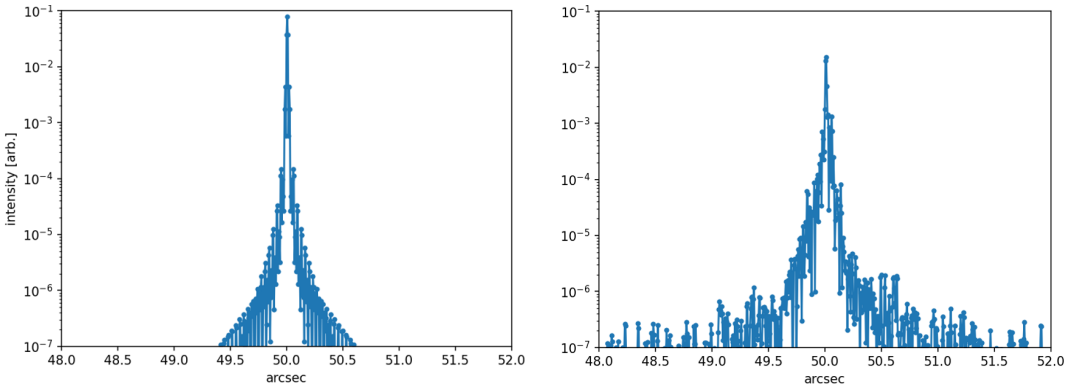

(a) PSF vertical profile of the ideal mirror at 108 Å .

(b) PSF vertical profile of the mirror with roughness at 108 Å .

Figure 2.11 Mid-vertical PSF profiles at 108 Å extracted from the simulations of Fig. 2.10, displayed with the same log-scale intensity with mirror and no filter. **Panel (a)** on the left shows the ideal mirror case, with an intense zero-order peak and visible secondary diffraction radial ripples. **Panel (b)** on the right displays the effect of realistic surface roughness. In the latter, the zero-order peak is less intense, broader, and diffused scattered light increases noise levels overall.

Table 2.4 Results for the study of the effects of mirror roughness on the PSF. The T_{mir} is evaluated as encircled energy within a 0.5″ radius. When an upper limit is set to the HEW, it means that the HEW becomes comparable in size to the diffraction-limited pixel size.

Channel (Å)	PSF Subject	Pixel Size (″)	HEW (″)	$\mathbf{T_{mir}}$ (%)
108	Mirror (Ideal)	0.006	≤ 0.012	99.3
	Mirror (Rough)	0.006	0.106	70.9
171	Mirror (Ideal)	0.009	≤ 0.019	98.8
	Mirror (Rough)	0.009	0.056	85.7
284	Mirror (Ideal)	0.015	≤ 0.062	98.0
	Mirror (Rough)	0.015	≤ 0.062	92.8

To summarize this section, even without including the filters, the roughness of the mirror never makes the HEW exceed the requirements for MUSE. At the same time, it plays a significant role in decreasing the integrated intensity in the PSF core. The larger the wavelength in the channel, the larger the HEW is, and the higher the T_{mir}, and these are expected since the HEW scales as the λ/D size, while diffused light induces a broadening that scales as $\sigma_{\text{RMS}}/\lambda$ where σ_{RMS} is the root-mean-squared, or RMS, roughness of the mirror [88] [58].

Results of PSF Studies on Filter Designs

The performance of the various filter designs detailed in Table 2.1 (heritage-filters), and Table 2.3 (STM CNT-based filters), was analyzed at the 108 Å, 171 Å, and 284 Å. The results are summarized in Table 2.5 where pixel sizes are the same as the ones listed in Table 2.4.

All of the filter designs are compliant with the HEW requirements of MUSE (0.5″). Furthermore, an important aspect is the Norm. value. If compared to the filters' design MF expected value present in the design tables, it is found that all the Norm. values are less and within 0.1% the expected one, except the Al/70 LPI filter which has a Norm. of 58.1% while the expected value would be 58.5% – still very close. This proves the consistency of the simulations and confirms that there is negligible power scattered out of the $100'' \times 100''$ FOV, and that in the 70 LPI case, some secondary order diffraction peaks lie outside of the simulation FOV, thus explaining the missing 0.4% (which is still negligible overall and less than 0.7% of the total signal).

Moreover, $M^2F \cdot T_{\text{mir}}$, which is the figure of merit (or prediction) adopted as per Equation (2.14), is within 1% of the T_{core} calculated with simulations. Only for the case of the STM CNT design at 108 Å, the difference exceeds 1.5%, which is probably a sign that the mesh is partially transmissive, thus not fulfilling part of the hypotheses of the derivation using Babinet's principle described in

Table 2.5 Results of the PSF analysis and simulations for various filter designs at different wavelengths, as detailed in Table 2.1, and Table 2.3. All of the values are evaluated from the PSF simulations, with $T_{\rm core}$ calculated within a $0.5''$ radius, except for the last column, $M^2F \cdot T_{\rm mir}$, which is reported to model the $T_{\rm core}$ of the filter setup, also including effects of the mirror's roughness, as per Equation (2.14).

Channel (Å)	Filter Design	Norm. Value(%)	HEW ($''$)	$\mathbf{T_{core}}$ (%)	$\frac{\mathbf{T_{core}}}{\mathbf{Norm.}}$ (%)	$\mathbf{M^2F \cdot T_{mir}}$ (%)
108	Zr/PI; 5 LPI	37.5	0.117	25.7	68.6	25.8
	Zr/CNT New	44.9	0.117	33.0	73.5	31.4
171	Al/PI; 5 LPI	38.0	0.056	31.5	82.8	31.6
	Al/CNT STM	57.3	0.056	47.4	82.7	47.4
284	Al; 70 LPI	58.1	0.093	44.5	76.6	43.7
	Al/CNT STM	30.2	0.093	25.3	83.8	26.1

Appendix C → p. 112. And it is always higher than the T_{core} values, reflecting the fact that such an approximation does not take into account the realistic mirror roughness effects that were detailed in Table 2.4.

CNT-based STM filters theoretically offer improvements in the core PSF transmittance w.r.t PI solutions at 171 Å and 108 Å. At the same time, in these two channels, the efficiency of the zero-order diffraction lobe is comparable in all the solutions.

An interesting case presented from the table is channel 284 Å comparing the Al/70 LPI geometry with the novel CNT-based STM one: almost double the signal ($\sim 44.5\%$) is transmitted to the core (compared to $\sim 25.3\%$ for the Al/CNT-based one), at the expense of 23.4% relative diffracted content outside of the core, vs 16.2% with Al/CNT – these latter estimates obtained by evaluating $1-T_{\rm core}/{\rm Norm.}$. Thus, in simplified terms, the trade-off between the two designs is almost $\sim 2\times$ signal at the core at the expense of $\sim 3/2\times$ worse relative diffraction. More on the comparison between designs is explored in the following subsection.

Comparison of the Point Spread Functions

In this section, I compare the PSF expected from the heritage filters vs. the STM designs. There are important differences in the peak distributions in the various designs.

I begin with the case of the 108 Å channel. A full FOV comparison is given in figure Fig. 2.12. The image resolution in the case of the full FOV pictures was degraded to realistic pixel sizes of $\Delta\theta_X = 0.167''$ and $\Delta\theta_Y = 0.4''$, which are the realistic values for the pixel sizes of the MUSE detectors [18].

In the case of the finely spaced mesh of the heritage filter, diffraction peaks

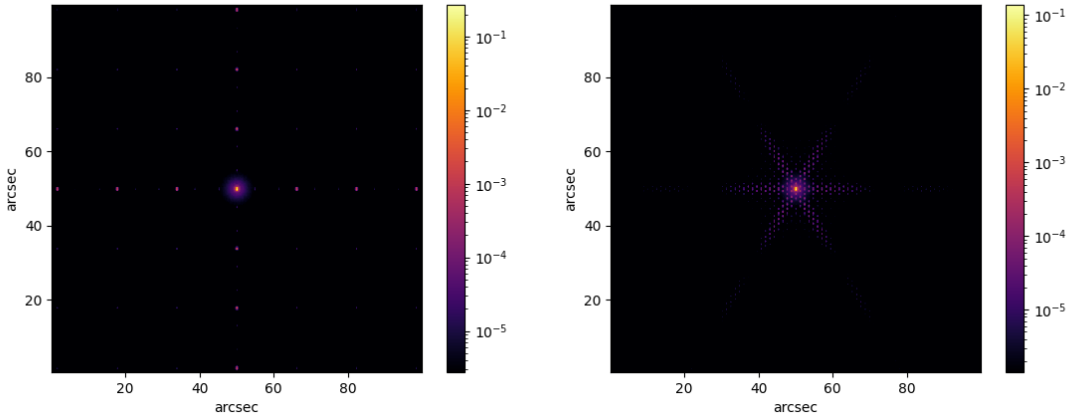

(a) Heritage 284 Å : Al, 70 LPI Ni **(b)** STM 284 Å : Al/CNT, CNT mesh

Figure 2.12 PSF comparison between (**panel (a)**) the heritage filter design and (**panel (b)**) the STM CNT filter design in the full $100'' \times 100''$ FOV at wavelength 284 Å. Pixels in the figure were degraded to the realistic resolution $\Delta\theta_X = 0.167''$ and $\Delta\theta_Y = 0.4''$. In these pictures and all the following ones, the color scale is proportional to the energy density flux collected by each pixel, normalized to the light intensity impinging onto the mirror area.

are regularly separated throughout the FOV near the central peak, forming a typical square cross-diffraction pattern. The peak angular distance is in full agreement with the expected spacing λ/p, using the mesh pitch for the 70 LPI design (Section 2.3 →p.29) and yielding a diffraction angle of $15.5''$. In contrast, the STM filter forms a diffraction pattern with a characteristic hexagonal geometry inherited from the hexagonal tessellation of the mesh. Secondary order diffraction peaks are much closer to the central peak due to the wider separation between consecutive mesh wires. Moreover, while for the heritage design the diffraction peaks remain very bright and occupy the full area, for the STM, the diffraction peak intensities fall off very quickly with increasing angular distance. This is clearly an advantage of the CNT mesh, as the dispersion of the PSF and the formation of ghost features is, from the point of view of intensity, reduced, while in number they are, of course, expected to increase. This can also be seen in Fig. 2.13, where I compare the radial density profiles in the two cases.

As can be seen from Fig. 2.13, the STM diffraction distribution in the radial shells has less impact on the whole FOV than the heritage case, where constant and bright diffraction peaks are present. The intensities fall off immediately below two orders of magnitude that of the zero-order in the CNT-STM case, progressively falling to negligible levels at $20''$ or farther, while the secondary peaks of the heritage-based case remain at the order of $10^{-1} \div 10^{-2}$ of the zero-order intensity. The effect close to the core can be seen in a close-up view ($5'' \times 5''$, Fig. 2.14).

In Fig. 2.14, it is noticeable that for the CNT-based design, the diffraction peaks introduced by the mesh form a regular hexagonal pattern, for the heritage-based design, no secondary diffraction lobe is present near the core, whereas in both

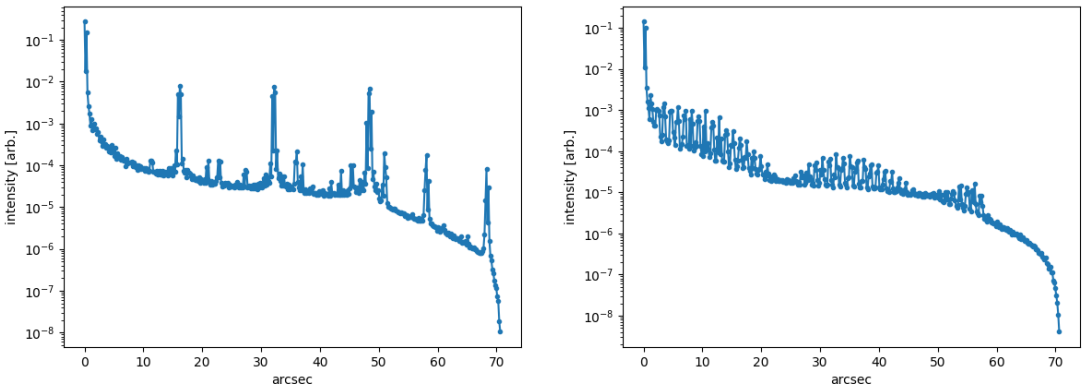

(a) Heritage 284 Å : Al, 70 LPI Ni **(b)** STM 284 Å : Al/CNT, CNT mesh

Figure 2.13 Comparison of the radial density profile between (**(a) panel**) the heritage filter design and (**(b) panel**) the STM CNT filter design in the full $100''\times100''$ FOV at wavelength 284 Å . The profiles are obtained from slicing Fig. 2.12 in a radial sector $\Delta\theta = 0.167''$-wide, up to an angular distance equal to the FOV semi-diagonal. Decay of intensity after $\sim 70''$ is related to the finite size of the simulation FOV

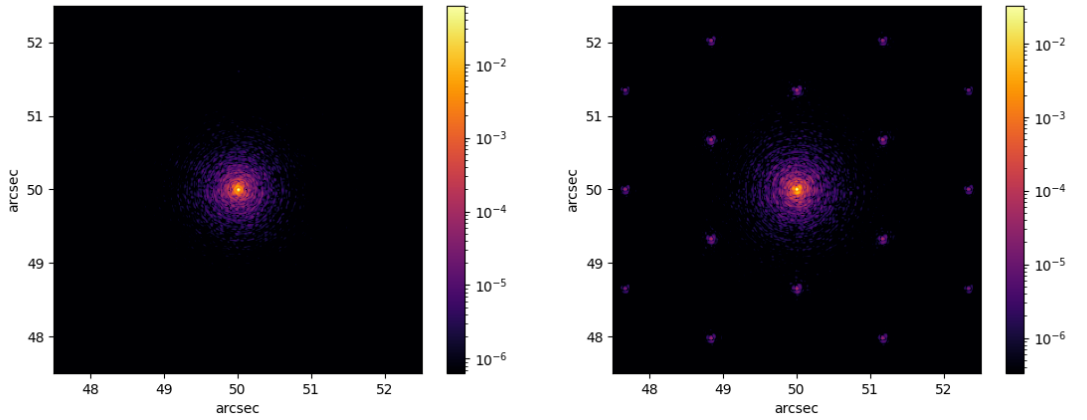

(a) Heritage 284 Å : Al, 70 LPI Ni **(b)** STM 284 Å : Al/CNT, CNT mesh

Figure 2.14 PSF comparison between (**(a) panel**) the heritage filter design and (**(b) panel**) the STM CNT filter design in a reduced $5''\times5''$ FOV at wavelength 284 Å . For the sake of image clarity, the diffraction-limited pixel size of the simulation was kept in these figures ($\Delta\theta = 0.015''$).

cases the central peak has a finite width due to the mirror imperfections. However, the circular diffraction fringes caused by the circular shape of the mirror remain clearly visible. Substituting the pitch size of the hexagonal mesh (described in Section 2.3) in the scattering spacing formula $1.1547\,\lambda/p$ yields a characteristic angular distance of $\theta \simeq 1.35''$, in agreement with the average spacing observed in the simulation.

As further examples of full-FOV comparisons of PSF between heritage designs and novel STM designs with the CNT technology, I display the difference between the respective PSFs at 171 Å in Fig. 2.15.

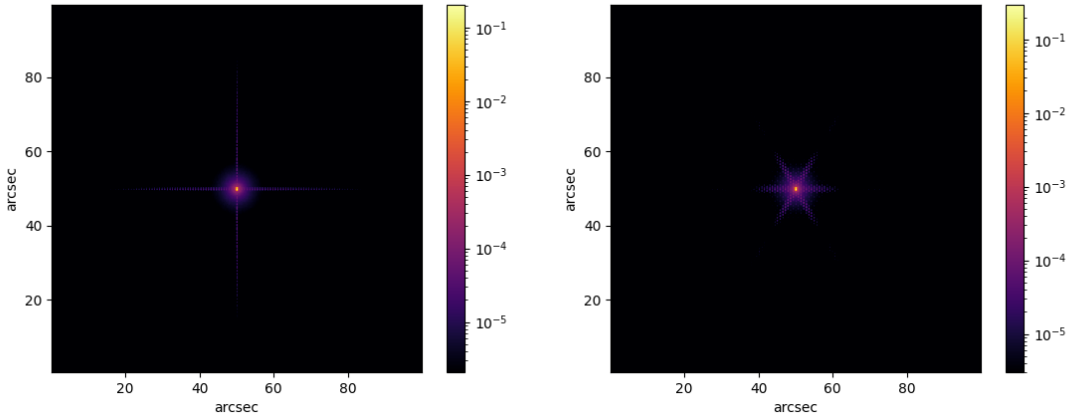

(a) Heritage 171 Å : Al/PI, 5 LPI Ni **(b)** STM 171 Å : Al/CNT, CNT mesh

Figure 2.15 PSF comparison between (**panel (a)**) the heritage filter design and (**panel (b)**) the STM CNT filter design in the full $100''\times100''$ FOV at wavelength 171 Å. Pixels in the figure were degraded to the realistic resolution $\Delta\theta_X = 0.167''$ and $\Delta\theta_Y = 0.4''$.

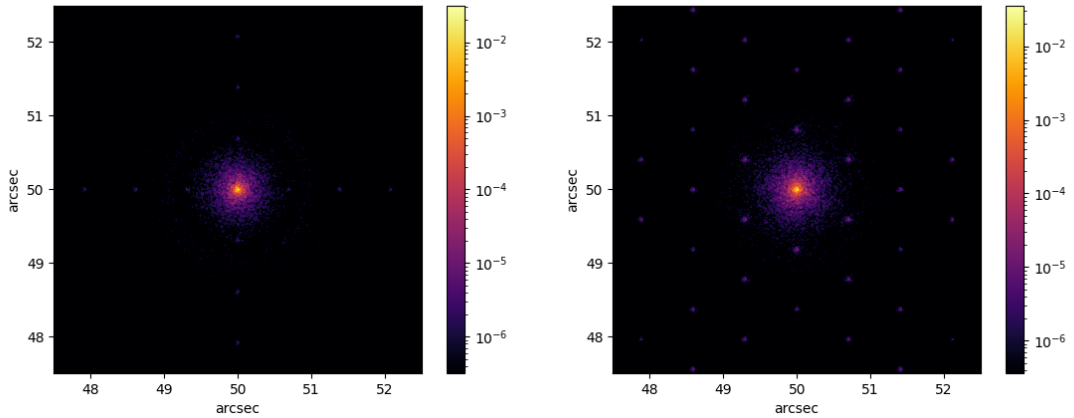

(a) Heritage 171 Å : Al/PI, 5 LPI Ni **(b)** STM 171 Å : Al/CNT, CNT mesh

Figure 2.16 PSF comparison between (**panel (a)**) the heritage filter design and (**panel (b)**) the STM CNT filter design in the restricted $5''\times5''$ FOV at wavelength 171 Å. For the sake of image clarity, the diffraction-limited pixel size of the simulation was kept for these figures, at $\Delta\theta = 0.009''$.

In this case, the distribution of peaks is different between the two designs, the main difference being the square versus hexagonal pattern diffraction. I also display the peaks near the center for the 171 Å channel and for the two given designs in Fig. 2.16. These meshes transmit about 97%, and their secondary order diffraction peaks start becoming much less intense, owing to the highly transmissive mesh. In this case, the effect of mirror profile errors and aperture diffraction can be seen near the central peak.

Finally, the comparison at 108 Å is shown, with (Fig. 2.17 and Fig. 2.18) and with similar features.

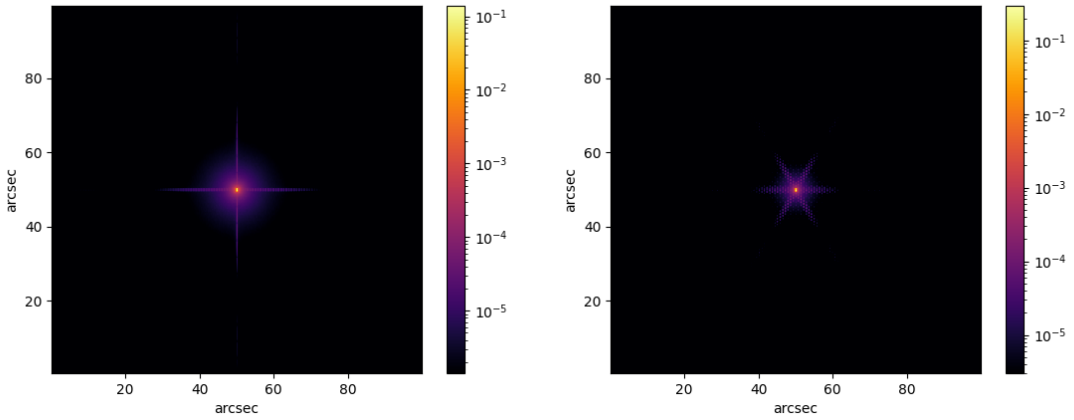

(a) Heritage 108 Å : Zr/PI, 5 LPI Ni **(b)** STM 108 Å : Zr/CNT, CNT mesh

Figure 2.17 PSF comparison between (**(a) panel**) the heritage filter design and (**(b) panel**) the STM CNT filter design in the full $100''\times100''$ FOV at 108 Å . Pixels in the figure were degraded to the realistic resolution $\Delta\theta_X = 0.167''$ and $\Delta\theta_Y = 0.4''$.

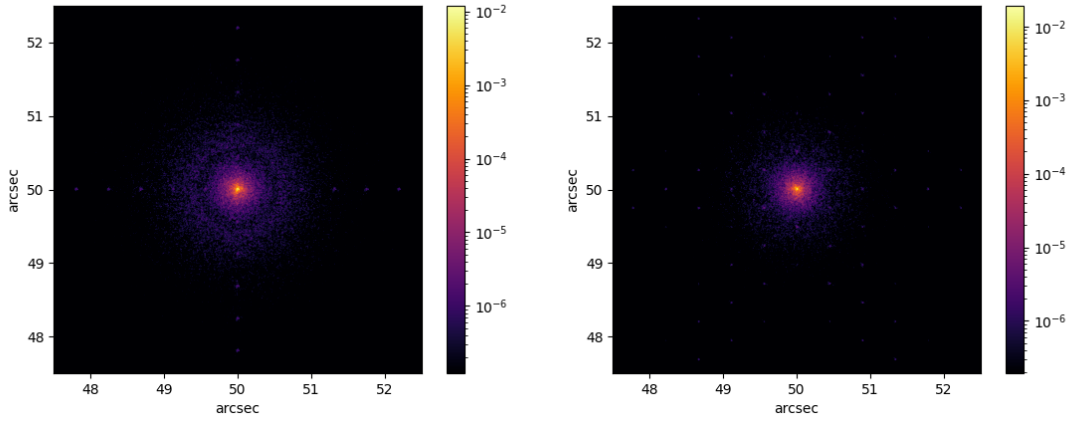

(a) Heritage 108 Å : Zr/PI, 5 LPI Ni **(b)** STM 108 Å : Zr/CNT, CNT mesh

Figure 2.18 PSF comparison between (**(a) panel**) the heritage filter design and (**(b) panel**) the STM CNT filter design in the restricted $5''\times5''$ FOV at 108 Å . For the sake of image clarity, the simulation diffraction-limited pixel was kept for these figures, at $\Delta\theta = 0.006''$.

Discussion of PSF results

General results

The simulations shown above have implications for the choice of the filter designs. In all cases seen so far, the HEW contribution is below the high angular resolution requirement of MUSE,i.e., 0.5″.

In the **108 Å** channel, the heritage filter (*Zr/PI; 5 LPI*) exhibits a (T_{core}) of 25.7%, with 37.5% of filter transmittance, resulting in approximately 69% of the transmitted energy concentrated within a 0.5″ radius, quite close to the result of the mirror alone (70.9%). The novel STM design represents a considerable improvement, achieving a T_{core} of 33% with a filter transmittance of 44.9%, thus implying about 73.5% of the energy within the core; remarkably, this is seemingly more efficient than the mirror alone, the reason being that the closest secondary order lobes fall at an angle within the MUSE resolution and thus contributing to the integral defining T_{core}. Thus, this filter would be comparable to the heritage filter design in terms of zero-order diffraction efficiency, and theoretically better in terms of core-PSF-transmittance.

In the **171 Å** channel, the heritage filter (*Al/PI; 5 LPI*) achieves a T_{core} of 31.5% and a filter transmittance of 38.0%, resulting in approximately 83% of the energy in the core. The STM design theoretically improves the performance, with a T_{core} of 47.4% and a filter transmittance of 57.3%, also concentrating about 83% of the energy within the core. Their zero-order efficiencies are thus comparable, but, neglecting the oxide content, the STM design provides more power, owing to the higher overall transmittance.

As for the **284 Å** channel, the heritage filter (*Al; 70 LPI*) has a T_{core} of 44.5% and a filter transmittance of 58.1%, with about 77% of the energy in the core. The STM design offers a lower performance in the core transmittance, achieving a T_{core} of 25.3% and a filter transmittance of 30.2%, concentrating about 84% of the energy within the core. Although the core transmittance is about half that of the heritage filter, the STM design is better in terms of zero-order diffraction efficiency: moreover, not only does the STM design exhibit less diffraction than the heritage one, but, as shown in Fig. 2.12, also the diffracted intensity is distributed among a much larger number of peaks. Follow-up studies will entail: (i) simulating the two different filter designs convoluting some scientific cases of observations (such as a solar flare or an active region) to assess which design is better in describing desired scientific scenarios, and (ii) a detailed study of the secondary order peak distribution, intensities, and comparison between the designs also in this aspect and not only in the zero-order efficiency one.

Generalization with Realistic Oxide Layers

Regarding the presence of realistic **oxide layers**: I will now combine the results of this section with those of Chapter 4 (i.e., Alaimo et al.[89]), reporting measured transmittance for the thin films of the different filter designs. A tabular form of

this merging is presented in Table 2.6.

Table 2.6 Results for various filter designs at different wavelengths, taken from Table 2.5, and compared to the realistic filter transmittance values obtained in Chapter 4 →p.71. Norm. is the simulated filter transmittance. Exp. Filter Tran. stands for experimental filter transmittance: it is comprised either entirely of experimental values, or those combined with simulated mesh transmittances such as those in Table 2.1 and Table 2.3. T_{core} is the encircled energy from simulated PSFs under 0.5″ angular size. Corr. T_{core} stands for corrected core transmittance. Bold columns employ experimental values.

Channel (Å)	Filter Design	Norm. Value (%)	**Exp. Filter Tran.** (%)	T_{core} (%)	**Corr. T_{core}** (%)
108	Zr/PI; 5 LPI	37.5	**33.4**	25.7	**22.9**
	Zr/CNT New	44.9	**35.5**	33.0	**26.1**
171	Al/PI; 5 LPI	38.0	**28.5**	31.5	**23.6**
	Al/CNT STM	57.3	**33.9**	47.4	**28.0**
284	Al; 70 LPI	58.1	**40.3**	44.5	**30.9**
	Al/CNT STM	30.2	**12.0**	25.3	**10.1**

The picture remains almost the same, although, as will be discussed in the relevant chapter, the CNT substrate does seem to increase the native oxide and thus worsen the transmittance of the thin film overall with respect to the ideal scenario ignoring the oxidation of Al and Zr. In channels 108 Å and 171 Å , and even accounting for realistic oxides, the T_{core} of CNT-based solutions is higher by a factor 3-6% than that of the heritage solutions. The aspect of channel 284 Å worsens: now the heritage-solution has a three-fold improvement in signal at the core, but the augmented diffraction to the secondary lobes remains the same as the picture in the ideal scenario.

Summarizing this aspect, the novel CNT-based STM filters, which already proved to be much better in terms of diffraction impact as compared to the DM filters [80], perform comparably or better than the heritage filters with regards to zero-order efficiency in all channels but the 284 Å where a trade-off between signal and diffraction to secondary lobes is present. The findings and the novel designs can thus be particularly beneficial for the mission's objectives.

On the Role of Simulations

The findings emphasize the importance of using simulations in the design and optimization of optical filters for EUV missions. Very simple models, such as the $M^2F \cdot T_{\text{mir}}$ for the core PSF T, are a preliminary metric of the overall performance, especially when dealing with complex geometries like hexagonal meshes, or considering the effects of mirror roughness. Thus, simulations such as those employed in this work are extremely useful to advance or optimize filter designs in the development of EUV space missions such as MUSE, and also to

predict the PSF contribution due to a particular mesh geometry, which makes it mechanically resistant.

Moreover, simulations allow for accounting for various factors influencing the PSF, including diffraction patterns arising from different mesh designs and geometries; the realistic mirror surface imperfections that contribute to PSF broadening, and finally, the potential use of a partially transparent mesh, which could be the case if CNT-based meshes or PI-based meshes are employed.

Outlooks

A couple of factors have not been included or delved into in this study and deserve future investigation.

- **Secondary Order Diffraction peaks**: A deep study of satellite peaks and their effect in the study of scientific observables (or simulated observables) might add further information to the results given here, as it is not clear yet whether having faint and widely-spaced peaks would be preferable over having peaks closer to the central focus. Similar studies have been developed in the case of SDO/AIA [28] and to extend the results found here it would be necessary to study further these different designs and their applicability to different scientific scenarios in the solar corona such as flares or active regions, especially given the situation displayed in Fig. 2.12 and Fig. 2.13 which show a totally different distribution of diffraction peaks from different filters designs.
- **Filter windowing effects**: Just like it happened in the past in the case of SDO/AIA [31], the filters will be mounted in windows that might introduce additional diffraction effects not accounted for in our current simulations. Including the window mask in future models could provide a more realistic and possibly empirical assessment.

2.5 Conclusion of Diffraction Studies

In these studies, I have analyzed simulations of the performance of heritage and novel CNT-based optical filters for their application in EUV coronal spectroscopy onboard the MUSE solar mission, focusing on the impact of the design choice on the Point Spread Function (PSF) at the focal plane and in figures such as core PSF transmittance and HEW.

Filter designs based on solar space mission heritage were studied and assessed successfully, determining that they would fully comply with requirements such as the $0.5''$ angular resolution for MUSE. Furthermore, our findings reveal that the CNT-based Structural Thermal Model (STM) filter designs, which are currently being developed, demonstrate promising improvements over both the heritage filters, while decisively outperforming the CNT Demonstration Models (DMs). They are expected to achieve higher filter transmittance and better energy con-

centration within the PSF core for channels 108 Å and 171 Å , while maintaining similar HEW values compliant to the ones required by MUSE, and also maintaining a similar or better zero-order diffraction efficiency – i.e., the percentage of light that is scattered within a 0.5″ radius. At the 284 Å channel, while the heritage filter outperforms the STM CNT-based one in terms of core PSF transmittance, they are worse in terms of zero-order diffraction efficiency, and the second-order diffraction peaks distribution is brighter in the FOV for the former.

Realistic oxide values are also implemented in the general framework, and they do not change the picture of better core-transmittance for the higher energy channels and better zero-order efficiency in the lower energy channel. However, they do worsen the performance of the CNT-based filters, as they develop relatively more native oxide as compared to the heritage-based ones.

Another result of this work is the showcasing of different distributions of diffraction peaks, having chosen different filter designs – particularly for the 284 Å filter designs, in which the heritage filter shows widely-spaced and bright diffraction spots in the whole FOV. In contrast, the STM filter shows a hexagonal pattern of diffraction peaks closer to the central peak and, generally, less bright. Such diversity could have a significant impact on the pursuit of some of the scientific goals of MUSE.

Future studies could therefore evaluate the performance of different filter designs in the simulation of observations of relevant case studies, such as solar flares and active regions, to better compare the various designs, including the role of the diffraction peaks. Subsequent work will focus on incorporating additional realistic factors, such as employing the filters' window masks at the entrance pupil, or employing a detailed study of the secondary order diffraction peaks.

3 Visible Performance

3.1 Introduction to the UV-VIS-IR requirements

As explained in detail in the Introduction → p. 1, the primary role of optical blocking filters on MUSE, whether they are entrance filters (EF) or filter wheel filters (FWF), is to transmit the EUV radiation that carries the scientific signal, while rejecting the predominant flux of solar photons in the UV-VIS-IR range. Visible light (in this chapter, a term that generally includes IR and UV) can reach the detectors and disrupt the signal.

These thin-film compounding the filters are partially transparent in the EUV, and they must be as thin as possible to maximize the effective area of the telescopes – which, as seen, means adopting low-Z metal coatings such as Al or Zr with about 100-200 nm thickness. In the visible and infrared, however, these same films must behave as nearly opaque optical screens, reducing the solar photon flux reaching the CCDs to a level where the generated signal is negligible compared to the detector readout noise.

This chapter is designed to both derive a sensible requirement for the MUSE mission, particularly tailored for the Context Imager (CI) telescope, and to study the optical blocking performance of various test samples experimentally. I will consider the CI instrument as a Cassegrain optical configuration with a 200 mm primary mirror and a secondary mirror that forms the image on a back-illuminated CCD detector. An example of a Cassegrain's geometry is given in Fig. 3.1

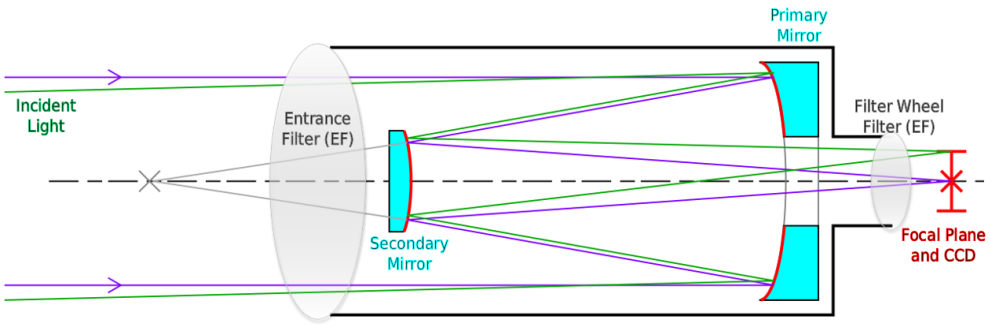

Figure 3.1 Schematic light path through a Cassegrain-geometry telescope. The primary mirror reflects incident parallel rays toward the secondary mirror, which focuses the light through the central hole to the focal plane. Entrance and filter wheel filters reject UV-VIS-IR radiation as much as possible while maintaining a high EUV throughput. A similar configuration is employed in the MUSE Context Imager (CI) instrument, while the Spectrograph (SG) uses a reflective grating in place of the secondary mirror, modifying the optical scheme. Credit: Krishnavedala. I added filter images and text descriptions. License: CC BY-SA 4.0

The findings can also be expanded to the MUSE SG telescope, although it has a

different way of optical path manipulation for EUV light to reach the detectors: in place of the secondary mirror, a reflective grating is used, operating in first or second order diffraction at the three channels of interest (108 Å , 171 Å and 284 Å). The reflective grating, thus, is not expected to reflect visible light to the CCD as the CI instrument would do: most of the visible light would end up in stray light, and a very small fraction, likely smaller than 10^{-6} of the incident light, is expected to reach the CCD detectors. Without exact measurements of the angle-dependent reflectivity in the visible light of the EUV reflective gratings employed, it is not possible to proceed further. The CI telescope geometry is used as a basis and as a worst case scenario for two main reasons: all of the visible light in its optical telescope geometry will reach the CCD detectors along with the EUV light coming from the input source, and, compared to the spectrograph, the CI instrument will sample a larger fraction of the solar disk in a single exposure and is therefore more sensitive to any residual UV-VIS-IR light transmitted by the filters.

UV-VIS-IR photons pose a problem for EUV detection and imaging because any residual transmission at these wavelengths ($300\,\text{nm} < \lambda < 1000\,\text{nm}$ where most of the solar light is present, as will be shown) have energy above the silicon (Si) band gap and generate electron-hole pairs with a high quantum efficiency, so even a small fraction of the solar continuum being let through by the filters can produce a significant background signal.

The main purpose of this chapter is to provide a *flat transmission requirement* in the UV-VIS-IR range for the CI filters, based on a simple but realistic model of the telescope, the solar spectrum, and the detector response. Meeting the CI requirement found in this way would provide a comfortable margin for both CI and SG filters.

After the requirement definition, I compare the requirement with the UV-VIS-IR absorption spectroscopy measurements of a set of aluminized witness samples, representative of both heritage-based polyimide and 70 LPI mesh filters designs and CNT-based STM designs described in Section 2.3 and Section 2.3, and made with the same technology and materials, although smaller in size as they are prepared in Standard TF110/111 Luxel Frames [90] [91].

3.2 Visible Requirement Definition and Calculation

Geometric configuration, solid angles, and assumptions

Although mission-level requirements were established prior to this work, the following derivation is presented to illustrate how to derive the UV-VIS-IR transmittance *upper-threshold* requirement in the context of the MUSE mission, in a transparent and traceable re-formulation whose end-result closely resembles the original requirement. I adopt the simplified Cassegrain-like optical scheme sketched in Fig. 3.1, starting from the solar spectral irradiance – detected by

the satellite that is orbiting Earth at a LEO-SSO orbit at a distance from the Sun of about $d_{\odot} = 1\,\mathrm{AU}$ – and propagating it through the CI optical light chain down to the electron-hole pairs generation in the CCD pixel. The derivation was accompanied by numerical implementations and computations that were performed with Python using NumPy and SciPy, while data visualization was accomplished with Matplotlib [81] [82] [83].

The basic idea is to calculate the number of electron-hole pairs that would be generated in the CCD per pixel per second by UV-VIS-IR photons in the absence of filters, and then require that the filters attenuate this flux sufficiently to make the residual signal negligible compared to the detector readout noise.

> **Note.** Any reference to values or pieces of equipment from the industry is used here as a useful tool to retrieve the UV-VIS-IR requirements, and because they are representative of realistic values or instrumentation, but they do not reflect in any way the exact values or pieces of equipment that will be employed in the MUSE payload. The NASA MUSE recently passed the key milestone of CDR (May 2025), and the approved payload information and their requirements are inside the CDR documentation of MUSE, which is not in the public domain. Exact payload information will be released in the form of technical and research papers as the mission progresses towards the Flight Readiness Review (FRR).

In this section, I use the following notation, values, and sources. Unless otherwise specified, the source employed for physical constants is the recommended values list from the Committee on Data of the International Science Council (CODATA) 2022 evaluation [92], while for astronomical constants, the source employed is the nominal values listed from the International Astronomical Union (IAU) 2015 RESOLUTION B3 [93]. Accuracy up to a fourth significant digit is enough for the scope of this investigation.

- λ is the wavelength, usually measured in nm;
- h is Planck's constant, c the speed of light in vacuum, and e, or e^{-} indicates either electron number or the electron charge depending on context;
- $\lambda_{\mathrm{Si\,gap}} \simeq 1106$ nm is the Si band-gap wavelength, corresponding to and-gap energy $E_{\mathrm{Si\,gap}} \simeq 1.12\,\mathrm{eV}$ [94];
- $\eta(\lambda)$ is the CCD quantum efficiency (QE);
- $T(\lambda)$ is the transmission of the thin-film of a single CI filter in the UV–VIS–IR band. This is the *unknown* that will be bounded by the requirement.
- $d_{\odot} = 1.495978707 \times 10^{11}\,\mathrm{m}$ is the distance from Earth to Sun, or the astronomical unit (AU).
- $R_{\odot} = 6.957 \times 10^{8}\,\mathrm{m}$ is the solar radius radius

– $P_\odot = 1366.1\,\mathrm{W\,m^{-2}}$ is the solar constant employed, based on ASTM-E490-00 [95]. This overestimates by about 0.4% recently found values for the constant [96], which is negligible for the intended scope of the investigation.

The main elements and assumptions that enter the calculation are listed hereinafter.

– The effective entrance pupil **geometric area** employed is $A_{\mathrm{geo}} = 83\ \mathrm{cm}^2$, as in the geometric area of the EUV channels in SDO/AIA [31].

– Here the **FOV and pixel size solid angles** are described. The CI images a FOV of $580'' \times 290''$ ($\Delta\theta_x = 580''$, $\Delta\theta_y = 290''$) with individual pixels of solid angle of approximately $0.14'' \times 0.14''$ ($\delta\theta_x = 0.14''$, $\delta\theta_y = 0.14''$) [17]. Using $1'' = \pi/(648000)$ rad, the solid angle (measured in steradians, or sr) of the CI FOV can be approximated as the solid angle of a small spherical rectangle as follows.

$$\Omega_{\mathrm{CI\ FOV}} = \sin(\Delta\theta_x)\,\Delta\theta_y \simeq \Delta\theta_x\,\Delta\theta_y \simeq 3.95 \times 10^{-6}\ \mathrm{sr}, \tag{3.1}$$

The last equality holds to high accuracy since angles are small. The solid angle of one pixel is

$$\delta\Omega_{\mathrm{pix}} \simeq \delta\theta_x\,\delta\theta_y, \tag{3.2}$$

– Thus, the **total number of pixels** that receives the solar light in the FOV is

$$N_{\mathrm{pix}} = \frac{\Omega_{\mathrm{CI}}}{\delta\Omega_{\mathrm{pix}}} \simeq 8.7 \times 10^6, \tag{3.3}$$

– The **Sun's solid angle** that is the following as seen from Earth.

$$\Omega_\odot = \pi\,\frac{R_\odot^2}{d_\odot^2} \simeq 6.794 \times 10^{-5}\ \mathrm{sr} \tag{3.4}$$

so that the CI covers approximately a fraction $f_{\mathrm{FOV}} = \Omega_{\mathrm{CI}}/\Omega_\odot = 5.8\,\%$ of the solar disk in a given exposure.

– Each of the two mirrors is assumed to have a wavelength–independent **mirror reflectivity** of $R_{\mathrm{mir}} = 80\%$ across the UV–VIS–IR band. The reflectivity is expected to be mildly wavelength dependent, as expected with gold-based (Au) mirrors. Still, the flat assumption is sufficient for the purpose of deriving an approximate requirement, and the realistic reflectance of the mirrors with the realistic multilayer coating is not currently available.

– The CI uses a back–illuminated CCD with a typical **detector quantum efficiency** of 80–90 % in the visible, $\sim 60\,\%$ in the near-UV, falling to 20 % at 1000 nm and to 5 % and below at 1100 nm, based on the realistic QE of a standard back-illuminated CCD by Hamamatsu [97]. For the requirement derivation these exact details are contained in the QE curve, and assume that every photon after the absorption of the filters and of the CCD, with

wavelength shorter than the Si band-gap limit, i.e. $\lambda < \lambda_{\text{Si gap}}$ nm, produces one electron–hole pair: an assumption backed up by experimental and scientific evidence in the UV-VIS-IR band [98] [99] [100]

– I adopt the ASTM E–490-00 as **reference solar spectrum** at 1 AU [95] for the wavelength dependence of the spectrum, and I normalized it in a way such that the spectral irradiance $I_\odot(\lambda)$ is expressed in energy per second per unit incident normal area per unit wavelength carried out by the incident light [$\mathrm{W\,m^{-2}\,nm^{-1}}$]. By construction:

$$\int_0^{+\infty} I_\odot(\lambda)\,\mathrm{d}\lambda = P_\odot \simeq 1366.1\ \mathrm{W\,m^{-2}} \tag{3.5}$$

i.e. the solar constant adopted for this study.

– To account for the limb darkening (LD) effect, i.e. the increase in the **limb-to-central solar intensity** when observing small regions of the sun with respect to the solar disk, and to be conservative with respect to bright active regions, I consider situations where, instead of an average along the disk, the detector is *observing* the center of the Sun. By evaluating the inverse of the weighted average over the spectral power in ASTM-490 of the ratio of mean to central intensity $F'_\lambda/I'_\lambda(0°)$, using values and notation from Cox [101], a multiplicative factor of $\Delta_{\text{LD}} = 1.32$ is found. It is applied to the above disk-averaged irradiance in the following way to obtain an effective spectral irradiance.

$$I_{\text{eff}}(\lambda) = \Delta_{\text{LD}}\, I_\odot(\lambda). \tag{3.6}$$

The CI optical scheme includes an entrance filter (EF) mounted at the front telescope pupil and a second filter in the filter wheel (FWF), much closer to the CCD detector at the focal plane position. Both filters are made of similar Al-based thin films, possibly on different substrates (polyimide, CNT pellicles, or freestanding Al foils). For the purpose of the requirement determination, I assume that the EF and FWF share the same average out-of-band transmission T; thus, the total out-of-band transmission of the pair is then T^2.

Under these assumptions, the interaction with the detector can be described via the product of the photon rate with the detector QE, producing electron-hole pairs. It is thus possible to derive a figure for the **spectral electron production rate** at the detector level, i.e. the electrons per unit wavelength and second being collected by the CCD due to the solar radiation and employing MUSE/CI geometric figures. The derivation is standard practice, and thus the detailed derivation of the intermediate steps is given in Appendix D: I provide the final formula in Equation (3.7).

$$\dot{N}_{e,\text{pix}}(\lambda) = \frac{\lambda}{hc}\,\frac{I_{\text{eff}}(\lambda)\,A_{\text{geo}}\,R_{\text{mir}}^2\,\eta(\lambda)}{N_{\text{pix}}}\,\frac{\Omega_{\text{CI}}}{\Omega_\odot} \quad [\mathrm{e^-\ pixel^{-1}\,s^{-1}\,nm^{-1}}]. \tag{3.7}$$

The following formula would encode the **electron production rate per pixel** produced at the detector, $\dot{N}_e$, if no filter were to be present, along with the numerically computed value.

$$\dot{N}_e = \int_0^{\lambda_{\text{Si gap}}} \dot{N}_{e,\text{pix}}(\lambda)\,\mathrm{d}\lambda \simeq 1.07 \times 10^{11}\ [\mathrm{e^-\ pixel^{-1}\ s^{-1}}]. \tag{3.8}$$

The latter figure is expressed visually in Fig. 3.2. The produced electrons are mainly distributed in the VIS-IR part, with a negligible contribution from the UV portion.

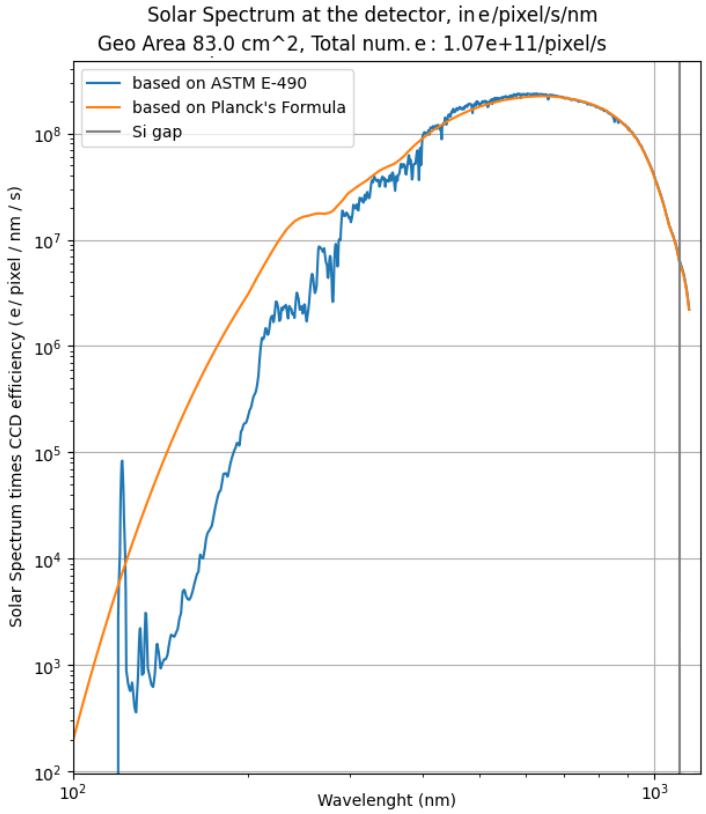

Figure 3.2 Simulated solar spectrum at the receiving end of MUSE CI detector expressed in num. of electrons $\mathrm{pixel^{-1}\,s^{-1}\,nm^{-1}}$, assuming all of the hypotheses specified in the text and multiplied by the CCD QE. Log-log scale. The blue curve shows the spectrum based on the ASTM E-490-00 reference [95], while the orange curve is obtained from a $T = 5778\,\mathrm{K}$ Planck's law prediction; the vertical line marks the silicon band-gap cutoff. In the range 200-400 nm: the Planck's based curve presents leftover trends due to the spectral dependency of the CCD's QE, while the discrepancy between the two curves is due to the Sun being not a perfect black-body emitter in the UV-range.

It is useful to split this flux into different wavelength ranges to understand the solar distribution better, and also to aid in some of the filter's transmittance general properties to be discussed later. Defining the following fractional contributions, as ratios between the total electron production rate in a given wavelength range and the total electron production rate, one gets the following ratios, respectively

in a mainly UV range up to 300 nm, a mainly VIS-(NIR) (near infrared) range between 300 nm and 750 nm, and a mainly IR range at wavelengths higher than 750 nm.

$$f_{\mathrm{IR}} = \frac{\dot{N}_{e,>750}}{\dot{N}_e} = \frac{\int_{750\mathrm{nm}}^{\lambda_{\mathrm{Si\,gap}}} \eta(\lambda)\, \dot{N}_{\gamma,\mathrm{pix}}(\lambda)\, \mathrm{d}\lambda}{\int_{0}^{\lambda_{\mathrm{Si\,gap}}} \eta(\lambda)\, \dot{N}_{\gamma,\mathrm{pix}}(\lambda)\, \mathrm{d}\lambda} \simeq 31.0\%, \tag{3.9}$$

$$f_{\mathrm{VIS-NIR}} = \frac{\dot{N}_{e,300\text{–}750}}{\dot{N}_e} = \frac{\int_{300\mathrm{nm}}^{750\mathrm{nm}} \eta(\lambda)\, \dot{N}_{\gamma,\mathrm{pix}}(\lambda)\, \mathrm{d}\lambda}{\int_{0}^{\lambda_{\mathrm{Si\,gap}}} \eta(\lambda)\, \dot{N}_{\gamma,\mathrm{pix}}(\lambda)\, \mathrm{d}\lambda} \simeq 68.5\%, \tag{3.10}$$

$$f_{\mathrm{UV}} = \frac{\dot{N}_{e,<300}}{\dot{N}_e} = \frac{\int_{0}^{300\mathrm{nm}} \eta(\lambda)\, \dot{N}_{\gamma,\mathrm{pix}}(\lambda)\, \mathrm{d}\lambda}{\int_{0}^{\lambda_{\mathrm{Si\,gap}}} \eta(\lambda)\, \dot{N}_{\gamma,\mathrm{pix}}(\lambda)\, \mathrm{d}\lambda} \simeq 0.5\% \tag{3.11}$$

Therefore, the bulk of the electron background in the detector is produced by photons in the 300–750 nm range, the long-wavelength tail above 750 nm contributes one third of the total electron rate, while the UV tail is quite negligible in its contribution.

Flat-band filter transmission requirement

The main idea behind the definition of the requirement is that the background signal generated by the out-of-band photons should remain small when compared with the readout noise of the detector which, for the CI CCDs, is expected to be of the order of $\sigma_{\mathrm{e\,RMS}} \simeq 10\,\mathrm{e}$ RMS per pixel [97].

Let's consider a typical quiet sun (QS) exposure of t_{exp} – *exposure time*. The electrons readout contribution by out-of-band photons in the presence of the two-stack filter transmission T^2 is here described as $N_e(T; t_{\mathrm{exp}})$ with the following formula (product between unshielded pairs per second, exposure time, and total filter transmittance).

$$N_e(T; t_{\mathrm{exp}}) = \dot{N}_e(T)\, t_{\mathrm{exp}} = T^2\, \dot{N}_e\, t_{\mathrm{exp}}. \tag{3.12}$$

Practically speaking, one can choose a maximum acceptable background rate $(\Delta N/\Delta t)_{e,\max} = N_{e,\max}/t_{\mathrm{exp}}$ in electrons per pixel per second – or, equivalently, a maximum acceptable background of electrons per pixel $N_{e,\max} = (\Delta N/\Delta t)_{e,\max} \cdot t_{\mathrm{exp}}$ integrated in the exposure – and then, via inversion of the inequalities, transform it into a constraint on T. Considering a typical QS cadence time for the dimmest observations possible of $t_{\mathrm{exp}} \lesssim 12\,\mathrm{s}$, it is sufficient to impose that the amount of electrons per pixel produced at the detector level in this time by out-of-band radiation is negligible – i.e., a factor 10 below – with respect to the readout noise. The inequality that will enable us to retrieve the maximum transmittances for the filters is the following.

$$N_e(T; t_{\mathrm{exp}}) \leq N_{e,\max} \iff T \leq T_{\max}(N_{e,\max}) = \sqrt{\frac{N_{e,\max}}{\dot{N}_e}} \tag{3.13}$$

Table 3.1 summarizes the results, in terms of values of $T_{\max}$ for a range of choices of $(\Delta N/\Delta t)_{e,\max}$. The case $(\Delta N/\Delta t)_{e,\max} = 0.1$ e$^-$ pixel^{-1} s^{-1} is particularly relevant, as it corresponds to a total background of $\lesssim 1$ electron per pixel in a 12 s exposure, i.e. negligible with respect to the readout noise in a relatively long QS CI exposure.

Table 3.1 Maximum flat-band transmission $T_{\max}$ per filter, assuming the CI Cassegrain telescope, ASTM E490-00 solar spectrum, and realistic values for the geometries in the optical setup, and exposure time of 12 s. The flat band maximum transmittance in the UV–VIS–IR band is described as a function of the maximum tolerable background rate $(\Delta N/\Delta t)_{e,\max}$. Both EF and FWF are assumed to have the same transmission T, so that the total transmission is T^2. In bold, the main requirement is highlighted, corresponding to a negligible $1\,e^-$ average readout in a ~ 12 s exposure observation.

$(\Delta N/\Delta t)_{e,\max}$ [e$^-$ pixel^{-1} s^{-1}]	$T_{\max}$ (per filter)
0.01	3.06×10^{-7}
0.05	6.83×10^{-7}
0.10	$\mathbf{9.66 \times 10^{-7}}$
0.20	1.37×10^{-6}
0.50	2.16×10^{-6}
1.00	3.06×10^{-6}

The requirement is thus denoted as the following, in an approximate fashion for ease of mnemonics, without loss of meaningful digits, given also the approximate nature of the derivation.

$$T_{\text{req}} \equiv T_{\max}(N_{e,\max} = 0.1 \text{ e}^- \text{ pixel}^{-1} \text{ s}^{-1}) \simeq 1.0 \times 10^{-6} \tag{3.14}$$

Two-band step-function approximation

Since the distribution of solar photons is not uniform across wavelengths, it can be useful to distribute energy requirements across different spectral bands. This is also useful because real filters do not have perfectly flat transmission over the entire UV-VIS-IR range. Given that the calculations described above show that approximately 69% of photons with wavelengths $\lambda < \lambda_{\text{Si gap}}$ are located at wavelengths below 750 nm, while 31% are located at longer wavelengths.

Defining a more flexible approach, a two-band step function for the filter transmittance could be the following, between UV-VIS-NIR and IR.

$$T(\lambda) = \begin{cases} T_{\text{UV-VIS-NIR}}, & \lambda < 750 \text{ nm}, \\ T_{\text{IR}}, & 750 \text{ nm} \leq \lambda \leq \lambda_{\text{Si gap}}. \end{cases} \tag{3.15}$$

The calculations above are usable. The fractional contributions of the produced pairs are: $f_{\text{UV-VIS-NIR}} = f_{\text{VIS-NIR}} + f_{\text{UV}} = 69\%$ and $f_{\text{IR}} = 31\%$, where clearly

they sum up to unity. Simply put, I am expanding the total produced electrons per pixel due to out-of-band radiation, i.e., $T^2 \cdot \dot{N}_e$, into their different wavelength band components. The two-band requirement $\dot{N}_e \leq N_{e,\max}$ would, thus, generalize the inequality of Equation (3.13) into the following one.

$$f_{\mathrm{UV-VIS-NIR}}\, T^2_{\mathrm{UV-VIS-NIR}} + f_{\mathrm{IR}}\, T^2_{\mathrm{IR}} \leq \frac{N_{e,\max}}{\dot{N}_e}\,. \tag{3.16}$$

This inequality involved the pair $(T_{\mathrm{UV-VIS-NIR}}, T_{\mathrm{IR}})$. This effort led to an interactive graphical tool that can be used for the retrieval of the amount of produced electrons/s in a given one or two-band prescription [102]. This might be necessary in future thin film prescriptions if they are quite asymmetric in their UV-VIS-IR absorption shape, and thus the two-band treatment was described for completeness. Equivalently, the same detailed procedure can be applied, using a given filter transmittance as a function of wavelength, to predict the expected electron production rate per pixel at the CCD.

For the remainder of the chapter, I will mainly use the flat-band requirement of Equation (3.14), i.e., $T \leq 10^{-6}$, for the filters, as it will suffice for the scope of this investigation.

3.3 Experimental Setup and UV-VIS-IR Principles

Perkin-Elmer Lambda 1050+ Instrument Employed

The ensuing transmission measurements were conducted in the spectral range $190 - 860\,\mathrm{nm}$ from ultraviolet to the near-infrared, utilizing the Perkin-Elmer Lambda 1050+ spectrophotometer instrument, which is hereby described, available at the INAF-OAPA/UNIPA X-ray Astronomy Calibration and Testing facility (XACT). The instrument itself is a traditional double-beam spectrometer, and while the covered range is in the UV-VIS-NIR, the instrument spectral range extends up to $\sim 3300\,\mathrm{nm}$. Since the samples measured are quite absorbing (transmittances $T \lesssim 10^{-6}$), it is challenging to perform accurate measurements in the IR range, while the measurements in the UV-VIS-NIR range could be performed with the correct experimental parameters that will be shortly described.

The instrumental photometric range has an upper limit in terms of absorbance of 8 OD (OD are Optical Density units, also called in this work *absorbances*, or A units, where context allows so). Additionally, the wavelength accuracy is of the order of 0.025 nm at 656.1 nm and 0.200 nm at 1312.7 nm. More details are available online [103] [104] or in the instrumentation manuals. The instrument is equipped with: two lamps, a deuterium (D_2) lamp, for the range $190 - 319.20\,\mathrm{nm}$ and a tungsten-halogen lamp emitting in the complementary range $(319.20 - 3300\,\mathrm{nm})$ – the instrument automatically changes the lamp in the given range. The detector employed is a photomultiplier tube (PMT). A simple diagram of the double beam spectroscopy used by the Perkin-Elmer Lambda

1050+ is laid out in Fig. 3.3. At the same time, greater details are available in the manual of the instrument.

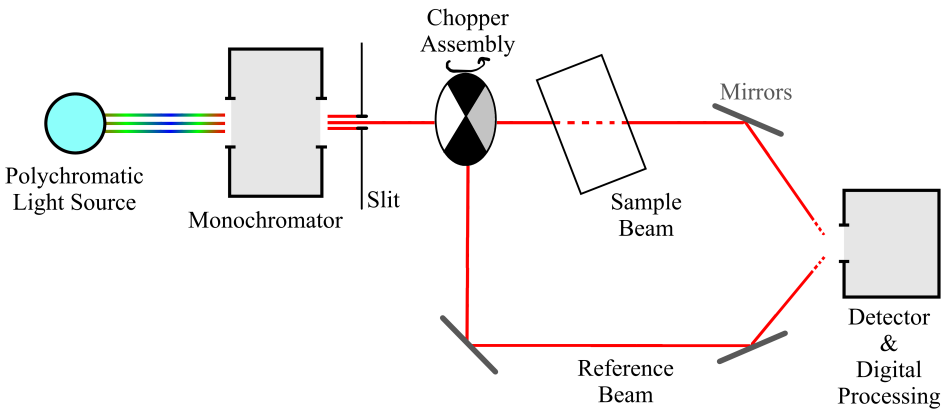

Figure 3.3 Scheme of a double-beam optical absorption apparatus analogous to that of Perkin-Elmer Lambda 1050+. A source emits white light that is selected by a monochromator and a tunable slit. The monochromatic beam interacts with a rotating disk (chopper assembly), which alternates between a hollow component, which forms the sample beam, two dark components, and a mirror component, which reflects the ray into the reference beam. The transmittance is computed as the ratio between the intensity of the transmitted beam and the intensity of the reference beam. Attenuators placed in the path of the reference beam (not shown in the figure) allow the measurement of strongly absorbing samples.

To create both the reference and sample beams, a chopper assembly (resembling a rotating disk) alternates four optical components–a mirror segment, a window segment, and two dark segments. When the window segment enters the beam, radiation passes through and creates the sample beam. When the mirror segment enters the beam, the radiation is reflected and, through a second set of mirrors, forms the reference beam. Three measures carried out with the same experimental parameters are required to output one sample transmission result. The first measure is done by the instrument without the sample, to measure the 100% T or 0 A – so-called *open beam baseline* – which the instrument automatically employs to auto-zero the measurement. The second measure is the 0% T (or the *blocked beam baseline*). It is obtained using an internal completely blocking attenuator and is used to correct for electronic and thermal detector noise. Finally, the third and final measurement is taken with the sample. To speed up the measurements (which can take up to hours), a semi-automatic positioning leverage system was designed by INAF-OAPA/XACT engineers, along with other manufacturers, to automatically bring the sample in and out of the beam path during the baseline and sample transmission measurements.

Usual experimental parameters involved the use of the gain of the PMT set on Automatic, its response is set at 8 s, and correspondingly, the UV/Vis slit spectral width fixed and set at 2 nm. At wavelengths lower than 319.20 nm, the

deuterium (D_2) lamp becomes operational. The data interval usually used was 5 nm. The common beam mask (CBM) was left at 100% aperture, the sample beam attenuator was not employed (100%). In contrast, the reference beam attenuator was set at the 0.1% attenuation setting – allowing the extension of the absorbance sensitivity of the instrument to the maximum potential.

The resolution of the spectrophotometer is usually limited by the resolving power of the monochromator and the accuracy of the detector, and the optical system favours the use of mirrors rather than lenses to minimise chromatic aberrations.

Principles of UV/Vis and NIR transmission spectroscopy

UV/Vis-NIR transmission spectroscopy is an experimental technique that is used in many scientific cases. Only an outline will be given, with further details available in general spectroscopy books [105] [106].

In general, UV/Vis transmission spectroscopy involves the study of transitions in absorption between the electronic states of an atom or a molecule (or a more complex aggregate of molecules) as excitation light is shone onto them in the wavelength range between $\lambda \in (200, 1000)$nm. At longer wavelengths, i.e. $(1000, 2000)$nm, the spectroscopy falls yet again in the infrared or vibrational regime already described, whereas in the lower range $\lambda \in (10, 200)$nm this is UV or Extreme-UV spectroscopy, which usually requires more care about the environment by employing vacuum technologies to be properly executed.

The goal is to measure the transmittance of a sample or, equivalently, its absorbance. If I_λ^0 is the spectral intensity sent by the source with no sample in between the beam path, and I_λ is the same spectral intensity being transmitted through the sample under study, their ratio gives the transmission–and the absorbance can be described via the use of the logarithm, as described in Equation (3.17). The spectral intensity is directly measured by actively resolving each wavelength through the monochromator.

$$T(\lambda) = \frac{I_\lambda}{I_\lambda^0} \quad \Longleftrightarrow \quad A(\lambda) = -\log_{10}(T(\lambda)) \tag{3.17}$$

The transmission is the true observable obtained with the technique describing the sample, containing all of the information obtainable. In the case of strongly absorbing samples, the transmittance may be affected by the presence of pinholes.

The absorption rate of a transition of a generic system is linked to its intrinsic properties, such as the dipole moment of the transition under study. Usual techniques to study electronic transmission spectra involve the employment of Einstein coefficients, fixed-line shapes, and the use of known physical laws such as Beer's law. This law does not generally hold for the study of very thin filters due to the multiple reflections and the Fabry-Perot-like interferences, which can affect the overall transmission. Conversely, the strongly absorbing samples have a

really high reflectance, and their transmittance can be affected by aspects such as inhomogeneity of the metal deposition, presence of pinholes, and the complex refractive index of the thin-film material components.

Note. The main metal deposition techniques employed for the samples manufacturing in this work are the e-beam physical vapor deposition and DC- or RF-sputtering. The quality of the coating with respect to the application in EUV solar astrophysics depends heavily on deposition parameters which drive the metal grain properties in the coating as discussed by Anders [107]. However, any discussion on the coating optimization is outside the scope of this work. Details on the manufacturing of thin films, and of their defects, can be found in Macleod [108].

Let's now proceed to the experimental investigation of the samples.

3.4 Experimental Investigation of Filters' Visible Performance

Here, I discuss the investigation of various samples that were probed with UV-VIS-IR absorption spectroscopy during the development of thin film filters for MUSE ever since their initial studies and designs. Only Al-coated samples will be discussed, as Zr-coated samples underwent a parallel and novel process of optimization of the coating that is under development and is intended for a future publication. Both a comprehensive UV-VIS-IR performance of both Al and Zr-coated samples for MUSE, and the coating optimization process, will be part of future technical reports and research articles from the INAF-OAPA/UNIPA team. Even though Zr-coated samples are not analyzed in this section, what can be stated is that the results for Al-coated samples are akin to those with Zr coating.

The experimental setup will be discussed, and then the samples and the measurements will be presented, both for older development filters, heritage-based, and CNT-based STM filters.

Witness samples and sample families

To evaluate the visible performance of the proposed MUSE filters, I performed, along with the INAF-OAPA/UNIPA and filters' team group, UV-VIS-IR transmittance spectroscopy on a set of small test samples with Standard Luxel geometry, either TF110 [90] or TF111 [91]. The investigated samples presented in this section were produced in parallel with demonstration filters and larger structural models, being representative of the materials of the larger model device, and they are part of three main families (each represented by letter-names OG, H, and STMs):

– **OG (or *original*) filters**, with TF110 geometry, representing the first research samples that were produced during initial CNT deposition studies

performed with unoptimized DC-sputtering Al-coating in 2023, exploring CNT film thicknesses and coating layers akin to the DM designs while also exploring passivating aluminum nitride (AlN) layers.

– **H (Heritage-based) filters**, with TF110 geometry, samples that reproduce the Al-on-polyimide and Al-on-mesh solutions described in Section 2.3, based on successfully flown designs in SDO/AIA and STEREO/SECCHI.

– **STM (STM-CNT-based filters**, with TF111 geometry, witnesses approximating the STM filter designs for MUSE described in Section 2.3, with 150 nm Al films coated on CNT films with optimized e-beam deposition techniques.

A list with all the samples probed and compared is provided in Table 3.2. The samples are made of SW-CNT pellicles with specified transmittance at 550 nm, following the same notations in the design sections such as Section 2.3 → p.31.

Table 3.2 Summary of aluminized witness samples used for visible-band measurements. Columns represent uniquely identifying short names encoding sample family (H, STM, OG), and materials in the multilayer or mesh. All samples are in TF110 Standard frames (ID aperture ∼1 cm). AlN pass. is an aluminum nitride small ($\lesssim$ 20 nm) passivation layer, initially studied to reduce native oxidation. SW is single-walled CNT pellicles whose thickness is described with the transmittance at 550 nm wavelength.

Short name	Substrate / mesh	Coating	Sample name
OG1	SW 45%T	Al 150 nm + AlN pass.	SW45-Al150+AlN
OG2	SW 45%T	Al 150 nm + AlN pass.	SW45-Al150+AlN_2
STM1	SW 55%T	Al 200 nm	SW55-Al200
STM2	SW 55%T	Al 200 nm	SW55-Al200_2
H1	PI 77	Al 150 nm	PI77-Al150
H2	70 LPI Ni-mesh	Al 150 nm	70LPI-Al150

While the OG samples are studied to detail the performance of aluminum-coated carbon nanotube films at the beginning of development (initial studies / pre-DM), the last two samples represent conventional solutions with optimized coating approaches (STM designs, or heritage-based designs). Moreover, samples H1 and H2 are the same samples that will be discussed in the studies of their EUV and X-ray transmittance in Chapter 4 → p.71. In this chapter, I limit the discussion to their out-of-band optical blocking performance.

Comparison of samples UV-VIS-NIR transmittance performance

The measured UV-VIS-NIR transmission curves of the heritage witness samples in Table 3.2 are compared, first with the old study samples, and secondly, with the STMs CNT-based witness samples. For ease of comparison, the shaded area corresponds to the required area defined in Equation (3.14) → p.60, i.e., $T(\lambda) \leq 10^{-6}$

over the entire spectral range considered, thus allowing us to easily check whether or not a given sample satisfies the requirement.

Early CNT-based samples versus heritage samples

The older samples studied, OG1 and OG2, both 150 nm of Al coated on a 45%T SW pellicle representative of a similar technology to that for the DM designs, while also employing a passivation layer of AlN, are compared with the traditional H1 and H2 samples in Fig. 3.4.

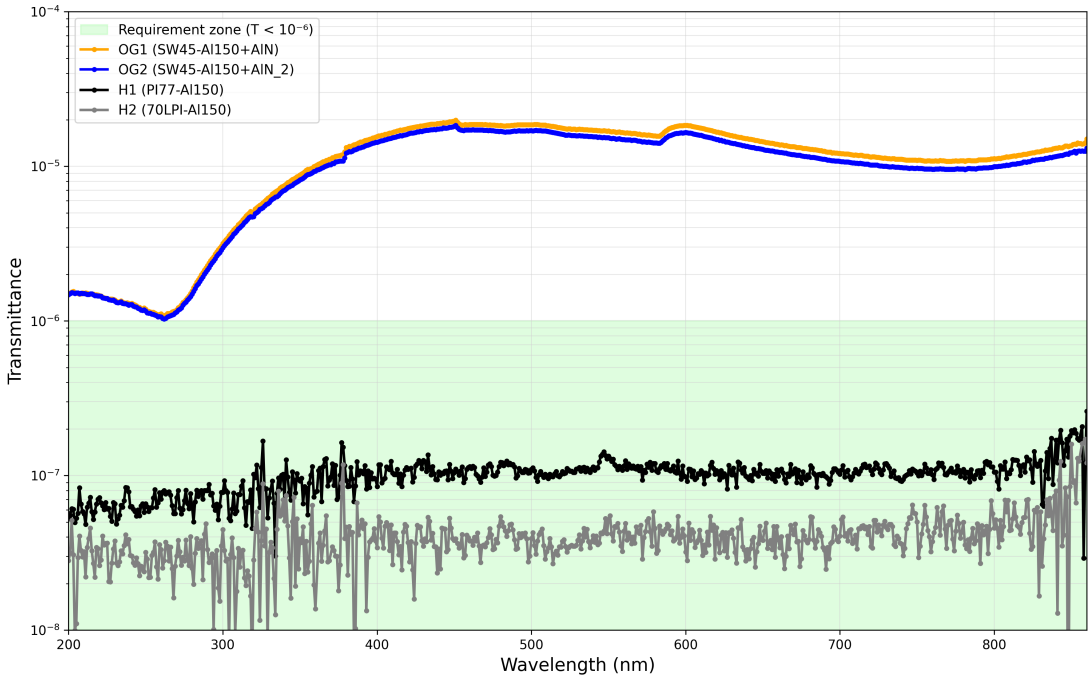

Figure 3.4 UV–VIS transmittance of CNT-based witness samples with Al + AlN coatings (OG1, OG2) compared with heritage filters (H1, H2) from Table 3.2. Wavelength range: $(200 - 860)$ nm, logarithmic transmittance scale. The green band again marks the requirement zone ($T < 10^{-6}$) derived from the solar-spectrum analysis for MUSE's context imaging observations

The two OG curves are virtually identical, confirming the good reproducibility of the coating process at the time, and show distinct spectral behavior compared to other traditional samples, such as the absorption band at ~ 270 nm which corresponds to π-plasmon absorption band – common to CNTs and to carbon allotropes with sp^2 hybridization, as seen in studies of optical properties of SW pellicles,[78]. At short wavelengths (about 200–270 nm), OG1 and OG2 nearly reach the requirement range. However, as wavelength increases in the visible range, transmittance increases monotonically by an order of magnitude, reaching values of about 10^{-5} around 400–800 nm, likely due to a worse coating quality due to the challenging substrate of CNT thin films. Therefore, in most of the visible range, OG samples are about an order of magnitude above the required threshold and two to three orders of magnitude above the H1 and H2 inheritance curve.

The heritage-based films maintain a transmittance between 10^{-7} and 10^{-8} across most of the spectrum, and the high instrumental noise suggests that the background noise level of the spectrophotometer – defining the lower limit in transmittance or the higher limit in absorbance of 8 as previously discussed – starts becoming relevant, suggesting also that the measured values closer to 10^{-8} should be interpreted as upper limits of the actual transmission, which could be even lower.

In terms of the requirements, a factor 10 of worse transmittance would translate in a factor 100 worse in terms of electron production at the CCD (since $N_e \propto T^2$, see Equation (3.13)) and, therefore, the OG samples are expected to produce about $10\,\mathrm{e^-\,pixel^{-1}\,s^{-1}}$ at the CCD, which would not be negligible in long ($\sim$12 s) exposures of the CI and would, in fact, surpass by a factor $5 \div 10$ the readout noise levels, $\sigma_{\mathrm{e^-\,RMS}} \simeq 10\,\mathrm{e^-\,pixel^{-1}}$. Therefore, the OG samples are inadequate for MUSE requirements as in-flight optical blocking solutions either as EFs or FWFs. At the same time, the heritage designs, with their low transmission levels ($T \lesssim 10^{-7}$), are confirmed as a robust option satisfying requirements.

STM CNT-based witnesses versus heritage samples

An optimization joint effort between INAF-UNIPA/OAPA filters' team and the industrial partners Ametek Finland Oy and Canatu Oy led to the development of the STM thin films. Fig. 3.5 compares the visible-light performance of two CNT-based STM thin films, STM1 and STM2, with that of the reference witness samples H1 and H2 from the aforementioned sample table and already described in Fig. 3.4. All curves are plotted between 200 and 860 nm and on a logarithmic transmittance scale.

Both STM1 and STM2 exhibit broadband attenuation in the UV-VIS-NIR range, with smooth transmittance curves that remain at or below 10^{-6} across the entire wavelength spectrum. The average transmittance level is higher for STM1 than STM2, with typical transmittance values of, respectively, 3×10^{-7} and 10^{-6}. Performance-wise, both CNT-based STMs meet the requirement for MUSE, with STM2 offering a more comfortable margin: the scientific reason behind this difference might be in a diverse distribution both in area and in homogeneity of pinholes, which is an ongoing study.

Following the CI requirements formalism seen in Section 3.2 and detailed in Table 3.1, the STM samples here studied would produce an electron per pixel per second rate at the CCD level of about $0.1\,\mathrm{e^-\,pixel^{-1}\,s^{-1}}$. Heritage-based samples H1 and H2 maintain the high blockage and, since their effective flat-band transmittance is about ten times better than the requirement, they are also expected to produce about $0.001\,\mathrm{e^-\,pixel^{-1}\,s^{-1}}$ at the CCD level.

Both samples suggest that the filter designs satisfy the T_{req} condition, though the heritage-based solution would guarantee it with a stronger margin.

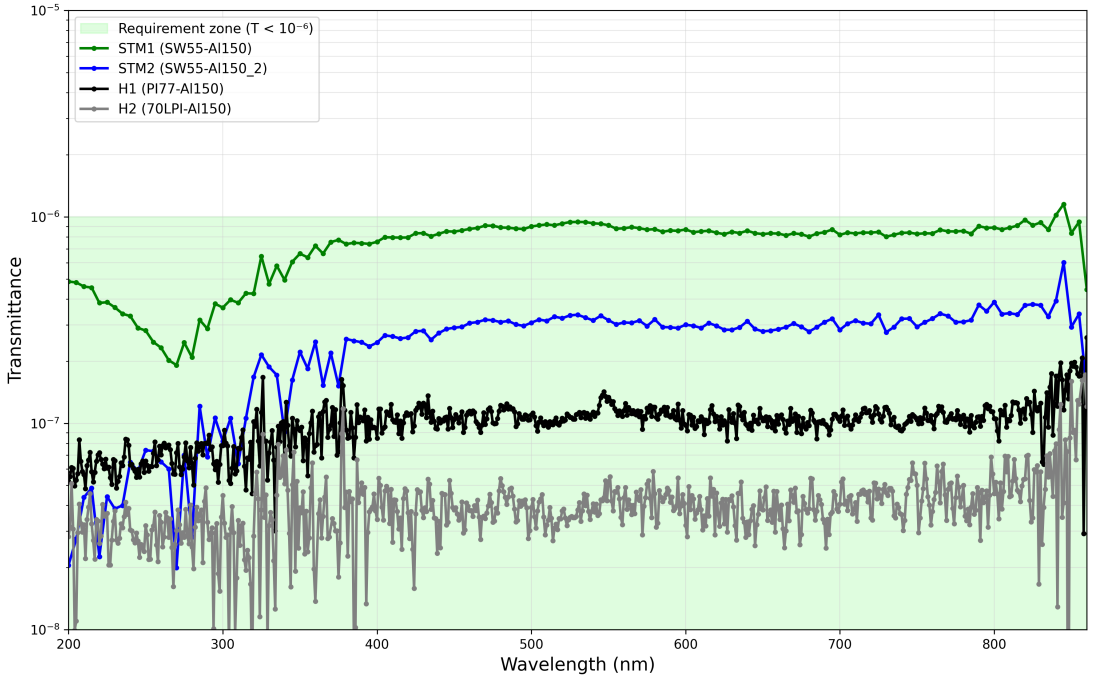

Figure 3.5 UV–VIS transmittance of STM CNT-based filters with Al coating (STM1, STM2) compared with heritage PI- and mesh-supported filters (H1, H2), all samples as described in Table 3.2. Wavelength range: $(200 - 860)$ nm, logarithmic transmittance scale. The shaded region indicates the requirement zone ($T < 10^{-6}$) derived from the solar-spectrum analysis for MUSE's context imaging observations.

Remarks on Uncertainties and Environmental tests

A few pieces of information regarding repeatability, uncertainties, and environmental tests are detailed in this section.

The photometric accuracy – in terms of Photometric Noise RMS – of the instrument, as stated in the Lambda 1050+ manual, is of the order of better than 0.005 A (absorbance units) when a measurement occurs with an average absorbance of 6. The accuracy of a repeated measurement without changing any specification or without moving or rotating the sample was found to be extremely precise for samples with absorbances around the 6 mark. For samples absorbing 7 A or 8 A, the measured fluxes are at the lower end of the allowed dynamic range and thus the RMS noise is higher in relative percentage (easily reaching $10 - 20\%$). Measurements with an absorbance higher than 8 A are not possible as, with the given setup, the minimum photometric RMS noise is found to be at the level of an 8 A measurement.

Another relevant source of uncertainty for these samples was found to be related to the uniformity of the samples. On average, considering the effect of both photometric RMS noise for these highly absorbing samples and of the uniformity of the sample – which was taken into account by rotating samples and averaging among various measurements – a typical relative uncertainty for the measured transmittance was found to be of the order $2 - 5\%$ for samples transmitting 10^{-6}

and of the order $10 - 30\%$ for samples transmitting less than 10^{-7}. It is not possible to single out the influence of the uniformity of the samples from these measurements due to the high impact of photometric RMS noise. A more detailed discussion on the uniformity of the samples in terms of thickness is given at the end of Section 4.1 → p. 71 where relevant literature involving X-ray mapping and other techniques is cited.

Finally, regarding environmental tests, there is an ongoing investigation that is happening to test how the transmittance properties of the samples – either with polyimide, with CNT or only with the mesh as substrates or supporting structures – change after being irradiated with UV light (simulating the irradiation and aging impact of observing the sun), and/or atomic oxygen exposure – which is present in the LEO orbit. This ongoing investigation by the INAF-OAPA/UNIPA team will result in published research in the near future to support the filters' development for MUSE, to scientifically assess eventual changes of properties of the thin film filters under study after the environmental conditions are applied, and to also assess end-of-life conditions for the MUSE system-level perspective.

3.5 Conclusion on Filters' Visible Performance

In this chapter, I established a quantitative requirement for the UV-VIS-IR transmittance of the optical blocking filters of the MUSE CI. I compared it to UV-VIS-IR transmittance measurements of aluminized thin-film samples, representative of development and STM designs, preliminary and candidate for flight.

From the ASTM-E490-00 tabulated solar spectrum at 1 AU, corrected for center-to-limb darkening effect, I propagated the solar irradiance through a simplified optical Cassegrain CI model, using realistic values for the geometric collection area, FOV, mirror reflectivity, and CCD quantum efficiencies. Assuming that one electron-hole pair is produced per photon with energy higher than the Si gap reaching the CCD, I obtained an unfiltered electron rate at the pixel level of $\dot{N}_e \simeq 1.07 \times 10^{11}\,\mathrm{e^-\,pixel^{-1}\,s^{-1}}$ due to the solar UV-VIS-IR band irradiation.

Assuming that in 12 s exposure time, reasonable for a long quiet sun exposure, the electrons produced must be negligible with respect to the value of the $\mathrm{e^-}$ RMS due to the readout noise (usually $\sim 10 \div 20\,\mathrm{e^-\,pixel^{-1}}$), a reasonable requirement is to impose that the stacked two-filter EF+FWF system yields a maximum electron production rate of $(\Delta N/\Delta t)_{e,\max} \simeq 0.1\ \mathrm{e^-\,pixel^{-1}\,s^{-1}}$. This implies a flat-band transmission required per filter of $T_{\mathrm{req}} \simeq 10^{-6}$,

After introducing some fundamentals of UV-VIS-NIR transmission spectroscopy, and the experimental setup used, I then showed the results of the UV-VIS-NIR spectroscopic transmission measurements of a series of aluminized witness thin film samples (all of them in 1 cm ID circular frames), including: old study samples of SWCNT pellicles coated with Al+AlN (OG1, OG2), developed in parallel to the designing of the CNT-based DMs; conventional Al/PI and Al/70LPI mesh

filters (H1, H2), representative of the heritage-based designs; and CNT-based witness samples for STM (STM1, STM2) that are close to the final designs of MUSE CNT-based STM filters.

The **heritage witness samples** H1 and H2 exhibit very low transmittances, in the range $10^{-8} - 10^{-7}$ over most of the analyzed UV-VIS-NIR band. Interpreted according to the CI requirements formalism, H1 and H2 both correspond to effective flat-band transmittances well below the requirement T_{req}, producing a negligible visible electron background noise ($N_e \ll 0.1$ $\text{e}^-\,\text{pixel}^{-1}\,\text{s}^{-1}$). Thus confirming even further the traditional designs as meeting requirements for flight and for MUSE. The **CNT-based STM samples**, STM1 and STM2, also meet this requirement. Their transmittances are higher than those of traditional filters, remaining within the range of $T \leq 10^{-6}$ across the entire measured range. In contrast, the **old study samples** OG1 and OG2 based on carbon nanotubes (CNTs), incorporating AlN passivation layers, exhibit far worse transmittances ($\sim 10^{-5}$), thus suggesting a worse coating quality in these past designs, which was surpassed with the efforts in research and development for the production of STMs in a group effort. Thus, this chapter also shows the evolution of the spectroscopic study and of the technological maturity of this novel material proposed.

It was, thus, demonstrated that Al-coated CNT-based witness samples of STM CNT-based filter designs follow the optical attenuation requirements needed for flight in the NASA MUSE mission, while heritage filters' performance was assessed and confirmed, achieving higher margins in meeting the requirement. As prospects, it is planned to extend this analysis to Zr-coated films, to couple the UV-VIS-IR characterization of the filters with an in-depth scientific investigation between the transmittance properties, the coating surface appearance structure as seen with Scanning Electron Microscopy (SEM), pinhole investigations and statistical assessments with optical microscopy, and effective complex refractive index modeling of the metal coating depending on the coating quality, to give a clear description of which factors drive the spectroscopic properties of these thin films. Moreover, an investigation exploring the optimization of the DC-sputtering technique of Al on CNT films is ongoing, in order to find optimal parameters to improve the absorption of the samples, as well as their spatial uniformity. In the next chapter, I will address the complementary issue of EUV in-band performance and inner-layer composition analysis of the thin films: using synchrotron radiation and X-ray absorption spectroscopy (XAS), I will characterize the transmittance and composition of witness samples of the heritage-based and STM CNT-based designs – in this case also including Zr-coated samples – via analyses of the extreme ultraviolet (EUV) and soft X-ray transmittances, also allowing for comparisons.

4 Extreme-Ultraviolet and X-ray Transmittance

This chapter focuses on presenting the in-band transmission curves of small witness samples representing candidate filter designs for MUSE, characterizing the inner-layer atomic composition of the film, and providing an initial condition on the filter transmittance calibration curves for various designs. In the case of SDO/AIA, previously mentioned in the Introduction → p. 1, the in-band transmittance characterization of the missions' filters and thin films was extensively documented [31]. A novel approach is presented here, by employing the technique of X-ray Absorption Spectroscopy (XAS) using the high spectral resolution EUV/X-rays beamline METROLOGIE [109] at the SOLEIL synchrotron facility, to characterize the filter samples both in the EUV band of MUSE from 108 Å to 304 Å with a fine energy step of $\Delta\lambda \approx 0.3$ Å and in the whole soft X-ray range of $30 - 1800$ eV with a spectral power > 1000. The XAS data analysis provides insight into the atomic composition of the layers of all samples, enabling the comparison, also by modelling, of the transmittance between different potential filter designs, while also providing a means to possibly model the transmittance of the filters in-flight by tuning the model areal densities of carbon (C) and oxygen (O). Clearly, the results are of the utmost importance for MUSE. However, they will also be beneficial for the upcoming spectrometer space mission by JAXA Solar-C/EUVST [23] and for all future EUV space missions. It is planned to extend this investigation soon in a journal paper via a similarly detailed experimental characterization and data analysis of the visible and infrared transmittance of such films, also considering the Zr-coated films – the Al-coated ones being already discussed in Chapter 3.

4.1 Witness Samples

Six filter samples were analyzed in this study, all of them mounted on a TF111 or TF110 standard Luxel frame, which have an internal open diameter of about 15 mm and 10 mm, respectively, and they are detailed in Table 4.1. All of the samples represent closely either the designs of heritage-based filters, presented in Section 2.3, or the STM CNT-based filters, presented in Section 2.3, except for a 70 LPI Ni mesh-based 200 nm Zr thin film sample, which was studied for completeness purposes and as a potential interesting alternative to the baseline for MUSE.

All of the samples are free-standing thin film membranes, thus requiring careful handling due to their fragility. They are witness samples representative of the same materials that would be used in the scaled-up entrance filters for MUSE, which will have roughly the dimensions of circular sectors of inner diameter 10 cm

Table 4.1 Summary of witness samples described and characterized in their EUV in-band and soft X-ray out-of-band transmittance. The geometries of all the frames are the TF110 or TF111 Luxel standard. The samples with LUXFilm ® Polyimide (PI) substrate or Ni structural mesh are manufactured by Luxel, the CNT pellicles by Canatu, and the coating of the CNT pellicles is done either by Luxel (Zr) or by AMETEK/Micronova (Al). The design represented is also pointed out (if heritage-based or supported by novel CNT pellicles). The description 55% in some entries of the Sample column refers to the percentage of transmittance of the sole CNT pellicle substrate at 550 nm wavelength. BF stands for blocking factor.

Sample	Substrate	Coating	Mesh (LPI; BF)	Design basis
Al 150 / PI 75	PI	150 nm Al	Ni (5; $\simeq 2.0\%$)	Heritage
Zr 200 / PI 75	PI	200 nm Zr	Ni (5; $\simeq 2.0\%$)	Heritage
Al 150 / 70 LPI	None	150 nm Al	Ni (70; $\simeq 18.4\%$)	Heritage
Zr 200 / 70 LPI	None	200 nm Zr	Ni (70; $\simeq 18.4\%$)	Heritage
Al 150 / 55%	SWCNT	150 nm Al	None	STM with CNT
Zr 200 / 55%	SWCNT	200 nm Zr	None	STM with CNT

and outer diameter 25 cm for the SG instrument [43].

Four of these samples were produced by the LUXEL Corp. (USA) and were provided by the Harvard & Smithsonian Center for Astrophysics (CfA) under the NASA MUSE collaboration activities. Two of these consist of a LUXFilm ® Polyimide (PI) substrate–the standard chemical formula of the PI monomer being $C_{22}H_{10}N_2O_4$–with Zr or Al metal coatings of $\sim 150 - 200$ nm, supported by a coarse square patterned Ni mesh with a 5 lines-per-inch (LPI) cell periodicity (following notation of Chapter 2), a total of $\sim$ 2.0% geometrical blocking factor. These samples are representative of the heritage filters used in STEREO/SECCHI, whose full entrance filter appearance can be seen in the original paper by Wuelser et al. [25]. The two other witness samples provided by CfA have the same amount of metal coating as the former ones. Still, they are supported solely by a finely spaced square Ni mesh with 70 LPI cell periodicity, and $\sim$ 18.4% geometrical blocking factor. Such values are representative of heritage filters used in both STEREO/SECCHI and SDO/AIA. The two remaining witness samples employ CNT pellicles manufactured by Canatu [39] in place of PI as substrate material. No mesh is used in these witness samples. One of the samples is coated with 200 nm of Zr–the coating being performed by Luxel Corp.–while the other sample is coated with 150 nm of Al by AMETEK Finland Oy and Micronova Nanofabrication research infrastructure. The appearance of one of the 5 LPI samples used, in a TF110 standard frame, is shown in Fig. 4.1.

The nickel mesh bars employed in the filter samples are completely opaque in the full EUV and soft X-ray bands. While for the 5 LPI Ni meshes the pitch size is much larger than the synchrotron spot size employed, the 70 LPI meshes pitch has a size comparable to the synchrotron beam size, and thus a different experimental

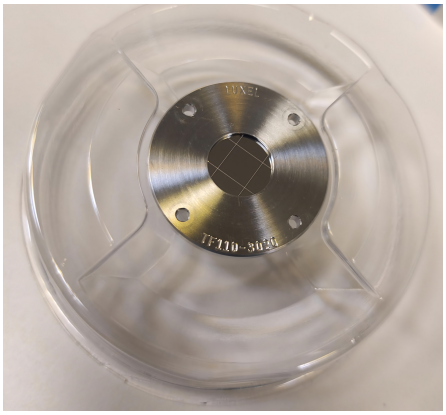

Figure 4.1 Picture of a filter witness sample with a free-standing thin 75 nm PI membrane coated with 150 nm Al and supported by a 5 LPI Ni mesh, made by Luxel, using a TF110 standard aluminum frame. The sample is shown in its plastic container. The circular opening in the center of the filter frame has a diameter of about 1 cm.

method will be employed for the transmittance measurement of those two samples, as detailed in sec. Section 4.2.

In the following and throughout the whole chapter, the samples are labeled as follows:

- The 5 LPI samples will be indexed via metal thickness / PI thickness in nanometers, e.g. Al 150 / PI 75 or Zr 200 / PI 75, keeping in mind that the manufacturers provide these thickness estimates with an uncertainty of 5 nm and such expectations could be compared with the data analysis results in Section 4.4.
- The 70 LPI samples shall be described via metal thickness/mesh description, e.g., Al 150 / 70 LPI or Zr 200 / 70 LPI. Their mesh will be directly referenced in the paper as it influences their transmittance, though Ni will be omitted for brevity.
- The CNT coated samples will be described via metal thickness / T_{550} CNT pellicle description, e.g., Al 150 / 55%, Zr 200 / 55%. Since the CNT pellicles are made of networks of bundles of single-wall CNTs [39], their thickness is hardly defined *a priori* even during manufacturing, thus I employ, as a figure of merit for their thickness, the transmittance at the visible wavelength of 550 nm which is the T_{550} symbol. This value can be related to the true thickness of the pellicle via an ad-hoc defined Lambert-Beer law [78]. However, this depends strictly on the manufacturing process parameters of the pellicles and for the case of the pellicles used as sample substrates and manufactured by Canatu Oy in this chapter, the thickness estimate is about 150 nm.

The spatial uniformity of the PI/Al samples' thickness layers over their $\sim \pi\,\mathrm{cm}^2$ area is $\approx$ 2%, considering reports of the measured uniformity resulting from X-ray transmission map studies over areas equal or larger than $4\,\mathrm{cm}^2$ for PI/Al

filters [110]. A spatial uniformity of ±2% is expected for the Al coating on CNT pellicles, as can be inferred from technical reports studying with soft X-ray transmittance mapping samples with 30 nm of Al deposited on top of CNT substrates [111]. Similar figures are expected for the Zr coatings. On the other hand, the expected thickness spatial uniformity of the CNT bare substrate is $\sim 10\%$, as retrieved in the thickness estimates by Atomic Force Microscopy (AFM) contact studies by Ermolaev et al. [78].

4.2 Experimental Setup with Synchrotron Radiation and Experimental Data Retrieval Protocol

The experimental activity was carried out at the METROLOGIE beamline of the SOLEIL Synchrotron – located in Saint-Aubin, France – which is a beamline specialized in the calibration of optical components and can allow measurements of the transmittance of our samples in a wide energy range ($30-1800$ eV), covering both the in-band EUV region relevant to MUSE ($40-120$ eV) and the soft X-ray out-of-band, with high spectral purity and resolution, allowing us to retrieve the calibration curves of the filters as well as modeling the EUV and XAS data obtained. Throughout this paper, 'transmittance' refers to the measured value at a specific wavelength or energy or a specified energy range, while 'transmittance spectra' denotes the full curve of transmittance as a function of wavelength or energy. In practice, these terms are used interchangeably unless otherwise specified.

Synchrotron facility METROLOGIE description

The METROLOGIE beamline operates with a bending magnet source and a monochromator with a spectral resolving power ($E/\Delta E$) ranging between 1000 and 5000, depending on working energy throughout the whole energy band of interest. The beamline is equipped with a series of interchangeable diodes, pass-band filters, and beamline filters for detection. In addition, three variable line spacing plane gratings (75, 300, and 1200 lines/mm) are used to cover the whole energy range. A minimum overlap between adjacent energy range regions allows one to clean the data better when ambiguities are present. A description of the experimental parameters employed at the METROLOGIE beamline SOLEIL synchrotron facility is detailed in Table 4.2.

The beam at the sample position was elliptically shaped, with FWHM sizes 250 µm horizontal and 150 µm vertical. These lengths are comparable to the pitch of the finely spaced mesh (e.g., 70 LPI), thus requiring a specialized measurement protocol for the filter samples using such mesh (see Section 4.2). Accuracy of translations in the motion stage is 1 µm (in both horizontal and vertical directions normal to the samples' surfaces), and the minimum step that can be traveled is 1 µm. In the whole energy range spanned by the monochromators at the beamline,

Table 4.2 METROLOGIE beamline soft X-ray branch optimal settings in each energy range. FPB stands for Filter Pass-Band. Diode 2 is an Al-coated photodiode, while Diode 3 is a Zr-coated one. These configurations are the basis for all the measurements performed during the experimental campaigns. The best resolution for each range is obtained by dividing the lowest energy in the range by the respective spectral power. The monochromator used for each energy range to optimize spectral resolution had the following properties: 75 grooves/mm for low-energy ranges and $300 - 1200$ grooves/mm for higher-energy ranges.

Energy Range (eV)	FPB (Material, Angle)	Line Filter & Thickness (µm)	Diode Employed	Average Spectral Power
30–55	Si, 3.5°	Al/Mg/Al 0.5	Diode 2	5000
45–75	Si, 3.5°	Al 0.5	Diode 2	4000
70–105	Si, 3.5°	Si 0.5	Diode 3	3000
95–165	Cr, 3.5°	B 0.4	Diode 3	2000
160–270	Cr, 2.8°	C 0.7	Diode 2	1500
260–305	Cr, 2.8°	Ti 0.5	Diode 2	1000
280–325	Cr, 2.5°	Ti 0.5	Diode 2	4000
320–445	Cr, 2.5°	Ti 0.5	Diode 2	3000
440–766	Si, 1.1°	Co 0.5	Diode 2	2000
760–908	Si, 1.1°	Cu 0.9	Diode 2	5000
895–1800	Extracted	B 0.4	Diode 2	4000÷2000

the beam spot is expected to drift slightly: in the vertical direction, it does not appreciably move, while in the horizontal direction, the spot stays within 100 µm.

Transmittance measurement protocol

The witness samples were placed in a custom-designed multi-sample holder, fabricated at the INAF-OAPA, and are shown in Fig. 4.2. The piece was designed by Ing. Fabio D'Anca (INAF), with inputs from the whole team, including myself, and two identical pieces were manufactured with the help of the technicians Mr. Gaspare di Cicca, Roberto Candia, and Salvatore Varisco. I performed the initial functionality tests of the sample holder's design by performing in the INAF-OAPA/XACT clean room the first mounting tests, aiding improved manufacturing and redesign of some aspects. Moreover, I also drafted the test plan of the experimental campaign (Proposal #20231204, Principal Investigator Edoardo Alaimo), mounted the sample holders with the samples, and sealed the sample holders for direct usage in the high vacuum chambers at the METROLOGIE beamline in SOLEIL's synchrotron. This holder allowed us to perform many measurements by automating the beamline procedures, and these augmented the efficiency of the beam-time utilization. Furthermore, the teamwork allowed for the successful employment of an extremely functional sample holder, which perfectly suits the needs of testing small thin film filter samples in X-ray spectroscopy at the synchrotron facility and beamline in question.

Before each measurement, the beamline alignment was optimized using reference scans on empty positions. Transmittance data were calculated by measuring both $I_0(E)$, the current reading of the photodiode proportional to the incident photon flux without a sample at energy E, and $I(E)$, the diode current reading proportional to the transmitted photon flux through a sample at energy E. Dark currents were monitored daily and they were found to be negligible. The SOLEIL synchrotron beam current is very stable, although there are friction losses of current, and thus electrons are injected periodically. The current is around 450 mA, and every three minutes there is an injection of current of the order of 0.5% of the total current. Such systematic variations in the beamline ring current were accounted for by normalizing the intensities (I_0, I) to the machine current (M_0, M) as follows in Equation (4.1), which is how I determine the transmittance at an energy value, as all of the quantities in the equation are energy-dependent:

$$T = \frac{I/M}{I_0/M_0}\,. \tag{4.1}$$

The relative errors associated with the measurements taken with Equation (4.1), for these not-completely transparent samples, are of the order of $1 - 2\%$.

Transmittance measurements were divided into 11 energy regions between 30 and 1800 eV as detailed in Table 4.2. With energy steps in the range $0.1 - 2$ eV across the 11 regions, a total of about 2500 points on average were collected for each filter sample. An energy point required 1.4 s of integration time, and, considering

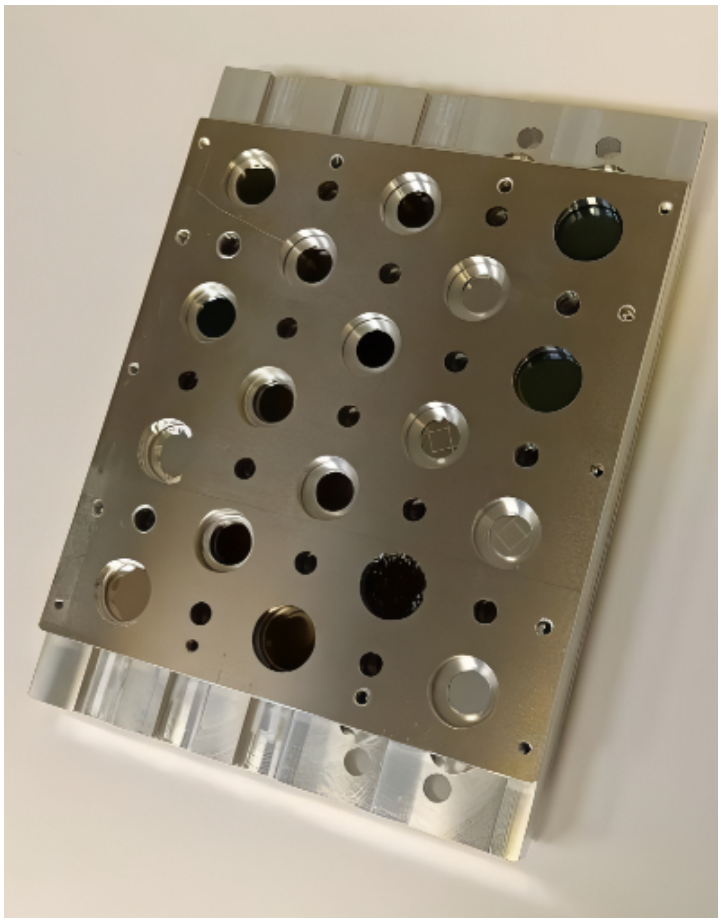

Figure 4.2 Figure of the sample holder manufactured at INAF/OAPA, loaded with 18 witness samples of TF110/111 frame geometry. The spaces between samples are open reference holes, which would be probed after each measurement of transmitted light through a sample to have a reference of the incident light.

that two reference measurements I_0 were taken for each sample measurement I, the acquisition of the full spectrum required 2 to 3 hours per filter sample. Since the allocation time is limited, I would tailor the energy step to each sample type, measuring more points in the in-band region of MUSE and around the energies of important atomic photo-absorption edges. Energy values for the atomic X-ray edges of relevance to our work are listed in Table 4.3.

Table 4.3 Photoabsorption edges for atoms relevant to the materials studied in this work, including zirconium, carbon, aluminum, oxygen, nitrogen, and iron, and with energy included in the energy range $30 - 1800$ eV of the METROLOGIE soft X-ray beamline. Reference energies are taken from Henke et al. and the respective up-to-date website. [75] [76]

Element	Edge	Energy (eV)
Zirconium (Zr)	M1	430.3
	M2	343.5
	M3	329.8
	M4	181.1
	M5	178.8
Carbon (C)	K	284.2
Aluminum (Al)	K	1559.6
	L1	117.8
	L2	72.95
	L3	72.55
Oxygen (O)	K	543.1
Nitrogen (N)	K	409.9
Iron (Fe)	L1	844.6
	L2	719.9
	L3	706.8

The following criteria were used for the measurement of the different sample types, where the X-ray photo-absorption edge regions are probed with the maximum possible energy step, avoiding resolution overfitting:

- For the case of Al-coated samples, 0.1 / 0.5 eV energy steps in the MUSE energy range were used, and the pairs of atoms and edges of Al L-K, O K, C K, N K, and Fe L were experimentally probed.
- For the case of Zr-coated samples, also 0.1 / 0.5 eV energy step in the MUSE energy range were employed, and the pairs of atoms and edges of Zr M1 to M5, O K, C K, N K, and Fe L were experimentally probed.

Carbon edge is always probed, as it is possible that it could be used as a passivation or capping layer in many scenarios. Nitrogen and iron absorption edges are always

probed as they are expected to be part of either the CNT films (with Fe being required nano-catalysts in their formation) or PI films naturally containing N.

Automated Python macros were written, allowing us to control sample-holder positioning, monochromator settings, and data acquisition parameters according to the required settings shown in Table 4.2, by giving instructions to each moving part of the beamline (see Automated Measurement Workflow, Listing Listing A.1 for a pseudo-code describing the procedure). As was mentioned, a calibration procedure was implemented for samples with finely spaced meshes involving the measurement of the transmittance over multiple points across a grid, to take into account the optical BF (blocking factor) due to the mesh, and it is detailed in the ensuing section. As discussed in the design chapter, mesh transmittance M and its blocking factor BF are related by $T = 1 - \mathrm{BF}$.

On the case of finely spaced meshes

For samples supported by nickel square meshes with finely spaced periodicity, i.e. samples Al 150 / 70 LPI and Zr 200 / 70 LPI, the mesh pitch has a nominal size of about 363 µm which is comparable in order of magnitude to the beam FWHM size estimates of 250 µm-horizontal and 150 µm-vertical. Thus, the standard transmittance measurement protocol described in section Section 4.2 would yield inaccurate results due to partial beam occlusion (i.e. *partialization* of the beam) by mesh bars in a single-point measurement. By averaging among the mesh and the partialized regions, it was deemed possible to reach a correct estimate of the witness samples' transmittance. Nine points were measured across a uniform grid on the sample, with a spacing interval of 250 µm. This ensured to probe with the X-ray beam both open and blocked regions of the mesh, and an average among all the measured transmittance would yield an average product $M \times F$ where M is the mesh transmittance and F is the filter transmittance.

I simulated the 9 points grid transmittance measurement average scenario to ensure the accuracy of the procedure by employing a Python script which, with a given selection of input values of the pitch of the mesh ($p = 363\,\mu\mathrm{m}$), bar width of the mesh ($w = 33\,\mu\mathrm{m}$), FWHM sizes of the incident beam (250 µm-vertical, 150 µm-horizontal), kind of beam profiles (Gaussian or Lorentzian), size of the grid spacing chosen, size of the witness sample open area, and amount of points in the grid would simulate the measured transmittance average among the simulated grid and would compare it to the theoretically expected one – that is, $1 - \frac{2w}{p}\left(1 - \frac{w}{2p}\right)$, an explanation of which was given in Section 2.2 → p. 21. Moreover, I replicated this nine-point average study for angles from 0° to 45° with 5° steps of rotation between the vertical axis of the beam and the position of the mesh. I found a maximum discrepancy of $\delta_{\mathrm{exp}} = 0.9\%$ between the averaged transmittance and true transmittance, in the worst case of 45° tilt and Gaussian beam, thus suggesting a reasonable approximation for the experimental error to be associated to this procedure and thus to the inference of the mesh transmittance value from the fitting procedure results detailed in Table 4.4. The simulation with the

Lorentzian beam shows a lower maximum difference from the true transmittance value of 0.11%, and it is considered a best case.

This procedure would increase the amount of time required for measuring one sample by a factor of at least 9. To maintain practicality, the 9-point averaging protocol was performed only in the MUSE bands between $30 - 165\,\text{eV}$, and in selected single energy points in all of the regions. Otherwise, the protocol detailed in section Section 4.2 was applied to the remainder of the energy range up to 1800 eV. In order to correct for any partialization effects due to the mesh and bars in the way of the beam, I would use the single points evaluated with the proper 9-point average as calibration standard points to correct the transmittance curve obtained from the standard protocol, using a piecewise-linear calibration method along different energy ranges. This provided high-quality transmittance data even in the $165 - 1800\,\text{eV}$ range, although some degree of partialization could be present due to the drift of the beam spot as described in Section 4.2.

4.3 Models Employed and XAS Data Analysis

Models employed: Exponential Attenuation

To model the data retrieved via the aforementioned protocols and gotten via Equation (4.1), I describe the transmittance formula for a multilayered solid filter as the following product of exponential functions, which has been extensively used for the study of thin films applied to X-ray astrophysics [112]. I extend this formula in Equation (4.2) to the case of samples with a fine mesh by using a coefficient M which incorporates the mesh transmittance coefficient where applicable.

$$T = M \cdot \prod_i exp\left[-\left(\frac{\mu_l}{\rho}\right)_i \cdot (\rho x)_i\right] \tag{4.2}$$

Where index i runs through all of the elements in the sample, $(\rho x)_i$ is the areal density of each element measured in $\text{g}\,\text{cm}^{-2}$ – i.e., grams of absorbing element per unit area perpendicular to the impinging X-ray flux – and the ratio $\left(\frac{\mu_l}{\rho}\right)_i$ is the corresponding atomic macroscopic mass attenuation coefficient, with μ_l being the atomic linear absorption coefficient in cm^{-1} and ρ the atomic volumic density in $\text{g}\,\text{cm}^{-3}$. For a given kind of element X, there is a precise relationship between $\left(\frac{\mu_l}{\rho}\right)_X$, and the absorptive portion of the atomic scattering factor for a single atom, $f_2^0(E)$, a theoretical description of which can be found in the textbook by D. Attwood [113]:

$$\left(\frac{\mu_l}{\rho}\right)_X = 2\,r_e\,\frac{N_A}{M_u\,A_r(X)}\,\lambda\,f_2^0(E) \tag{4.3}$$

This ratio depends solely on physical constants, the classical electron radius r_e, Avogadro constant N_A, the molar mass constant M_u, as well as on the atomic species and the energy via the relative atomic mass of the element $A_r(X)$ and the atomic scattering factor $f_2^0(E)$, thus the right side of the equation does not depend directly on the density. A relevant source of literature values for $f_2^0(E)$ for various atoms can be found in the pioneering work by Henke et al.[75] and the related website[76]. In case the i-th element $\mathrm{X_i}$ is solely part of a precise compound *mat* with known chemical formula $\mathrm{X_{1_{n_1}}\,X_{2_{n_2}}\,X_{3_{n_3}}}$..., I can calculate the compound thickness with the following equation.

$$x_{mat} = \frac{(\rho x)_i}{\rho_{mat} \cdot f_{i|mat}} \tag{4.4}$$

where $f_{i|mat}$ is the atomic mass fraction of the i-th element $\mathrm{X_i}$ in the compound, and it is given by the customary:

$$f_{i|mat} = \frac{n_i \cdot A_r(X_i)}{\sum_j [n_j \cdot A_r(X_j)]} \tag{4.5}$$

With each $A_r(X_j)$ being the relative atomic mass of element $\mathrm{X_j}$ with the respective number of atoms stoichiometry n_j.

In the most general case, the areal density of an element is the direct sum of the effective areal densities of each compound containing it. That is, if the index K runs through all of the different materials in the sample that contain element i, I have the following decomposition formula for the element's areal density:

$$(\rho x)_i = \sum_K (\rho x)_K \cdot f_{i|K} \tag{4.6}$$

I will model all of our witness samples as multilayer structures with definite layers with given chemical formulas and physical densities, as shown in Fig. 4.3, for EUV/soft X-ray characterization and XAS modeling of the bulk layer compositions and thicknesses, and as successfully demonstrated in previous filter characterization studies[114]. The multilayer simplistic structure neglects the presence of interface layers, as the XAS technique is only sensitive to the bulk thicknesses[115] and the interface widths (diffusion/roughness inter-layers) are of the order of $\sim 1\,\mathrm{nm}$ or lower[116].

The physical constants values employed for Equation (4.3) are taken from the CODATA2022 evaluation[92]. As for the relative atomic weights, the abridged standard atomic weights listed in the 2021 IUPAC technical report are employed[117]. The atomic scattering factors used in this work in the energy range $30\,\mathrm{eV} < E < 1800\,\mathrm{eV}$ for all the elements involved are taken from the tabulated values detailed in the up-to-date website by Henke et al.[76] For the case of aluminum and in the range $30\,\mathrm{eV} < E < 1300\,\mathrm{eV}$ the optical constants employed are the ones detailed by Burcklen et al.,[118] which greatly improve the accuracy

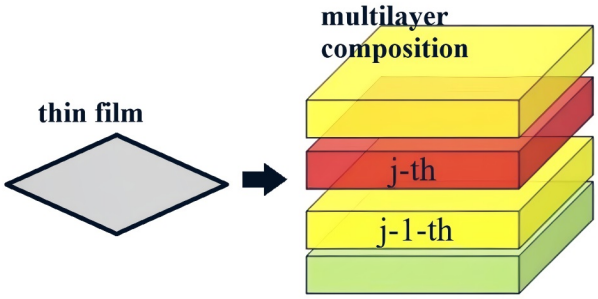

Figure 4.3 Visual description of the multilayer model of a given witness sample or thin film. The different colors identify a pure material in a layer. Interface effects between layers are neglected.

on the Al scattering form factor particularly for energies lower than L-edge range ($\sim 72\,\text{eV}$).

The main contributor to the $f_2^0(E)$ in Equation (4.3) is the phenomenon of photo-absorption. Since Henke scattering factors are mostly based on X-ray measurements carried out on standard references of pure materials or gases, the analysis of the XAS data with the model in Equation (4.2) cannot accurately model near-edge phenomena or extended fine-structures in the post-edge phenomena, both of which are sensitive to chemical bonding neighborhood and the oxidation state of the absorbing atom [119]. These post-edge effects are not taken into account in the ensuing analyses, and, if they were of interest, a different kind of sample-specific modeling procedure would be considered [114]. By experimentally detecting and accurately modeling the jump in transmittance around edges, excluding the pre- and post-edge energy ranges, I aim to study the exact chemical composition of the material, with the jump being more sensitive to the atomic interaction.

For each filter sample in Table 4.1, the following atoms are chosen for the ensuing analyses, detailing the materials that are expected to compound the multilayer structure of each sample and to contribute to Equation (4.2):

- for Al 150 / 70 LPI, I use: Al and O, along with the M mesh transmittance free parameter. As for layer materials, metallic Al and Al_2O_3.
- for Al 150 / 55% CNT, I use: Al, C, O, and Fe. The following materials are expected: metallic Al, Al_2O_3, and bare CNT pellicle with traces of O and Fe.
- for Al 150 / PI 75, the following atomic species: Al, C, N, H, and O. The following materials are expected to compound the sample: metallic Al, Al_2O_3, and PI.
- for Zr 200 / 70 LPI, I use: Zr and O, along with the M mesh transmittance free parameter. Regarding layer materials, metallic Zr and ZrO_2.
- for Zr 200 / 55% CNT, I use: Zr, C, O, and Fe. The expected materials are:

metallic Zr, ZrO_2, and bare CNT with traces of O and Fe.

– for Zr 200 / PI 75, the following atomic species: Zr, C, N, H, and O. As for materials, metallic Zr, ZrO_2, and PI.

Unless otherwise specified, these atomic species correspond to areal density free parameters in the fitting algorithm.

N is not used as a free parameter for the case of sample Zr 200 / PI 75 because, even though it would cause an absorption edge at roughly 409.9 eV as expected from Table 4.3, the presence of the relatively thick Zr layer with the onset of the Zr M-edge absorption renders the N K-edge very hard to detect – estimates from Henke et al.[75] [76] suggest that a single layer of 75 nm of PI would yield a relative jump in transmittance of about 1% at 409.9 eV while 200 nm of Zr would transmit only about 4% of light at the same energy, thus only a small jump in transmittance would be expected. It would be buried in the Zr M post-edge fluctuations. However, for such a sample, the absorption of nitrogen is still taken into consideration in equation Equation (4.2) as a parameter fixed to the carbon quantity by employing the known stoichiometry of N in the PI material (i.e., $C_{22}H_{10}N_2O_4$), and by using the areal density of C as guidance in equations Equation (4.4) to Equation (4.6) during the fitting procedure. Similarly, in the case of sample Zr 200 / 55% CNT the areal density of C is fixed to a value determined by the independent XAS analyses of bare 55% CNT pellicles, i.e. $(44 \pm 4) \times 10^{-7}\,\mathrm{g\,cm^{-2}}$. The high absorption of the filter sample and the presence of post-M-edge Zr oscillations made it challenging to reliably model the transmittance around the C K-edge region with a free C parameter without obtaining inconsistent results. The value of the carbon areal density found in the case of sample Al 150 / 55% CNT, for which carbon is a free parameter, is in line with the mentioned fixed estimate, as will be shown in Section 4.4 and Table 4.4. For the samples containing PI, since the stoichiometry of hydrogen atoms in the PI layer is known, H is added as an areal density parameter fixed to the polyimide thickness resulting from the fit in a similar way as described above in the case of N, because it can have a detectable absorption effect in the lower EUV energy range. By employing Equation (4.2) and using known values of scattering factors of Henke et al.[75] [76], the areal density of H atoms in 75 nm of PI can be responsible for transmitting $\sim 95\%$ at 40 eV. For samples with CNTs, although they can have some hydrogen in their composition[120], its exact stoichiometry is not known – it could be as high as one hydrogen atom per carbon atom for a non-realistic benzene stoichiometry scenario C_6H_6, or negligible for the graphene-case with stoichiometry of pure C. XAS is not sensitive enough to reliably derive the amount of hydrogen per cm^2 in a given material, as H is fairly transparent and lacks notable experimental features in the EUV and X-ray energy range[113]. For these reasons, the hydrogen areal density is used as a fixed parameter in the case of samples with PI, and it is not used at all in the case of CNT samples.

As a last note, the following physical parameters are the densities used in this work during the ensuing calculations. These are approximations of the true densities,

which serve as a basis for the layer thickness estimations and are sufficient for our purposes. The exact estimation of the layers' densities, particularly for the case of the thin film native oxide layers, which can be under 10 nm, is quite challenging and outside the scope of this research. Unless stated otherwise, the source database used for the densities is TPSX, the Aerospace Materials Property Database [121].

- Aluminum (Al): $2.7\,\mathrm{g\,cm^{-3}}$, assuming the usual cubic-phase metal density.
- Aluminum Oxide (Al_2O_3): $3.3\,\mathrm{g\,cm^{-3}}$, more typical of an expected amorphous phase in the native oxide-like thicknesses (i.e. <20 nm) of aluminum oxide thin films as can be found in Krautheim et al. [122]
- LUXFilm® Polyimide (PI): $1.4\,\mathrm{g\,cm^{-3}}$, as provided by the manufacturer (Luxel)
- Iron (Fe): $7.87\,\mathrm{g\,cm^{-3}}$, a density typical of the metallic cubic-phase.
- Carbon Nanotube (CNT): $0.3\,\mathrm{g\,cm^{-3}}$, a rough estimate for the pellicles in this work based on discussions with Canatu.
- Zirconium (Zr): $6.52\,\mathrm{g\,cm^{-3}}$, typical of the metallic cubic phase.
- Zirconium Oxide (ZrO_2): $5.85\,\mathrm{g\,cm^{-3}}$. This value is an average of the values obtained in the deposition of thin films of zirconium oxide with sputtering techniques as obtained by Venkataraj et al. [123]

4.4 Results and Discussion of EUV/XAS Data Analyses

MUSE In-band EUV experimental transmittance curves

The in-band transmittance is shown in Fig. 4.4 for all of the Al and Zr coated witness samples of Table 4.1.

Many pieces of information can be gathered from the data shown in Fig. 4.4, with relevant aspects to be considered for EUV space missions such as MUSE that observe in the EUV spectrum.

Regarding the transmittance of Zr-based witness samples at 10.8 nm, of direct applicability to the MUSE SG channel 108 Å, the most performing sample in terms of transmittance is the one supported by the finely spaced Ni mesh, which transmits 40.4 %. This configuration would cause non-negligible diffraction at the focal plane, particularly in the case of bright lines during flares due to Fe XIX and Fe XXI being at temperatures of the order of 10^7 K [20], as was shown for SDO/AIA's channels employing finely spaced mesh-supported filters [4]. The two less transparent samples, Zr 200 / 55% CNT and Zr 200 / PI 75, are representative of filters with much more transmissive structural meshes that are expected to cause much less

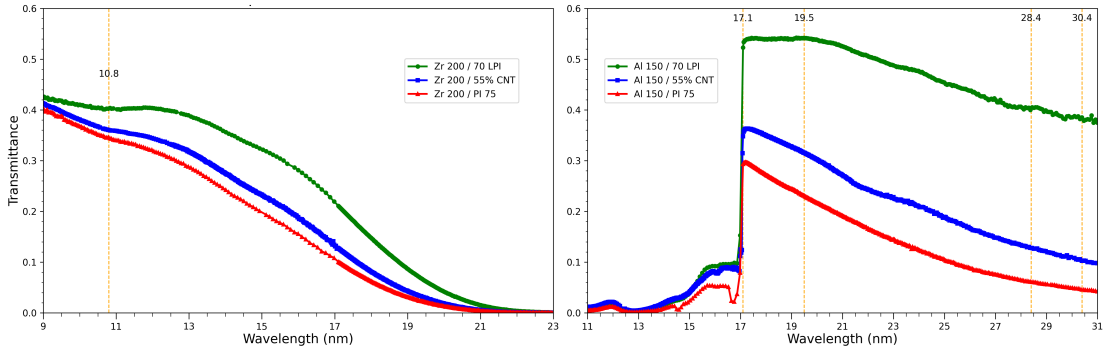

Figure 4.4 The experimental EUV transmittance spectra for the witness samples described in Table 4.1. In all cases, the transmittance values shown for the 70 LPI samples represent the combined transmittance of both the mesh and the filter (i.e., the product of their transmittances), and panels have the same Y-axis range for ease of comparison. **Left:** Spectra for the Zr-based samples. The Zr 200 nm coating is supported by either 75 nm of PI, a fine Ni mesh (70 LPI), or a CNT pellicle with 55% visible transmittance at 550 nm. The vertical dashed line indicates the MUSE spectrograph wavelength channel at 10.8 nm. **Right:** The experimental EUV transmittance spectra for witness samples based on Al and described in Table 4.1. The Al 150 nm coating is supported by either 75 nm on PI, a fine Ni mesh (70 LPI), or a CNT pellicle with 55% visible transmittance at 550 nm. Vertical dashed lines indicate the MUSE spectrograph wavelength channels at 17.1 nm, 19.5 nm, 28.4 nm, and 30.4 nm.

diffraction effects, as shown in Section 2.4. Thus, even though it is the most performing, the Zr 200 / 70 LPI filter configuration is less likely to be the one adopted to minimize the impact of diffraction on MUSE. The Zr / CNT-supported sample exhibits a transmittance at the same channel of 36.0 % while the PI-supported filter transmits 34.4 %. This means that the difference between the two samples is $\Delta T \approx 1.6\%$ with the CNT-based sample being slightly more efficient than the PI-based one. Such small differences, although with high values for their transmittance, represent how both materials of choice are nice candidates for MUSE for this band.

The Al-based witness samples respect the same trend as before, with the sample of Al 150 / 70 LPI outclassing the other samples in both channels. More precisely, in the 171 Å channel, it transmits 52.6 %, and it transmits 40.3 % at 284 Å. The Al 150 / 55% CNT witness sample transmits 35.1 % in the 171 Å channel, and 12.8 % at 284 Å, while sample Al 150 / PI 75 transmits 29.4 % in the 171 Å channel and 6.1 % at 284 Å. The values found are in line with the trend expected by using equations Equation (4.2) and Equation (4.3) to simulate the theoretical transmittances of the studied films in the witness samples, ignoring oxide layers. However, one would generally expect a higher transmittance, especially in the channel 284 Å [80] [43]. As a theoretical prediction, the transmittance at 284 Å , neglecting oxide and assuming a pure layer of 150 nm of Al deposited on top of an ideal membrane of CNT with a thickness of 200 nm and density of 0.3 g/cm^3, both of which transmit respectively about 71.7% and 45.20%, would imply a transmittance of the bi-layer

of 32.4% (i.e. the value of the Film Tran. registered in Table 2.3: the measured transmittance of 12.8% is significantly reduced, suggesting that the models need to take into consideration realistic values for the metal oxide thicknesses, as detailed in the following Section 4.4.

Summarizing these results, I find that the CNT-based samples in the MUSE bands demonstrate a higher in-band transmittance efficiency than the heritage filters based on the metal coating on PI. In the 108 Å channel-related samples, the Zr film supported by the 70 LPI Ni mesh shows a very high transmittance. However, it would be expected to cause non-negligible diffraction effects at the detection focal plane, followed by similarly in-band performing Zr / CNT and Zr / PI samples. With regards to aluminum-based filters, the Al with 70 LPI Ni mesh sample surpasses all the other choices in terms of raw transmittance. Currently, the technology and science teams behind the MUSE mission are engaged in an ongoing discussion to assess–via simulation-based approaches–the impact on MUSE's science observations of both the diffraction caused by the 70 LPI mesh and the reduction in the signal transmitted by the Al 150 / 55% CNT sample. The design of the latter is expected to cause less diffraction [80]. Moreover, while an in-band improved performance for the CNT-based metal-coated samples was shown as compared to the samples with the PI substrate, this is not the full trade space, since there are many aspects involved in the assessment of the maturity of an integrated filter system – like it was discussed in Chapter 1. A detailed analysis of the trade-offs is beyond the scope of this study.

Soft X-ray and EUV experimental transmittance curves and models

A complete showcase of the soft X-ray transmittance spectra measurements is given in Fig. 4.5, which also allows us to detail the inner-layer composition of our samples in Table 4.1. For these plots, the model used is from Equation (4.2)-Equation (4.3), and best-fit values are retrieved via the Levenberg-Marquardt algorithm [124]. The plots shown in Fig. 4.5 reveal Al L-edge and Zr M-edge post-edge features for the respective samples. These features are not present in the tabulated Henke scattering factors, and, while the pre- and post-Al L-edge behavior is nicely modeled with the optical constants obtained in the recent work by Burcklen et al.,[118], this is generally not the case. It is certainly not the case for the Al K-edge or all of the other atoms and absorption edges of interest to this work. Thus, the energies corresponding to the pre-/post-edge effects are neglected for the best-fit modelling. Only the *jumps* on the sides of the absorption edges are under the study of the fitting process, and all of the models accurately follow the experimental data for our samples. Results of the fitting algorithms regarding the areal densities corresponding to the model curves shown in Fig. 4.5 are shown in Table 4.4 while the inferred thicknesses are shown in Table 4.5.

These values allow us to infer the thicknesses of oxide layers present in the samples,

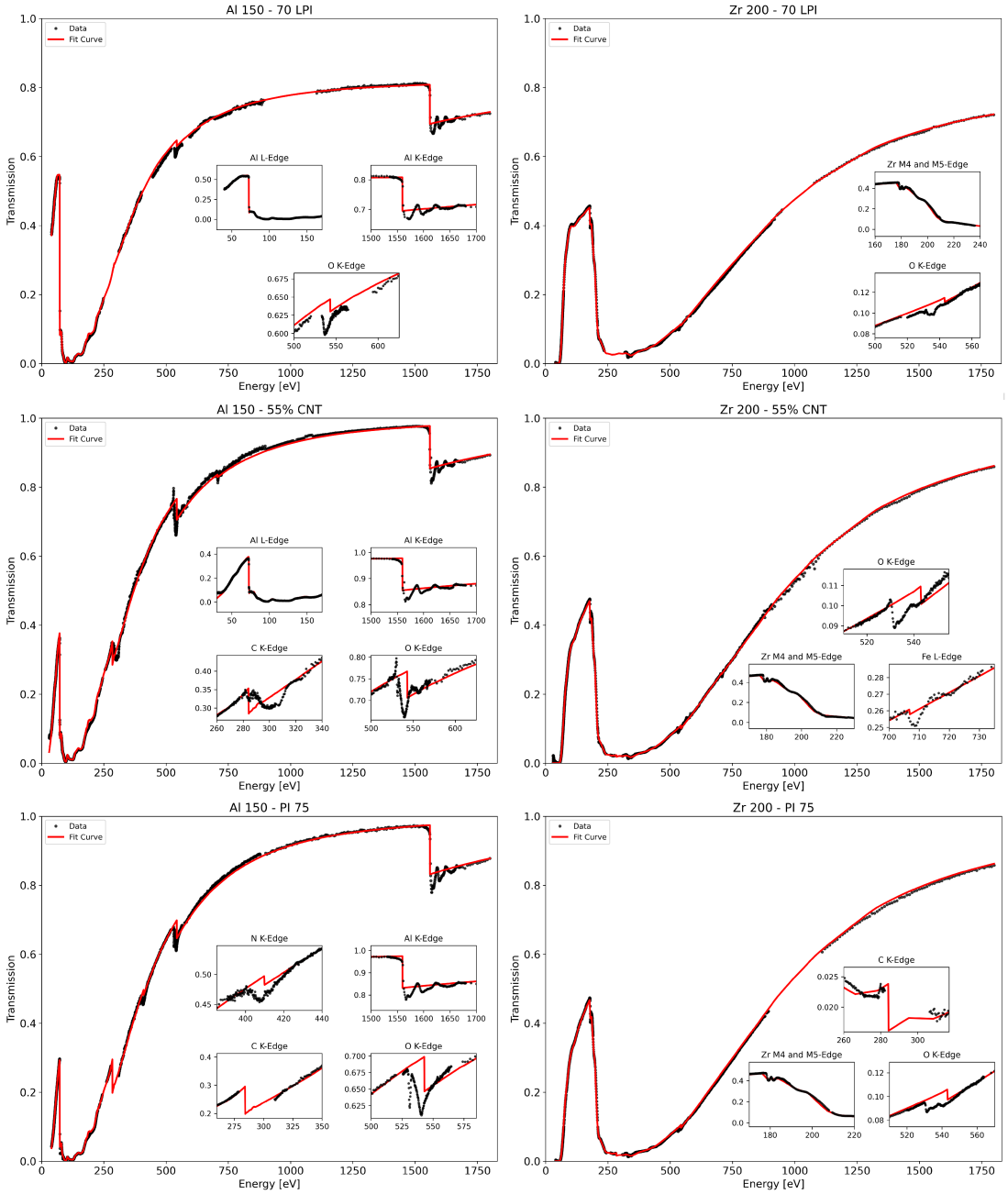

Figure 4.5 EUV and soft X-ray transmittance spectra of the samples under study. Transmittance Y-axis ranges are all between 0 and 1 to ease comparisons, insets highlight relevant photo-absorption edges during model fitting, black dots represent experimental data points, and red lines show the best-fit model curves. **Left column:** Al-based filters with 150 nm coating supported by (top to bottom) 70 LPI Ni mesh, 55% CNT pellicle, and 75 nm PI membrane. **Right column:** Zr-based filters with 200 nm coating supported by (top to bottom) 70 LPI Ni mesh, 55% CNT pellicle, and 75 nm PI membrane.

Table 4.4 Areal densities of elements in filter samples determined from the XAS analyses shown in Fig. 4.5, along with mesh transmittances M retrieved from the fit procedure (where applicable). The areal density unit of 10^{-7} g/cm^2 corresponds to nm · g/cm^3 in practical units. Uncertainties are reported at $3\,\sigma$ level, derived from the uncertainties provided by the fitting procedure and confirmed via a Bayesian inference approach using Chi-squared contour plots. Dashes (–) indicate elements not detected or not present in the sample. In sample Zr 200 / 55% (CNT substrate assumed), the fit assumes the carbon areal density fixed to $(44 \pm 4) \times 10^{-7}$ g/cm^2, a value based on independent XAS analyses of bare 55% CNT pellicles. For sample Zr 200 / PI 75, the nitrogen areal density was fixed to the carbon one via the known PI stoichiometry. For M's, the total error is the quadratic sum of the $3\,\sigma$ uncertainty and the 0.9% error estimation by simulations of the experimental procedure explained in Section 4.2

Witness Sample	Areal Density [10^{-7} g/cm^2]					M [%]
	Al / Zr	C	N	O	Fe	
Zr 200 / 70 LPI	1221.0(1.6)	–	–	18.3(5)	–	82.4(9)
Zr 200 / 55%	1335.3(1.1)	44(4)	–	42.1(1.1)	7.4(1.5)	–
Zr 200 / PI 75	1326.5(1.9)	79(2)	8.3(3)	41.8)	–	–
Al 150 / 70 LPI	396.8(1.1)	–	–	13.1(2)	–	82.1(9)
Al 150 / 55%	351.7(1.0)	43.9(7)	–	40.9(6)	5.7(9)	–
Al 150 / PI 75	414.8(7)	80.7(7)	10.4(7)	38.6(5)	–	–

which might justify many of the experimental features of Fig. 4.4 and of the discussions in Section 4.4. The mesh transmittance values, free parameters in the fitting algorithm, are completely in line with the expected transmittance of a 70 LPI Ni mesh, which should be ∼81.6 % – that is for a mesh of pitch 363 µm and bar width 33 µm – which also is an experimental confirmation of the procedure detailed in Section 4.2. For the correct oxide thickness estimations, while it is expected for the PI membrane to have a predictable amount of oxygen areal density from its thickness and stoichiometry, it is assumed that the CNT membrane holds some pre-existing oxygen amounting to an areal density of about $(5.4 \pm 1.0) \times 10^{-7}$ g cm^{-2}, as inferred from transmission measurements and model analysis performed separately on bare CNT pellicles of the same type of the substrate pellicles (in preparation work by Alaimo et al.[41]). Then, the strategy employed is to evaluate the amount of oxygen areal density present in the substrate (be it CNT or PI), subtracting this amount from the oxygen areal density resulting from the fitting process, and then using the remainder to evaluate an oxygen contribution due to the presence of the metal oxide. This procedure was carried out for all the samples shown in Table 4.5 but the samples with a 70 LPI mesh.

The evaluations found and listed in the table are in line with expectations. Traces of iron are found in the CNT pellicles, which have, on average, a very small impact on transmittance. Uncertainties found in the bulk layers (Metal, Substrate) reflect uncertainty on the XAS data, which contains effects due to the beam size and

Table 4.5 Layer thicknesses derived from XAS analysis of Fig. 4.5. Where applicable, the thicknesses described refer to the adjacent material detailed in square brackets. All uncertainties are reported at the 3σ level based on the fitting procedure. Dashes (–) indicate the absence of the corresponding layer. For samples containing a CNT pellicle substrate, an areal density of oxygen amounting to $(5.4 \pm 1.0) \times 10^{-7}\,\mathrm{g\,cm^{-2}}$, a value based on independent XAS analyses of bare 55% CNT pellicles, is expected to be part of the substrate of these samples, and this is taken into account for the metal oxide estimates.

Witness Sample	Layer Thicknesses [nm]			
	Metal	Metal Oxide	Substrate	Fe
	Al / Zr	Al_2O_3 / ZrO_2	PI / CNT	
Zr 200 / 70 LPI	179.2(5) [Zr]	12.1(4) [ZrO_2]	–	–
Zr 200 / 55%	188.0(9) [Zr]	24.8(1.0) [ZrO_2]	147(13) [CNT]	0.94(19)
Zr 200 / PI 75	193.5(1.2) [Zr]	15.0(1.3) [ZrO_2]	77.9(2.5) [PI]	–
Al 150 / 70 LPI	141.5(5) [Al]	8.43(13) [Al_2O_3]	–	–
Al 150 / 55%	115.5(9) [Al]	22.9(8) [Al_2O_3]	146(2) [CNT]	0.72(12)
Al 150 / PI 75	145.7(5) [Al]	12.3(4) [Al_2O_3]	79.9(7) [PI]	–

possibly the small beam drift as described in Section 4.2, not considering the effect of spatial uniformity addressed in section Section 4.1. For most of the samples, the amount of metal recovered is very similar to the manufacturer-recommended estimates, accounting for the presence of a metal oxide layer, which deducts metal atoms from the pure metal layer. However, in the case of Al 150 / 55% CNT, there is less Al than expected. Thin film metal samples are known to naturally produce a very thin oxide layer when exposed to air, which in the case of Al is expected to be of $\sim$4 nm or less at each interface between Al and other layers and/or on the air-exposed surface [77] [125]: since PI is quite hygroscopic, and both the 70 LPI meshes and the CNT pellicles are very transparent to air, the metal layer can be thought to be subject to two air (or one air and one humidity-related) interfaces. On average, the amount of oxide found on Al-coated PI samples is slightly higher than expected, suggesting some augmentation of oxidation due to the presence of PI from 4 nm per interface to about 6.15 nm. On the other hand, the amount of oxide per interface found on the samples with aluminum deposited on the 70 LPI Ni mesh is $\sim$4.2 nm, which is close to the expected amount. For the Al 150 / 55% CNT sample, I find nearly twice the oxidation amount as compared to the other filter samples, i.e. $\sim$11.45 nm of Al_2O_3 per interface. This result suggests that the higher specific surface of the CNT pellicle [39] increases the number of spots where oxidation might occur, particularly if the metal partially diffuses deep in the CNT substrate and does not just form a uniform layer. Similar results are inferred for the thickness of ZrO_2 per interface found on the zirconium-based samples, with $\sim$6.05 nm for the 70 LPI sample, $\sim$7.5 nm for the PI-supported one and $\sim$12.4 nm for the CNT-supported one.

4.5 Conclusions on EUV/XAS

This study of EUV transmittance conducted on small filter samples has provided useful pieces of information regarding the materials of choice in the design of the MUSE NASA space mission entrance and filter wheel filters. Filter samples were studied in their in-band transmittance for MUSE and also in their out-of-band transmittance in the soft X-ray range. Both filter samples based on the heritage from space missions, such as SDO/AIA, and samples made with novel materials, such as those with a CNT-pellicle substrate, were probed in this study. Our experimental investigation has provided the in-band transmittance, which can be incorporated into the effective area calculations for MUSE via direct implementation of the calibration data. In addition, the use of the high-resolution, intense, and non-destructive X-ray beam of the METROLOGIE beamline of the SOLEIL synchrotron, combined with a detailed XAS analysis using scattering factors obtained from literature, [75] [118] allowed us to perform an experimental characterization and an inner-layer thickness quantification of all the investigated filter samples. In particular, I derived the thicknesses of oxide and metal layers with their different amount of oxidation depending on the substrate, and the small amount of Fe present in CNT pellicles, and also provided an alternative method to precisely determine the fine Ni mesh transmittance in the samples. Such experimental characterization provides crucial insights for the space mission as a whole.

It is noteworthy, and a result of this work, that CNT-supported filters consistently outperform PI-supported designs across all wavelength bands in their in-band transmittance: at 10.8 nm, CNT-Zr transmits 36.0% versus 34.4% for PI-Zr; at 17.1 nm, CNT-Al achieves 35.1% compared to 29.4% for PI-Al; and at 28.4 nm, CNT-Al transmits 12.8% versus 6.1% for PI-Al. The EUV transmittance data assess the performance of the space-grade PI-based filters, and these measurements also contribute to CNT pellicles as promising filter substrates for MUSE and future EUV space observatories.

The mesh-supported witness samples based on heritage from previous missions demonstrate a much superior raw transmittance value of 40.4% at 10.8 nm for Zr / 70 LPI and 52.6% at 17.1 nm for Al / 70 LPI. The improvement at the higher-energy channel is negligible since the other samples employing CNT or PI substrate would be transmissive enough (>34% at 10.8 nm), causing no relevant diffraction content at the focal plane, being supported by a very transmissive 5 LPI structural mesh. The same cannot be said for channel 284 Å, as the Al 150 / 70 LPI sample, with its measured 40.3% transmittance, would provide more than 3 times the signal of the CNT-based alternative (transmitting 12.8%) and more than 6 times that of the PI based one (transmitting 6.1%) in terms of raw photon counts – at the cost of an expected increase of relative diffraction signal content in the focal plane [80], for which there is considerable expertise in its removal and treatment [28]. The trade-off between signal strength and image quality remains

a key aspect for the realization of MUSE's scientific objectives, particularly for observations of bright solar features where diffraction patterns could complicate data interpretation.

The EUV and X-ray Absorption Spectroscopy (XAS) technique has proven effective for the characterization of these samples being studied for MUSE. Particularly, coupled with the data analysis, it allowed us to determine the total oxide layer thicknesses of our samples. As examples, I have found a value of (8.43 ± 0.13) nm of Al_2O_3 for the sample of Al / 70 LPI, and (24.8 ± 1.0) nm of ZrO_2 for the Zr / CNT sample. This detailed analysis of the transmittance data allowed us to determine that oxidation is more pronounced in CNT-supported samples than in PI-supported ones, and this also explained some of the offsets that the transmittance data showed as compared to pure models that did not take into account the real oxidation of the samples, such as the relatively low transmittance observed in the Al / CNT sample at the channel 284 Å, which can be attributed to the oxidation at the CNT interface which was detectable by our XAS data analysis and proved to be at least double the expected amount from native oxide theory forming on bulk metal. This suggests that employing other means to reduce oxidation – i.e., a passivation layer using nitrogen or more carbon, or means to remove the pre-existing oxygen on the CNT pellicles – could improve the efficiency of CNT-based solutions at channels 171 Å and 284 Å.

Moreover, this detailed characterization forms a basis for future accurate modeling of transmittance properties in general – say, finding differences in the atomic layer properties before and after potential destructive or degrading phenomena such as aging, vibration loads, and atomic oxygen tests – providing a valuable framework for monitoring potential in-flight oxidation effects, such as those studied by Berg et al. [35] for SDO/EVE. More precise high-resolution laboratory assessments of the atomic scattering factors or optical constants of various thin film materials of interest for their EUV space applications, such as the work by Burcklen et al. [118] for atoms other than Al, could allow for improving the applicability of XAS analyses such as this one even further.

In conclusion, this work establishes an initial estimate of areal densities, oxide layers, substrates, and metal thickness amounts, and a first assessment of the calibration in the EUV transmittance of small witness samples of thin films as filter candidates for the MUSE mission, both based on heritage from previous space missions and also on novel technologies, while also providing a foundation for the future optimization of such thin film filters. Concerning the in-band performance, the heritage solutions employing either aluminum on finely spaced mesh, or aluminum or zirconium deposited on polyimide, are confirmed to be solid and functional, while also zirconium and aluminum deposited on the novel technology of CNT were characterized, showing a better in-band transmittance performance as compared to PI-based designs. Thus, Al or Zr-coated CNT-based filters are a promising material of choice for MUSE and for future spectroscopic applications in EUV space missions beyond MUSE.

5 Setup of a Penning Discharge Source for MUSE calibration

5.1 Motivation and role in the MUSE context

In addition to the development of designs, simulations, and analyses of filters in terms of diffraction, and characterization and/or analyses of UV-VIS-IR, EUV, and X-ray Transmission Spectroscopy measurements, an important objective of this PhD project is to enable band calibration, using spectral lines, of telescope assemblies in the EUV (such as MUSE) using laboratory sources. The Penning discharge source (PDS) [126] is a well-known class of continuous EUV sources in which a low-pressure noble gas discharge, confined by intense crossed electric and magnetic fields, pulverizes and ionizes matter from metallic electrodes, producing intense, narrow emission lines between approximately 5 nm and 35 nm. It differs from other EUV or X-ray sources for a variety of reasons, making it favorable for the testing of the MUSE mock-up optics and detectors in detecting EUV lines.

One difference is from the Hollow Cathode EUV sources in that it reaches lower gas pressures while employing very strong magnets, allowing to reach higher excitations to the metal, allowing to emit bright lines even at $\sim$108 Å – usually suppressed when gas pressure is higher, and magnets present are not strong enough. Another difference is from the X-ray sources emitting lines and/or bremsstrahlung radiation, such as emission from Synchrotron Laboratories (i.e. such as the beamline employed in Chapter 4) or X-ray Roentgen Tubes: in the former case, the EUV selection is due to the monochromator and optics acting on the broadband X-ray emission, which can be a limiting factor as it does not mimic physically the EUV emission lines of an ionic species with realistic broadening at high temperature and Doppler shifts due to motion velocity which is one of the targets of MUSE; in the latter, the voltage used is about 25 kV, emitting in X ray range, while the PDS employs $\lesssim$2 kV of voltage and this allows to reach lower emission energies for the photons emitted by the source which do come, besides a dimmer continuum, also from recombination. Various literature studies explored the PDS in various forms, materials employed as cathodes, and various characterization analyses [127] [128] [129], with also recent studies interested in its study and simulations [130] [131] [132]. From a historic perspective, during the last two decades, the usage of the source for EUV calibration and characterization has fallen off progressively, with the EUV Lithography industry adopting different EUV sources such as Laser-Produced Plasma Source Systems [133], and radiometric synchrotron-based standards being preferred for modern and future space instrumentation calibration [134] [135]. However, there are cases where line emissions might be preferred.

For MUSE, a PDS is particularly interesting because it is known that with appropriate combinations of gas and electrode materials, it is possible to generate lines, with realistic broadening scenarios too, close to the three main diagnostic channels used by the mission (108 Å , 171 Å , and 284 Å). The latter two lines can be efficiently emitted with a Hollow Cathode Source, and its calibration in these ranges has been reported in the literature in Hollandt et al. [136]. Since Aluminum cathodes used in an argon discharge can produce Al V (i.e., aluminum ionized 4 times in atomic physics notation) with recombination lines at around 10.8 nm, while aluminum or magnesium cathodes in neon generate emission lines around 17.1 nm and 28.4 nm (via Al III-IV and Ne III) [127] [128] [129], the PDS is a useful tool that can be explored either as an alternative or a main source for calibration purposes for MUSE, and also as a way to test MUSE's capabilities to assess line intensities, line broadening and Doppler shifts particularly at the 108 Å wavelength. There are close to no literature reports on the calibration of line-emitting EUV sources at exactly 108 Å . Even though there are reports that suggest these emissions, such as in Heise et al. [129], there are no exact calibration or optimization studies of emissions at this particular wavelength, at least in the rigorous way that was done in Hollandt et al. in the range $15 - 160$ nm. This creates a scientific literature gap, which forms the main core of the interest in developing the source.

During my studies, I helped to assess the functionality of the historic PDS available at the INAF-OAPA X-ray Astronomy Calibration and Testing Center (XACT), refurbishing it, integrating it into the EUV beamline, and putting it back into operational mode for the first time in many years. A figure of the source can be seen in Fig. 5.1.

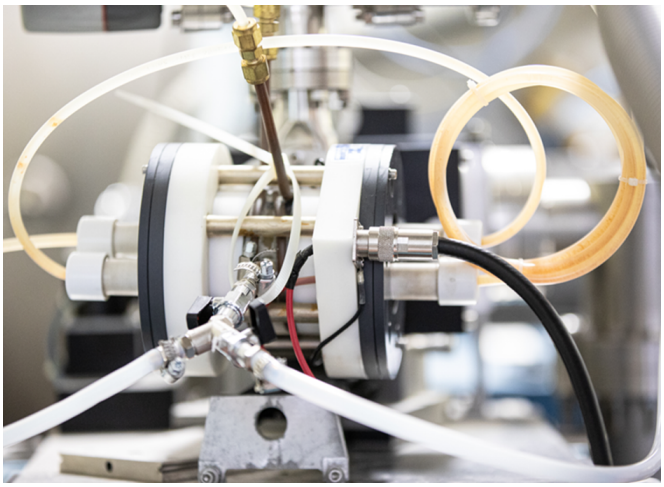

Figure 5.1 Penning Discharge Source in one of its mountings at INAF-OAPA/XACT. Polytetrafluoroethylene (PTFE) tubes for the gas inlet systems are visible, attached to the source. Credit: INAF/ Riccardo Bonnuccelli, all rights reserved. Used with permission.

This chapter provides a general description of the source, its underlying physics, its

current implementation at XACT, and its potential use in the MUSE calibration program.

> **Note.** In the INAF-OAPA/XACT facility, there is a Penning Discharge Source Manual available for interested readers, the exact contents of which are not divulged here for copyright reasons. The source manufacturer was Berkeley Photonics Inc., a US company terminated on 03/09/1999, which was located at 147 Overhill Road, Orinda, California, 94563. The owner of the source is INAF-OAPA, and both the source and the manual are currently located in Via G.F. Ingrassia 31, Palermo (PA), Italy, 90123. Elements of the manuals can be shared under reasonable request and for fair use to the structure [137].

Fairly recently, PTFE tubings for the gas inlet and the inlet-hose system of the source were replaced entirely with a Swagelok-based system, which ensures compatibility with high vacuum and minimizes outgassing, allowing for reaching base pressures of 10^{-5} mbar during operation in the absence of discharge. The work is in progress as the potential integration to the MUSE mock-up telescope and detector system is yet to be defined, and the activities on the source tests, calibration, plasma chamber imaging, and/or potential simulation of the source are ongoing.

5.2 Principles of the Penning discharge

The Penning discharge operates in a crossed electric– and magnetic–field configuration. The main body of the source has cylindrical symmetry. Two facing cathodes and a central cylindrical/annular anode define a quadrupolar electrostatic potential, while (typically) a set of permanent SmCo magnets – employed for the high Curie temperature of $\sim 700\,^{\circ}\mathrm{C}$ [138] – imposing an approximately uniform axial magnetic field in the discharge region of order $B \sim 0.1$–$10\,\mathrm{T}$, depending on the strength of the magnets employed. About 5 T are estimated to be currently present in the source's discharge area in-house, although this can be changed if needed by replacing magnets. The physics summarizing the PDS is described in the following diagram in Fig. 5.2, which conceptualizes in general the source, and in particular the current PDS available at INAF-OAPA. The physics will be described alongside the diagram, which will be referenced throughout the text.

I will start from the situation with static electric and magnetic fields, when no current is flowing, as the **scheme A** in the figure. The magnets impose a cylindrical axial magnetic field in the central region, whereas the anode/cathode geometry induces a quadrupolar electric field in the system, the instant the Direct Current (DC) high-voltage is set on. In this plane geometry, the gas flux inlet is normal to the plane of the diagram; hence, most of the gas will be at the center.

Once the dielectric breakdown occurs, electrons start moving from the cathode to the anode (**scheme B**). Closer to the anodes, electrons pick up velocity

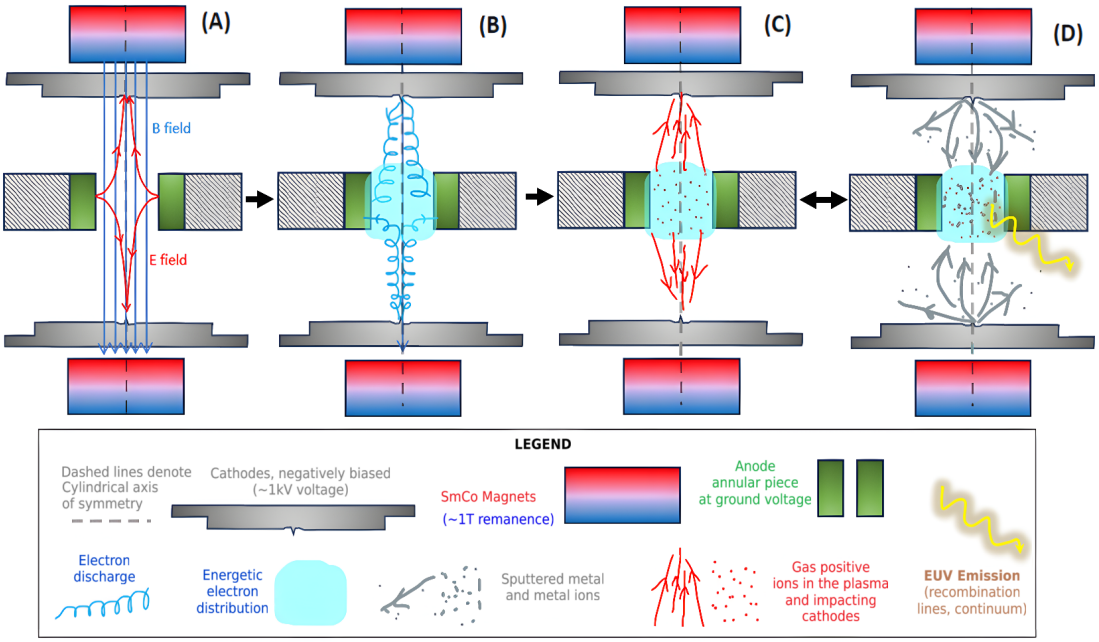

Figure 5.2 Penning Discharge Source diagram, with a legend specifying the objects, and detailed in its different phases: (A) Static system with no current flowing with the high-voltage on. Representative of the non-discharging situation; (B) Dynamic system during the discharge of the electrons from cathodes to anode. Plasma starts forming at the center; (C) and (D) Stationary situation. Metal ions are scattered from the anode. EUV continuum and bright lines are emitted, characteristic of the anodes and gas materials. Figure partially enhanced with Picsart.

perpendicular to the magnetic field lines and circle around them. Thus, the electrons' path length is increased, along with the number of collisions. The Larmor gyration radius, a function of voltage, path, and magnetic field, is about $10 \div 100$ µm, while the anode size is various millimeters, so the collisions between electrons and gas atoms are increased hundreds-fold. In this situation, a very high-energy electron distribution is thereby developed in the discharge region between the two anodes, in equilibrium with highly energized and ionized gas atoms.

The gas cations at the center are then attracted towards the anodes (**scheme C**). As a consequence, metal ions are scattered from the anode, also gaining full energy from the erosion of the cathode as being imprinted from the gas cations. This is the onset of the Penning Effect [139] [140] [126], a theory on which all Penning Discharge Sources are based. Calling gas atoms $\mathfrak{A}$, target atoms $\mathfrak{M}$, and excited gas atoms as $\mathfrak{A}^*$, in the penning ionization reaction the excited metastable gas atom $\mathfrak{A}^*$ can ionize the target atom or molecule $\mathfrak{M}$ as follows:

$$\mathfrak{A}^* + \mathfrak{M} \rightarrow \mathfrak{A} + \mathfrak{M}^+ + e^-. \tag{5.1}$$

At a stationary situation (**scheme D**), the center is in equilibrium between the ionized plasma of the gas, an energetic central electron distribution, and metal cations. This resembles the full operational condition of the source, and EUV light is emitted with a continuum and bright lines intrinsic to the gas and anode materials, and also depending on the gas pressure employed and the strength of the voltage.

Some relevant lines, close to MUSE channels and that can be emitted by a PDS, with the combinations of materials, gases, pressures, and currents, are presented here, as retrieved from the literature:

- emission from Ne III at 283.5 Å, Mo cathodes, Ne discharge, Pressure $\sim 1 \times 10^{-3}$ mbar, Current 1 A, by Deslattes et al. [128];
- emission line from Al III near 171.8 Å, Al cathodes, Ne discharge, Pressure $\sim 8.7 \times 10^{-5}$ mbar, Current 500 mA, by Finley et al. [127]. In the same emission, also the Ne III 283.5 Å emission is present;
- emission line from Al V near 108 Å, Al cathodes, Ar discharge, Pressure $\sim 8.7 \times 10^{-5}$ mbar, Current 600 mA, by Finley et al. [127].

The values of these lines are also confirmed by the NIST Atomic Spectra Database Lines Database [141]: for example, observed wavelength lines for Al V at 107.948, 108.005 Å, and in general between 107 Å and 109 Å, are reported by M.-C. Artru and W.-Ü L. Brillet [142].

By selecting the gas and electrode composition, and by tuning voltage, current, and pressure, the line ratios and overall brightness can be optimized for specific calibration requirements. This is detailed further in the ensuing paragraph regarding the first characterization tests.

5.3 Implementation of the PDS Source

Overall layout

The current system at XACT couples the Penning source to an EUV beamline equipped with monochromators and detectors. The source also needs to be equipped with a chilling system, a high-voltage system, and a gas distribution line. A scheme for the PDS setup closely resembling the scheme employed at the facility, during the commissioning I made of the source for its operational phase, is given in Fig. 5.3.

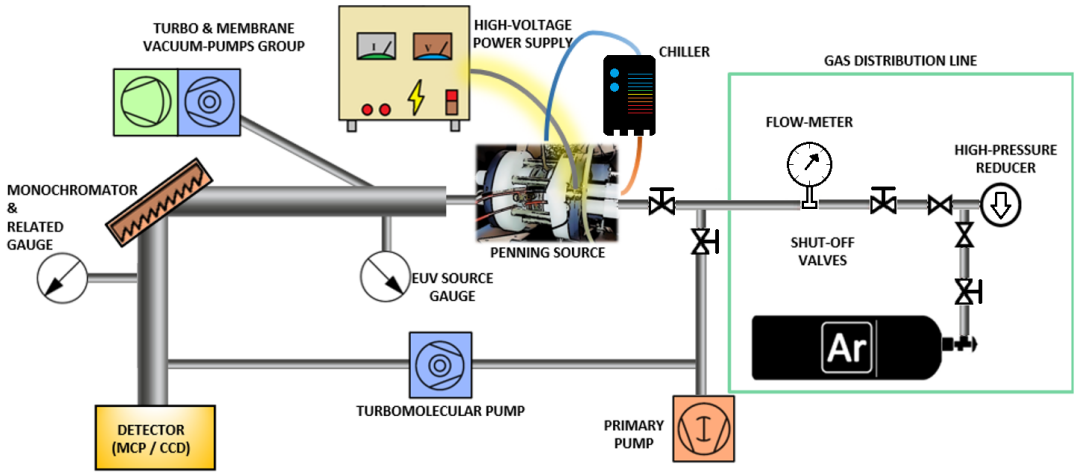

Figure 5.3 Example Diagram of the System in use at INAF-OAPA. In its operational state, the PDS is connected to: the high voltage supply, the cooling water pipes, the inlet gas, and the vacuum system. Flow meters are used to gradually change the pressure of the system. The EUV source gauge is the closest monitor of the pressure of the plasma chamber.

The schematic of the setup comprises the following main subsystems:

- **Penning source**, hosting the electrode assembly, permanent magnets, water–cooled anode body, and gas inlet. Both cathode inserts and the central cylindrical anode are replaceable, allowing the use of different metal materials and the refurbishment of eroded pieces.
- **Vacuum system**, based on turbo-molecular pumps backed by dry primary pumps, achieving a base pressure $\lesssim 10^{-5}$ mbar in the non-operating configuration. Vacuum is monitored with combined Pirani/Penning pressure gauges placed near the monochromator.
- **Gas handling**, with a stainless-steel gas distribution system with multiple mass–flow–controlled lines (Ar, Ne, He, O_2, CO) and valves.
- **High-voltage and cooling**, where a (maximum of) 2 kV DC power supply provides up to ~ 1 A of discharge current, and a closed–loop water chiller maintains the anode body and magnets within their allowed temperature

range during operation. The use of demineralized water is crucial to avoid the buildup of minerals near the magnets, potentially causing clogging of the cooling circuit and a rise in temperatures.

– **Spectrometers**, namely McPherson Rowland–circle monochromators with different gratings (e.g. 300 and 600 lines/mm), coupled to various **detectors**.

Some further details on the capabilities of the XACT beamline can be found in the related website [143]. I now transition to summarize the main technical elements relevant for later scientific use for MUSE in the near future.

Initial Tests and Typical PDS Operating Parameters

The operational parameters of the source depend on all of the experimental conditions employed, which can be varied – i.e., cathode materials, DC voltage, and type of gas used. Consequently, there are no standard operating parameters to be specified, and the user has to characterize their experimental setup, although the source's manual contains some guidelines. In particular, the character of the radiation is sensitive to the pressure in the discharge region in the source, and this pressure is intrinsically unknown. Practically, one measures the pressure at some point near the source and obtains a pressure reading related to such pressure by the intervening conductance. Generally speaking, typical operating parameters involve the use of a discharge gas with a pressure reading of the order of 10^{-4} mbar, and full operational voltages of the order of 1 kV.

In preparation for the full absolute-intensity EUV characterization, I performed an initial series of tests to map the electrical behavior of the PDS source at XACT using argon discharge gas and aluminum cathodes in the exploitable range. The discharge was ignited by gradually increasing the high voltage until a glow appeared at the gas inlet region (discharge being visible as a continuous current flow). Then the operating point was adjusted by small changes in voltage and gas flow to obtain stable currents. The glow suggests some visible light emission from the source, which could contaminate signal detection by the detectors during calibration of the source (exactly in a similar fashion as described in Chapter 3 for the solar visible light). Thus, filters are expected to be used.

I was able to confirm the operation of the source at pressures of a few 10^{-4} mbar, voltages between about 1.0 and 1.5 kV, and discharge currents in the range 0.3–0.6 A. A figure representing the characteristic I−V curve in these operating ranges is given in Fig. 5.4. It is noteworthy that immediately after the onset of the discharge, the pressure reading decreases a little, because a fraction of the pressure of the gas becomes "trapped" in the partially-ionized plasma chamber, becoming involved in the electric fields – the Penning Discharge Source almost acts as a Penning Gauge in terms of the underlying physics.

In this pressure range, the found operation follows the technical details of the manual in the given range. The same tests also showed the expected progressive

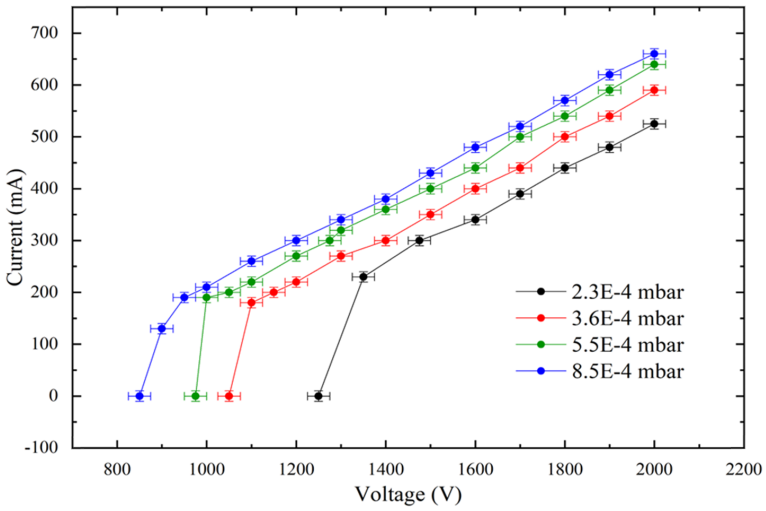

Figure 5.4 PDS source current as a function of voltage. The gas is argon. The pressure was measured before applying the voltage. Each characteristic I-V dataset was measured after the discharge had occurred. The different colored lines show these parameters at different pressures, as shown in the color legend. In particular, from the top to the bottom curve, pressures are (in unit 10^{-4} mbar) 8.5, 5.5, 3.6, and 2.3. Absolute uncertainties are ± 25 V for voltages and ± 10 mA for currents.

erosion of aluminum cathodes at high currents, visible as a recession of the cathode surface after several hours of operation. It is estimated that for a current of 2 A, which is the maximum possible in the setup, refurbishment of cathodes should happen with a frequency of about $1 \div 2$ h. This is quite critical as, if the cathode is worn down, the discharge would directly erode the tantalum shields which connect the cathodes to the cooling circuits: in turn, this might enhance clogging around the magnets and rise of temperatures.

These tests were performed with the PTFE gas-inlet tubes shown in Fig. 5.1, which did not allow for reaching lower pressures. In a later moment, after the change to a fully-compatible Swagelok system for the gas-inlet was made, I tested the base pressure of the source and operating pressure in non-discharge conditions, confirming that the source could operate with an inlet gas pressure of $\sim 1 \times 10^{-5}$ mbar or higher, with the possibility of gradually increasing this value. This will be important, as demonstrated in the next subsection, to increase the signal produced by the PDS at 108 Å.

Conditions to maximize the 108 Å EUV line-emission of Al V

Due to technical difficulties, an intensity calibration was not carried out; it is intended to carry out a calibration of the source in these ranges. Even before the full radiometric calibration, I will, in this subsection, estimate the expected EUV line flux by combining literature measurements with the planned operating range of the XACT PDS, at ever-improving accuracies. However, it is clear that the following figures are but estimates and only encompass the order of magnitude of

the expected emission intensities.

In Heise et al. [129], Table 1 from the paper, an estimation of the radiant intensity emitted by the source is $\Phi_{(1)} \simeq 3\,\mu W/sr$ at the line 104 Å, with Ne gas at pressure 2×10^{-4} mbar and current at 2 A. Figure 4b from the same paper also shows the comparison between 104 Å and 108 Å showcasing a similar order of magnitude between the two lines. It is noteworthy that the conditions are not optimized for the emission of the Al V lines, neither in the gas used nor in the pressure values.

Finley et al. [127] shows that (Figure 5 of the paper) by changing gas from Ne to Ar, the signal can be increased by a factor $3 - 5$ for the Al V line, at similar pressure values. Therefore, a more correct estimate for the radiant intensity of 108 Å line emitted by Al V would be $\Phi_{(2)} \simeq 3\Phi_{(1)} \simeq 10\,\mu W/sr$.

Finally, in the same paper by Finley et al., Figure 9 shows a relevant dependency on the source pressure: as pressure decreases, ionized Al emitted lines become brighter, suggesting a multiplicative factor of about $2 \div 4$ as the pressure halves from a starting value of 2×10^{-4} mbar. Thus at expected operating conditions of Ar gas, 7×10^{-5} mbar pressure, and 2 A current, the intensity should rise at about $\Phi_{(3)} \simeq 3\Phi_{(2)} \simeq 30\,\mu W/sr$.

Using a filter is highly likely required due to the visible emission contamination of the plasma glow. A perfect filter for the scope could be the 70 LPI / 200 nm Zr filter described and characterized in Section 4.4 → p. 84, which transmitted around 40% at 108 Å. Therefore, a better estimate would be $\Phi_{(4)} \simeq 40\% \cdot \Phi_{(3)} \simeq 12\,\mu W/sr$ in a pratical scenario.

A relationship translating (radiant) power intensity Φ and (radiant) photon intensity P at a given wavelength λ of emission is given by Equation (5.2), the left part of the equivalence being a symbolic equation. At the same time, the right term is written in practical units and valid to four significant digits (ph is intended as an adimensional *photon number count* unit).

$$P = \frac{\Phi}{h\nu} = \frac{\Phi \cdot \lambda}{hc} \iff \Phi_{[\mu W]} = 1.989 \times 10^{-10} \cdot \frac{P_{[ph/s]}}{\lambda_{[nm]}} \tag{5.2}$$

Thus, the emission calculated applying the conversion equation Equation (5.2) to the estimate $\Phi_{(4)}$ would yield, in the case of Al V emitted 108 Å line with a Zr-filter effect included.

$$P_{(4)} \simeq \frac{12 \cdot 10.8}{1.989 \times 10^{-10}}\ ph/s/sr = 6.5 \times 10^{11}\ ph/s/sr$$

On this basis, internal simulations of the MUSE test configuration employing a EUV photon collimator, collimating the light emitted from the PDS (the exit flange from the source is 1 cm in exit pupil size), and using realistic factors for the de-magnification and efficiency of the refocusing EUV optics to the detector

– courtesy of Dr. Paul Boerner, although this is quite a raw estimate – suggest that, **the number of 108 Å photons reaching the detector**, per pixel per second, is $\sim$ **46 ph/pixel/s**. The order of magnitude of brightness in the range is deemed optimal for the detection of the EUV source light in the MUSE reading simulation setting, confirming the interesting contribution that the source might bring to the development of MUSE.

Aluminum anodes

A crucial aspect for MUSE-related calibration is the purity and stability of the electrode materials. To maximize line brightness and minimize contamination from unwanted elements, I have helped design and manufacture high-purity Al cathodes (99.999 % purity of Al) sufficient for $\sim$ 50 interchangeable cathode inserts, with invaluable aid from technicians and engineers at INAF-OAPA/XACT.

Pure aluminum is mechanically soft and challenging to machine with tight tolerances, so the production required dedicated tooling and careful quality control of dimensions and surface finish. These anodes, due to the purer Al, are expected to increase further the signal of Al V recombination lines with respect to usual Al alloys which were employed in the past. A visualization of one produced batch of anodes is provided in Fig. 5.5

Figure 5.5 Batch in a tray of machined and cleaned high-purity (99.999%) aluminum anodes produced for the refurbishment and future test activities of the Penning source. In conditions of low Ar pressure ($\sim 7 \times 10^{-5}$ mbar), high current ($1 \div 2$ A), the intensity of recombination lines of Al V near 108 Å produced by the source will be maximized.

5.4 Summary and Outlook

In this chapter, I have summarized the motivation, physical principles, and current status of the Penning Discharge Source at the INAF–OAPA/XACT facility, with emphasis on my initial characterization activities, ongoing optimization, and on its potential role as calibration standard in EUV lines at 108 Å. The main points can be summarized as follows:

- A PDS can provide intense EUV emission lines from a given combination of noble gas, electrode material, along with respective pressures and negatively biased DC high-voltage and breakdown current values.
- The source, under declared experimental parameters, is indeed able to provide emission lines at 108 Å, with recombination lines of Al V. This aspect can be of the utmost interest to MUSE.
- The source has been refurbished and integrated into the XACT EUV beamline, with tests of the source, the cooling circuit, the vacuum levels, and the high-voltage electronic power supply. Initial electrical tests confirm behavior consistent with the literature and the manual of the source.
- Conditions to maximize the 108 Å line intensity have been stated. For this reason, high-purity aluminum rods have been manufactured in order to enhance spectral purity and guarantee many trials of operability for the source without contaminating ions being present (such as Mg in Al alloys).

The work carried out so far has brought the Penning Source to an operational state. Still, a few steps remain before it can be fully exploited as an EUV calibration facility for MUSE and/or future missions.

One of the short-term priorities is to complete the investigation of characteristic I–V curves with varying pressure characterization in the low-pressure regime, mainly to assess the discharge properties and current flow stability of the source in the relevant regime for the 108 Å emission.

A final objective is to obtain an absolute radiometric calibration of the PDS at 108 Å. Considering that the INAF-OAPA/XACT beamline is currently unavailable because of an ongoing refurbishment activity, we are presently investigating the possibility of calibrating the source either at the German national metrology institute PTB/BESSY II [144], in a similar fashion to what was done by Hollandt et al. [136] for a Hollow Cathode Source, or at the Lockheed Martin Advanced Technology Center LMATC.

The long-term role expected, after completing the source calibration in time, is for the source to be available for supporting the MUSE SG instrument calibration procedures throughout 2026. The experience gained in characterizing, operating, and calibrating the source will be, in any case, beneficial to support the development of other future solar physics missions or laboratory EUV spectroscopy

experiments.

6 Conclusion

6.1 Summary of Work

The main objective of my thesis was to contribute to the optical and technological consolidation of the MUSE (Multi-slit Solar Explorer) mission through the study, design, characterization, and scientific analysis of thin-film filters for extreme ultraviolet (EUV) observations, with participation in the experimental characterization of representative filter samples, data analysis, and development of scientific software (expanded in the appendix) supporting the filter design.

From an instrumental perspective, the work focused on the Entrance Filters (EFs) of the spectrograph (SG) and the context imager (CI) telescopes for MUSE, which must meet restrictive requirements for their successful implementation: high transmission in the EUV-wavelength bands of interest to MUSE; high rejection of the UV-VIS-IR solar irradiance impinging on the filters, which can degrade the image quality at the focal plane also in-band due to electron-hole pairs production in the CCDs; minimal or manageable diffraction-induce degradation of the focal plane images, due to the EUV diffraction of the meshes, which has occurred in past missions such as SDO AIA or HMI; and a high mechanical robustness during launch, allowing the filter to resist launch while mantaining the required properties for the scientific goals of the mission. From a data analysis perspective, my work investigated a novel approach to mitigate the impact of multi-slit spectral contamination, with a few promising results.

In Chapter 1, Introduction → p. 1, I presented the astrophysical context of coronal EUV observations, the current state-of-the-art, and the relevant open problems. Then, I introduced the MUSE mission, with its scientific objectives and payload architecture, and introduced how it plans to fulfill some knowledge gaps in current observational coronal astrophysics. Subsequently, I introduced the role of thin-film filters in the mission, which form the technological and scientific backbone for the thesis. I also described the state of the art of space missions outside of those primarily connected to MUSE, and broader applications of the thin film filters in general. Finally, I introduced the recent interest in carbon nanotube (CNT) films as an alternative to traditional polyimide (PI) substrates, particularly due to their potentially higher EUV transmittance and compatibility with coarser and less obstructive structural meshes, which opens up the potential of implementing less-impactful diffractive solutions for EUV space missions.

In Chapter 2, Filter Designs and Diffraction Studies → p. 19, I presented a detailed introduction to the problem of diffraction caused by thin film optical filters in the EUV, with some simple physical-based models to aid their analysis. In addition, I presented the detail of optical designs for the EFs, and also filter wheel filters (FWFs), both for the design based on heritage space missions, and for novel designs

implementing the CNT-based technology – for the CNT-based design, I presented both the Demonstration Model (DMs) and the Structural and Thermal Models (STMs) to showcase the development of the filter designs that occurred during my work. I then evaluated the various filter designs' impact on the MUSE telescope focal plane observations by analyzing the Point Spread Functions (PSF) of an EUV plane wave through the EFs with the use of diffraction simulations. I demonstrated that all of the filters satisfied the 0.5 " angular resolution requirement of MUSE, ensuring that all of the designs and meshes implemented do not degrade the filter performance to a point where the eventual broadening caused by diffraction could hinder the instrumental performances. I have shown that structural thermal models (STMs) based on CNTs can achieve comparable, or even superior, encircled-energy core PSF transmittance at channels 108 Å and 171 Å of the SG, while maintaining similar diffracted intensity outside of the core with respect to heritage-based solution. At 284 Å , the heritage-based design of an Al film supported by a 70 lines-per-inch (LPI) Ni-based mesh (or, in short, Al/70 LPI) solution offers significantly higher core-PSF-transmittance than the CNT-based model, at the cost of brighter and more widely distributed diffraction peaks. I also implemented the realistic values obtained by the characterization that I have performed in the EUV band in Chapter 4, leaving the picture almost unchanged. However, the realistic oxide does degrade the transmittance of the CNT-based solutions a bit more. The simulations have highlighted the diversity of diffraction patterns, which depends on the filter model, materials, and channels, emphasizing that the optimal filter choice depends not only on the throughput but also on how the diffraction might impact the specific scientific objectives and analysis chains.

In Chapter 3, Visible Performance $^{\rightarrow p.53}$, I established a quantitative evaluation of the optical blocking performance requirement for the thin film filters to be used for MUSE. The UV-VIS-IR flat-band and two-band transmittance properties of the CI input filter system, and its requirement by imposing a negligible level of electrons produced at the CCD, were obtained by propagating the standard solar irradiance spectrum through a simplified CI telescope assembly model, also employing realistic values for all of the relevant elements in the payload. A transmittance (T) upper-limit threshold requirement on the order of 10^{-6} per filter over the broadband UV-VIS-IR was obtained. On top of that, I described the experimental setup and measurements performed on Al-coated witness samples of heritage-based filter designs, and on Al-coated witness samples for the CNT-based STM filter designs, while also showcasing some of the older measurements with samples during initial development stages. The measurements showed that the heritage-based samples with Al-coated polyimide (PI), or Al/PI in short, and Al/70 LPI samples exhibited UV-VIS-IR transmittances well below the requirement, and that the latest CNT-based STM witness samples meet such requirement, unlike earlier CNT DM filter samples with Al coating initially developed without optimization of the coating process for the specific CNT substrates. This chapter, therefore, established the readiness of the design choices for candidate flight model filters from an optical blocking perspective, also providing a substantiated

requirement comparison.

In Chapter 4, Extreme-Ultraviolet and X-ray Transmittance →p.71, I studied the performance of witness samples of heritage-based and CNT-based Al/Zr-coated filters in the EUV band and in the soft X-ray range. With experiments carried out at the METROLOGIE beamline of the SOLEIL synchrotron, I measured the absolute EUV transmittance and performed X-ray absorption spectroscopy (XAS) on a set of samples. The XAS data, interpreted using tabulated values of the atomic scattering factors, allowed me to carry out an inner-layer composition and thickness analysis of the substrate, the metal, and the oxide layers compounding the thin-film filters. Values of the different oxidation extents on the native oxide grown on the metal coating with different substrates (PI or CNT pellicles), as well as the presence of iron catalyst contaminant species in the CNT film, were assessed. The resulting EUV transmittance curves were compared to quantify the relative efficiency of the different filter designs at the various channels of the MUSE SG telescope. It was found that CNT-based filters consistently outperform, though not by huge margins in the current configuration, heritage-based filters' samples with PI-substrates in terms of raw EUV transmittance across the entire band, although the mesh-supported Al/70 LPI sample with no substrate was the most transmissive of all the investigated samples in channel 284 Å .

Chapter 5, Setup of a Penning Discharge Source for MUSE calibration →p.92, presented a work-in-progress description of the refurbishment, integration, and initial testing of a Penning Discharge Source (PDS) at the INAF-OAPA/XACT facility aimed to support the calibration of the MUSE SG instrument. I discussed the fundamental physical principles of these sources, and their potential to produce line-rich EUV spectra in the 5–35 nm range, including the 108 Å region, which is of particular interest to MUSE. Via coupling to the XACT beamline, with cooling circuits, a full-steel gas inlet system, a high-vacuum system, and a high-voltage system, I refurbished and confirmed the source's operational state. Furthermore, I identified the parameters required to optimize the potential 108 Å Al V line intensity from the PDS, by carrying out an extensive literature review, and described the remaining steps required to transform the source into a practical calibration tool for MUSE-type instruments, and also presented the manufacture of 99.999% pure Al-cathodes at the INAF-OAPA/XACT laboratory.

Finally, in the appendices, I describe five complementary contributions that support, and reduce the weight of the experimental work in the main text. Appendix A Automated Measurement Workflow →p.110 details the automated measurement workflow developed for carrying out the experiments at the SOLEIL synchrotrons' METROLOGIE beamline: enabling the systematic and reproducible acquisition of large datasets and optimizing available resources and beamtime allocation. Appendix B Proof: Blocking Factor of a 2D Periodic Mesh →p.111 and Appendix C Proof: Fraction of Light Diffracted by a 2D Mesh →p.112 include derivations of relevance to Chapter 2 regarding the blocking factor and fraction of light diffracted by 2D periodic meshes. Appendix D Intermediate Radiometric Quantities →p.115

includes auxiliary quantities for Chapter 3, such as photon rate read per pixel. Appendix E Bi-Gaussian Fitting Software for MUSE →p.117 presents the Bi-Gaussian Fit Analysis (BGFA) software I have initially developed and tested for MUSE spectral data processing. With mock observations based on provided simulations of the solar corona environments, BGFA explicitly models a predicted contamination line as a second Gaussian component whose intensity is limited by Chianti-based emissivity relations and the instrument's effective area: the approach showed minor improvements over established approaches such as the single-gaussian fitting analysis (SGFA), suggesting a way to mitigate the complexity in data analysis induced by the novelty of the multi-slit approach of MUSE.

6.2 Outlooks for Environmental Qualification and Long-term stability

While this work has focused mainly on the optical (out-of-band) and EUV (in-band) transmittance properties of structural and thermal models (STMs) of thin-film EUV filters for MUSE, their suitability for space missions in general also depends on the retention of properties in tandem with resistance to thermal, mechanical, and other sources of stress under realistic LEO environmental conditions (such as contamination, atomic oxygen, and UV irradiation).

Although preliminary tests on demonstration models (DMs) were carried out, the ongoing qualification tests are aimed at investigating their impact on the filter's resistance and long-term service. Thermal cycling and mechanical vibration testing are being conducted by the INAF-OAPA/UNIPA team both in-house and in collaboration with external organizations to evaluate the structural integrity and stability under environmental conditions of launch and orbital operation. UV irradiation and atomic oxygen exposure (either concurrently or separately) test campaigns are also ongoing to investigate potential degradation mechanisms that may impact the optical and in-band properties of the qualification models of filters in Low Earth Orbit (LEO). All of the tests are performed on the Qualification Models (DMs), which are closer in philosophy to the design of the flight models (FMs).

The results of these campaigns are to be published in peer-reviewed journals or communicated at upcoming space optics and missions conferences. Beyond the MUSE mission, these studies will contribute to a better understanding of the long-term usage and environmental stability of advanced EUV filter technologies in their usage in future solar science and astrophysics missions. Furthermore, they will aid in the consolidation and advancement of the novel filter technology based on carbon nanotubes (CNTs) with Al/Zr coatings even more.

6.3 Endnotes

The development of space instrumentation is necessarily a collective and iterative effort, involving the interplay between technology and science in which hardware, modeling, and data analysis are developed together, and need to communicate to deliver the best feasible solution, on time, and within the desired requirements.

This thesis focused mainly on one part of this ecosystem: the thin films found at the entrance of telescopes, along with the analytical, technical tools, and the physics needed to understand their impact on the data. By combining diffraction studies on filter designs, synchrotron characterization of witness samples with EUV and X-ray Absorption Spectrocopy, UV-VIS-IR Transmission Spectroscopy, the development of a laboratory source, and the development of novel and promising data-processing pipelines, I have attempted to bridge the gap between the diverse communities of materials science, X-ray metrology, solar physics, and space mission engineering, with the main aim of enabling and optimizing EUV solar coronal observations with MUSE and/or future similar missions alike.

MUSE will open a new, unexplored window into the observation of the dynamics and energy release at small angular and temporal scales of the solar corona. The filters and methods I studied here are a small but crucial element that will enable these observations, providing a starting point for future missions that will advance high angular-temporal resolution EUV imaging of our Sun. I hope that the results and approaches presented in my work will be useful not only for MUSE but also for the wider community that plans and interprets EUV observations of our star.

Appendixes

Automated Measurement Workflow

Listing A.1 contains the pseudo-code of the automated measurement process. Positions must be defined and confirmed, for references and samples alike, before proceeding. The variable `macro` in the listing codifies the first three rows described in Table 4.2. Energy steps must be chosen carefully to balance experimental campaign duration and acquisition of finely-spaced data.

```
# 1) Relevant input parameters defined and initiation of code
# Holder positions example list (open references and samples treated alike)
positions_map = {
'Sample_1': (0, 0), 'Ref_1': (19, 0), 'Sample_2': (38, 0), ...
}
# Example macro for three regions
macro = {
    'Region1': {'E_Range': (30,  55), 'mono': 1, 'FPB': 'Si', 'angleFPB': 3.5,
     'filter': 'Al Mg Al 0.5', 'diode': 'Al', 'E_Step': 0.1},
    'Region2': {'E_Range': (45,  75), 'mono': 1, 'FPB': 'Si', 'angleFPB': 3.5,
     'filter': 'Al 0.5', 'diode': 'Al', 'E_Step': 0.1},
    'Region3': {'E_Range': (70, 105), 'mono': 1, 'FPB': 'Si', 'angleFPB': 3.5,
     'filter': 'Si 0.5', 'diode': 'Zr', 'E_Step': 0.1},
}
# 2) Iterate over each measurement region defined in the macro
for region in macro:
    # 3) Configure all beamline and detection devices for this region
    #    - Select monochromator/grating, slits, passband filter and angle
    #    - Set detector/photodiode channel
    #    - Wait until every device reports 'ready'; abort on timeout
    configure_devices(region.targets)
    # 4) Loop through holder's positions
    for pos in positions_map:
        move_to_stage(pos)
        # 5) Sweep regions' energy grid (e.g.,\,30-55\,eV in 0.1\,eV steps for
     'Region1')
        for E in energy_grid(region):
            # 5a) Tune monochromator to energy E
            set_energy(E)
            # 5b) Read diode's signal and synchrotron's ring current
            I  = read_diode_signal()
            M  = read_ring_current()
            # 6) Register all relevant data for traceability and save
            log_and_save({
                'region': region.name,
                'position': pos,
                'diode_signal': {'I': I},
                'ring_current': {'M': M},
                'device_states': get_device_states(),
                'timestamp': time_now()
            })
```

Listing A.1 Pseudo-code describing the process detailed in Section 4.2 for the automated measurement workflow

B Proof: Blocking Factor of a 2D Periodic Mesh

In this appendix, the formula detailed in Equation (2.1), i.e. the optical blocking factor of a 2D periodic mesh, is proven with all of its assumptions.

Borrowing terminology from solid state physics [68] [69], the structure described in Fig. 2.1 is a 2D Bravais square lattice whose basis (or, for the ensuing discussion, *basis cell*), is a fictitious square centered at the center of one of the cell squares of the structure and with a side with length p. Translational primitive vectors in this case would be $\mathbf{a_1} = p\,\hat{\mathbf{x}}$, $\mathbf{a_2} = p\,\hat{\mathbf{y}}$ with $\hat{\mathbf{x}}$, $\hat{\mathbf{y}}$ oriented along the perpendicular directions of the mesh bars. The blocking factor of the whole structure, supposedly infinite, is, by symmetry, equal to that of the basis, which is one minus the ratio between the open area of the basis cell (a square with side $\ell = p - w$) and the total area of the basis cell (a square with side p). Therefore, assuming $w < p$:

$$\begin{aligned} \mathrm{BF} &= 1 - \frac{(p-w)^2}{p^2} = \\ &= \left(1 - \frac{p-w}{p}\right)\left(1 + \frac{p-w}{p}\right) = \\ &= \frac{w}{p}\left(1 + \frac{p-w}{p}\right) = \frac{2w}{p}\left(1 - \frac{w}{2p}\right) \quad \square \end{aligned} \tag{B.1}$$

Which is the proof of the formula for the *geometric blocking factor* of the mesh. It can also be extended to honeycomb grids, with the same reasoning as above, but considering side lengths and apothems instead of pitches and widths. The first line of Equation (B.1) is equivalent to:

$$1 - \frac{(p-w)^2}{p^2} = 1 - \frac{\left(\frac{p-w}{2}\right)^2}{\left(\frac{p}{2}\right)^2}$$

And half $p - w = \ell$, or half-side, is none other than the square's apothem. Considering a hexagonal 2D Bravais lattice with a hexagonal basis cell, and considering that: the area of a hexagon with apothem a is $\mathrm{A} = 2\sqrt{3}a^2$; the inner, open-area hexagon would have the apothem $\frac{p-w}{2}$; and the total basis cell hexagon would have the apothem $\frac{p}{2}$. Since the same mathematical passages for the ratio between open area of the basis cell and total area of the basis cell would follow, with the $2\sqrt{3}$ constants simplifying in numerator and denominator of the ratio, this proves that the same BF from Equation (B.1) applies to both square and honeycomb grids, provided that pitch p and width w are known $\square$.

C Proof: Fraction of Light Diffracted by a 2D Mesh

I would like in this appendix to detail the answer the following question regarding the fraction of light diffracted by a 2D periodic mesh. **What fraction of the transmitted light is in the core, and how much is distributed inside the diffraction lobes?** To answer this question, it will be useful to employ Babinet's Principle [65] [63].

> **Note.** This proof is first attributed to Prof. Charles C. Kankelborg, with acknowledgments to Adrian Daw and Leon Golub for helpful discussions, and Jean-Pierre Delaboudinière is credited with bringing this application of Babinet's Principle to the attention. I added to the original proof a few clarifying statements, discussions on constructive and destructive interferences, discussions regarding the presence of a focusing scenario, and figures. This proof arrives at the same conclusion as the original.

Treatments of the diffraction usually employ a Green's function integral approach [145], in which the far field intensity $E_1(\mathbf{r})$, as registered on the screen, can be described as an integral of the incident electric field wave function $E(\mathbf{r})$ over the transparent domain $\mathcal{D}$ of the 2D-mesh ($\mathbf{r}$ is a 2D vector over the screen). To simplify the approach, the electromagnetic wave will be treated as a scalar wave function.

$$E_1(\mathbf{r}) = \iint_{\mathcal{D}} G(\mathbf{r}-\mathbf{r}')\, E(\mathbf{r}')\, d^2\mathbf{r}' \tag{C.1}$$

I now consider the diffracted wave $E_2(\mathbf{r})$ by a *complementary screen*, which is completely blocking over the region $\mathcal{D}$ and completely open on $\mathbb{R}^2\backslash\mathcal{D} = \tilde{\mathcal{D}}$. The appearance of this complementary mesh is laid out in the right of Fig. C.1, next to the normal mesh. Since integrating over the whole plane with no blocking points would leave the incident plane wave undisturbed, the sum of the two cases would just yield the incident plane:

$$E_1(\mathbf{r}) + E_2(\mathbf{r}) = E(\mathbf{r}) \tag{C.2}$$

Which is a statement of the Babinet's Principle. The figures of diffraction in the two distinct cases (encoded in E_1, E_2) are supposed to be different, but since a plane wave brings no lobes, it can be inferred from Equation (C.2) →p.112 that both figures of diffraction share similar lobes and core positions. Let's now divide the statement between the core c and lobes ℓ positions.

$$E_{1\ell}(\mathbf{r}) + E_{2\ell}(\mathbf{r}) = E_\ell(\mathbf{r}) \tag{C.3}$$

$$E_{1c}(\mathbf{r}) + E_{2c}(\mathbf{r}) = E_c(\mathbf{r}) \tag{C.4}$$

Denoting the electromagnetic wave intensities as integrals of $|E(\mathbf{r})|^2$ over regions of interest (say, core or lobe positions), and since the incident wave does not

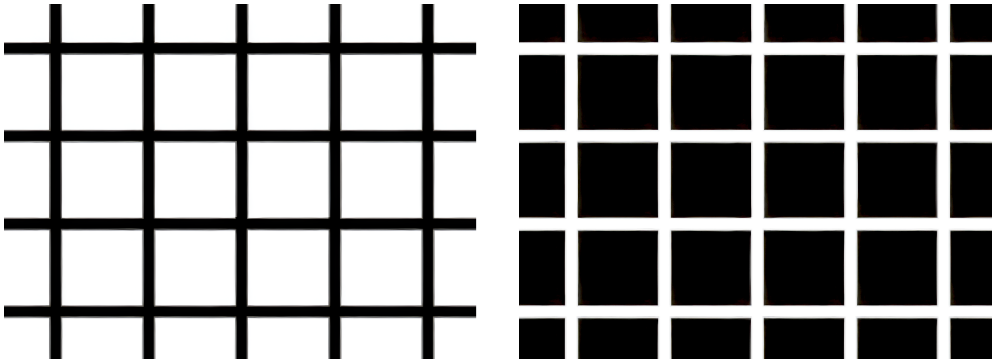

Figure C.1 Example of 2D periodic square mesh structures. Meshes are supposedly *infinite* in extension. The mesh on the left is the same as Fig. 2.1, where points of the mesh that are transmissive to the incident light are white, and points that are completely blocking are in black. The negative of the mesh is given in the right, where the mesh would be completely opaque in the basis cells and would only be transmissive through the open *mesh bars*.

produce diffraction lobes – i.e., $E_\ell = 0 \rightarrow$ – it follows from Equation (C.3) $^{\rightarrow \text{p.112}}$ that $I_{1\ell} = I_{2\ell}$. The latter statement implies that the intensity at the lobes in the two cases is equal, a peculiar consequence of Babinet's Principle. Clarifying further, the incident wave would be imaged to the screen as an ideal Airy disk shape (say, only due to the ideal mirrors) whose behaviour is akin to a Dirac-delta in the angular space carrying unitary power and bearing no secondary lobes of diffraction besides the central zero-order.

It is considered that $I = I_c = 1$ as it refers to the incident plane wave, which would produce no lobes and a core of assumed normalized intensity at the detection screen after the interaction with the optical system, as a consequence of Babinet's Principle. Therefore, Equation (C.4) has two extreme possibilities: either the two incident waves completely interfere constructively (i.e., there are instances where both are positive on average), or they interfere completely destructively (i.e., cases in which it is always true that one is positive, and one is negative). By considering the conservation of energy, that is that the normal mesh transmits M as total intensity, and that the complementary mesh transmits $1 - M$ – implicitly assuming that the wavelength is much smaller than mesh openings, otherwise near field diffraction effects might be relevant – I have the following four equations that are valid in the given assumptions, and four unknowns in ($I_{1\ell}$, I_{1c}, $I_{2\ell}$, I_{2c}). The first equation is the absence of lobes in the free incident wave scenario, the following two equations are energy conservation statements, and the fourth and final equation encodes either purely constructive (+) or destructive (−) interference as obtained

by squaring Equation (C.4).

$$I_{1\ell} = I_{2\ell} \tag{C.5}$$
$$I_{1\ell} + I_{1c} = M \tag{C.6}$$
$$I_{2\ell} + I_{2c} = 1 - M \tag{C.7}$$
$$I_{1c} + I_{2c} \pm 2\sqrt{I_{1c}}\sqrt{I_{2c}} = 1 \tag{C.8}$$

Using Equation (C.5) to eliminate $I_{2\ell}$, and rewriting the last in clearer terms, I get the following set of equations:

$$\begin{aligned} &I_{1\ell} + I_{1c} = M \\ &I_{1\ell} + I_{2c} = 1 - M \\ &\left(\sqrt{I_{1c}} \pm \sqrt{I_{2c}}\right)^2 = 1 \end{aligned}$$

The third equation can be used to eliminate I_{2c} via the following position.

$$I_{2c} = \left(\mp 1 \pm \sqrt{I_{1c}}\right)^2 = 1 + I_{1c} - 2\sqrt{I_{1c}}$$

Substituting this value in the energy conservation equations, obtaining:

$$\begin{aligned} &I_{1\ell} + I_{1c} = M \\ &I_{1\ell} + 1 + I_{1c} - 2\sqrt{I_{1c}} = 1 - M \end{aligned}$$

After a few simple algebraic passages, I finally obtain the result

$$I_{1\ell} = M(1 - M) \tag{C.9}$$
$$I_{1c} = M^2 \quad \square \tag{C.10}$$

Remark 5. This is the desired outcome, which can be expressed as follows. *If M is the transmitted percentage of the incident power through a 2D periodic mesh structure with completely opaque mesh bars, then the diffraction core contains a fraction M of the transmitted intensity, while the lobes contain a fraction $1 - M$.* ⌟

D Intermediate Radiometric Quantities

This appendix gives intermediate details, hypotheses on the derivations and assumptions made in Chapter 3 regarding the illustrative definition of the visible and infrared rejection requirement in the context of the MUSE CI instrument.

Solar spectral irradiance at the detector level

Under the assumptions given in Section 3.2, the spectral power $P(\lambda)$ from the Sun per unit wavelength reaching the CI detector plane, in the *absence* of any filter absorption or of the CCD quantum efficiency, can be written schematically as follows

$$P(\lambda) = I_{\text{eff}}(\lambda)\, A_{\text{geo}}\, R_{\text{mir}}^2\, \frac{\Omega_{\text{CI}}}{\Omega_{\odot}} \quad [\text{W nm}^{-1}]. \tag{D.1}$$

For convenience, all of the results are also written as rates per second. Multiplying by a finite exposure time t_{exp} would thus generalize the results.

Integrating Equation (D.1) up to the silicon band-gap yields the total energy power carried by the photons and reaching the detector (before interaction with filters or CCD), capable of generating electron-hole pairs (whose value is also described):

$$P_{<\lambda_{\text{Si gap}}} = \int_0^{\lambda_{\text{Si gap}}} P(\lambda)\, \mathrm{d}\lambda \simeq 0.415\, \text{J s}^{-1}. \tag{D.2}$$

i.e., about 0.4 J per second would reach the detector in a Si-photosensitive energy range.

Photon and electron rates per pixel

Transitioning from power to photons – photons are indexed as γ subscripts while electron rates with e subscripts – produced at the pixel level, the Planck relation implies the following photon's energy E_γ and wavelength λ:

$$E_\gamma(\lambda) = \frac{hc}{\lambda}\,. \tag{D.3}$$

The corresponding spectral photon rate incident on the detector without filters, $\dot{N}_\gamma(\lambda)$, would be derived from the above equations by dividing the total energy by the single-photon energy as follows:

$$\dot{N}_\gamma(\lambda) = \frac{P(\lambda)}{E_\gamma(\lambda)} = \frac{\lambda}{hc}\, P(\lambda) \quad [\text{s}^{-1}\,\text{nm}^{-1}]. \tag{D.4}$$

And assuming that the out-of-band radiation is spatially uniform over the CI FOV, with each pixel receiving an equal share of energy, the **spectral photon rate per pixel** before interacting with filters, $\dot{N}_{\gamma,\text{pix}}(\lambda)$, would be the following.

$$\dot{N}_{\gamma,\mathrm{pix}}(\lambda) = \frac{\dot{N}_{\gamma}(\lambda)}{N_{\mathrm{pix}}} = \frac{\lambda}{hc}\,\frac{P(\lambda)}{N_{\mathrm{pix}}} \quad [\mathrm{s}^{-1}\,\mathrm{nm}^{-1}]. \tag{D.5}$$

To obtain from the photon rate, the electron rate, it is needed to multiply the former by the quantum efficiency of the detector, obtaining the equation Equation (3.7) → p. 57 stated in the main text.

E Bi-Gaussian Fitting Software for MUSE

E.1 Motivation and Scientific Context

The Multi-slit Solar Explorer (MUSE) spectrograph (SG) is designed to observe the solar corona in three narrow bands of the extreme ultraviolet (EUV) spectrum, centered on the Fe XIX lines at 108 Å, the Fe IX line at 171 Å, and the Fe XV line at 284 Å. Within each band, MUSE simultaneously acquires spectra from 35 parallel slits, projected onto a common detector. This multi-slit detection is essential to achieve the required frame rate and spatial coverage for achieving novel observations in the solar physics panorama, enabling breakthroughs in observations, analysis, and modeling, but it also introduces a new category of systematic effects: spectral contamination between slits and between lines, which will be discussed hereinafter.

Because the gratings operate in the first and second orders, spectral features from different slits can overlap within the same spectral window. The contaminant configurations are predicted by instrumental models and line lists, as explicitly shown in De Pontieu et al. (2020) [17]. The relative intensities of these contaminants depend on the temperature and density structure of the emitting plasma, as well as the effective area of MUSE, which varies with wavelength.

An approach involving a *Single Gaussian Fitting Analysis* – which will be dubbed SGFA in all of the ensuing treatment – is usually used to extract line profile properties (integrated intensity, Doppler shift, and non-thermal linewidth) by fitting a single Gaussian to each spectral line at each slit, at each spatial location, and for each exposure, as stated in the same paper introducing the multi-slit principle of MUSE, i.e., De Pontieu et al. (2020) [17], which also implemented the single Gaussian approach/technique. The SGFA approach works very well in the absence of intense contamination by different slits. Still, in cases of strong line mixing, it can produce distorted line profile properties, and in some cases, make it hard to retrieve the plasma properties of velocity – e.g., Doppler shift – correctly, and line broadening with single Gaussian fits, introducing an amount of *outliers* in the results. The concept of outlier will be defined more rigorously in the following sections.

A complementary approach is also being developed, called the Spectral Disambiguation Code (SDC), based on the multi-component decomposition strategy described by Cheung et al. [146] while also being described in De Pontieu et al. (2020) [17]. The SDC approach is a much more advanced fitting strategy that usually benefits from improved initial conditions (provided, for example, by an SGFA analysis), and which internally takes care of contaminating components –

thus, it is a great way of taking care of subtracting contaminants. A potential weak point of SDC is the variance of this strategy with respect to the dynamic range observed in the sun, particularly in the case of low counts, other than the dependence on the final result on the initial conditions used for the minimization procedure described in the papers.

In this context, to both potentially improve the existing SGFA strategy, while also potentially aiding the SDC strategy with better seeds/initial conditions, I developed an alternative strategy in collaboration with Lockheed Martin Solar and Astrophysics Laboratory (LMSAL), the Harvard-Smithsonian Center for Astrophysics (CfA), and UNIPA: the *Bi-Gaussian Fitting Analysis*, or BGFA, strategy. The basic idea is to model one contaminant explicitly – theoretically the most commonly intense one in average scenarios – as a second Gaussian component whose properties are predicted, rather than left free, using atomic physics and instrumental modeling. I drafted a strategy involving the BGFA concept, an algorithm, and a template using it. Then, I tested it on realistic MHD simulations provided by the science teams of LMSAL/CfA, representing quiet sun (QS), active region (AR), and flaring events, to assess the performance of BGFA in possibly reducing the amount of outliers found by the algorithm. A software simulating pipeline that provided the *mock*-observations of the MUSE SG telescope of such simulations was employed, and a full comparison between the true properties of the plasma and those retrieved by a fitting algorithm was assessed.

This chapter aims to introduce the physical assumptions of the strategy, its numerical implementation, and the performance of the BGFA software in some cases. I will also address some of the weak points of the strategy and describe how it can be a foundation of a more comprehensive approach to be considered in the future for MUSE's data analysis and processing pipeline.

> **Note.** While the detailed strategy is valid in a general multi-slit context where contamination is expected, exact instrumental values are needed for the correct bi-Gaussian application to MUSE. The values employed here are indicative of the particular state MUSE's data processing pipeline, and instrumentation was at during my studies in 2023/2024. Therefore, the treatment might not be applicable *as is* to the current state of development of MUSE, and should be seen as a software development example, with a set of explanations that could allow repeatability and/or aid future developments of a similar kind.

E.2 On the Development of the Bi-Gaussian Approach

Preliminary Definitions

I will start with some definitions that will be used throughout the treatment.

A *line* or *main-line*, $\ell_{\rm m}$, indicates the line that MUSE actively seeks as a main line to predict plasma properties by probing a narrow band. It could be literal (Fe XIX, Fe IX, or Fe XV) or numerical (108 Å , 171 Å or 284 Å).

The numerical value $i \in \mathbb{N}$ indexes the *slit of analysis* number in which a main line is probed, and $1 \leq i \leq N$ is valid, where $N = 35$ is the total number of slits. In older studies, there were $N = 37$ slits, as this is a value that changed throughout MUSE's development and payload components design.

A given slit i, from a spectral point of view, covers the whole $x-$axis range of the MUSE SG FOV. Every point or *pixel* x in the FOV is associated, via the response $R_\ell(i, x) = \lambda_i(x)$, to a wavelength of the point in the slit i observation. Physically speaking, this corresponds to the expected wavelength observed at this point due to the dispersion of the reflective grating through the multi-slit. The main line emission is expected to occur only in a very narrow angular region in x for each slit i.

In the y-axis, the slit i extends freely, and emissions are, to the extent of the ensuing analyses, independent at different y-pixels. Unless directly specified, a $\bar{y}$ value is deemed fixed for these discussions.

A *contaminant*, or *contaminating line*, $\ell_{\rm c}$, is an emission line that appears in the spectral window of the main-line position at slit i due to the multi-slit geometry and dispersion, but is originated from the observation of plasma at a different slit (the *contaminating slit*, or *slit of the contaminant*, $i' = i + n(\ell_{\rm c})$, $n(\ell_{\rm c}) \in \mathbb{Z}$). There is a limited pool of potential contaminants for a given main line.

Wavelength of a main line will be described as $\lambda(\ell_{\rm m})$, that of a contaminating line, $\lambda(\ell_{\rm c})$.

The *Doppler shift* at a point (i, x) of the main line wavelength is defined, thus, as $S_{\ell_{\rm m}}(i, x) = [\lambda_i(x) - \lambda(\ell_{\rm m})]/\lambda(\ell_{\rm m}) \equiv z_{i,\ell_{\rm m}}(x)$.

The main-line *Doppler velocity* would then be defined as $v_{i,\ell_{\rm m}}(x) = c \cdot S_{\ell_{\rm m}}(i, x)$, with c speed of light. $v_{i,\ell_{\rm m}} < 0$ would imply a blue shift with plasma flowing towards the observer, while $v_{i,\ell_{\rm m}} > 0$ would be a redshift, and plasma flowing opposite to the observer.

A slit i is *uncontaminated* by $\ell_{\rm c}$ if there is no contaminating slit possible for the contaminating line. Logically, this happens when $0 \leq i + n(\ell_{\rm c}) \leq N$ is false, equivalent to stating that the contaminating slit is nowhere to be found.

In a given slit i, a window of points around the main-line position is given by $[x_k]$, or $x_{[k]}$, which defines a finite list of x pixel points. This is used to define an effective spectrum for the Gaussian fits. Via the following transformations:

$$x_{[k]} \rightarrow \lambda_{[k]} = R_\ell(i, x_{[k]}) \rightarrow v_{[k]} = c \cdot S_{\ell_{\rm m}}(i, x_{[k]}) \tag{E.1}$$

one can map a set of x-pixels in the angular FOV line to a spectral axis (λ) or to a velocity Doppler-axis (v). Since the descriptions are mutually equivalent, the

latter is commonly used as fitting Gaussian peaks in the plane of flux observed as a function of pixel's doppler shift – i.e., line spectrum as a function of velocity – is a very practical way of obtaining, directly, the mean doppler shift and line broadening of a given observed line. The flux velocity distribution will also be discussed as *velocity space*, where the other domains will be discussed as *pixel space*, *angular space*, or *wavelength space*. The index $k \in \mathbb{Z}$ runs from $-$npix to $+$npix and denotes the number of pixels around the local maximum of the flux that the analysis, or fits, are restricted to. The total number of pixels used for one fit analysis is $2 \cdot \text{npix} + 1$.

The term *moment* can be used to address line intensity, line Doppler shift, and line broadening as respectively the 0^{th}, 1^{st}, and 2^{nd} moment of a given line spectrum velocity distribution [20], keeping in mind that when single or bi-Gaussian fitting analyses are considered, only the moments of the Gaussian profiles are intended. This will also be addressed in a following paragraph. In the case of a true observed (i.e., simulated) emission line in the velocity space — for which the symbol $\Phi(v_{[k]}, i)$ will be used in slit i – the second moment of line broadening might contain both elements of thermal broadening σ_T, which is encoded in the Gaussian profile, as well as non-thermal broadening, $\sigma_{\neg T}$, which might be caused from relevant multi-component flows in the analyzed cell plasma. In general, a Gaussian profile is not enough to account for non-thermal broadening effects, and the study of physical explanations and analysis of non-thermal broadening is state-of-the-art current research in EUV solar astrophysics [147] [20].

The *emission measure* (EM) of a volume element dV of plasma being observed is defined as $N_e^2 dV = d(EM)$, proportional to the number of free electrons in the volume $N_e dV$ and to the electron density in the volume, N_e, which strictly depends on the physical conditions of the emitting plasma. [148] The total emission measure EM of the plasma in a given finite volume V of plasma is given by the following formula (units will be c.g.s. for this section):

$$EM = \int_V N_e^2 dV \quad [\text{cm}^{-3}] \tag{E.2}$$

The flux $F_{j \to i}$ observed at distance d for an optically thin plasma (which is assumed to be the case in EUV astrophysics of the solar corona), line emission due to a transition $j \to i$ is modeled as follows:

$$F_{j \to i} = \frac{1}{4\pi d^2} \int_V G_{j \to i}(T, N_e)\, N_e^2 \, \mathrm{d}V, \quad [\text{erg cm}^{-2}\,\text{s}^{-1}] \tag{E.3}$$

Where $G_{j \to i}(T, N_e)$ is defined as the *contribution function*, including all of the atomic physics involved in the line formation process, and also being a function of the element abundances used. This equation also shows that the higher the emission measure, the higher the flux emission.

An alternate definition to the former EM per unit area δS of emitting plasma is the *column* emission measure, defined as follows, with the idea being that the

volume $V = \delta S \cdot h$ is the volume of plasma observed with depth h along the line of sight (LOS) in the solar atmosphere.

$$EM_h = \int_{\mathrm{LOS}} N_e^2 dh \quad [\mathrm{cm}^{-5}] \tag{E.4}$$

The aforementioned flux equation can also be normalized per unit surface of the emitting plasma, without loss of generality. Thus, the column emission measure is an equivalent model of the plasma, to the extent of the emission line forecasting.

In case a distribution of plasma as a function of temperature is considered, i.e., with the line of sight containing multiple temperature components, the emission measure can be written as an integral of the differential emission measure (DEM) over the temperature range of relevance, i.e., the following description [31].

$$EM_h = \int DEM_h(T) dT \iff DEM_h(T) = N_e^2 \frac{dh}{dT} \quad [\mathrm{cm}^{-5}\,\mathrm{K}^{-1}] \tag{E.5}$$

Depending on context, the subscript h of the quantities will be dropped in the following treatment. To discriminate between total and column (differential) emission measure, the unit of measurement suffices (as one is the other per unit surface of the emitting plasma observed along the line of sight). Routines available in CHIANTI [149] [150], either with their IDL or Python implementation, can allow for the synthesis of line-emissions with their flux as in Equation (E.3) from given DEM, abundance, and electron density prescriptions.

The fact that a higher DEM provides a higher line emission can be written as follows in general terms.

$$F_{j\to i} \propto \int G_{j\to i}(T, N_e)\, DEM(T)\, \mathrm{d}T. \tag{E.6}$$

The effective photon flux recorded by MUSE for a line ℓ at wavelength $\lambda(\ell)$ is modulated by the SG telescope effective area $A_{\mathrm{eff}}(\lambda)$, which includes effects from mirrors, gratings, and filters:

$$I_\ell^{(\mathrm{det})} \propto A_{\mathrm{eff}}[\lambda(\ell)] \int G_\ell(T, N_e)\, DEM(T)\, \mathrm{d}T, \tag{E.7}$$

If the DEM distribution is not only provided as a function of temperature, but as a distribution depending on the plasma's temperature T and velocity $\mathbf{v}$ (i.e. doppler velocity towards the observer, v_{Dopp}, and in the FOV directions in the observed surface, v_x, v_y), it is intended as a Velocity-Differential Emission Measure (VDEM) cube (De Pontieu et al. (2020) [17]). A simulation, ready to be observed by a given mock-up simulation of the SG telescope instrumental response, is to be provided as a set of VDEM cubes over a given solar FOV, in similar ways to what is described in De Pontieu et al. (2022), [18], and Cozzo et al. [20] – this is considered a kind of *forward-modeling*. If MUSE's FOV requires several rasters to reproduce the simulation's FOV, a series of `steps` is required: these *simulate* the rastering procedure of MUSE's SG detection over the solar surface. No time dependence of the simulation is assumed in this treatment (the simulation being *frozen in time*).

Relevant contaminating lines

The starting point for the BGFA analysis is the identification of contaminating lines of profiles for each main line of interest to MUSE. I will list the main ones, drafting from De Pontieu et al. (2020) [17], though I confirmed the values via the CHIANTI database [149] [150]. Fig. E.1 showcases the main contaminants as compared to main line emissions, modelled with realistic CHIANTI DEMs of AR, QS, and Flare scenarios. The contaminant lines' peaks have an intensity usually $\lesssim 5\%$ that of the main line, thus they are usually of negligible nature even in the case of fitting a main line with a single Gaussian.

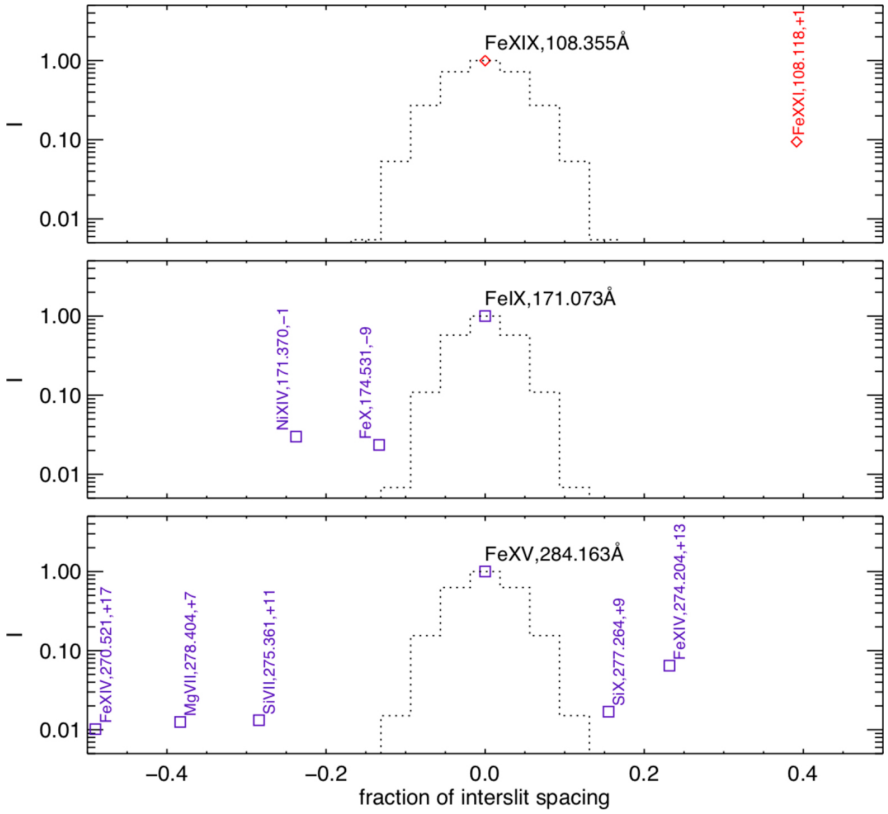

Figure E.1 Plot of line-intensities of various emitting ions at various DEM prescriptions, convoluted with realistic MUSE effective area at the various wavelengths of emission. The horizontal axis shows the wavelength offset from the main-line rest wavelength, expressed in units of the inter-slit spectral spacing. The vertical axis shows the relative strength of each line with respect to the main line, assuming CHIANTI DEMs for Flare in 108 Å channel, AR in 171 Å channel, and QS in 284 Å channel. Secondary lines are labeled with the ion and with the slit offset (for example, "Fe XIV 274.20 +13" in the bottom panel marks the ion, wavelength, and location where the line from slit $i+13$ falls in the main-line slit i reference frame. The dotted curves show the thermally and instrumentally broadened profiles of the main lines (usual line profiles contain no more than 5 to 10 points). Credit: Fig. 4 from De Pontieu et al (2020). [17]. License: CC BY 3.0.

I will list all of the relevant lines and contaminants for MUSE. For the 108 Å channel, the main-line is Fe XIX at 108.35 Å with its main contaminant Fe XXI at 108.12 Å,

caused by slit $i + 1$. In the work detailed here, I will not cover these lines.

For the 171 Å channel, the main line is Fe IX at 171.07 Å, while the related most important contaminants are the following two:

- Fe X at 174.53 Å in slit $i - 9$
- Ni XIV at 171.37 Å in slit $i - 1$

Both contaminants can appear at the same time. The dependence of the intensities of these contaminants with respect to the emitting plasma temperature will be discussed in a later setting. With regards to my work, only a single contaminating component was analyzed at a time, hence the Bi-Gaussian name – main-line and contaminating Gaussians being used.

In the 284 Å channel, the Fe XVline at 284.16 Åcan be contaminated by several lines, including:

- Si X at 277.26 Å in slit $i + 9$
- Fe XIV 274 at 274.20 Å in slit $i + 13$
- Fe XIV 270 at 270.52 Å in slit $i + 17$
- Si VII at 275.36 Å in slit $i + 11$
- Mg VII at 274.40 Å in slit $i + 7$

Bi-Gaussian Fitting Analysis (BGFA) algorithm

Philosophy and design choices

The Bi-Gaussian Fitting Analysis strategy, thus, extends SGFA analysis by explicitly modeling a contaminant line as a second Gaussian component whose properties are not entirely free, but constrained by the assumption of plasma self-interaction and the Chianti factor $R_{\mathrm{c|m}}$. The scientific interest is primarily in the main-line moments, while the contaminant component is used as a physically constrained *nuisance* term to be removed from the fit. In the future, there might be scientific interest in the investigation of these contaminants. However, the primary objective of MUSE – and the lines it is optimized to observe – are the main lines in the SG channels.

The key design elements for the BGFA algorithm are:

- To identify, for each principal line and slit, whether a single dominant contaminant is expected and from which slit it originates;
- use the single Gaussian fitting procedure for the principal line in the contaminant slit, also meaning that, depending on the sign of $n(\ell_{\mathrm{c}})$, if the contaminating slit precedes the main slit ($n(\ell_{\mathrm{c}}) < 0$) the SGFA needs to proceed with increasing i values starting from the uncontaminated slits. In

contrast, if $n(\ell_c) > 0$, the SGFA is required to proceed from the max slit $i = N$ with decreasing steps.

– once a contaminated slit i is reached, the contaminant intensity from the principal line intensity in the contaminant gap is evaluated using relative intensity ratio values $R_{c|m}$ depending on the kind of DEM/region, and evaluated with CHIANTI, and making some assumptions of the plasma emitting the contaminating Gaussian;

– fit a large-scale Gaussian model in which the principal component is free, and these prior variables constrain the contaminant component via some described *wiggle*.

I will detail all of the parts of the BGFA algorithm now.

The same plasma hypothesis

A hypothesis I assumed during the development of the BGFA is that of *identical plasma*: it is assumed that the plasma emitting the main line in the contaminating slit is the same as that emitting the contaminating line in the target slit. In other words, if slit i' contaminates slit i for a given pair of lines, both the emissivity of the main line in slit i' and that of the contaminating line in slit i are determined by the same local plasma thermodynamic state (temperature, density, and elemental abundances). Utilizing this assumption, it is possible, via CHIANTI and emission line intensity predictions, to relate the intensities of the two lines.

Under this assumption of homogeneous physical properties of the plasma, I can express the intensity of the contaminant I_c as a multiple of the intensity of the main line I_m in the contaminant slit:

$$I_c \simeq R_{c|m}\, I_m \tag{E.8}$$

where $R_{c|m}$ is an intensity ratio that depends on the values employed for this calculation, i.e., on the DEM chosen, the electron density in the plasma N_e employed, the contribution functions of the two lines, and the wavelength-dependent effective MUSE area. I call these factors the *contaminating line intensity ratios*. Practically speaking, the ratio between a contaminant line ℓ_c and a main line ℓ_m, both intensities being integrated, is therefore calculated as:

$$R_{c|m} \equiv \frac{I_c^{(\mathrm{det})}}{I_m^{(\mathrm{det})}} = \frac{A_{\mathrm{eff}}\Big[\lambda(\ell_c)\Big] \int G_{\ell_c}(T, N_e)\, DEM(T)\, \mathrm{d}T}{A_{\mathrm{eff}}\Big[\lambda(\ell_m)\Big] \int G_{\ell_m}(T, N_e)\, DEM(T)\, \mathrm{d}T}\,. \tag{E.9}$$

CHIANTI allows for estimating these ratios [149] [150], along with some post-processing to take into account MUSE's effective area. I evaluated these ratios for all contaminants for MUSE at various stages of development of the payload, and confirmed that their value was within $5 \div 10\%$ to those used by De Pontieu et

al. (2020) displayed visually in Fig. E.1: small differences to be related to small tweaks in the N_e or DEMs used to generate the line intensities, and/or to the different MUSE effective area – a common circumstance for a mission developing towards launch, also considering that these studies preceded CDR.

The naive exploration and intensity wiggle bounds

The ratios $R_{\mathrm{c|m}}$ are, by construction, *fixed*, being dependent on the assumed DEM, abundances, and density. To estimate how robust these ratios, in this particular case for the most intense ones of Fe X andFe XIV 274 , are under realistic variations of the plasma properties, a naive exploration was carried out, detailed here.

For each relevant pair of lines $(\ell_{\mathrm{m}}, \ell_{\mathrm{c}})$, the ratio $R_{\mathrm{c|m}}(T)$ was computed for isothermal DEMs (i.e. delta-function DEMs at each T), spanning the temperature domain where both of the main and contaminating line contribution functions are non-negligible and overlapping. The ranges were: for the pairs (Fe IX, Fe X) in channel 171 Å , $\log(T\ [\mathrm{K}]) \in (5.95, 6.05)$, while for the pairs (Fe XV, Fe XIV 274) in channel 284 Å , $\log(T\ [\mathrm{K}]) \in (6.25, 6.40)$. The central intensity was taken as the average value, and the *wiggliness* allowed was studied as the maximum possible relative deviation from the central value in the studied range.

For both of the iron lines pairs, the resulting $R_{\mathrm{c|m}}(T)$ varied by at most a factor of $w_r \simeq 2$ over the temperature range of interest. w_r is defined as *wiggle room*.

As a result of this exploration, the contaminant intensity in the ensuing fits for the BGFA is allowed to vary, from the given initial condition $I_{\mathrm{c}} = R_{\mathrm{c|m}}\, I_{\mathrm{m}}$, within an interval defined by the factor w_r,

$$\frac{1}{w_r}\, R_{\mathrm{c|m}}\, I_{\mathrm{m}} \;\leq\; I_{\mathrm{c}} \;\leq\; w_r\, R_{\mathrm{c|m}}\, I_{\mathrm{m}}, \tag{E.10}$$

This $w_r = 2$ factor, i.e., the wiggle room allowed for the intensity of the contaminant, is intended to overcome the limitation of the *same plasma* hypothesis that, by assuming also a *same temperature* feature, does not consider the possibility of plasmas at different temperatures emitting these lines from the originating contaminating line. This value is quite crucial for the success/failures of the BGFA procedure. While I assumed it to be constant throughout the whole fitting process, future studies could aim at optimizing its value, and/or decide a dynamic evaluation of it depending on the observations from the contaminating slits, either in a systematic approach, or with tentative machine learning approaches.

A special mention is the contaminant Ni XIV, which is also quite important, but cannot be predicted with the 171 Å main-line: its central energy for the contribution function is closer to that of Fe XV, than to that of Fe IX: therefore, a future idea for a bi-(multi-)Gaussian approach is to predict this contaminant in the 171 Å channel using the main-line prediction of the main-line from 284 Å .

Gaussian modeling of spectral lines: from SGFA to BGFA

In both SGFA and BGFA, each spectral line profile is described, locally in wavelength or velocity space, by Gaussian components. In this subsection, I introduce the models that are employed in the two approaches.

Assuming fixed slit i, y-pixel $\bar{y}$, step value, and window of points $v_{([k],i)}$ in slit i's velocity space constrained by a constant dubbed npix limiting the usable points for fitting, a single Gaussian component, appropriate for SGFA, and also for BGFA in the uncontaminated case, is written as follows (only explicit dependence on velocity points and slit is given):

$$I_{\mathrm{SGFA}}(v_{[k]}, i) = I_{(\mathrm{m},i)} \exp\left[- \frac{(v_{([k],i)} - v_{(\mathrm{m},i)})^2}{2\sigma^2_{(\mathrm{m},i)}} \right], \tag{E.11}$$

where $I_{\mathrm{m},i}$ is the main-line peak intensity at slit i, $v_{\mathrm{m},i}$ the centroid velocity of the main-line at the same slit, and $\sigma_{\mathrm{m},i}$ the Gaussian dispersion in $\mathrm{km\,s^{-1}}$. The Gaussian line moments are:

$$I_{\mathrm{int}(m,i)} = \int_{-\infty}^{+\infty} I_{\mathrm{SG}}(v, i)\, \mathrm{d}v \simeq \sqrt{2\pi}\, I_{\mathrm{m},i}\, \sigma_{\mathrm{m},i}, \tag{E.12}$$

for the 0^{th} moment, while $v_{\mathrm{m},i}$, and $\sigma_{\mathrm{m},i}$, respectively for the 1^{st} , and 2^{nd} moment of the Gaussian.

This explains why the former values are considered as Gaussian *moments*. It should be noted that the readily accessible figure in both the mock-observation is the practical summed line intensity, i.e. $I_{\mathrm{sum}} = \sum_{v_{[k]}} \Phi(v_{[k]}, i)$, to be confronted with the model $I_{\mathrm{mod}} = \sum_{v_{[k]}} I_{\mathrm{SG}}(v_{[k]}, i)$. These sums are not related to the integral of the Gaussian I_{int}. Practically speaking, increasing npix too much could allow more contaminants to be present in the fitted velocity space, with the consequence that one has to optimize the procedure also with respect to this parameter.

In the presence of a contaminant with a partially overlapping profile, a bi-Gaussian model is adopted in BGFA:

$$I_{\mathrm{BGFA}}(v_{([k],i)}) = I_{(\mathrm{m},i)} \exp\left[- \frac{(v_{([k],i)} - v_{(\mathrm{m,i})})^2}{2\sigma^2_{(\mathrm{m,i})}} \right] + I_{(\mathrm{c},i)} \exp\left[- \frac{(v_{([k],i)} - v_{(\mathrm{c,i})})^2}{2\sigma^2_{(\mathrm{c,i})}} \right], \tag{E.13}$$

where the (m) and (c) subscripts refer to the main line and contaminant, respectively, while subscript i refers to the slit being investigated by the model.

Chosen Initial and Boundary Conditions of BGFA

In this section, I describe the initialization of initial conditions and boundary conditions on the parameters of the bi-Gaussian model, also in light of the same-plasma hypothesis.

Assuming given main line ℓ_{m}, contaminant ℓ_{c}, contaminating slit index $i' = i + n(\ell_{\mathrm{c}})$, with $n(\ell_{\mathrm{c}})$ defined in Appendix E.2, the same-plasma hypothesis translates in

how the best-fit, single-Gaussian parameters of ℓ_{m} in slit i' provide the initial the following initial conditions on the parameters defining the contaminating Gaussian in slit i:

$$v_{(\mathrm{c},i)} = v_{(\mathrm{m},i')}, \tag{E.14}$$

$$\sigma_{(\mathrm{c},i)} = \sigma_{(\mathrm{m},i')}, \tag{E.15}$$

$$I_{(\mathrm{c},i)} \simeq R_{\mathrm{c|m}}\, I_{(\mathrm{m},i')}, \tag{E.16}$$

where $(v_{(\mathrm{m},i')}, \sigma_{(\mathrm{m},i')}, I_{(\mathrm{m},i')})$ are the main-line moments returned by SGFA in slit i', and $I_{\mathrm{c},i}$ is the predicted contaminant intensity predicted via the aforementioned procedure.

An explanation of the equations follows. The Doppler shift is the same because it is related to the flow of the plasma towards the observer: if the same plasma emits the line, it should be equal. The Gaussian line broadening σ_T is related to the mean-square velocity of the particles emitting the line, following Boltzmann-based statistics,

$$\sigma_T = \sqrt{\frac{2k_bT}{m_{\mathrm{Fe}}}} \tag{E.17}$$

The ion's mass is always iron, while the temperature of the emitting plasma in the same-plasma hypothesis is also the same, therefore explaining the equating of the line broadening. Regarding the intensity evaluation, the equal sign also comes from evaluating the ratio of the intensities from those predicted via CHIANTI. Furthermore, the line intensity integrated in the velocity space of the main line in the contaminating slit is proportional to the product of both the line peak and the broadening, $I_{(\mathrm{m},i')}\sigma_{(\mathrm{m},i')}$, as described in Equation (E.12), thus, since the broadening is kept the same between this and the contaminating Gaussian, this ratio in the simplistic hypotheses adopted does not depend on the broadening, as these cancel out.

With regards to the initialization of the main-line principal Gaussian, the peak and centroid Doppler shift are initialized using as initial conditions the local maximum of $\Phi(v_{[k]}, i)$ within a specified v_{range}. At the same time, the line broadening was set at an initial value of $\simeq 10\,\mathrm{km\,s^{-1}}$.

For the boundary conditions on the parameters of the Bi-Gaussian model in Equation (E.13):

- The main-line intensity $I_{(\mathrm{m},i)}$ was allowed to vary within a range of $(0, 1.1 \cdot I_{(\mathrm{m},i)-\mathrm{init}})$,
- The contaminating line intensity $I_{(\mathrm{c},i)}$ could vary within $(I_{(\mathrm{c},i)-\mathrm{init}}/w_r, I_{(\mathrm{c},i)-\mathrm{init}} \cdot w_r)$, following the aforementioned wiggle room treatment.
- The main-line broadening $\sigma_{(\mathrm{c},i)}$ was allowed to vary in a conservative range of velocities of $(0, 200)\,\mathrm{km\,s^{-1}}$, allowing for very broad and very thin peaks to be probed on average.

– The boundaries adopted for the Doppler velocity of the contaminating Gaussian, $v_{(\mathrm{c},i)}$, are retrieved from the simulations' VDEM cubes in a way similar to the DEM-weighted average temperature calculation in Cheng et al. [151]. In particular, I calculated the maximum VDEM-weighted average of Doppler velocity differences between two log(T) values $(\log T_1, \log T_2)$ among all given slits i, steps step, and y-coordinates, in the simulations. The log(T) values employed are the same of Appendix E.2, and I found values for a 3σ wiggle of $\sim 15\,\mathrm{km\,s^{-1}}$: the boundary conditions on the lower and higher bounds of the contaminant mean velocity parameter was then coded to $\pm 15\,\mathrm{km\,s^{-1}}$. Due to convergence issues, in most cases the $v_{(\mathrm{c},i)}$ was used as a fixed parameter.

– For the boundary conditions on the line broadening, I could not find a proper way on the whole moments space (i.e., covering all of the pixels, steps, slits) to make the BGFA converge properly if the contaminating-slit line broadening was let *free*: as a consequence, I fixed it to the initial condition value, i.e. equal to the main-line of the contaminating slit's broadening.

The fact that two of these parameters were fixed, and only the intensity of the contaminant was evaluated via a fitting procedure, is indeed a weak point of the software approach. Moreover, fixing the line-broadening also hid another relevant aspect: a high relative difference between the contaminating Gaussian's broadening $\sigma_{(\mathrm{c,i})}$ and the main-line broadening from the contaminating slit $\sigma_{(\mathrm{m,i'})}$ could influence also the intensity of the contaminating Gaussian, as should follow interpreting the consequences of Equation (E.12). If all of the free parameters of the bi-Gaussian model were employed (i.e., six parameters), one should have used at least 7 pixel points (or more, for example, $\gtrsim 11$) to ensure a meaningful fitting procedure, though opening a very large fitting window could open up to more contamination near the main-line. I am sure it could be possible to circumvent this limitation by finding a better approach in general; however, for the ensuing analyses, the approach was limited only to the specified four free parameters. I will now proceed to describe the algorithmic workflow.

Algorithmic flow and hybrid procedure

I now proceed to summarize all of the above information in a sound description of the procedure employed to implement the BGFA algorithm for practical studies and scenarios. The BGFA workflow is as follows, starting from a fresh simulation.

(1) For each main line, and each slit i:

(a) If slit i is uncontaminated, i.e., if $\neg[0 \leq i + n(\ell_\mathrm{c}) \leq N]$, then perform SGFA fit (single Gaussian) with the chosen $(\mathrm{npix}, v_\mathrm{range})$ among the flux in velocity space $\Phi(v_{[k]}, i)$.

(b) If slit i is contaminated, i.e., if $0 \leq i + n(\ell_\mathrm{c}) \leq N$:

(i) Retrieve the SGFA results for the main line in slit $i' = i + n(\ell_\mathrm{c})$.

(ii) Use these to initialize and constrain the contaminant Gaussian in slit i, as in Appendix E.2

(iii) Fit a bi-Gaussian model (Equation (E.13)) of the flux $\Phi(v_{[k]}, i)$ in velocity space

(2) For each fit in each slit i, check convergence with basic fit criteria (i.e., no NaN resulting in the fit). If the bi-Gaussian fit in a contaminated slit i fails with no convergence, perform SGFA moments evaluation for that slit. This was called a *hybrid* procedure between BGFA and SGFA, ensuring that BGFA never leaves gaps or NaNs in the moment maps and that the final product is at least as complete as the SGFA analysis.

It is noted that the hybrid procedure was a minor improvement when the Doppler shift and the line broadening for the contaminating Gaussians were fixed.

Tests on VDEM simulations and definition of outliers

The performance of BGFA relative to SGFA was assessed using the provided numerical simulations in the form of VDEM cubes, as introduced in Appendix E.2. These simulations, produced by magnetohydrodynamics (MHD) based codes and post-processed through CHIANTI-based emissivity calculations, provide $VDEM(T, \mathbf{v})$ distributions over solar fields of view representative of quiet Sun, plage, and active-region conditions. A description of analogue simulating setups for these simulations is provided by De Pontieu et al. (2022) [18]. In this appendix, I will show results for a plage simulation.

A forward-modeling strategy was employed to generate mock MUSE SG observations from those VDEM cubes. The simulations provide, for each slit i, spatial position in the y-pixel axis, step, a way to create ground truth (GT) mock-observations containing only main-line profiles. The GT approach does not include contaminating lines, because they are intentionally flagged out, and, by fitting this GT profile with a single-Gaussian approach, it is possible to define GT moments $(I_{\rm int}^{\rm GT}, v^{\rm GT}, w^{\rm GT})$ for the main line set of values of *true* moments. The GT moments can be compared to the inferred moments by *any* fitting strategy applied to the mock-observations including contamination (or noise, i.e., effects of realistic relevance), such as the BGFA or SGFA routine. The effect of noise on BGFA was not explored.

On Defining Outliers

For each pixel y, each step, each slit i, and each main-line, the Doppler velocity and linewidth errors returned by a given fitting strategy (SGFA or BGFA) are defined, using v as a shorthand for $v_{(\mathrm{m},i)}$, and w for $\sigma_{(\mathrm{m},i)}$, as follows

$$\Delta v = v_{\rm fit} - v^{\rm GT}, \tag{E.18}$$

$$\Delta w = w_{\rm fit} - w^{\rm GT}, \tag{E.19}$$

where $(v_{\rm fit}, w_{\rm fit})$ are the moments obtained from the mock observation including contamination by contaminating lines, and $(v^{\rm GT}, w^{\rm GT})$ are the moments from the GT profile.

With guidance from LMSAL/CfA/UNIPA science teams, I classified as a *velocity outlier* one velocity Doppler-shift evaluated moment if

$$|\Delta v| > 5 \text{ km s}^{-1}, \tag{E.20}$$

and as a *linewidth outlier* if

$$|\Delta w| > 10 \text{ km s}^{-1}. \tag{E.21}$$

These thresholds were chosen to be larger than the expected measurement errors, given MUSE's high-resolution specifications and typical exposure times. Additionally, only pixels whose integrated intensity exceeds a minimum threshold $I_{\rm thresh.}$ are counted as *eligible* for the statistics, to avoid noise-dominated fits as outliers. The usual threshold I employed was of $I_{\rm thresh.} \sim 100$ ph.

The performance of SGFA and BGFA is then quantified by the fractions of outliers in the eligible set, defined as in the following equations:

$$f_{v,\rm out} = \frac{N(|\Delta v| > 5 \text{ km s}^{-1})}{N_{\rm elig}}, \qquad f_{w,\rm out} = \frac{N(|\Delta w| > 10 \text{ km s}^{-1})}{N_{\rm elig}}, \tag{E.22}$$

where $N(...)$ is a counting function for v or w-values satisfying the inequality with eligible moments, and $N_{\rm elig}$ is the total number of eligible moments. These fractions, computed separately for each line, simulation, and choice of $(\text{npix}, v_{\rm range})$, are the main figures of merit used here to assess whether BGFA provides an improvement over SGFA. I now proceed towards the results for the initial tests of BGFA.

E.3 Some Results for the Bi-Gaussian Fitting Analysis

In this section, I will provide results on the simulation, which will be called **plage**. I acknowledge support in providing the simulations, aid in their processing, and moment-evaluation analyses by Juan-Martinez Sykora, Vishal Upendran, Bart De Pontieu (LMSAL), and Paola Testa (CfA).

Note. The following results for both the BGFA and SGFA are a result of my own work. As a disclaimer, the simulations provided were developed at the same time as the development of MUSE, and they were indicative of regions of the sun (AR, QS, plage). I was granted permission to perform tests and comparisons for the BGFA procedure on the simulations, though these are the property of other researchers. The results provided are not in any way final regarding the potential performance of both single and bi-Gaussian fitting approaches, due to various reasons: (i) changes in the effective area

of MUSE, (ii) changes in the simulations in the current research, and (iii) optimization of the SGFA/BGFA procedures. The results are shown solely to the extent of showcasing the potential and the limitations of the bi-Gaussian approach detailed in the appendix.

Tests on the plage simulation

I begin with results carried out on the plage simulation, for one particular case choice of (npix, vrange) = (2, 100 km s^{-1}) and exposure time of 1 s. The total moments per line analyzed were $\simeq 1.27 \times 10^5$, i.e., the number of singular fits. The hybrid approach was adopted for BGFA, resulting in the effect being minor, as only 2 moments were found to be NaN for the pure bi-Gaussian fitting in line Fe IX, and less than 10 were NaNs for line Fe XV. In Table E.1, these results in tabular form are shown.

Table E.1 Results for one analysis of the plage simulation using both SGFA and BGFA approaches, in terms of the outlier fractions defined in Equation (E.22). The analysis was performed with npix = 2, $v_{\rm range} = 100$ km s^{-1}, and exposure time of 1 s. Lines used: Fe IX and Fe XV, with respective contaminants Fe X and Fe XIV 274. Total available moments per line are $\approx 1.27 \times 10^5$.

Line	Metric	SGFA	BGFA
Fe IX	Eligible moments	$\simeq 9.60 \times 10^4$	
	Velocity outliers	3.538%	3.418%
	Linewidth outliers	2.134%	1.937%
Fe XV	Eligible moments	$\simeq 1.085 \times 10^5$	
	Velocity outliers	0.353%	0.330%
	Linewidth outliers	0.174%	0.161%

On average, I found that the BGFA approach improved the results for plage, but on a not-so-relevant scale, as the number of outliers was always at the same order of magnitude between the two approaches. Since one of the main motifs behind the development of the approach was to improve the performance of the code at greater npix, and $v_{\rm range}$ windows, I carried out parametric studies-tests covering the range of npix $\in \{2, 4, 6\}$ and $v_{\rm range}$ [km s^{-1}] $\in \{50, 75, 100, 125, 150, 200\}$. The results based on the BGFA approach are shown in Fig. E.2, those for SGFA, to be compared to the former ones, in Fig. E.3.

Similar qualitative results were found for the active region simulation: overall, a reduction of outliers when going from an SGFA to a BGFA approach, with modest improvements. An aspect of relevance is that by increasing the npix window, the number of outliers found increased: this goes against the intention of the development of the bi-Gaussian approach.

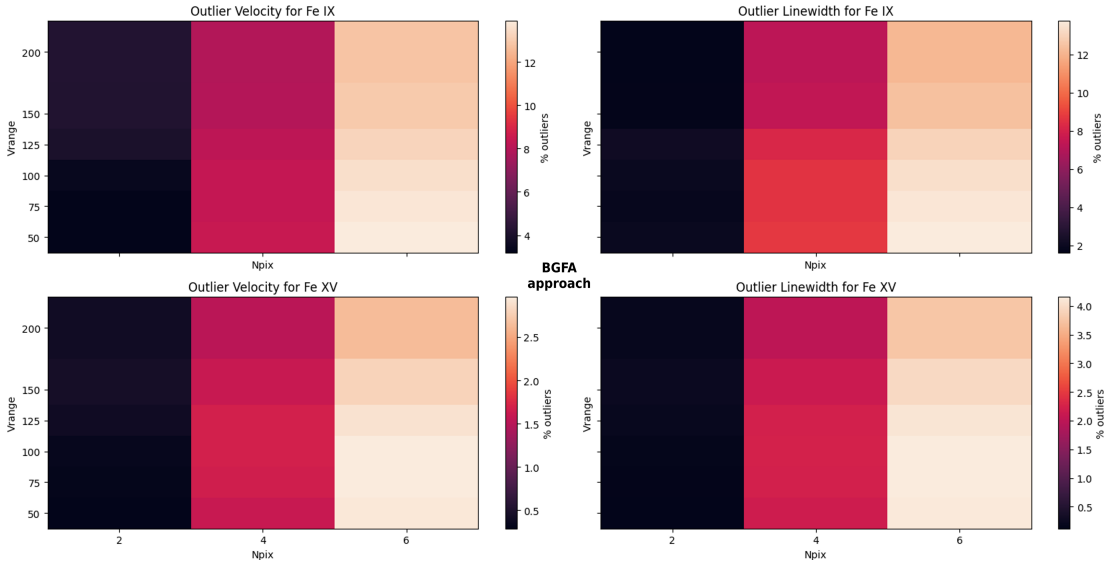

Figure E.2 Fraction of outliers obtained with the BGFA approach for the plage simulation, explored in a parametric study involving npix $\in \{2, 4, 6\}$ and v_{range} $[\text{km s}^{-1}] \in \{50, 75, 100, 125, 150, 200\}$. The horizontal axis in each panel shows npix, while the vertical shows v_{range} in km s^{-1}. **Top row:** Fe IX, with Doppler-velocity outliers on the left and linewidth outliers on the right. **Bottom row:** Fe XV, same quantities. The color map gives the fraction % of outliers (Equation (E.22)).

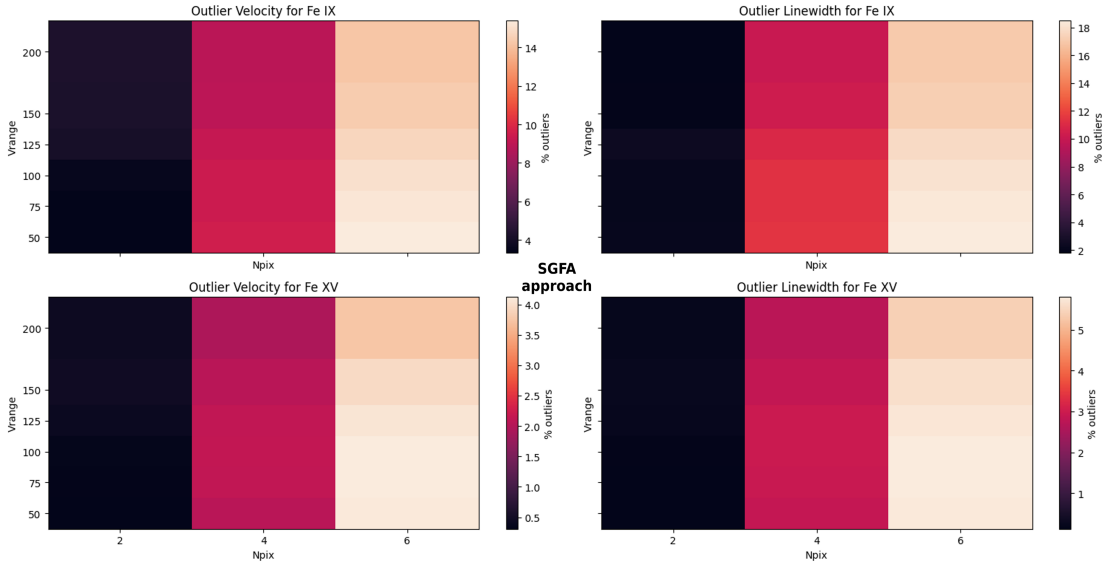

Figure E.3 Same as Fig. E.2, but for the SGFA (single-Gaussian) analysis. The four panels show the fraction of Doppler-velocity and linewidth outliers for Fe IX (**top row**) and Fe XV (**bottom row**), depending on npix (horizontal axis) and v_{range} (vertical axis, in km s^{-1}). Color maps indicate the fraction of outliers as per Equation (E.22).

Summary of performance and limitations

In the test cases studied (VDEM simulations of QS, plage, and AR) with different values of v_{range} and npix, a consistent finding emerges:

- In the presence of a single dominant contaminant with a reasonably well-characterized $R_{\text{c|m}}$, BGFA reduces the proportion of large linewidth outliers
- In more complex contamination scenarios (multiple relevant contaminants, very low counting regimes, or significant deviations from the assumption of identical plasma), the single-contaminant BGFA model may be insufficient, and its performance gains compared to SGFA diminish.
- At increasing npix windows for the fits, the outliers increased in both algorithmic schemes, therefore suggesting that the contaminant prediction aspect is not the most relevant contribution to the flux when increasing window size.

Thus, as a conclusion derived from the results, minor improvements were seen, but the overall strategy suffers from some systematic errors. NaNs, although rare, did occur when only the intensity of the contaminant was being probed in the fitting, requiring a hybrid approach to be devised. Moreover, even if the contaminating Gaussian parameters in Equation (E.13) were constrained in the way specified in Appendix E.2, if all of the parameters were let free in the bi-Gaussian model (6 free parameters in total), the fits would never be entirely stable, producing a non-negligible quantity of NaNs. Furthermore, considering the fact that if the pixel window increased in size, the fraction of outliers would as well, it is evident that the procedure does not capture the complexity of the contaminants by fitting one contaminant component only in a decisive way.

E.4 Discussion and Outlooks on the Bi-Gaussian Approach

The systematic presence of contamination is one of the important aspects of the novelty of MUSE: the multi-slit geometry allows for capturing large portions of the sun with an unprecedented time resolution, though the price to pay is the fact that the multi-slit geometry introduces complexities in the data analysis, in the form of contaminating lines and contaminating slits. The Bi-Gaussian Fitting Analysis (BGFA) strategy presented in this chapter is a first attempt to integrate atomic physics and instrumental knowledge with the Gaussian fitting of MUSE SG spectra, explicitly targeting spectral contamination due to the novel multi-slit geometry. This is also an extension to the Single-Gaussian (SGFA) strategy.

The devised BGFA strategy uses the effective areas of MUSE, and DEM-based strategies to evaluate line-intensities with CHIANTI [149] [150]. Rather than treating the contaminating Gaussian(s) as completely free in terms of free parameters during fitting, their parameters are constrained on the main line from

the contaminating slit using a few physically motivated approaches (based on the *same-plasma hypothesis*). Only the intensity of the contaminating Gaussian was left free during fitting. These initial conditions aided the implementation of a scheme for fitting the contaminants for which the MUSE mission is not optimized to observe – if anything, the MUSE payload is optimized for minimizing the contamination intensity.

The development of the BGFA approach has shown improvements over the SGFA one, showing that even a relatively simple and physically informed extension of SGFA can lead to tangible improvements in the recovery of line moments in contaminated slits, main-line Gaussian moments, and plasma properties retrieved (Doppler shifts, thermal line broadenings). In addition to being potentially useful in itself, BGFA can provide better initial conditions for more complex fitting strategies such as SDC, thus helping to reduce the risk of convergence to nonphysical solutions.

However, a few limitations remain in the approach and were seen in the results:

- The assumption of an identical plasma is an idealization. The approach is not optimized to the case where the same plasma emitting as perceived by the LOS contains distributions spanning relevant contributions from the contaminating line (for example, temperature $\log T \simeq 6$ for Fe X, and $\log 5.8$ for Fe IX).
- Only one contaminant per main line is explicitly modeled. This in itself is a limitation because if another relevant contaminant occurs, it is not being modeled. This can worsen the performance of the code in itself with respect to the ideal scenario.
- The CHIANTI-evaluated factors representing the ratio between a contaminating line and the respective main-line with the same plasma emitting it, and convoluted with MUSE's effective area, $R_{\mathrm{c|m}}$, are currently computed for a set of canonical DEMs. They are fixed in the whole analysis for all of the slits.
- During the parametric studies, it was seen that as the npix window increased, the number of fraction outliers retrieved from the fitting did, in a way that did not depend on the technique. This suggests that a similar systematic error in the BGFA and SGFA occurred alike when the window was increased.

The BGFA algorithm can inspire different approaches that could improve on its limitations. I will list a few that I considered and did not implement, or that I tried to implement, though unsuccessfully, but any hypothesis can be relaxed to check for improvements in the results.

- This BGFA could inspire a Multi-Gaussian Fitting Analysis (MGFA) approach, where all of the predictable contaminants are taken into consideration, whose initial conditions are evaluated analogously to the contaminating Gaussian evaluated in BGFA. This strategy would be more complex, increase the number of free parameters, and, considering the huge dynamic range of a

VDEM-provided simulation in terms of intensity, would require extensive care in its programming.

- Furthermore, for the evaluation of initial conditions of one of the expected contaminants in 171 Å channel, Ni XIV, the main-lines from Fe XV should be employed because of the more similar characteristic temperature of the line emission: a kind of cross-prediction among different channels could improve the results overall when increasing the number of contaminants in this channel.
- More advanced strategies, such as a *subtraction* procedure to remove the expected contaminant before beginning the fitting, could remove systematic case where a very intense contaminant could be perceived as a main-line by the algorithm initializing condition (which retrieves the local maximum as perceived by a slit for the evaluation of the initial condition of the main-line).
- Instead of an inflexible framework for the evaluation of the line-intensity ratios in a given 35-slit scenario could be devised, a more flexible framework could be evaluated, in which local DEM information (e.g., from multi-line inversions) is used to dynamically update the most optimal line-intensity ratio $R_{\mathrm{c|m}}$ to be used. Systematic procedures of machine-learning approaches could also be evaluated.

These extensions could be important to exploit this technique of bi-/multi-gussian implementation of contaminants to their full potential. However, it is also noteworthy that alternative approaches, which I did not consider, could also work in a better way.

References

Back-references linking to the pages where the citation occurred are given by the boxes, •.

[1] F. Clette and L. Lefèvre. SILSO Sunspot Number V2.0. Published by WDC SILSO - Royal Observatory of Belgium (ROB). **July 2015**.
DOI: 10.24414/qnza-ac80 4

[2] National Research Council. Severe Space Weather Events: Understanding Societal and Economic Impacts: A Workshop Report. The National Academies Press, **2008**. ISBN: 978-0-309-12769-1.
DOI: 10.17226/12507 4

[3] G. Vaiana et al. X-Ray Observations of Characteristic Structures and Time Variations from the Solar Corona: Preliminary Results from SKYLAB. *ApJ* 185, **Oct. 1973**, p. L47.
DOI: 10.1086/181318 4

[4] J. R. Lemen et al. The atmospheric imaging assembly (AIA) on the solar dynamics observatory (SDO). *Sol. Phys.* 275, **2012**, pp. 17–40.
DOI: 10.1007/s11207-011-9776-8 4, 5, 7, 84

[5] P. Rochus et al. The Solar Orbiter EUI instrument: The Extreme Ultraviolet Imager (Corrigendum). *A&A* 665, **2022**, p. C1.
DOI: 10.1051/0004-6361/201936663e 4

[6] T. Kosugi et al. The Hinode (Solar-B) Mission: An Overview. *Solar Physics* 243.1, **June 2007**, pp. 3–17. ISSN: 1573-093X.
DOI: 10.1007/s11207-007-9014-6 4, 9

[7] J. L. Culhane et al. The EUV Imaging Spectrometer for Hinode. *Solar Physics* 243.1, **June 2007**, pp. 19–61. ISSN: 1573-093X.
DOI: 10.1007/s01007-007-0293-1 4, 9

[8] P. C. Chamberlin, W. D. Pesnell and B. J. Thompson. The Solar Dynamics Observatory (SDO). Springer, **2012**. ISBN: 978-1-4614-3672-0.
DOI: 10.1007/978-1-4614-3673-7 4, 7

[9] P. Testa and F. Reale. The Solar X-ray Corona. In: *Handbook of X-ray and Gamma-ray Astrophysics*. Springer Nature Singapore, **2024**, pp. 3075–3112. ISBN: 978-981-19-6960-7.
DOI: 10.1007/978-981-19-6960-7_77 4, 6

[10] S. R. Cranmer. Coronal Holes. *Living Reviews in Solar Physics* 6.1, **Sept. 2009**, p. 3. ISSN: 1614-4961.
DOI: 10.12942/lrsp-2009-3 4

[11] F. Reale. Coronal Loops: Observations and Modeling of Confined Plasma. *Living Reviews in Solar Physics* 11.1, **July 2014**, p. 4. ISSN: 1614-4961.
DOI: 10.12942/lrsp-2014-4 4

[12] M. J. Penn. Infrared Solar Physics. *Living Reviews in Solar Physics* 11.1, **Mar. 2014**, p. 2. ISSN: 1614-4961.
DOI: 10.12942/lrsp-2014-2 4

[13] S. Parenti. Solar Prominences: Observations. *Living Reviews in Solar Physics* 11.1, **Mar. 2014**, p. 1. ISSN: 1614-4961.
DOI: 10.12942/lrsp-2014-1 4

[14] M. C. M. Cheung and H. Isobe. Flux Emergence (Theory). *Living Reviews in Solar Physics* 11.1, **July 2014**, p. 3. ISSN: 1614-4961.
DOI: 10.12942/lrsp-2014-3 4

[15] J. A. Klimchuk. On Solving the Coronal Heating Problem. *Solar Physics* 234.1, **Mar. 2006**, pp. 41–77. ISSN: 1573-093X.
DOI: 10.1007/s11207-006-0055-z 6

[16] N. Viall et al. The Heating of the Solar Corona. IN: *Solar Physics and Solar Wind*. American Geophysical Union (AGU), **2021**. chap. 2, pp. 35–82. ISBN: 9781119815600.
DOI: 10.1002/9781119815600.ch2 6

[17] B. De Pontieu et al. The Multi-slit Approach to Coronal Spectroscopy with the Multi-slit Solar Explorer (MUSE). *ApJ* 888.1, **2020**, p. 3.
DOI: 10.3847/1538-4357/ab5b03 6, 7, 56, 117, 121, 122

[18] B. De Pontieu et al. Probing the physics of the solar atmosphere with the multi-slit solar explorer (MUSE). I. coronal heating. *ApJ* 926.1, **2022**, p. 52.
DOI: 10.3847/1538-4357/ac4222 6, 38, 44, 121, 129

[19] M. C. M. Cheung et al. Probing the physics of the solar atmosphere with the multi-slit solar explorer (MUSE). II. flares and eruptions. *ApJ* 926.1, **2022**, p. 53.
DOI: 10.3847/1538-4357/ac4223 6, 8

[20] G. Cozzo et al. Coronal energy release by MHD avalanches: II. EUV line emission from a multi-threaded coronal loop. *A&A* 689, **2024**, A184.
DOI: 10.1051/0004-6361/202450644 6, 84, 120, 121

[21] B. De Pontieu et al. The interface region imaging spectrograph (IRIS). *Sol. Phys.* 289, **2014**, pp. 2733–2779.
DOI: 10.1007/s11207-014-0485-y 7

[22] T. R. Rimmele et al. The Daniel K. Inouye Solar Telescope – Observatory Overview. *Solar Physics* 295.12, **Dec. 2020**, p. 172. ISSN: 1573-093X.
DOI: 10.1007/s11207-020-01736-7 7

[23] T. Shimizu et al. The Solar-C_EUVST mission. In: *UV, X-Ray, and Gamma-Ray Space Instrumentation for Astronomy XXI*. vol. 11118. International Society for Optics and Photonics. SPIE, **2019**, p. 1111807.
DOI: 10.1117/12.2528240 7, 71

[24] P. Cheimets et al. SDO-AIA telescope design. In: *Solar Physics and Space Weather Instrumentation III*. vol. 7438. International Society for Optics and Photonics. SPIE, **2009**, 74380G.
DOI: 10.1117/12.830594 7

[25] J.-P. Wülser et al. EUVI: the STEREO-SECCHI extreme ultraviolet imager. In: *Telescopes and Instrumentation for Solar Astrophysics*. vol. 5171. International Society for Optics and Photonics. SPIE, **2004**, pp. 111–122.
DOI: 10.1117/12.506877 9, 11, 12, 14, 29, 72

[26] J.-P. Delaboudinière et al. EIT: Extreme-Ultraviolet Imaging Telescope for the SOHO Mission. *Sol. Phys.* 162, **1995**, pp. 291–312.
DOI: 10.1007/BF00733432 9

[27] N. I. Chkhalo et al. Thin film multilayer filters for solar EUV telescopes. *Appl. Opt.* 55.17, **2016**, pp. 4683–4690.
DOI: 10.1364/AO.55.004683 9, 12, 16

[28] B. Poduval et al. Point-spread Functions for the Extreme-ultraviolet Channels of SDO/AIA Telescopes. *ApJ* 765.2, **2013**, p. 144.
DOI: 10.1088/0004-637X/765/2/144 10, 12, 20, 51, 90

[29] F. R. Powell and T. A. Johnson. Filter windows for EUV lithography. In: *Emerging Lithographic Technologies V*. vol. 4343. Publisher: SPIE. International Society for Optics and Photonics. **2001**, pp. 585–589.
DOI: 10.1117/12.436709 10

[30] J. Zhu et al. Component and performance evolution of Zr filters induced by annealing and synchrotron radiation in EUV range. *Chin. Opt. Lett.* 23.3, **Mar. 2025**. Publisher: Optica Publishing Group., p. 033401.
DOI: 10.3788/COL202523.033401 10

[31] P. Boerner et al. Initial Calibration of the Atmospheric Imaging Assembly (AIA) on the Solar Dynamics Observatory (SDO). *Sol. Phys.* 275, **2012**, pp. 41–66.
DOI: 10.1007/s11207-011-9804-8 12, 14, 29, 31, 51, 56, 71, 121

[32] H. L. Marshall et al. Composition of the Chandra ACIS contaminant. In: *X-Ray and Gamma-Ray Instrumentation for Astronomy XIII*. vol. 5165. International Society for Optics and Photonics. SPIE, **2004**, pp. 497–508.
DOI: 10.1117/12.508310 12

[33] A. BenMoussa et al. On-Orbit Degradation of Solar Instruments. *Sol. Phys.* 288, **2013**, pp. 389–434.

DOI: 10.1007/s11207-013-0290-z 12

[34] C. Tarrio et al. The Hazard of UV-Induced Oxidation to Solar-Viewing Spacecraft Optics. *Sol. Phys.* 298, **2023**, p. 32.
DOI: 10.1007/s11207-023-02112-x 13

[35] R. F. Berg et al. Oxidation Caused by Water Outgassed from the Thermal Blanket on the SDO Spacecraft. *Sol. Phys.* 298, **2023**, p. 81.
DOI: 10.1007/s11207-023-02148-z 13, 91

[36] L. F. G. Dos Santos et al. Multichannel autocalibration for the Atmospheric Imaging Assembly using machine learning. *A&A* 648, **2021**, A53.
DOI: 10.1051/0004-6361/202040051 13

[37] J. C. Mankins. Technology readiness assessments: A retrospective. *Acta Astronautica* 65.9, **2009**, pp. 1216–1223. ISSN: 0094-5765.
DOI: 10.1016/j.actaastro.2009.03.058 13

[38] European Cooperation for Space Standardization (ECSS). ECSS-E-HB-11A — Technology Readiness Level (TRL) Guidelines. Handbook supporting ECSS-E-AS-11C (Adoption Notice of ISO 16290). Attachments available in pdf or docx. Last accessed: 2025-11-17. ECSS Secretariat, European Space Agency (ESA), ESTEC. **Mar. 1, 2017**.
URL:
www.ecss.nl/wp-content/uploads/2017/03/ECSS-E-HB-11A(1March2017).pdf
13

[39] J. Etula et al. Carbon nanotube membranes for EUV photolithography: a versatile material platform. In: *International Conference on Extreme Ultraviolet Lithography 2023*. vol. 12750. International Society for Optics and Photonics. SPIE, **2023**, p. 127500M.
DOI: 10.1117/12.2686790 13, 31, 72, 73, 89

[40] M. Barbera et al. Carbon nanotubes thin filters for x-ray detectors in space. In: *Space Telescopes and Instrumentation 2022: Ultraviolet to Gamma Ray*. vol. 12181. International Society for Optics and Photonics. SPIE, **2022**, 121814H.
DOI: 10.1117/12.2631516 13, 14

[41] E. Alaimo et al. Comparative Experimental Study of Single- and Multi-walled Carbon Nanotube Pellicles for EUV/Soft X-ray Space Filters. *[Manuscript submitted for publication]*, **2026**. Paper in preparation
13, 31, 88

[42] F. D'Anca et al. Mechanical qualification of metal-coated carbon nanotubes optical blocking filters developed for the NASA MIDEX solar mission MUSE. In: *International Conference on Space Optics (ICSO2024)*. vol. 13699. **2025**, p. 136995M.
DOI: 10.1117/12.3075220 14, 32

[43] M. Barbera et al. Metal coated carbon nanotube ultra-thin pellicles: a high-performance solution for the optical blocking filters of the NASA MIDEX solar mission MUSE. In: *International Conference on Space Optics (ICSO2024)*. vol. 13699. **2025**, 136991P.
DOI: 10.1117/12.3075219 14, 31, 33, 34, 35, 36, 72, 85

[44] D. B. Seaton et al. The SWAP EUV Imaging Telescope Part I: Instrument Overview and Pre-Flight Testing. *Solar Physics* 286.1, **Aug. 2013**, pp. 43–65. ISSN: 1573-093X.
DOI: 10.1007/s11207-012-0114-6 14

[45] J.-P. Halain et al. The SWAP EUV Imaging Telescope. Part II: In-flight Performance and Calibration. *Solar Physics* 286.1, **Aug. 2013**, pp. 67–91. ISSN: 1573-093X.
DOI: 10.1007/s11207-012-0183-6 15

[46] S. Jonckheere et al. Filter failure analysis for the SWAP instrument on-board of PROBA2. English. In: *COMPDYN*. **May 2011**.
URL: https://hdl.handle.net/2268/97629 15

[47] P. Zhang et al. FY-3E: The First Operational Meteorological Satellite Mission in an Early Morning Orbit. *Advances in Atmospheric Sciences* 39.1, **Jan. 2022**, pp. 1–8. ISSN: 1861-9533.
DOI: 10.1007/s00376-021-1304-7 15

[48] B. Chen et al. Solar X-ray and EUV imager on board the FY-3E satellite. *Light: Science & Applications* 11.1, **Nov. 2022**, p. 329. ISSN: 2047-7538.
DOI: 10.1038/s41377-022-01023-z 15

[49] S. Seetha and S. Megala. Aditya-L1 mission. *Current Science* 113.4, **Feb. 2026**. Full publication date: 25 August 2017, pp. 610–612. ISSN: 00113891.
URL: http://www.jstor.org/stable/26293897 15

[50] K. Sankarasubramanian et al. Solar Low Energy X-ray Spectrometer (SoLEXS) on Board Aditya-L1 Mission. *Solar Physics* 300.7, **June 2025**, p. 87. ISSN: 1573-093X.
DOI: 10.1007/s11207-025-02494-0 15

[51] D. Tripathi et al. The Solar Ultraviolet Imaging Telescope on Board Aditya-L1. *Solar Physics* 300.3, **Mar. 2025**, p. 30. ISSN: 1573-093X.
DOI: 10.1007/s11207-025-02423-1 16

[52] J. Sarkar et al. Science filter characterization of the Solar Ultraviolet Imaging Telescope (SUIT) on board Aditya-L1. *Experimental Astronomy* 59.1, **Dec. 2024**, p. 3. ISSN: 1572-9508.
DOI: 10.1007/s10686-024-09973-5 16

[53] J. Sarkar et al. Design, fabrication, and characterization of the thermal filter assembly on the Solar Ultraviolet Imaging Telescope onboard Aditya-L1.

Journal of Astronomical Telescopes, Instruments, and Systems 11.3, **2025**. Publisher: SPIE., p. 034004.
DOI: 10.1117/1.JATIS.11.3.034004 16

[54] S. V. Kuzin et al. The TESIS experiment on the CORONAS-PHOTON spacecraft. *Sol. Syst. Res.* 45.2, **2011**, pp. 162–173.
DOI: 10.1134/S0038094611020110 16

[55] V. D. Kuznetsov et al. The Sun and heliosphere explorer – the Interhelioprobe mission. *Geomagnetism and Aeronomy* 56.7, **Dec. 2016**, pp. 781–841. ISSN: 1555-645X.
DOI: 10.1134/S0016793216070124 16

[56] European Cooperation for Space Standardization (ECSS). ECSS-E-HB-10-02A — Space engineering verification guidelines. Handbook supporting ECSS Standard: ECSS-E-ST-10-02C (6 March 2009). Section 5.2 mentions DM and STM definitions. Attachments available in pdf or docx. Last accessed: 2026-02-13. ECSS Secretariat, European Space Agency (ESA), ESTEC. **Mar. 6, 2009**.
URL:
www.ecss.nl/wp-content/uploads/handbooks/ecss-e-hb/ECSS-E-HB-10-02A17December2010.pdf
19

[57] D. Spiga et al. Modelling diffractive effects in silicon pore optics for the ATHENA X-ray Telescope. In: *Space Telescopes and Instrumentation 2022: Ultraviolet to Gamma Ray*. vol. 12181. International Society for Optics and Photonics. SPIE, **2022**, 121814J.
DOI: 10.1117/12.2628133 20, 37

[58] D. Spiga et al. The focusing mirrors of the MUSE extreme-ultraviolet solar telescope. In: *Optics for EUV, X-Ray, and Gamma-Ray Astronomy XI*. vol. 12679. International Society for Optics and Photonics. SPIE, **2023**, p. 1267908.
DOI: 10.1117/12.2678191 20, 38, 43

[59] B. N. Handy et al. The transition region and coronal explorer. *Solar Physics* 187.2, **July 1999**, pp. 229–260. ISSN: 1573-093X.
DOI: 10.1023/A:1005166902804 20

[60] C. E. DeForest, P. C. H. Martens, and M. J. Wills-Davey. SOLAR CORONAL STRUCTURE AND STRAY LIGHT IN TRACE. *The Astrophysical Journal* 690.2, **Dec. 2008**, p. 1264.
DOI: 10.1088/0004-637X/690/2/1264 20

[61] E. Pantin J. L. Starck and F. Murtagh. Deconvolution in Astronomy: A Review. *Publications of the Astronomical Society of the Pacific* 114.800, **Oct. 2002**, p. 1051.
DOI: 10.1086/342606 20

[62] D. L. Snyder and R. L. White. Modification of the Richardson-Lucy iteration for restoration of Hubble Space Telescope Images. In: *Optical Society of America Annual Meeting*. Optica Publishing Group, **1991**, MQQ3.
DOI: 10.1364/OAM.1991.MQQ3 20

[63] G. R. Fowles. Introduction to Modern Optics. 2nd. Dover Publications, **1975**. ISBN: 978-0-486-65957-2 22, 25, 28, 112

[64] P. Grigis, Y. Su, and M. Weber. AIA PSF Characterization and Image Deconvolution. tech. rep. version 2012-Feb-13. For the AIA team, Solar Dynamics Observatory (SDO). Last Accessed: 2025-11-19. NASA Goddard Space Flight Center, **Feb. 2012**.
URL: www.hesperia.gsfc.nasa.gov/ssw/sdo/aia/idl/psf/DOC/psfreport.pdf 25

[65] P. A. Martin. What is Babinet's principle? *Wave Motion* 122, **2023**, p. 103191. ISSN: 0165-2125.
DOI: 10.1016/j.wavemoti.2023.103191 25, 112

[66] G. O. Reynolds. The New Physical Optics Notebook: Tutorials in Fourier Optics. SPIE, **1989**.
DOI: 10.1117/3.2303 25

[67] J.W. Goodman. Introduction to Fourier Optics. McGraw-Hill, **1996**. ISBN: 9780070242548 25, 28, 37

[68] N. W. Ashcroft and N. D. Mermin. Solid State Physics. Holt-Saunders, **1976** 26, 111

[69] C. Kittel. Introduction to Solid State Physics. Eighth. John Wiley & Sons, Inc, **2005**. ISBN: 0-471-41526-X 26, 28, 111

[70] S. H. Sung et al. Stacking, strain, and twist in 2D materials quantified by 3D electron diffraction. *Phys. Rev. Mater.* 3, 6 **June 2019**, p. 064003.
DOI: 10.1103/PhysRevMaterials.3.064003 27

[71] C. M. Krowne. Chapter Two - Determination of reciprocal lattice from direct space in 3D and 2D – Examination of hexagonal band structure. In: *Advances in Imaging and Electron Physics*. ed. by P. W. Hawkes and M. Hÿtch. vol. 210. Elsevier, **2019**, pp. 7–22.
DOI: 10.1016/bs.aiep.2019.01.002 28

[72] J. E. Harvey and R. N. Pfisterer. Understanding diffraction grating behavior: including conical diffraction and Rayleigh anomalies from transmission gratings. *Optical Engineering* 58.8, **2019**, p. 087105.
DOI: 10.1117/1.OE.58.8.087105 28

[73] J. I. Halman et al. Predicted and measured transmission and diffraction by a metallic mesh coating. In: *Window and Dome Technologies and Materials*

XI. vol. 7302. International Society for Optics and Photonics. SPIE, **2009**, 73020Y.
DOI: 10.1117/12.818760 28

[74] Dunwei Liao, Le Kang, and Jianhua Zhou. Calculation and verification of optical diffraction performance of random metallic meshes. *Journal of Applied Physics* 137.12, **Mar. 2025**, p. 123108. ISSN: 0021-8979.
DOI: 10.1063/5.0254916 28

[75] B. L. Henke et al. X-Ray Interactions: Photoabsorption, Scattering, Transmission, and Reflection at E = 50-30,000 eV, Z = 1-92. *At. Data Nucl. Data Tables* 54.2, **1993**, pp. 181–342.
DOI: 10.1006/adnd.1993.1013 30, 31, 78, 81, 83, 90

[76] E. M. Gullikson. Henke Optical Constants and Transmission Models Website. Tool for transmittance calculator available in the X-ray transmission of a thin solid film section. Last Accessed: 16 Oct 2024. **2025**.
URL: https://henke.lbl.gov/optical_constants/ 30, 31, 78, 81, 83

[77] N. Cabrera and N. F. Mott. Theory of the oxidation of metals. *Rep. Prog. Phys.* 12.1, **1949**, pp. 163–184.
DOI: 10.1088/0034-4885/12/1/308 30, 89

[78] G. A. Ermolaev et al. Express determination of thickness and dielectric function of single-walled carbon nanotube films. *Applied Physics Letters* 116.23, **June 2020**, p. 231103.
DOI: 10.1063/5.0012933 32, 66, 73, 74

[79] G. Parodi et al. Structural modelling and mechanical tests supporting the design of the ATHENA X-IFU thermal filters and WFI optical blocking filter. In: *Space Telescopes and Instrumentation 2018: Ultraviolet to Gamma Ray*. vol. 10699. International Society for Optics and Photonics. SPIE, **2018**, p. 106994C.
DOI: 10.1117/12.2314451 34

[80] E. Alaimo et al. Investigation on the Role of Optical Filters on the Point Spread Function of the NASA MIDEX Solar Mission MUSE. In: *International Conference on Space Optics (ICSO2024)*. vol. 13699. **2025**, 136995J.
DOI: 10.1117/12.3075223 37, 50, 85, 86, 90

[81] C. R. Harris et al. Array programming with NumPy. *Nature* 585, **2020**. URLs Last Accessed: 2026-02-11, pp. 357–362.
DOI: 10.1038/s41586-020-2649-2 GitHub: numpy/numpy 38, 55

[82] P. Virtanen et al. SciPy 1.0: fundamental algorithms for scientific computing in Python. *Nature Methods* 17, **2020**. URLs Last Accessed: 2026-02-11, pp. 261–272.
DOI: 10.1038/s41592-019-0686-2 GitHub: scipy/scipy 38, 55

[83] John D. Hunter. Matplotlib: A 2D graphics environment. *Computing in Science & Engineering* 9.3, **2007**. URLs Last Accessed: 2026-02-11, pp. 90–95.
DOI: 10.1109/MCSE.2007.55 GitHub: matplotlib/matplotlib 38, 55

[84] The Astropy Collaboration. Astropy: A community Python package for astronomy. *A&A* 558, **2013**. URLs Last Accessed: 2026-02-11, A33.
DOI: 10.1051/0004-6361/201322068 GitHub: astropy/astropy 38

[85] The Astropy Collaboration. The Astropy Project: Building an Open-science Project and Status of the v2.0 Core Package*. *The Astronomical Journal* 156.3, **Aug. 2018**. URLs Last Accessed: 2026-02-11, p. 123.
DOI: 10.3847/1538-3881/aabc4f GitHub: astropy/astropy 38

[86] Rew Russell, Edward Hartnett, and John Caron. NetCDF-4: Software Implementing an Enhanced Data Model for the Geosciences. In: *Conference: 22nd International Conference on Interactive Information Processing Systems for Meteorology, Oceanography, and Hydrology*. URLs Last Accessed: 2026-02-11. **Jan. 2006**.
GitHub: Unidata/netcdf4-python
URL: www.ams.confex.com/ams/Annual2006/webprogram/Paper104931.html 39

[87] P. Hariharan. Optical Holography: Principles, Techniques and Applications. Cambridge University Press, **1996**. ISBN: 9780521439657 40

[88] Metin Tolan. X-Ray Scattering from Soft-Matter Thin Films: Materials Science and Basic Research. vol. 148. Springer Berlin, Heidelberg, **1999**. ISBN: 978-3-662-14218-9.
DOI: 10.1007/BFb0112834 43

[89] E. Alaimo et al. Optical blocking filters for the Multi-slit Solar Explorer mission: in-band extreme ultraviolet and soft X-ray transmittance spectroscopy measurements and analysis. *Journal of Astronomical Telescopes, Instruments, and Systems* 11.4, **2025**. Publisher: SPIE., p. 048001.
DOI: 10.1117/1.JATIS.11.4.048001 49

[90] Luxel Corporation. TF110 Standard Filter Frame: Technical Drawing and Specifications. tech. rep. TF110S, Revision B. Revised July 2013. Last Accessed: 2025-11-28. Luxel Corporation, **Jan. 2009**.
URL:
www.luxel.com/wp-content/uploads/2021/04/Luxel-Frame-TF110-RevB.pdf
54, 64

[91] Luxel Corporation. TF111 Standard Filter Frame: Technical Drawing and Specifications. tech. rep. TF111S, Revision A. Revised May 2015. Last Accessed: 2026-01-03. Luxel Corporation, **Jan. 2009**.
URL:

www.luxel.com/wp-content/uploads/2021/04/Luxel-Frame-TF111-RevA.pdf
54, 64

[92] P. J. Mohr et al. CODATA recommended values of the fundamental physical constants: 2022. *Rev. Mod. Phys.* 97, **2025**, p. 025002.
DOI: 10.1103/RevModPhys.97.025002 55, 81

[93] A. Prša et al. NOMINAL VALUES FOR SELECTED SOLAR AND PLANETARY QUANTITIES: IAU 2015 RESOLUTION B3. *The Astronomical Journal* 152.2, **Aug. 2016**. The American Astronomical Society, p. 41.
DOI: 10.3847/0004-6256/152/2/41 55

[94] S M Sze. Physics of semiconductor devices (2nd edition). New York, NY, USA. Wiley-Interscience, **Dec. 1980**, pp. 14–15. ISBN: 9780471098379.
URL: https://www.osti.gov/biblio/5381484 55

[95] ASTM International. Standard Solar Constant and Zero Air Mass Solar Spectral Irradiance Tables. Last Accessed: 2025-11-28. **2000**.
URL: www.nrel.gov/grid/solar-resource/spectra-astm-e490.html
56, 57, 58

[96] C. A. Gueymard. A reevaluation of the solar constant based on a 42-year total solar irradiance time series and a reconciliation of spaceborne observations. *Solar Energy* 168, **2018**. Advances in Solar Resource Assessment and Forecasting, pp. 2–9. ISSN: 0038-092X.
DOI: 10.1016/j.solener.2018.04.001 56

[97] Hamamatsu Photonics K.K. CCD Area Image Sensor S7030/S7031 Series: Back-thinned FFT-CCD. tech. rep. KMPD1023E21. Last Accessed: 2025-11-28. Hamamatsu Photonics K.K., Solid State Division, **Oct. 2023**.
URL: www.hamamatsu.com/resources/pdf/ssd/s7030-0906_etc_kmpd1023e.pdf
56, 59

[98] O. Christensen. Quantum efficiency of the internal photoelectric effect in silicon and germanium. *Journal of Applied Physics* 47.2, **Feb. 1976**, pp. 689–695. ISSN: 0021-8979.
DOI: 10.1063/1.322635 57

[99] Jon Geist and Edward F. Zalewski. The quantum yield of silicon in the visible. *Applied Physics Letters* 35.7, **Oct. 1979**, pp. 503–505. ISSN: 0003-6951.
DOI: 10.1063/1.91187 57

[100] J. Fang et al. Understanding the Average Electron–Hole Pair-Creation Energy in Silicon and Germanium Based on Full-Band Monte Carlo Simulations. *IEEE Transactions on Nuclear Science* 66.1, **2019**, pp. 444–451.
DOI: 10.1109/TNS.2018.2879593 57

[101] Arthur N. Cox. Allen's Astrophysical Quantities. 4th ed. Springer, **2002**, pp. 355–357. ISBN: 978-0-387-95189-8.

DOI: 10.1007/978-1-4612-1186-0 57

[102] E. Alaimo. Graphical tool for UV/VIS/IR Requirement, MUSE CI. Made with Desmos. Last Accessed: 2025-11-28. **2025**.
URL: https://www.desmos.com/calculator/xfshjds8s9 61

[103] Perkin Elmer. LAMBDA 1050+ UV/Vis/NIR Spectrophotometer. Technical Details available in the manufacturer's website under the Resources, Events & More panel. Last Accessed: 2025-11-29. **2025**.
URL: https://shop.perkinelmer.com/product/L6020055 61

[104] Jcano Ingenieria. Jcano Ingenieria Manuals Catalogue. Technical Manuals providing Photometric Accuracies for some Lambda Spectrometers available in the URL provided. Last Accessed: 2026-02-12. **2026**.
URL: https://jcanoingenieria.com/catalogo/UV-Vis/ 61

[105] J.M. Hollas. Modern Spectroscopy. Review of the book by Edward W. Castner Jr. at DOI: 10.1021/ed082p43.1. Wiley, **2004**. ISBN: 9780470094716 63

[106] D. C. Harris and M. D. Bertolucci. Symmetry and Spectroscopy: An Introduction to Vibrational and Electronic Spectroscopy. Dover Publications, **1989**. ISBN: 9780486661445 63

[107] A. Anders. A structure zone diagram including plasma-based deposition and ion etching. *Thin Solid Films* 518.15, **2010**, pp. 4087–4090. ISSN: 0040-6090.
DOI: 10.1016/j.tsf.2009.10.145 64

[108] H. A. Macleod. Thin-Film Optical Filters. CRC Press, **2018**. ISBN: 9780367781606 64

[109] P. Mercere and P. Da Silva. METROLOGIE: A metrology test facility for the R&D of optical components and detectors. Last accessed on 2025-11-30. **2026**.
URL: https://www.synchrotron-soleil.fr/en/beamlines/metrologie 71

[110] I. Mitsuishi et al. The GEO-X optical blocking filter. In: *Space Telescopes and Instrumentation 2024: Ultraviolet to Gamma Ray*. vol. 13093. SPIE, **2024**, p. 130937D.
DOI: 10.1117/12.3018683 74

[111] M. Barbera et al. TN8 – Athena filters characterization and qualification report. tech. rep. Study Contract under European Space Agengy Project: CNT-based filters for X-ray Applications. Istituto Nazionale di Astrofisica (INAF), **2023**.
URL: http://hdl.handle.net/20.500.12386/34467 74

[112] M. Barbera, U. Lo Cicero and L. Sciortino. Filters for X-Ray Detectors on Space Missions. In: *Handbook of X-ray and Gamma-ray Astrophysics*.

ed. by C. Bambi and A. Santangelo. Springer Nature Singapore, **2022**, pp. 1–44.
DOI: 10.1007/978-981-16-4544-0_30-1 80

[113] D. Attwood. Soft X-Rays and Extreme Ultraviolet Radiation. 1st. Cambridge University Press, **1999**. ISBN: 9781139164429.
DOI: 10.1017/CBO9781139164429 80, 83

[114] E. Puccio et al. Synchrotron X-ray transmission measurements and modeling of filters investigated for Athena. *J. Astron. Telesc. Instrum. Syst.* 6.3, **2020**, p. 038003.
DOI: 10.1117/1.JATIS.6.3.038003 81, 82

[115] L. Sciortino et al. Multi-technique investigation of silicon nitride/aluminum membranes as optical blocking filters for high-energy space missions. *J. Astron. Telesc. Instrum. Syst.* 10.1, **2024**. Publisher: SPIE., p. 018002.
DOI: 10.1117/1.JATIS.10.1.018002 81

[116] A. Chandrasekaran. Surface and interface diffusion processes in nanoscale thin films. English. ISBN: 978-90-365-5476-3. Publisher: University of Twente. PhD Thesis - Research UT, graduation UT. University of Twente, **Nov. 2022**.
DOI: 10.3990/1.9789036554763 81

[117] T. Prohaska et al. Standard atomic weights of the elements 2021 (IUPAC Technical Report). *Pure Appl. Chem.* 94.5, **2022**, pp. 573–600.
DOI: 10.1515/pac-2019-0603 81

[118] C. Burcklen et al. Optical constants of magnetron sputtered aluminum in the range 17-1300 eV with improved accuracy and ultrahigh resolution in the L absorption edge region. *J. Appl. Phys.* 136.19, **2024**, p. 195106.
DOI: 10.1063/5.0233781 81, 86, 90, 91

[119] D. C. Koningsberger and R. Prins. X-ray absorption: Principles, applications, techniques of EXAFS, SEXAFS and XANES. John Wiley and Sons Inc., **1988**. ISBN: 978-0-471-87547-5 82

[120] T. Chen and A. Li. Synthesizing carbon nanotubes in space. *A&A* 631, **2019**, A54.
DOI: 10.1051/0004-6361/201935789 83

[121] T. H. Squire et al. Aerospace Materials Property Database (TPSX). *J. Spacecraft Rockets* 46.3, **2009**. URL last accessed on 2025-02-18, pp. 733–736.
DOI: 10.2514/1.43777 84

[122] G. Krautheim et al. Mechanical stress in ALD-Al2O3 films. *Appl. Surf. Sci.* 252.1, **2005**, pp. 200–204.
DOI: 10.1016/j.apsusc.2005.01.118 84

[123] S. Venkataraj et al. Structural and optical properties of thin zirconium oxide films prepared by reactive direct current magnetron sputtering. *J. Appl. Phys.* 92.7, **2002**, pp. 3599–3607.
DOI: 10.1063/1.1503858 84

[124] W. H. Press et al. Numerical Recipes: The Art of Scientific Computing. 3rd. Cambridge University Press, **2007**. ISBN: 0521880688 86

[125] L. Sciortino et al. Surface investigation and aluminum oxide estimation on test filters for the ATHENA X-IFU and WFI detectors. In: *Space Telescopes and Instrumentation 2016: Ultraviolet to Gamma Ray*. vol. 9905. **2016**, p. 990566.
DOI: 10.1117/12.2232376 89

[126] J. A. Samson and D. L. Ederer. Vacuum Ultraviolet Spectroscopy. 1st ed. eBook ISBN: 978-0-08-054348-2. Academic Press, **Dec. 2000**, pp. 65–80. ISBN: 978-0-12-617560-8 92, 96

[127] D. S. Finley et al. Continuous discharge Penning source with emission lines between 50 Å and 300 Å. *Appl. Opt.* 18.5, **Mar. 1979**. Publisher: Optica Publishing Group, pp. 649–654.
DOI: 10.1364/AO.18.000649 92, 93, 96, 100

[128] R. D. Deslattes and T. J. Peterson and D. H. Tomboulian. Penning Discharge as a Source in the Extreme Ultraviolet. *J. Opt. Soc. Am.* 53.2, **Feb. 1963**. Publisher: Optica Publishing Group, pp. 302–304.
DOI: 10.1364/JOSA.53.000302 92, 93, 96

[129] C. Heise et al. Radiometric characterization of a Penning discharge in the vacuum ultraviolet. *Appl. Opt.* 33.22, **Aug. 1994**. Publisher: Optica Publishing Group, pp. 5111–5117.
DOI: 10.1364/AO.33.005111 92, 93, 100

[130] N. V. Mamedov et al. The Penning discharge experimental study and its simulation. *Plasma Physics and Technology* 3.3, **Feb. 2016**, p. 158.
DOI: 10.14311/ppt.2016.3.158 92

[131] A. S. Rokhmanenkov and S. E. Kuratov. Numerical simulation of Penning gas discharge in 2D/3D setting. *Journal of Physics: Conference Series* 1250, **2019**. APhM2018 Conference, p. 012036.
DOI: 10.1088/1742-6596/1250/1/012036 92

[132] A. S. Dikalyuk. Numerical simulation of electrodynamic structure of Penning discharge in large volume discharge chamber with annular anode. *Journal of Physics: Conference Series* 1250, **2019**. APhM2018 Conference, p. 012038.
DOI: 10.1088/1742-6596/1250/1/012038 92

[133] V. Bakshi. EUV Lithography, Second Edition. SPIE Press, **2018**.
DOI: 10.1117/3.2305675 92

[134] J. Hollandt et al. Primary sources for use in radiometry. In: *Optical Radiometry*. ed. by A. C. Parr, R. Datla, and J. L. Gardner. vol. 41. Academic Press, **2005**, p. 213. ISBN: 978-0-12-475988-6 92

[135] R. Klein et al. Calibration of space instruments at the Metrology Light Source. *AIP Conference Proceedings* 1741.1, **July 2016**, p. 030013. ISSN: 0094-243X.
DOI: 10.1063/1.4952836 92

[136] J. Hollandt and M. C. E. Huber and M. Kühne. Hollow Cathode Transfer Standards for the Radiometric Calibration of VUV Telescopes of the Solar and Heliospheric Observatory (SOHO). *Metrologia* 30.4, **Jan. 1993**, p. 381.
DOI: 10.1088/0026-1394/30/4/033 93, 102

[137] INAF. Astronomical Observatory of Palermo "Giuseppe S. Vaiana" (OAPa). Research centre affiliated with the University of Palermo, Department of Physics and Chemistry. Staff contacts available in the OSSERVATORIO » PERSONALE panel. Last Accessed: 2026-02-13. National Institute for Astrophysics (INAF), **2025**.
URL: http://www.astropa.inaf.it/ 94

[138] S. Liu. Sm–Co high-temperature permanent magnet materials. *Chinese Physics B* 28.1, **Jan. 2019**. Publishers: IOP Publishing Ltd, Chinese Physical Society, p. 017501.
DOI: 10.1088/1674-1056/28/1/017501 94

[139] W. H. Miller. Theory of Penning Ionization. I. Atoms. *The Journal of Chemical Physics* 52, **Apr. 1970**, pp. 3563–3572.
DOI: 10.1063/1.1673523 96

[140] F. Penning. Über Ionisation durch Metastabile Atome. *Naturwissenschaften* 15, **Jan. 1927**, pp. 818–818.
DOI: 10.1007/BF01505431 96

[141] A. Kramida, Yu. Ralchenko, J. Reader, and and NIST ASD Team. NIST Atomic Spectra Database (ver. 5.12), [Online]. National Institute of Standards and Technology, Gaithersburg, MD. Last Accessed: 2025-12-01. **2024**.
URL: https://physics.nist.gov/asd 96

[142] M.-C. Artru and W.-Ü L. Brillet. Analysis of the spectrum of quadruply ionized aluminum (Al v). *J. Opt. Soc. Am.* 64.8, **Aug. 1974**. Publisher: Optica Publishing Group, pp. 1063–1071.
DOI: 10.1364/JOSA.64.001063 96

[143] INAF-Osservatorio Astronomico di Palermo. XACT laboratory: X-ray calibration and testing facility. Last accessed: 2026-02-13. **2025**.
URL: http://www.astropa.inaf.it/facilities/il-laboratorio-xact/ 98

[144] Physikalisch-Technische Bundesanstalt. PTB Laboratory at BESSY II. Last Accessed: 2025-12-01. **2023**.
URL: www.ptb.de/cms/en/ptb/fachabteilungen/abt7/ptb-sr/ptbatbessy2 102

[145] J. D. Jackson. Classical electrodynamics. 3rd ed. Wiley, **1999**. ISBN: 9780471309321 112

[146] M. C. M. Cheung et al. Multi-component Decomposition of Astronomical Spectra by Compressed Sensing. *The Astrophysical Journal* 882.1, **Aug. 2019**. Publisher: The American Astronomical Society, p. 13.
DOI: 10.3847/1538-4357/ab263d 117

[147] K. Cho, B. De Pontieu and P. Testa. On the Nature of Nonthermal Broadening of Spectral Lines Observed by IRIS. *The Astrophysical Journal* 975.1, **Oct. 2024**. Publisher: The American Astronomical Society, p. 33.
DOI: 10.3847/1538-4357/ad7586 120

[148] K. J. H. Phillips, U. Feldman and E. Landi. Ultraviolet and X-ray Spectroscopy of the Solar Atmosphere. Cambridge University Press, **2008**, pp. 104–105.
DOI: 10.1017/CBO9780511585968 120

[149] K. P. Dere et al. CHIANTI - an atomic database for emission lines* - I. Wavelengths greater than 50 Å. *Astron. Astrophys. Suppl. Ser.* 125.1, **1997**, pp. 149–173.
DOI: 10.1051/aas:1997368 121, 122, 124, 133

[150] G. Del Zanna et al. CHIANTI—An Atomic Database for Emission Lines. XVI. Version 10, Further Extensions. *The Astrophysical Journal* 909.1, **Mar. 2021**. Publisher: The American Astronomical Society, p. 38.
DOI: 10.3847/1538-4357/abd8ce 121, 122, 124, 133

[151] X. Cheng et al. Differential Emission Measure Analysis of Multiple Structural Components of Coronal Mass Ejections in the Inner Corona. *The Astrophysical Journal* 761.1, **Nov. 2012**. Publisher: The American Astronomical Society, p. 62.
DOI: 10.1088/0004-637X/761/1/62 128

Formal Acknowledgments

I acknowledge funding from Implementation Agreement No. 2022-29-HH.0 between the Italian Space Agency (ASI) and the National Institute for Astrophysics (INAF) for the Italian participation in the NASA-MUSE mission (Principal Investigator: Prof. Fabio Reale), funding from the Università degli Studi di Palermo (UNIPA), via the 10% research budget allocated to PhD students (Resp. Prof. Marco Cannas), and funding from Instituto Nazionale di Astrofisica (INAF) Transformative Agreements.

The experiment at the METROLOGIE beamline was carried out by the acceptance of the proposal "VUV and XAS transmission response analysis of the Zr and Al coated CNT filters studied for the NASA space solar mission MUSE". I acknowledge SOLEIL Synchrotron for providing access to its synchrotron radiation facilities and for financial support (Proposal #20231204, Principal Investigator Edoardo Alaimo). I acknowledge the assistance of the beamline team, Dr. Pascal Mercère and Da Silva Paulo, who helped gather high-quality data, and aided my understanding of synchrotron laboratories.

I acknowledge INAF for providing access to its facilities, and I acknowledge the filters' group and the MUSE team at INAF/OAPA/UNIPA for their help, guidance, and support: Prof. Marco Barbera, Dr. Michela Todaro, Dr. Luisa Sciortino, Dr. Ugo Lo Cicero, Eng. Fabio D'Anca, Prof. Fabio Reale, Prof. Paolo Pagano, and Dr. Gabriele Cozzo. This work would not have been possible without their support and the rigorous scientific environment they foster. I also acknowledge technical help and assistance over the years from the technicians, researchers, and directors at the INAF/OAPA XACT laboratory: Mr. Gaspare Di Cicca, Mr. Roberto Candia, Mr. Salvatore Varisco, Mr. Claudio Saitta, Mr. Alberto Gulizzi, Dr. A. Jimenez-Escobar, Dr. Alfonso Collura, Dr. Davide Cardinale, M.Sc. Federico Fiorentino, the past director of INAF-OAPA, Dr. Fabrizio Bocchino, and the current director, Dr. Angela Ciaravella.

I acknowledge help, guidance, and support during my 3-month stay in Palo Alto, California, as a visiting student at the LMSAL, during the development and testing of the BGFA procedure detailed in Appendix E, and during the development of the studies of diffraction content from Araya Silpikul, Prof. Fabio Reale, Dr. Paola Testa, Dr. Bart De Pontieu, Dr. Juan Martinez Sykora, Dr. Vishal Upendran, Dr. Nabil Freij, Dr. Adrian Daw, Prof. Charles Kankelborg, and Dr. Aimee Norton.

I acknowledge continuous scientific and technical support from Dr. Daniele Spiga for providing the simulation inputs for the Point Spread Functions, and the useful discussions along the way. I acknowledge support from Dr. Paul Boerner in aiding the calculation of the UV-VIS-IR requirement. I acknowledge helpful discussions, improving the quality of the scientific inquiries carried out during my research, with Dr. Ben Zeiger, and technical support from Dr. Pekka T. Törma, M.Sc. Bjørn Mikladal, and Dr. Peter Cheimets. I also acknowledge the esteemed referees for the honest and high-quality review of my work and for the prompt feedback, which allowed me to improve the content of the thesis.

For the thesis typesetting, I acknowledge usage and modification of the `Overleaf` TEXtured — LATEX Template, authored by Dr. J. Dujava.

Informal Acknowledgments

While in the formal acknowledgments, I tried my best not to let my heart slip in, this section proves to be the best place to hold down. This thesis involved enabling solar observations, and thus, this section must be the warmest.

I have been extremely fortunate to have had so many opportunities at the University of Palermo, cultivating national and international collaborations, and also visiting many different places all around the world to learn about others' science and communicate my own. For this reason, I am extremely thankful to the entirety of the University.

Many thanks go to all of the professors and researchers who have guided me during the doctoral years. I deeply thank Prof. Marco Cannas, the head of the Ph.D. program in Physical and Chemical Sciences at the University of Palermo, for ensuring that the program could progress without a hitch. I thank Prof. Fabio Reale for believing in my capabilities and for heading the international collaboration that enabled so much science and discovery for the whole group in the context of an exciting space mission. I thank Prof. Marco Barbera, the leader of the INAF-OAPA/UNIPA filters' group, for managing with the eye of an eagle the scientific projects and collaborations while promoting scientific insights and aiding my understanding at every level. I thank the professors for the doctoral program, Prof. Giampiero Buscarino, Prof. Simonpietro Agnello, Prof. Giuseppina Micela, and Prof. Ciro Pinto, for providing me with highly advanced lectures on many complementary aspects to my research.

I also thank all of the Master's and Ph.D. students whom I've met in the Astrophysical Laboratory at UNIPA for all of the stories and laughs – such as (and not limited to) Vladimiro, Claudia, Simona, Francesco, Alessio, Carlotta, Mario, and also all of the younger Bachelor's colleagues. A warm thought goes to Dalila: we met fairly recently, but it feels like we have been friends for a very long time. A kind thought goes to Federica (or *Nika*, the God of freedom): you are very kindhearted, and I truly hope that you live as happily as you can, and that you accomplish your dreams even in the harsher times. I thank the Comitato Locale of the Associazione Italiana Studenti di Fisica (AISF-Palermo, local committee), all of its presidents (particularly Mario, forming the *Mario brothers* combo with the earlier Mario), for providing, as warmly as I could remember in my Master's studies, one of the best places fostering science and communication between students. Physics would be nothing without animated communication, and you all should be proud. I deeply thank my older colleagues, who are dear friends today: Vincenzo, Mattia, Kora, Jasmine, Francesca, Alessandro, Elena, Alessandro, and Gloria.

During my studies, I carried out many activities that I would never have considered possible for me to understand or accomplish. If this has been possible, it is thanks to my wonderful colleagues. I give my deep thanks to Ing. Fabio D'Anca, who helped me so much in developing my mechanical sense, and aided me also to grow as a person, and as a scientist – particularly in obscure fields such as mechanical vibrations. I thank Dr. Michela Todaro, Dr. Luisa Sciortino, and Dr. Ugo Lo Cicero, because their sheer will and passion are the burning fuel of the laboratory, and their indomitable attitude

serves as guidance and inspiration. Their aid was crucial for the success of the many EUV/X-ray synchrotron radiation-based campaigns. Guiding an X-ray Absorption experiment is an experience I will always treasure, though not the part regarding a few sleepless nights.

I have had the opportunity to visit many places and follow relevant schools. A hearty thanks goes to all of LMSAL's scientists and engineers. LMSAL is a flourishing environment for science: the stay and all of the scientific discussions that sparked from it have left a permanent mark on me regarding what is relevant and what is not, during the development of a space mission. I would like to thank the European Space Agency for accepting my request to participate in the Product Assurance Awareness Training Course (2023). This course, while not being *directly* useful to anything, was *indirectly* one of the most important sources of context for my work. I thank the Società Italiana Luce di Sincrotrone (SILS) for organizing and allowing me to participate in the School on Synchrotron Radiation (2024), where I could learn more about this exciting science and where many Master and Ph.D. Students such as myself could exchange projects, thoughts, experiences, and – *outside of the lectures* – drinks. I thank the Centre spatial de Liège (CSL) for providing access to its facility and allowing me to learn, understand, and obtain high-quality data of Spectroscopic Ellipsometry - an activity funded under the AHEAD2020 program. I thank Prof. Maria Pelizzo and Dr. Alain Corso for organizing the international workshop on Physics of X-Ray and Neutron Multilayer Structures (PXRNMS2025), which was such an eye-opening event. I also extend my gratitude to all of the scientists, engineers, representatives from space, research agencies and industries, professors, tutors, students, colleagues, and friends I met in these places.

Carrying out a Ph.D. is a tough journey both mentally and physically: one of study, hard work, improvements, burnouts, failures, glow-ups, and successes. A story that is lived and crafted, in which, as much as there is building up confidence, scientific maturity, and autonomy in the *outwards* direction – towards the masters, the scientific community, the academia, the laboratories, and the very nice resume appearance – a similar build-up happens in the *inwards* direction, where the relationships with the kindred, the important, and the loved ones are found, alongside with the relationship with Self. Both directions are important, and equilibrium is key.

As for my dearest colleagues, friends, and travelmates. I thank Gabriele, who has been a colleague, a dear friend, a *co-blogger* during our stay in California, and the co-organizer of possibly the best New Year's and Carnival parties in Palermo (though, we all know the true merit goes to your sister). I thank Federico: our duo and creative minds together would prove to be fatal while in scientific missions, especially when the *karateka* arrived, or when you ordered the menu *a few days ago*. I thank Davide, who has joined the XACT laboratory fairly recently, and has proven to be a great asset, other than a wonderful (~~chaotic~~) human being. I believe Davide told me "*Go! Go! Go!*" to cheer me up more than any other in my life during the hard times.

I thank my closest friends. Riccardo, a brother of mine: we have shared more than half our lives together, as well as Sake cups, and I wonder what else is to come. Enrico, for your humor and zest. Ciccio, for your lucidity and temper. Fabiola, for being one of the best human beings I know. Davide, for being sensible and kind. Giulio, for being gentle and authentic. Claudia, for your irony, depth, and strength. Claudio, for your

resilience, and honesty. You all are simply home to me, not just friends, even thousands of kilometers away, and even during dire times: I always treasure our bonds.

A huge portion of my heart is devoted to my family – Tiziana, Vincenzo, Giuseppe, Roberta, Silvia, Roberto, and all my relatives. Thank you for your unwavering love and support, and be assured of mine.

To Gaia. You are my companion, my best friend, and my love. I have met you (again) recently, but I feel such a deep connection, and I feel very lucky to have found such complicity together. I am deeply grateful for what we are building together. Ti amo *pappala*.

To all of the colleagues, students, and friends that I have met as a Ph.D. student, and to everyone who encountered and supported me during these three years, I would like to extend my fervent thanks.